Search for Bs Mixing with Inclusive Lepton Events at SLD

Thomas Moore

Stanford Linear Accelerator Center
Stanford University
Stanford, CA 94309

SLAC-Report-551

ABSTRACT

Search for B_s Mixing with Inclusive Lepton Events at SLD

Thomas Moore

Yale University

2000

We have performed a sensitive search for $B_s^0 - \bar{B}_s^0$ mixing using a sample of 400,000 hadronic Z^0 decays collected by the SLD experiment at the SLC between 1996 and 1998. B_s^0 and $\bar{B}_s^0$ events were produced by $Z^0 \rightarrow b\bar{b}$ decays where each side hadronized independently to b hadrons. The analysis determines the b hadron flavor at production by exploiting the large polarized forward-backward asymmetry of the b quark as well as information from the hemisphere opposite that of the reconstructed B decay. The final state b quark flavor is determined by the charge of a high p_T lepton. A novel, highly efficient vertexing technique has been developed to locate the B decay vertex by exploiting the high p_T lepton and the semileptonic decay topology. No significant mixing signal was found and the following ranges of the oscillation frequency of $B_s^0 - \bar{B}_s^0$ mixing are excluded at 95% CL from the analysis presented in this thesis:

$$\Delta m_s \quad < 1.3 \text{ ps}^{-1},$$
$$2.0 < \quad \Delta m_s \quad < 8.6 \text{ ps}^{-1}, \text{ and}$$
$$9.8 < \quad \Delta m_s \quad < 12.2 \text{ ps}^{-1}.$$

The gaps extending from 1.3 to 2.0 ps^{-1} and 8.6 to 12.2 ps^{-1} are excluded by other analyses. Combining results, $\Delta m_s < 12.3$ ps^{-1} can be excluded at 95% CL. This limit puts significant constraints on the CKM unitarity triangle as shown in figure 6.11.

Search for B_s Mixing with Inclusive Lepton Events at SLD

A Dissertation

Presented to the Faculty of the Graduate School

of

Yale University

in Candidacy for the Degree of

Doctor of Philosophy

By

Thomas Moore

Dissertation Director: Charles Baltay

2000

acknowledgements

There are many people I should thank for their contributions to this thesis. First, my advisor, Charles Baltay, for giving me the opportunity to work with the SLD experiment. I've always admired Professor Baltay's ability to see the long term goals and future directions of particle physics. His insight has allowed the Yale group to continually be at the forefront of physics research.

I'd also like to thank Steve Manly who introduced me to the SLD experiment and the B mixing analysis. He has given me alot of excellent advice over the years both on physics and also on how to survive in the scientific community. This work owes much to former Yale graduate student Ming Liu. Ming's excellent thesis work on B_d^0 mixing laid the groundwork for the subsequent search for B_s^0 mixing described here. Thanks also to Jeff Snyder who patiently shared an office with me while I struggled to learn the SLD software.

I'm grateful to all the people at SLAC who made my brief stay in California a pleasant and very rewarding experience. I am particularly indebted to Stephane Willocq, the organizer of the SLD B mixing and lifetimes group. Stephane has kept a close eye on my work and provided me with guidance and many helpful discussions. He has continually kept the B mixing effort at SLD focused and motivated by his example. I've also obtained much invaluable advice from Su Dong, John Jaros, Tracy Usher, David Jackson, Richard DuBois and Ken Baird. Thanks also to Jerry Va'vra and John Coller who taught me all about the endcap CRID.

My greatest thanks and admiration go to my parents, Harvey and Michael Moore. They have continually supported my interest in physics through many years of college and graduate school. It is mostly due to them that I have had the opportunity to

pursue my goals.

Finally, it has been a pleasure working on the SLD experiment. I can't possibly mention all the people who have contributed to this work, possibly in ways I probably don't even realize. Thanks to them, the SLD and SLC have been a great success.

Contents

List of Tables

List of Figures

Chapter 1

Introduction and Theory

The phenomenon of $B^0 - \bar{B}^0$ mixing refers to particle-antiparticle oscillations in the neutral B meson system where B^0 can be either B_d^0 or B_s^0. The mixing is due to the fact that the flavor eigenstates are not the same as the mass eigenstates. Therefore, oscillations occur with a frequency determined by Δm_d or Δm_s, the mass difference between the two mass eigenstates. $B^0 - \bar{B}^0$ mixing is currently a very active area of research in high energy physics. As we will see shortly, mixing measurements address many of the outstanding questions relating to the Standard Model (SM) of particle physics. In particular, measurements of Δm_d and Δm_s can be directly related to Cabibbo-Kobayashi-Maskawa (CKM) matrix elements and may, therefore, shed light on the processes of CP violation and mass generation.

Many experiments including LEP, CDF, and SLD are currently producing results on B_d^0 and B_s^0 mixing. Over the past few years B_d^0 mixing has been well established and Δm_d has been measured to better than 4% uncertainty [1]. B_s^0 mixing, on the other hand, has yet to be observed directly. Only lower limits on Δm_s have been established. This thesis describes one of several $B_s^0 - \bar{B}_s^0$ mixing analyses performed at the SLD (SLAC Large Detector) experiment at SLAC (Stanford Linear Accelerator Center).

This chapter will begin with a brief overview of the Standard Model. We will then concentrate on the aspects of the SM which are relevant to physics at the Z^0 pole and particle-antiparticle oscillations. The discussion will include electroweak unification,

the Higgs mechanism, and the CKM matrix. Next, we will discuss the significant features of e^+e^- annihilation at the Z^0 pole, particularly with a polarized e^- beam, as performed at SLC (Stanford Linear Collider). Finally, the phenomenology of $B^0 - \bar{B}^0$ mixing will be discussed as well as the current activity in the field.

1.1   The Standard Model

The Standard Model provides the framework for our current understanding of elementary particle physics. It is a mathematical theory that describes the fundamental fermions (quarks and leptons) as well as their interactions through the strong, electromagnetic, and weak forces. To date, the SM has been extraordinarily successful in explaining the observed phenomena of high energy physics. Physics beyond the SM has yet to be firmly established unless we count the recent indication by SuperKamiokande that the neutrino may have a small mass [2]. Therefore, the main objectives of experimental particle physics at this time include precision tests of the Standard Model and searches for physics beyond the Standard Model.

The SM includes a description of the strong, electromagnetic, and weak forces. It assumes that these forces are transmitted by particles called mediators or gauge bosons that arise naturally through the requirement of *local gauge invariance*. That is, the theory is required to be invariant under local phase transformations based on various symmetry groups. The standard model symmetry is $SU(3) \otimes SU(2)_L \otimes U(1)_Y$. The $SU(3)$ symmetry describes the strong interactions between quarks and gluons due to their color charge. The resulting theory is known as quantum chromodynamics (QCD). The $SU(2)_L \otimes U(1)_Y$ term is the combined symmetry of the weak and electromagnetic interactions which have been unified into a single electroweak force. The mediators of the electroweak interaction are the $W^\pm$, Z^0, and γ. Gravity has not yet been successfully incorporated in the SM. Fortunately, the gravitational force is much weaker than the strong and electroweak forces at energy scales relevant to particle physics. The four known forces are listed in table 1.1 with the properties of their gauge bosons.

The fundamental fermions described by the SM are the quarks and leptons. The

force	gauge boson	charge	spin	mass (GeV)[1]
Strong	gluon(g)	0	1	0
Electromagnetic	photon(γ)	0	1	0
Weak	$\left\{ \begin{array}{c} W^\pm \\ Z^0 \end{array} \right.$	± 1 0	1 1	80.41 ± 0.10 91.187 ± 0.007
Gravity	graviton(G)	0	2	0

Table 1.1: The 4 known fundamental forces and gauge bosons

quarks come in six *flavors* denoted up, down, charmed, strange, top, and bottom. They are naturally grouped into three *families* or *generations* consisting of an *up* type and a *down* type quark. The second and third generations are essentially heavier copies of the first generation. This family structure is not explained by the SM nor are the irregular mass splittings between generations understood. The *up* type quarks have an electromagnetic charge of $+2/3$ while the *down* type quarks have an electromagnetic charge of -1/3. The quarks also carry color charge and, therefore, participate in all interactions described by the SM. Quarks are bound together by the strong force to form *hadrons*. The hadrons consist of quark-antiquark pairs ($q\bar{q}$) called mesons and three quark combinations (qqq) called baryons. In fact, the strong force binds all quarks into combinations that are color singlets such that free quarks are not observed. This phenomenon is known as quark confinement.

The leptons also display the family structure observed in the quark sector. The three charged leptons are the electron (e^-), muon (μ^-), and tau (τ^-). Each charged lepton has its own associated neutrino (ν_e, ν_μ, and ν_τ). Leptons do not carry color charge and, therefore, are unaffected by the strong interactions. The charged leptons participate in the weak and electromagnetic interactions but the neutrinos are electrically neutral and are only affected by weak interactions.

Finally, the SM includes mass generation by a process known as the Higgs mechanism which will be described in detail in section 1.2.2. In the Minimal Standard Model (MSM) we assume an isodoublet of scalar Higgs fields. Fermion mass generation results from the Yukawa couplings of the fermions to the Higgs. The Higgs particle has yet to be observed and the composition of the Higgs sector is not well known. Higgs searches are a very active area of research at this time.

1.2 Electroweak Physics

$B^0 - \bar{B}^0$ mixing is the result of second order weak interactions. As we shall see, mixing measurements provide access to V_{td}, one of the least well measured elements of the CKM matrix. This matrix describes the extent of cross generation couplings in the charged weak currents. It is intimately related to the processes of mass generation and CP violation. These two areas of the SM have not been precisely tested and are likely candidates for new physics. Therefore, this section will describe electroweak physics in the SM in more detail and describe how mass generation and CP violation are explained in the SM.

1.2.1 Unification

In the SM, the structure of the interactions between fermions and mediators is derived from the principle of local gauge invariance. As mentioned above, the strong, weak, and electromagnetic forces are transmitted by spin 1 particles known as gauge bosons. These gauge bosons are simply the quanta of the gauge fields that must be introduced to enforce invariance of the theory under local phase transformations. As an example of the technique, we will consider quantum electrodynamics, the simplest gauge field theory [3].

The free particle lagrangian density for a Dirac field $\psi(x)$ is given by,

$$\mathcal{L}_1 = \bar{\psi}(x)(i\gamma^\mu \partial_\mu - m)\psi(x) \tag{1.1}$$

where m is the fermion mass. Suppose we apply a global phase transformation such that the phase of the field is changed by a constant amount at each space-time point x,

$$\psi(x) \rightarrow e^{-iq\Lambda}\psi(x). \tag{1.2}$$

It is apparent that the lagrangian density will remain unaltered by this transformation of the fields. Thus the theory is invariant under global phase transformations. It seems reasonable that the theory should also be invariant under a *local* phase transformation which we express as,

$$\psi(x) \rightarrow e^{-iq\Lambda(x)}\psi(x) \tag{1.3}$$

where Λ is an arbitrary function. Note that the phase we have introduced is now a function of the space-time coordinate x. Due to the derivative term, the lagrangian density $\mathcal{L}_1$ is no longer invariant. It becomes,

$$\mathcal{L}_1 \to \mathcal{L}_1 + q\bar{\psi}(x)\gamma^\mu\psi(x)\partial_\mu\Lambda(x). \tag{1.4}$$

If we wish to enforce local gauge invariance, we are required to introduce another term in the lagrangian. This can be accomplished by replacing the derivative with the *covariant derivative* defined by,

$$D_\mu\psi(x) = (\partial_\mu + iqA_\mu)\psi(x) \tag{1.5}$$

where A_μ is called the gauge field. We recover the invariance of the lagrangian if A_μ is required to transform as,

$$A_\mu \to A_\mu + \partial_\mu\Lambda \tag{1.6}$$

under the local phase transformation defined by equation 1.3. It can be shown that the covariant derivative transforms like the fermion field $\psi(x)$,

$$D_\mu\psi(x) \to \mathrm{e}^{-iq\Lambda(x)}D_\mu\psi(x). \tag{1.7}$$

Therefore, the new lagrangian density is invariant under the combined transformation given in equations 1.3 and 1.6.

Since we have introduced a new field A_μ we must also consider its free field contributions to the lagrangian. The following term can be shown to be gauge invariant,

$$F_{\mu\nu} = \partial_\mu A_\nu - \partial_\nu A_\mu. \tag{1.8}$$

The final gauge invariant lagrangian is given by,

$$\mathcal{L} = \bar{\psi}(x)(i\gamma^\mu D_\mu - m)\psi(x) - \frac{1}{4}F_{\mu\nu}F^{\nu\mu}. \tag{1.9}$$

In the language of group theory, the transformation we applied above is a representation of the $U(1)$ group, the set of unitary 1×1 matrices. This symmetry apparently describes the electromagnetic interaction very well. Can we employ a larger symmetry group to describe the weak interactions? One problem is immediately apparent. The

three weak gauge bosons are very massive as evidenced by their strength at low energy and short range. The technique described above results in massless gauge bosons as a mass term $\propto A_\mu A^\mu$ would not be gauge invariant. However, this complication will be dealt with at a later stage.

Generalizing the procedure described above, we would look for a symmetry group with three generators (resulting in three gauge bosons) to describe the weak interactions. $SU(2)$ seems to be a likely candidate. However, we would like to unify the weak and electromagnetic forces under a common symmetry. One problem is that the weak interactions are known to violate parity. The weak couplings contain vector and axial vector components in a form $\sim \gamma^\mu (1 - \gamma^5)$. The sum of vector and axial vector components results in the observed parity violation. This would seem to preclude unification with the electromagnetic interactions which are purely vectorial and, therefore, conserve parity. The solution is to group only the *left handed* components of the quark and lepton fields into $SU(2)$ doublets while the right handed components remain $SU(2)$ singlets [4],

$$\text{Leptons}: \begin{pmatrix} \nu_e \\ e \end{pmatrix}_L, \begin{pmatrix} \nu_\mu \\ \mu \end{pmatrix}_L, \begin{pmatrix} \nu_\tau \\ \tau \end{pmatrix}_L, e_R, \mu_R, \tau_R \qquad (1.10)$$

$$\text{Quarks}: \begin{pmatrix} u \\ d \end{pmatrix}_L, \begin{pmatrix} c \\ s \end{pmatrix}_L, \begin{pmatrix} t \\ b \end{pmatrix}_L, u_R, d_R, c_R, ...$$

The SM assumes that there are no right handed neutrino states. The subscript L actually refers to the left *chiral* projection where the left and right chirality projection operators are,

$$P_L = \frac{1}{2}(1 - \gamma^5), \qquad (1.11)$$
$$P_R = \frac{1}{2}(1 + \gamma^5).$$

In the limit of massless fermions, the chirality operators reduce to the helicity operator. The doublets have total weak isospin $T = 1/2$. The upper member is assigned $T_3 = 1/2$ while the lower member is assigned $T_3 = -1/2$. Each fermion is also assigned a value of *weak hypercharge Y* by the Gell-Mann-Nishijima formula originally

fermion	T	T_3	$\frac{1}{2}Y$	Q
ν_{eL}	$\frac{1}{2}$	$\frac{1}{2}$	$-\frac{1}{2}$	0
e_L	$\frac{1}{2}$	$-\frac{1}{2}$	$-\frac{1}{2}$	-1
u_L	$\frac{1}{2}$	$\frac{1}{2}$	$-\frac{1}{6}$	$\frac{2}{3}$
d_L	$\frac{1}{2}$	$-\frac{1}{2}$	$-\frac{1}{6}$	$-\frac{1}{3}$
e_R	0	0	-1	-1
u_R	0	0	$\frac{2}{3}$	$\frac{2}{3}$
d_R	0	0	$-\frac{1}{3}$	$-\frac{1}{3}$

Table 1.2: Fermion weak isospin and hypercharge assignments.

applied to strong isospin:

$$Q = T_3 + \frac{1}{2}Y, \tag{1.12}$$

where Q is the fermion charge. Table 1.2 lists the weak isospin and hypercharge assignments for the fermions in the first generation.

The electroweak symmetry group is taken to be $SU(2)_L \otimes U(1)_Y$ where the L indicates that the weak isospin symmetry only applies to the left chiral projections and Y refers to weak hypercharge. Coupling constants of g and g' are assumed for the isospin and hypercharge symmetries respectively. Applying local gauge invariance in this case is more complicated due to the non-abelian $SU(2)$ symmetry but the process is the same. The resulting covariant derivative is [4],

$$D_\mu = \partial_\mu + ig\mathbf{W}_\mu \cdot \mathbf{T} + ig'\frac{1}{2}B_\mu Y \tag{1.13}$$

where we have introduced the gauge fields $\mathbf{W}^\mu$ and B^μ resulting from the $SU(2)_L$ and $U(1)_Y$ symmetries respectively and $\boldsymbol{T} = \boldsymbol{\tau}/2$ in terms of the Pauli matrices.

The covariant derivative D_μ contains terms describing the interactions of fermions and the gauge fields. If the covariant derivative above is to describe the electromagnetic interaction, then the neutral component, $igW_{3\mu}T_3 + ig'\frac{1}{2}B_\mu Y$, must contain a term iQA_μ where A^μ is the electromagnetic 4-vector potential describing the photon field. Therefore, we express the fields A and Z as a linear combination of the gauge fields W_3 and B,

$$A \equiv B\cos\theta_w + W_3\sin\theta_w \tag{1.14}$$
$$Z \equiv -B\sin\theta_w + W_3\cos\theta_w$$

fermion	v_f	a_f	A_f
ν_e, ν_μ, ν_τ	$\frac{1}{2}$	$\frac{1}{2}$	1
e, μ, τ	$-\frac{1}{2} + 2\sin^2\theta_w$	$-\frac{1}{2}$	0.15
u, c, t	$\frac{1}{2} - \frac{4}{3}\sin^2\theta_w$	$\frac{1}{2}$	0.67
d, s, b	$-\frac{1}{2} - \frac{2}{3}\sin^2\theta_w$	$-\frac{1}{2}$	0.94

Table 1.3: The neutral vector and axial vector couplings. Also given is the asymmetry $A_f = 2a_f v_f / (a_f^2 + v_f^2)$ calculated for $\sin^2\theta_w = 0.231$.

where θ_w is an input parameter that must be measured by experiment known as the weak mixing angle. The neutral term can then be expressed as,

$$igW_3 T_3 + ig'\frac{1}{2}BY = iA[g\sin\theta_w T_3 + g'\cos\theta_w \frac{1}{2}Y] \tag{1.15}$$
$$+ iZ[g\cos\theta_w T_3 - g'\sin\theta_w \frac{1}{2}Y].$$

We know that the coefficient of the A term should be iQ. Using $Q = T_3 + \frac{1}{2}Y$, we obtain $g = e/\sin\theta_w$ and $g' = e/\cos\theta_w$ or,

$$\theta_w \equiv \tan^{-1}\left(\frac{g'}{g}\right). \tag{1.16}$$

We can define the charged fields $W^\pm$ as,

$$W^\pm \equiv \frac{1}{\sqrt{2}}(W^1 \mp iW^2) \tag{1.17}$$

so that $\mathbf{W} \cdot \mathbf{T} = W^+ T^+ + W^- T^- + W^3 T^3$ where $T^{+-} = (T^1 \pm iT^2)/\sqrt{2}$. Note that T^+ and T^- are just weak isospin raising and lowering operators. They couple the upper and lower members of SU(2) doublets which differ in charge by $\Delta Q = \pm 1$. Therefore, the $W^\pm$ fields carry electromagnetic charge $Q = \pm 1$.

In terms of the physical fields $W^\pm$, Z^0, and A, we can now construct expressions for the charged, neutral, and electromagnetic currents,

$$J_L^{\pm\mu} = \sqrt{2}\bar{\psi}\gamma^\mu T_L^\pm \psi \tag{1.18}$$
$$J_Z^\mu = \bar{\psi}\gamma^\mu[T_{3L} - Q\sin^2\theta_w]\psi$$
$$J_{em}^\mu = \bar{\psi}\gamma^\mu Q\psi.$$

It is understood that ψ consists of left-handed isospin doublets and right-handed singlets for each quark and lepton generation. Also the $SU(2)$ operators T vanish when acting on the right-handed isosinglets. Since the charged current is proportional to $T_L^\pm$, only the left-handed fields are involved. Therefore, the coupling is $\propto \gamma^\mu(1-\gamma^5)$ which is referred to as purely 'V-A'. It is this sum of vector and axial vector terms that results in parity violation in the weak interaction. Since the vector and axial vector parts contribute equally, the charged weak interactions violate parity maximally. The neutral weak current, on the other hand, can be expressed as $\bar{f}\gamma^\mu(v_f - a_f\gamma^5)f$ for each fermion f where,

$$
\begin{aligned}
v_f &= T_3 - 2Q\sin^2\theta_w \\
a_f &= T_3.
\end{aligned}
\tag{1.19}
$$

This is not a pure 'V-A' coupling and, therefore, involves both left and right handed states. Parity violation at the Z^0 vertex can be expressed in terms of an 'interference' factor $A_f = 2a_f v_f/(a_f^2 + v_f^2)$. The larger A_f, the more strongly parity is violated for fermion f. Table 1.3 lists the SM values of v_f and a_f for the various fermions.

Finally, the electroweak interaction lagrangian can be expressed as,

$$
-\mathcal{L} = eJ_{em}^\mu A_\mu + \frac{g}{\sqrt{2}}(J_L^{+\mu}W_\mu^+ + J_L^{-\mu}W_\mu^-) + g_Z J_Z^\mu Z_\mu
\tag{1.20}
$$

where $g_Z \equiv e/(\sin\theta_w \cos\theta_w)$. The fermions and gauge bosons are all massless at this point since mass terms break the gauge invariance. This problem will be discussed in the next section.

1.2.2 The Higgs Mechanism and Mass Generation

The major shortcoming of the $SU(2)_L \otimes U(1)_Y$ unified electroweak theory presented above is that the gauge fields as well as the fermion fields are left massless. In the SM, this problem is partially resolved by the Higgs Mechanism. The procedure is to introduce an $SU(2)$ doublet of complex scalar fields Φ [4],

$$
\Phi = \begin{pmatrix} \phi^+ \\ \phi^0 \end{pmatrix}.
\tag{1.21}
$$

The lagrangian then acquires terms,

$$\mathcal{L}_\Phi = |D_\mu \Phi|^2 - V(|\Phi|^2) + \mathcal{L}_\Phi^F \tag{1.22}$$

where D_μ is the electroweak covariant derivative, $|\Phi|^2 = \Phi^\dagger \Phi$, $\mathcal{L}_\Phi^F$ is the Yukawa coupling of the fermions to the Φ and the potential is,

$$V(|\Phi|^2) = \mu^2 |\Phi|^2 + \lambda |\Phi|^4. \tag{1.23}$$

This is the most general renormalizable form for the scalar potential. Minimizing V with respect to $|\Phi|^2$ we find that the ground state corresponds to $|\Phi|^2 = -\mu^2/2\lambda$ ($\mu^2 < 0$). Therefore, the vacuum expectation value (vev) of the Φ fields is non-zero. Also, since $|\Phi|^2 = |\phi^+|^2 + |\phi^0|^2$, there is a continuous set of allowed ground state values for $|\phi^+|^2$ and $|\phi^0|^2$. By selecting any particular choice of these allowed values of the ground state, the $SU(2) \otimes U(1)$ symmetry is 'spontaneously broken'. As we shall see, breaking this symmetry allows the weak gauge bosons and fermions to obtain mass.

The field Φ should then be expressed relative to the ground state:

$$\Phi(x) = \exp\left(\frac{i\boldsymbol{\xi}(x) \cdot \boldsymbol{\tau}}{2v} \right) \begin{pmatrix} 0 \\ (v + H(x))/\sqrt{2} \end{pmatrix} \tag{1.24}$$

where $v/\sqrt{2} \equiv \sqrt{-\mu^2/2\lambda}$. The two complex fields ϕ^+ and ϕ^- have been replaced by four real fields $\boldsymbol{\xi}$ and H. The phase factor can be removed by applying an $SU(2)$ gauge transformation with $\boldsymbol{\alpha}(x) = \boldsymbol{\xi}(x)/v$. Thus $\Phi(x)$ is expressed in terms of a single real scalar field H known as the Higgs field.

It can be shown that the lagrangian, expressed in terms of H is,

$$\mathcal{L}_\Phi = \frac{1}{2}(\partial H)^2 + \frac{1}{4}g^2 W^+ W^- (v + H)^2 + \tag{1.25}$$
$$\frac{1}{8}g_Z^2 ZZ(v + H)^2 - V[\frac{1}{2}(v + H)^2] + \mathcal{L}_\Phi^F.$$

The terms proportional to W^+W^- and ZZ are mass terms . Thus the $W^\pm$ and Z fields have acquired masses $M_W = \frac{1}{2}gv$ and $M_Z = \frac{1}{2}g_Z v = M_W/\cos\theta_w$. The photon field A has remained massless as required. Note that the spin 1 $W^\pm$ and Z^0 now have three allowed polarization states. In the unbroken gauge theory, the massless gauge

bosons are only allowed the two transverse polarization states. It may be said that the three $\xi(x)$ degrees of freedom that were removed by an $SU(2)$ gauge transformation have returned as longitudinal polarization states of the $W^{\pm}$ and Z^0.

We now turn to $\mathcal{L}_{\Phi}^F$ which describes the Yukawa couplings of the Higgs field to the fermion fields. First we will consider the more general case of quarks. The most general $SU(2)_L \otimes U(1)_Y$ gauge invariant Yukawa interaction is,

$$\mathcal{L} = -\sum_{i=1}^{3}\sum_{j=1}^{3}[\tilde{G}_{ij}\bar{u}_{iR}(\tilde{\Phi}^{\dagger}D_{jL}) + [G_{ij}\bar{d}_{iR}(\Phi^{\dagger}D_{jL})] + \text{h.c.} \quad (1.26)$$

where

$$D_{jL} \equiv \left(\begin{array}{c} u_j \\ d_j \end{array} \right)_L \quad (1.27)$$

is an $SU(2)_L$ doublet of weak interaction eigenstates with generation index j. The right handed $SU(2)$ singlets are denoted u_{iR} and d_{iR} for the up-type and down-type quarks respectively. G_{ij} and $\tilde{G}_{ij}$ each contain nine complex coupling constants which are parameters of the theory and $\tilde{\Phi} = i\tau_2\Phi^*$.

The quark mass terms produced by the Yukawa couplings can be expressed as,

$$\overline{(u_1\ u_2\ u_3)_R}\ \mathcal{M}^u \left(\begin{array}{c} u_1 \\ u_2 \\ u_3 \end{array} \right)_L + \text{h.c.}, \quad (1.28)$$

$$\overline{(d_1\ d_2\ d_3)_R}\ \mathcal{M}^d \left(\begin{array}{c} d_1 \\ d_2 \\ d_3 \end{array} \right)_L + \text{h.c.}$$

where $\mathcal{M}_{ij}^u = \frac{v}{\sqrt{2}}\tilde{G}_{ij}$ and $\mathcal{M}_{ij}^d = \frac{v}{\sqrt{2}}G_{ij}$ are the weak eigenstate mass matrices for the up-type and down-type quarks. Each is composed of nine complex parameters. The off-diagonal elements couple weak interaction eigenstates of different generations.

To obtain the quark mass eigenstates we diagonalize the mass matrices by applying a 'bi-unitary transformation'. Any complex matrix can be diagonalized by multiplying it on the left and right by the appropriate unitary matrices,

$$U_R^{-1}\mathcal{M}^u U_L = \text{Diag}(m_u,\ m_c,\ m_t) \quad (1.29)$$

$$D_R^{-1}\mathcal{M}^d D_L = \text{Diag}(m_d,\ m_s,\ m_b).$$

The quark mass eigenstates are then defined by,

$$
\begin{pmatrix} u \\ c \\ t \end{pmatrix}_{L,R} = U_{L,R}^{-1} \begin{pmatrix} u_1 \\ u_2 \\ u_3 \end{pmatrix}_{L,R} \quad , \quad \begin{pmatrix} d \\ s \\ b \end{pmatrix}_{L,R} = D_{L,R}^{-1} \begin{pmatrix} d_1 \\ d_2 \\ d_3 \end{pmatrix}_{L,R} \quad . \tag{1.30}
$$

From equation 1.19, the charged weak currents couple the upper and lower members of $SU(2)$ doublets due to the off-diagonal elements in $T^{\pm}$. We can express the charged current as,

$$
\overline{(u_1\ u_2\ u_3)_L}\gamma^{\mu} \begin{pmatrix} d_1 \\ d_2 \\ d_3 \end{pmatrix}_L = \overline{(u\ c\ t)_L}U_L^{\dagger}D_L\gamma^{\mu} \begin{pmatrix} d \\ s \\ b \end{pmatrix}_L \quad . \tag{1.31}
$$

We define $V \equiv U_L^{\dagger}D_L$ so that

$$
U_L^{\dagger}D_L \begin{pmatrix} d \\ s \\ b \end{pmatrix} = V \begin{pmatrix} d \\ s \\ b \end{pmatrix} \equiv \begin{pmatrix} d' \\ s' \\ b' \end{pmatrix} \quad . \tag{1.32}
$$

Therefore, the $W^{\pm}$ couples the up-type mass eigenstates u, c, t to the *rotated* down-type states d', s', b' where d', s', b' are each linear combinations of the down-type mass eigenstates as shown above. The matrix V is the Cabibbo-Kobayashi-Maskawa matrix. It arises from the diagonalization of the quark mass matrices and expresses the extent of cross generational couplings in the charged weak interactions. The left handed neutral weak currents can similarly be expressed as,

$$
\overline{(u_1\ u_2\ u_3)_L}\gamma^{\mu} \begin{pmatrix} u_1 \\ u_2 \\ u_3 \end{pmatrix}_L = \overline{(u\ c\ t)_L}U_L^{\dagger}U_L\gamma^{\mu} \begin{pmatrix} u \\ c \\ t \end{pmatrix}_L \quad . \tag{1.33}
$$

But $U_L^{\dagger}U_L = 1$ so there is no cross generation mixing in the neutral weak interactions.

For leptons the situation is simplified due to the absence of right handed neutrinos. Of course, this is simply an assumption of the SM which is due to the fact that no right handed neutrinos have been observed. If neutrinos do turn out to have a small

mass, as the recent SuperKamiokande results suggest [2], then right handed neutrinos would exist and mass generation in the lepton sector would be identical to that in the quark sector. For now, we will simply observe that the absence of right handed neutrinos would cause the equivalent terms involving $\tilde{\Phi}$ in equation 1.26 to vanish. Furthermore, since the neutrinos are massless, then inter-generation couplings are not physically meaningful. To illustrate this point, consider the quark states u, c, t and d', s', b' defined above. These states represent a perfectly good set of weak interaction eigenstates since they are directly coupled by the $W^{\pm}$. We have simply arranged the rotation V on the down type states such that the weak eigenstates coincide with the mass eigenstates for the up-type quarks. A similar procedure could be performed for the leptons with $u, c, t \rightarrow e, \mu, \tau$ and $d', s', b' \rightarrow \nu_e, \nu_\mu, \nu_\tau$. The difference is that in the quark sector we must retain the concept of the down-type mass eigenstates d, s, b because they are physically distinguishable due to their masses. Neutrinos are all massless so there are no mass eigenstates. The states ν_e, ν_μ, ν_τ are simply defined to be the weak interaction partners of e, μ, τ.

Therefore, the Yukawa coupling lagrangian for the lepton sector can be expressed as,

$$\mathcal{L} = -G_e[\bar{e}_R(\Phi^\dagger l_L) + (\bar{l}_L \Phi)e_R] \tag{1.34}$$

where G_e is an arbitrary coupling constant and

$$l_L = \begin{pmatrix} \nu_e \\ e \end{pmatrix}_L. \tag{1.35}$$

A similar expression exists for both the μ and τ. The lagrangian reduces to,

$$\mathcal{L} = -(G_e v/\sqrt{2})\bar{e}e - (G_e v/\sqrt{2})H\bar{e}e. \tag{1.36}$$

Thus, the electron obtains a mass $m_e = G_e v/\sqrt{2}$ and a coupling to the Higgs boson. So by the spontaneous symmetry breaking produced by the scalar Higgs field and the Yukawa couplings to the fermions, all fermions and gauge bosons have obtained masses. However, we have introduced many new parameters to the theory such as the Higgs vev and Yukawa couplings that can not be calculated. Therefore, mass generation remains one of the more intriguing puzzles in particle physics.

1.2.3 The CKM Matrix

As we saw in the previous section, the CKM matrix is defined as,

$$V_{CKM} \equiv U_L^\dagger D_L = \begin{pmatrix} V_{ud} & V_{us} & V_{ub} \\ V_{cd} & V_{cs} & V_{cb} \\ V_{td} & V_{ts} & V_{tb} \end{pmatrix}. \qquad (1.37)$$

For three generations, V_{CKM} is a 3×3 unitary matrix. In general an $n \times n$ complex matrix has $2n^2$ parameters. But unitarity requires $V^\dagger V = 1$ which implies n^2 constraints [4],

$$(V^\dagger V)_{ij} = \sum_{k=1}^{n} V_{ki}^* V_{kj} = \delta_{ij} \qquad (1.38)$$

Therefore, we are left with n^2 free parameters. However, the CKM matrix is defined by its operation on the quark fields. In general, each of the $2n$ fields can absorb an arbitrary phase factor. But since the CKM matrix is left unchanged by a common phase transformation of all the quark fields, only $2n - 1$ arbitrary phases can be removed. Finally, we are left with $(n - 1)^2$ physically independent parameters. Furthermore, a real unitary matrix can be shown to have $n(n - 1)/2$ independent parameters. Therefore, the number of complex phases is $(n - 2)(n - 1)/2$. So for three generations, the CKM matrix has four independent parameters including a single complex phase. Note that for n less than three no phases are left in the matrix. As we shall see shortly, this phase in the CKM matrix is the SM explanation for CP violation. This observation originally inspired Kobayashi and Maskawa to propose a third generation.

A popular representation of the CKM matrix is the Wolfenstein parametrization [5],

$$V_{CKM} \approx \begin{pmatrix} 1 - \lambda^2/2 & \lambda & A\lambda^3(\rho - i\eta) \\ -\lambda & 1 - \lambda^2/2 & A\lambda^2 \\ A\lambda^3(1 - \rho - i\eta) & -A\lambda^2 & 1 \end{pmatrix} \qquad (1.39)$$

where the four CKM parameters are λ, A, ρ, and η. Note that the upper 2×2 submatrix is simply a small angle approximation to a 2×2 rotation matrix through an angle λ. For two generations, the CKM matrix reduces to the familiar Cabibbo-GIM

$$(\rho, \eta)$$

$$\frac{|V_{ud}^* V_{ub}|}{|V_{cd}^* V_{cb}|} \qquad \alpha \qquad \frac{|V_{td}^* V_{tb}|}{|V_{cd}^* V_{cb}|}$$

$$\gamma \qquad \qquad \beta$$

$$(0,0) \qquad \qquad (1,0)$$
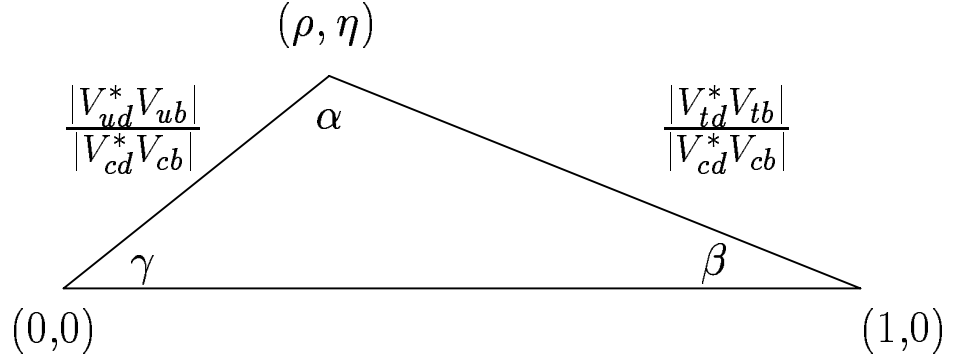
Figure 1.1: The unitarity triangle.

scheme with $\lambda = \sin \theta_C$. A, ρ, and η are of order 1 so the Wolfenstein parametrization has the important feature of characterizing quark transitions as an expansion in powers of λ.

The unitarity constraints involving complex elements can be expressed as a triangle in the complex plane. One of the more interesting is,

$$V_{ud}^* V_{ub} + V_{cd}^* V_{cb} + V_{td}^* V_{tb} = 0. \tag{1.40}$$

Figure 1.1 shows the resulting *unitarity triangle* and defines the angles α, β, and γ. The apex of the triangle is located at (ρ, η). A non-zero phase factor η provides the SM explanation for CP violation. This can be understood by noting that $\eta \neq 0$ implies a complex SM Hamiltonian since the CKM matrix factors into the charged weak currents [6]. But if the Hamiltonian is complex then the theory is not invariant under time reversal, $THT^{-1} \neq H$, due to the complex conjugation produced by the T operation. We know that the combined operation CPT is a good symmetry for all quantum field theories so violation of the T symmetry implies that CP must be violated as well. Therefore, by measuring the sides and the angles we can overconstrain the shape of the triangle and test the SM explanation of CP violation. Any discrepancies could provide insight on sources of new physics.

CP violation and the unitarity triangle are currently the subjects of much activity in high energy physics. It is unclear whether the single phase η can explain the observed CP violation in the neutral Kaon system as well as the many CP asymmetries expected in the B system. Dedicated B factories are currently operating at SLAC and KEK. These should allow direct measurements of the angles of the unitarity triangle. The CDF experiment at Fermilab has recently released preliminary results on a measurement of the angle β from ~ 400 $B \to J/\psi K_S^0$ events [7]. The result is $\sin 2\beta = 0.79^{+0.41}_{-0.44}$ (stat + syst). This is the best direct indication for CP violation in the neutral B meson system to date. $B^0 \bar{B}^0$ mixing measurements can also have a large impact on constraining the unitarity triangle. As we shall see shortly, measurements of Δm_d and Δm_s are the most precise method of measuring $|V_{td}|$ which is responsible for the largest uncertainty in the triangle's shape.

1.3 Physics at the Z^0 Pole

The SLC collides positrons with longitudinally polarized electrons at a center of mass energy $E_{cm} \approx m_{Z^0}$ in order to study decays of the Z^0. One of the advantages of studying the Z^0 is that it decays to all SM fermion pairs $f\bar{f}$ except for the top quark which is too heavy. Therefore, we may probe many aspects of the SM, particularly electroweak interactions. The dominant Z^0 branching ratios are listed in table 1.4 [1].

A sketch of the process $e^+e^- \to f\bar{f}$ is shown in figure 1.2. We define θ to be the angle between the incident electron beam direction and the emerging fermion.This process may be mediated by an exchange of either γ or Z^0. Therefore the total amplitude is the sum of the two processes, $\mathcal{M} = \mathcal{M}_\gamma + \mathcal{M}_{Z^0}$ so that $\mathcal{M}^2 = \mathcal{M}_\gamma^2 + \mathcal{M}_{Z^0}^2 + 2\mathrm{Re}(\mathcal{M}_{Z^0}\mathcal{M}_\gamma)$. The final term represents γ-Z^0 interference. However, near the Z^0 resonance, the Z^0 exchange process dominates and $\sigma_{Z^0}/\sigma_\gamma \approx 200$ [8]. Therefore, the electromagnetic contributions may be neglected. Applying the Feynman rules for electroweak interactions we obtain the amplitude [9],

$$\mathcal{M} = -\frac{g^2}{4\cos^2\theta_w}[\bar{f}\gamma^\mu(v_f - a_f\gamma^5)f]\left(\frac{g_{\mu\nu} - q_\mu q_\nu/M_Z^2}{q^2 - M_Z^2 + iM_Z\Gamma_Z}\right)[\bar{e}\gamma^\nu(v_e - a_e\gamma^5)e]. \quad (1.41)$$

Z^0 Decay Mode	Fraction(Γ_i/Γ)%
e^+e^-	(3.366 ± 0.008)
$\mu^+\mu^-$	(3.367 ± 0.013)
$\tau^+\tau^-$	(3.360 ± 0.015)
invisible($\nu\bar{\nu}$)	(20.01 ± 0.16)
hadrons	(69.90 ± 0.15)
$(u\bar{u} + c\bar{c})/2$	(10.1 ± 1.1)
$(d\bar{d} + s\bar{s} + b\bar{b})/3$	(16.6 ± 0.6)
$c\bar{c}$	(12.4 ± 0.6)
$b\bar{b}$	(15.16 ± 0.09)

Table 1.4: Measured Z^0 branching ratios.

where e and f represent the electron and fermion spinors and q is the energy-momentum four-vector of the virtual Z^0. The term $iM_Z\Gamma_Z$ must be included near the Z^0 resonance to prevent the Z^0 propagator from blowing up at $q^2 = M_Z^2$.

At this point, the general procedure is to calculate $|\mathcal{M}|^2$ averaged over initial state spins and summed over final state spins. However, the SLC produces a highly polarized electron beam. For the 1996-98 data presented here, the average beam polarization was $|P_e| \approx 73\%$. We define the polarization of a single electron bunch to be

$$P_e = \frac{N(R) - N(L)}{N(R) + N(L)} \tag{1.42}$$

where $N(R)$ is the number of right handed electrons in the bunch (spins aligned along the momentum direction) and $N(L)$ is the number of left handed electrons. Therefore, P_e varies from -1 to 1 and is negative when the beam is predominantly left handed.

For the case of longitudinally polarized electrons colliding with unpolarized positrons the differential cross section can be derived as [9],

$$\frac{d\sigma^f(P_e)}{d\cos\theta} \propto (1 - A_e P_e)(1 + \cos^2\theta) + 2A_f(A_e - P_e)\cos\theta \tag{1.43}$$

where $A_f = 2a_f v_f/(a_f^2 + v_f^2)$ as derived previously.

In section 1.2.1 we saw that the fermion couplings to the Z^0 involve both vector and axial vector components whose relative strengths are parametrized by a_f and
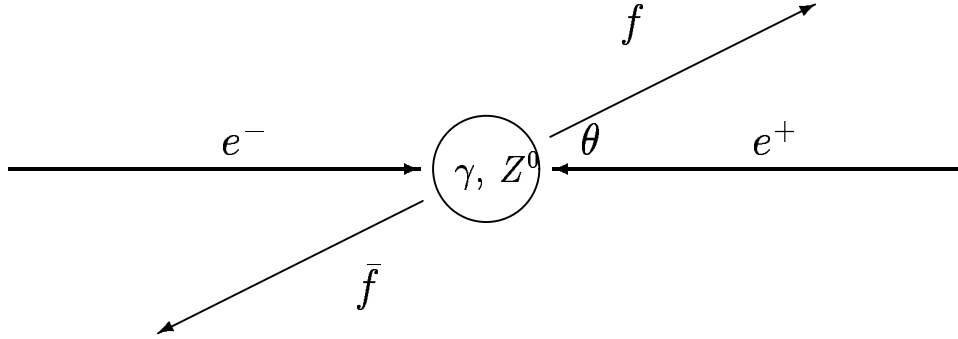
Figure 1.2: Sketch of the process $e^+e^- \rightarrow f\bar{f}$. θ is the angle between the e^- beam and the outgoing fermion direction.

v_f. The interference of vector and axial vector currents results in parity violation in the weak interactions. Figure 1.3 shows the differential cross section $d\sigma^f/d\cos\theta$ in the case of the b quark ($A_b = 0.935$ in the SM) for beam polarizations of $\pm$ 75% and unpolarized beams. There are two important features to note about this plot. First, the b quark is more likely to scatter in the positive direction ($\cos\theta > 0$) when $P_e < 0$ and in the negative direction ($\cos\theta < 0$) when $P_e > 0$. This effect is called the polarized forward-backward asymmetry. It results from the second term in the differential cross section which is linear in $\cos\theta$. Note also that this term does not vanish if $P_e = 0$. Therefore, the forward-backward asymmetry persists for unpolarized beams but is reduced in magnitude. Second, the total cross section is greater for $P_e < 0$ than for $P_e > 0$. Therefore, more Z^0 events are produced from negative beam polarizations. This is a result of the Z^0 vertex factor $\propto \gamma^\mu(v_f - a_f\gamma^5)$. In the limit that v_f, $a_f \rightarrow 1$, this reduces to the left chiral projection operator. Therefore, the Z^0 couples more strongly to left handed fermions. This effect is known as the left-right asymmetry.
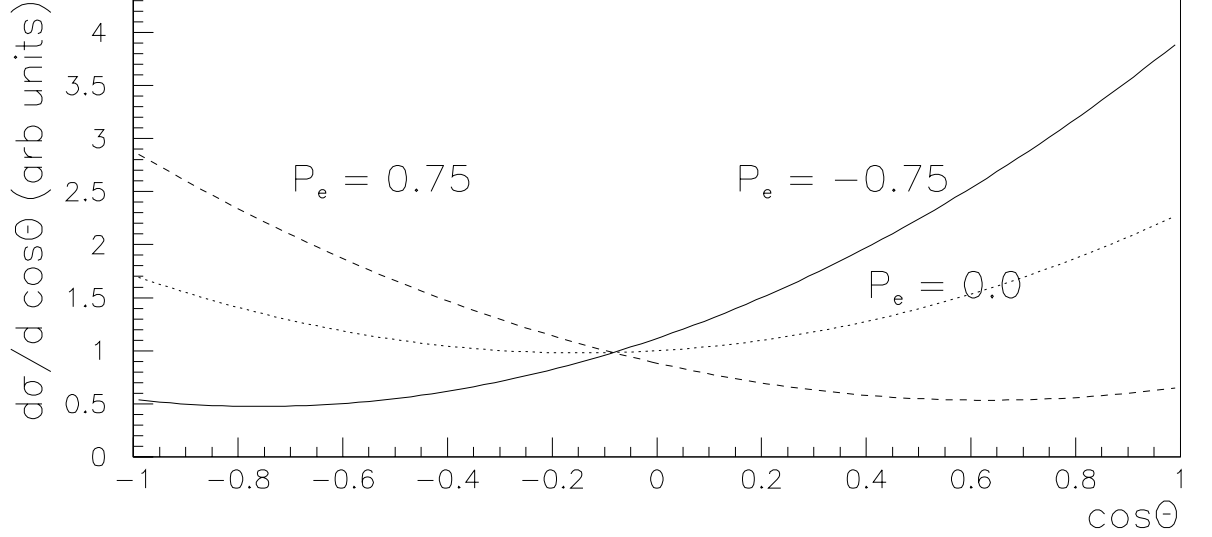
Figure 1.3: The differential cross section $d\sigma^b/d\cos\theta$ for beam polarizations of $\pm 75\%$.

The forward-backward asymmetry for a fermion f is defined by,

$$A^f_{FB} = \frac{\sigma_f(F) - \sigma_f(B)}{\sigma_f(F) + \sigma_f(B)} \qquad (1.44)$$

where $\sigma_f(F)$ is the unpolarized differential cross section ($P_e \to 0$ in equation 1.43) integrated over the forward hemisphere,

$$\sigma_f(F) = \int_0^1 \left(\frac{d\sigma^f}{d\cos\theta} \right) d\cos\theta \qquad (1.45)$$

and $\sigma_f(B)$ is defined analogously for the backward hemisphere. The result is,

$$A^f_{FB} = \frac{3}{4} A_e A_f. \qquad (1.46)$$

If the electron beam is polarized, the polarization can be included to form the left-right forward-backward asymmetry of the fermion,

$$\tilde{A}^f_{FB} = \frac{[\sigma_L(F) - \sigma_L(B)] - [\sigma_R(F) - \sigma_R(B)]}{[\sigma_L(F) + \sigma_L(B)] + [\sigma_R(F) + \sigma_R(B)]} \qquad (1.47)$$

where the L and R subscripts refer to right and left handed beam polarizations. Using equation 1.43, this can be calculated as,

$$\tilde{A}^f_{FB} = \frac{3}{4} |P_e| A_f. \qquad (1.48)$$

Notice that the polarized forward-backward asymmetry is the same as the unpolarized case except that $A_e \to P_e$. Since $A_e \approx 0.15$ and $|P_e| \approx 75\%$ at the SLC, the forward backward asymmetry is enhanced by a factor of about 5. $\tilde{A}^f_{FB}$ can also be calculated without integrating out the $\cos\theta$ dependence. In that case we obtain,

$$\tilde{A}^f_{FB}(\cos\theta) = 2A_f \left(\frac{A_e - P_e}{1 - A_e P_e}\right)\left(\frac{\cos\theta}{1 + \cos^2\theta}\right). \tag{1.49}$$

Finally, A_{LR} is defined to be,

$$A_{LR} = \frac{\sigma_L - \sigma_R}{\sigma_L + \sigma_R} \tag{1.50}$$

where σ_L and σ_R are the total cross sections for $e^+e^- \to Z^0$ with left handed and right handed incident electrons respectively. Therefore, A_{LR} depends only on the electron coupling to the Z^0,

$$A_{LR} = A_e = \frac{2(1 - 4\sin^2\theta_w)}{1 + (1 - 4\sin^2\theta_w)^2}. \tag{1.51}$$

At SLD, we may simply count the number of Z^0s produced with positively polarized beams and negatively polarized beams disregarding the final state (except $e^+e^- \to e^+e^-$ which has a large γ contribution). Then,

$$A^{\mathrm{meas}}_{LR} = \frac{n_L - n_R}{n_L + n_R} = |P_e| A_e \tag{1.52}$$

from which $\sin^2\theta_w$ may be extracted. The latest SLD result averaged over leptonic and hadronic final states gives an effective value at the Z^0 pole of $\sin^2\theta^{eff}_w = 0.23102 \pm 0.00031$ [10].

1.4 $B^0 - \bar{B}^0$ Mixing

1.4.1 Phenomenology

Particle/anti-particle oscillations were first predicted for the $K^0\bar{K}^0$ system in 1955 by Gell-Mann and Pais [11]. Their arguments predicted the existence of a long lived neutral strange particle which is now known as the K^0_L. The K^0_L was subsequently observed by K. Lande *et al.* in 1956 [12]. Mixing in the B^0 meson system is completely
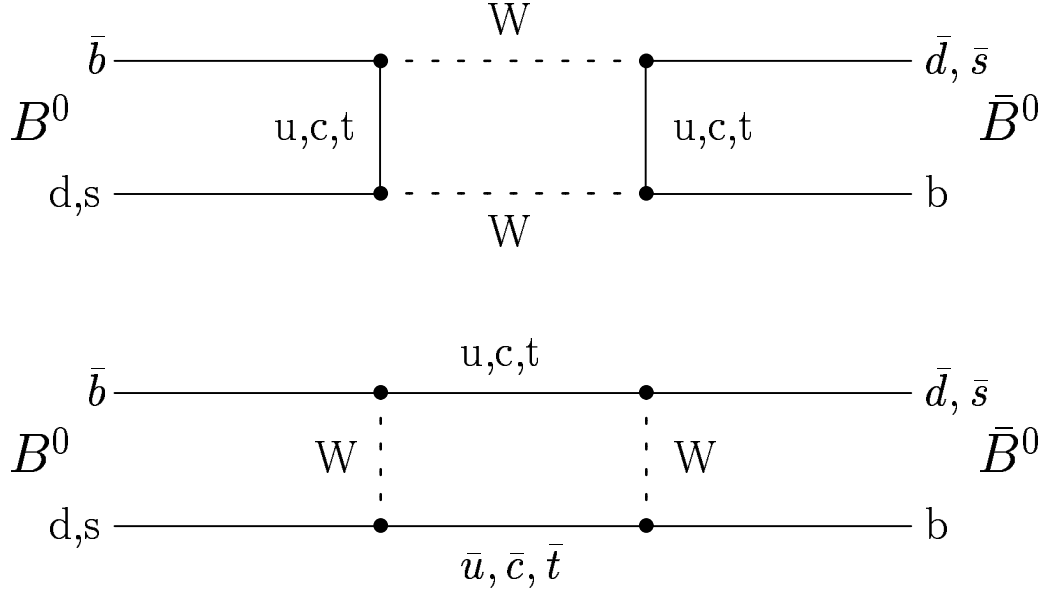
Figure 1.4: Box diagrams for $B^0\bar{B}^0$ transitions.

analogous to mixing in the kaon system . Like the K^0 and $\bar{K}^0$, the B^0 and $\bar{B}^0$ mesons are created by the strong interaction as eigenstates of flavor ($B^0 = \bar{b}q$, $\bar{B}^0 = b\bar{q}$ where q can be either d or s). However, the full Hamiltonian also involves the weak interactions. As we saw in section 1.2.2, the charged currents of the weak interaction mediated by the $W^\pm$ boson result in flavor changing transitions as described by the CKM matrix. Second order weak interactions are able to couple the flavor eigenstates as shown by the box diagrams in figure 1.4. The physical particles, those with a definite mass and lifetime, become linear combinations of B^0 and $\bar{B}^0$. Therefore, the mass eigenstates are not the same as the flavor eigenstates which leads to $B^0 - \bar{B}^0$ oscillations.

The Schroedinger equation for the $B^0\bar{B}^0$ system can be expressed phenomenologically as [13],

$$i\frac{\partial}{\partial t}\left(\begin{array}{c} B^0 \\ \bar{B}^0 \end{array}\right) = \left[\begin{array}{cc} H_{11} & H_{12} \\ H_{21} & H_{22} \end{array}\right]\left(\begin{array}{c} B^0 \\ \bar{B}^0 \end{array}\right) \tag{1.53}$$

$$= \begin{bmatrix} M - \frac{i}{2}\Gamma & M_{12} - \frac{i}{2}\Gamma_{12} \\ M_{12}^* - \frac{i}{2}\Gamma_{12}^* & M - \frac{i}{2}\Gamma \end{bmatrix} \begin{pmatrix} B^0 \\ \bar{B}^0 \end{pmatrix}.$$

So the Hamiltonian matrix can be expressed in terms of the $\mathbf{M}$ and $\mathbf{\Gamma}$ matrices as $\mathbf{H} = \mathbf{M} - (i/2)\mathbf{\Gamma}$. In general, the $\mathbf{M}$ and $\mathbf{\Gamma}$ matrices are complex and Hermitian. M and Γ in the diagonal Hamiltonian matrix elements describe the mass and decay width of the flavor eigenstates. CPT invariance requires that $H_{11} = H_{22}$ so that the particle and antiparticle have the same mass and lifetime [14]. The off-diagonal elements are responsible for $B^0\bar{B}^0$ transitions where M_{12} represents virtual transitions and Γ_{12} represents the real transitions through common decay modes. These common modes are Cabibbo suppressed so that the $B^0\bar{B}^0$ mixing amplitude is dominated by virtual transitions [13].

Diagonalization of the Hamiltonian matrix leads to the eigenstates,

$$|B_L\rangle = \frac{1}{\sqrt{|p|^2 + |q|^2}}(p|B^0\rangle + q|\bar{B}^0\rangle) \tag{1.54}$$

$$|B_H\rangle = \frac{1}{\sqrt{|p|^2 + |q|^2}}(p|B^0\rangle - q|\bar{B}^0\rangle)$$

where $p^2 = iH_{12}$ and $q^2 = iH_{21}$. The subscripts L and H denote the light and heavy mass eigenstates. The eigenvalues can be expressed as $M_{H,L} - i\Gamma_{H,L}/2$ where,

$$M_{H,L} = M \pm \mathrm{Re}\sqrt{H_{12}H_{21}} \tag{1.55}$$

$$\Gamma_{H,L} = \Gamma \mp 2\,\mathrm{Im}\sqrt{H_{12}H_{21}}.$$

The mass and width differences are,

$$\Delta m = 2\,\mathrm{Re}\sqrt{H_{12}H_{21}} \tag{1.56}$$

$$\Delta\Gamma = 4\,\mathrm{Im}\sqrt{H_{12}H_{21}}.$$

In the absence of CP violation, the elements of the $\mathbf{M}$ and $\mathbf{\Gamma}$ matrices are real which implies $p = q$. CP violation has been observed in the $K^0\bar{K}^0$ system to be of the order 10^{-3} [1]. These effects are expected to be small for the $B^0\bar{B}^0$ system as well. If we define $a = \mathrm{Im}\,(\Gamma_{12}/M_{12})$ then $|q/p|^2 = 1 - a + \mathcal{O}(a^2)$. Theory predicts

$a < 10^{-2}$ (10^{-3}) for B_d^0 (B_s^0) [15]. Therefore, CP violation can be safely neglected in $B^0 \bar{B}^0$ mixing studies.

B_L and B_H, therefore, reduce to the CP eigenstates B_1 and B_2,

$$|B_1\rangle = \frac{1}{\sqrt{2}}(|B^0\rangle + |\bar{B}^0\rangle) \tag{1.57}$$

$$|B_2\rangle = \frac{1}{\sqrt{2}}(|B^0\rangle - |\bar{B}^0\rangle)$$

with masses $M_{1,2}$ and decay widths $\Gamma_{1,2}$. The time evolution of $|B_1\rangle$ is given by,

$$|B_1(t)\rangle = \exp(-iM_1 t)\exp(-\Gamma_1 t/2)\,|B_1(0)\rangle \tag{1.58}$$

and similarly for B_2. Suppose at time $t = 0$ we create a B^0. By inverting equation 1.57 above, the B^0 can be expressed as a linear combination of B_1 and B_2. At a later time t, the state will have evolved as,

$$|B^0(t)\rangle = \frac{1}{\sqrt{2}}\exp(-iM_1 t)\exp(-\Gamma_1 t/2)\,|B_1(0)\rangle \tag{1.59}$$

$$+\frac{1}{\sqrt{2}}\exp(-iM_2 t)\exp(-\Gamma_2 t/2)\,|B_2(0)\rangle$$

If we now re-express $|B_1(0)\rangle$ and $|B_2(0)\rangle$ in terms of the flavor eigenstates $|B^0\rangle$ and $|\bar{B}^0\rangle$ we see that the time evolution has resulted in the generation of a $|\bar{B}^0\rangle$ component to a state that was initially pure $|B^0\rangle$,

$$|B^0(t)\rangle = \frac{1}{2}[\exp(-iM_1 t)\exp(-\Gamma_1 t/2) + \exp(-iM_2 t)\exp(-\Gamma_2 t/2)]\,|B^0\rangle \tag{1.60}$$

$$+\frac{1}{2}[\exp(-iM_1 t)\exp(-\Gamma_1 t/2) - \exp(-iM_2 t)\exp(-\Gamma_2 t/2)]\,|\bar{B}^0\rangle.$$

The probability that a state created as a B^0 $(\bar{B}^0)$ will decay as a B^0 $(\bar{B}^0)$ at time t is,

$$P_{unmix}(t) = |\langle B^0|B^0(t)\rangle|^2 = \frac{1}{4}[e^{-\Gamma_1 t} + e^{-\Gamma_2 t} + 2e^{-\Gamma t}\cos\Delta m t] \tag{1.61}$$

The probability that it *mixes* into it's antiparticle is,

$$P_{mix}(t) = |\langle \bar{B}^0|B^0(t)\rangle|^2 = \frac{1}{4}[e^{-\Gamma_1 t} + e^{-\Gamma_2 t} - 2e^{-\Gamma t}\cos\Delta m t]. \tag{1.62}$$

If we neglect Γ_{12} due to the Cabibbo suppression mentioned above then $\Delta m \approx 2\,|M_{12}|$ and $\Delta\Gamma \approx 0$. This is known to be a good approximation for $B_d^0 - \bar{B}_d^0$ mixing.
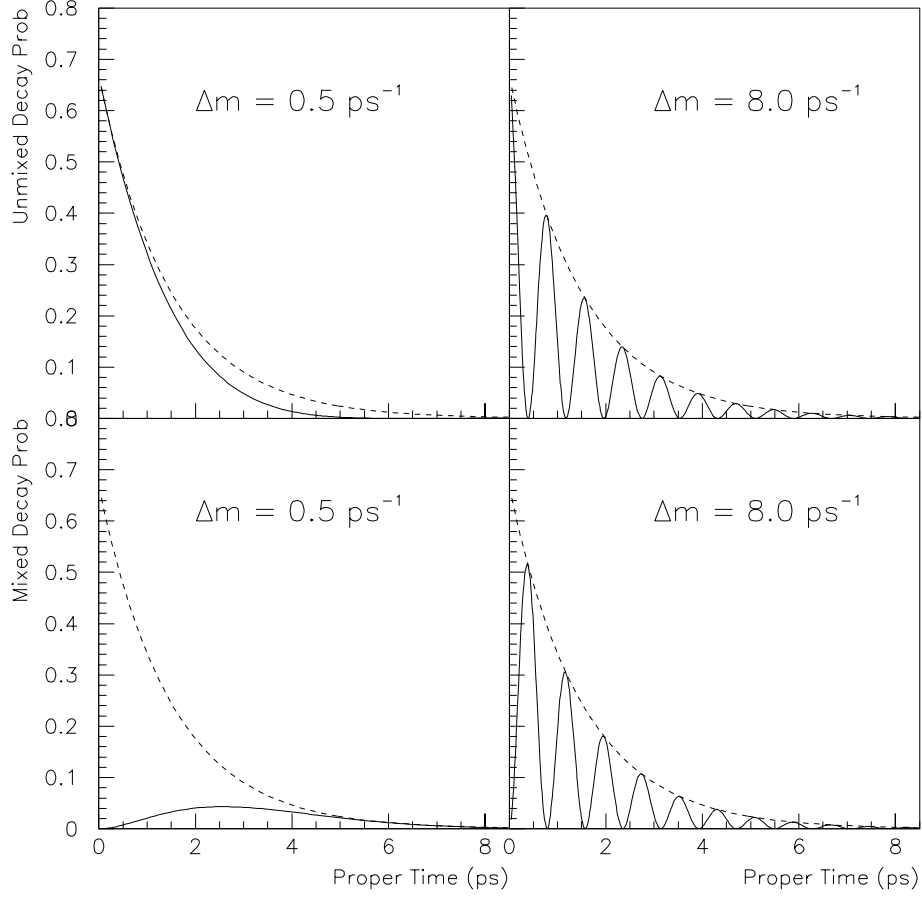
Figure 1.5: The mixed and unmixed decay probabilities versus proper time for $\Delta m_s = 0.5$ ps^{-1} and $\Delta m_s = 8.0$ps^{-1} The dashed curve is the total decay rate for mixed and unmixed events.

For $B_s^0 - \bar{B}_s^0$ mixing, however, theoretical predictions are more uncertain. Initial estimates based on leading order QCD calculations resulted in $\Delta\Gamma/\Gamma \approx 15\text{-}20\%$[16]. More recent calculations incorporating next-to-leading logarithmic corrections in the heavy quark expansion approach find $\Delta\Gamma/\Gamma \approx 5\text{-}10\%$[17]. Experimentally, a non-negligible $\Delta\Gamma$ would lead to two distinct lifetime distributions for the heavy and light B_s^0 mass eigenstates. For $\Delta\Gamma/\Gamma \sim 10\%$ the effect on the fraction of mixed decays versus time is negligible, especially at small time. Therefore, we will assume that $\Delta\Gamma$

can be neglected so that,

$$P_{unmix}(t) = \frac{1}{2}e^{-\Gamma t}(1 + \cos \Delta m t) \tag{1.63}$$

$$P_{mix}(t) = \frac{1}{2}e^{-\Gamma t}(1 - \cos \Delta m t).$$

We see that the oscillation frequency is equal to Δm, the mass difference between the two mass eigenstates. Figure 1.5 shows the mixed and unmixed decay probabilities versus proper time for two values of Δm.

1.4.2 Motivation

In principle, Δm can be calculated from the box diagrams. The result, as discussed in [13] is,

$$\Delta m_q = \frac{G_F^2}{6\pi^2} B_{B_q} f_{B_q}^2 m_{B_q} |V_{tb}^* V_{tq}|^2 m_t^2 \, F\left(\frac{m_t^2}{M_W^2}\right) \eta_{QCD} \tag{1.64}$$

where q can be either d or s. B_{B_q} is the 'bag parameter' arising from the vacuum insertion approximation which is of order 1 due the the heaviness of the b quark. The parameters f_{B_q} and η_{QCD} are the B_q decay constant and QCD correction factor respectively. The function F is given by,

$$F(z) = \frac{1}{4} + \frac{9}{4(1-z)} - \frac{3}{2(1-z)^2} - \frac{3}{2}\frac{z^2 \ln z}{2(1-z)^3}. \tag{1.65}$$

This result suggests that a measurement of Δm_d should allow the extraction of the CKM matrix element V_{td}. Unfortunately, there are large theoretical uncertainties in the non-perturbative QCD factors, B_{B_q} and f_{B_q}. A review of the current status of these calculations may be found in [18]. The decay constant f_{B_d} is obtained from f_{D_s} deduced from measurements of the $D_s^+ \to \tau^+ \nu_\tau$ and $D_s^+ \to \mu^+ \nu_\mu$ branching ratios. Lattice QCD calculations are then employed to extrapolate from the D to the B sector. The current value is:

$$f_{B_d} = 181 \pm 24 \text{ (exp)} \pm 7 \text{ (theo.stat.)} \pm_5^{20} \text{ (theo.nonstat.) MeV.} \tag{1.66}$$

B_{B_d} is also calculated from lattice QCD to be $B_{B_d} = 1.35 \pm 0.15$.

Expressing Δm_d and Δm_s in the Wolfenstein parametrization of the CKM matrix yields,

$$\Delta m_d \quad \propto \quad A^2 \lambda^6 [(1 - \rho)^2 + \eta^2] \qquad (1.67)$$

$$\Delta m_s \quad \propto \quad A^2 \lambda^4$$

Δm_d can, therefore, be represented as a circle centered at $(1,0)$ in the ρ-η plane. Recall that ρ and η are the coordinates which define the apex of the unitarity triangle (see figure 1.1). Figure 1.7 shows a graphical representation of several constraints on the parameters ρ and η. Note the wide allowed region coming from current measurements of Δm_d. Although B_d^0 mixing is well measured, the theoretical uncertainties limit the effectiveness of the measurement to constrain V_{td} or, equivalently, ρ and η. Unless significant improvements can be made in the calculation of hadronic matrix elements, more precise measurements of Δm_d will have little effect on constraining the CKM matrix [19].

One solution to this problem would be to measure both Δm_d and Δm_s and form the ratio,

$$\frac{\Delta m_d}{\Delta m_s} = \xi^{-2} \frac{m_{B_d}}{m_{B_s}} \left| \frac{V_{td}}{V_{ts}} \right|^2 \qquad (1.68)$$

where $\xi \equiv f_{B_s}\sqrt{B_{B_s}}/f_{B_d}\sqrt{B_{B_d}}$. The top quark mass and most of the theoretical uncertainties cancel so that ξ can be calculated to about 10%. The current best value is $\xi = 1.11 \pm 0.02^{+0.06}_{-0.04}$ [18]. This factor expresses the extent of $SU(3)$ symmetry breaking effects. Note that Δm_s contains no factors of ρ or η so that a measurement of Δm_s is effectively a measurement of $f_{B_s}\sqrt{B_{B_s}}$. Therefore, B_d^0 and B_s^0 mixing measurements can be combined to constrain the ratio of CKM matrix elements V_{ts} and V_{td}. Furthermore, we expect $|V_{ts}| \approx |V_{cb}|$ which is fairly well known from B decay measurements. Thus strong constraints may be placed on V_{td}. In addition, if we approximate $|V_{tb}| \approx |V_{ud}| \approx 1$ and $|V_{cb}| \approx |V_{ts}|$ then the unitarity triangle can be drawn as in figure 1.6. We see that the length of the right side is essentially determined by the ratio $\Delta m_d/\Delta m_s$.

Of course Δm_s has yet to be measured. Even so, there is very useful information in the lower limit. Equation 1.68 indicates that a lower limit on Δm_s corresponds to

$$|V_{cd}| = \sin\theta_C$$
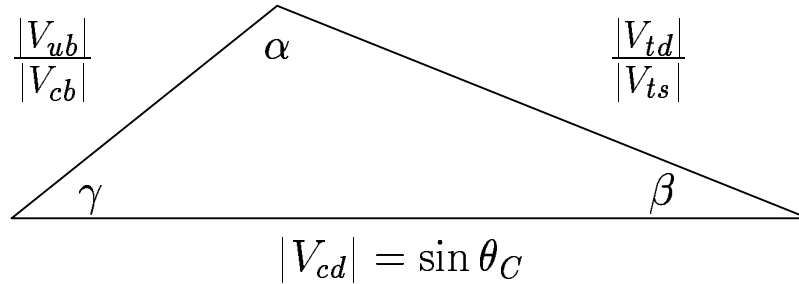
Figure 1.6: The rescaled unitarity triangle demonstrating that one side is essentially determined by B mixing.

an upper limit on $|V_{td}|$. Rearranging equation 1.68 we obtain,

$$\Delta m_s = \Delta m_d \; \xi^2 \; \frac{m_{B_s}}{m_{B_d}} \; \frac{1}{\lambda^2} \frac{1}{(1-\rho^2) + \eta^2} \tag{1.69}$$

where we have substituted the Wolfenstein approximations to the CKM matrix elements. Therefore, limits on Δm_s can also limit the allowed region of the ρ-η plane. The dashed curves in figure 1.7 correspond to lower limits of 5.0, 10.0, 15.0, 20.0 and 25.0 ps^{-1}. The apex of the unitarity triangle is constrained to lie to the right of these curves. As the limits increase, the curve moves to the right.

Measurements of the unitarity triangle are a test of the SM explanation of CP violation. The B factories currently getting underway at SLAC ant KEK are expected to make direct measurements of the angles of the unitarity triangle. A measurement of $\sin 2\beta$ is orthogonal to mixing measurements as shown in figure 1.8. Therefore, B_s^0 mixing provides complimentary information which can be combined with the B factory results.

1.4.3 Mixing Measurements

The first observation of $B^0 - \bar{B}^0$ mixing was made by the ARGUS Collaboration in 1987 by completely reconstructing a single $\Upsilon(4S) \to B^0 B^0$ event [20]. In $\Upsilon(4S)$ decays, a pair of B mesons is produced *coherently* as either $B^0 \bar{B}^0$ or $B^+ B^-$ (only one
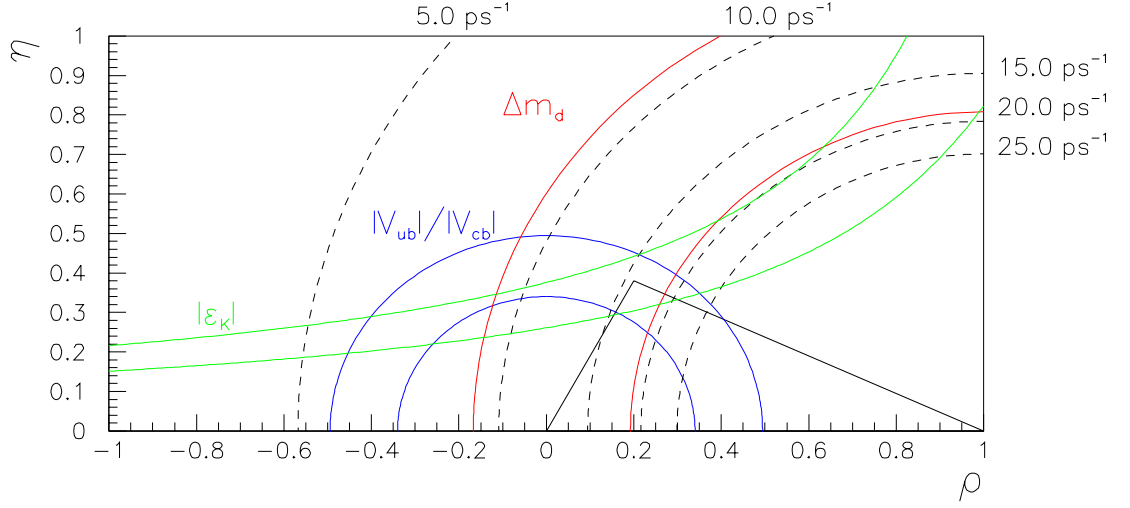
Figure 1.7: Constraints on the apex of the unitarity triangle in the ρ-η plane.

$q\bar{q}$ pair is pulled from the vacuum and there are no additional fragmentation particles). Also, the $\Upsilon(4S)$ is too light to produce a $B_s^0 \bar{B}_s^0$ pair or b baryons. Therefore, the observation of two B^0 decays in a single event is a clear indication of mixing. In this particular event, both B^0s decayed to $D^{*-}\mu^+\nu$. The first D^{*-} decayed as $D_1^{*-} \rightarrow \pi^- \bar{D}^0$ with $\bar{D}^0 \rightarrow K^+\pi^-$. The second D^{*-} decayed as $D_2^{*-} \rightarrow \pi^0 D^-$ with $D^- \rightarrow K^+\pi^-\pi^-$.

The first measurements of Δm_d were produced by ARGUS [20] and CLEO [21] using a time integrated mixing technique. In $\Upsilon(4S)$ decays the $B^0\bar{B}^0$ pair is created almost at rest. Due to the short B lifetime and small boost it is not possible to measure the proper time of the B decay. Therefore, one must measure the total time integrated ratio of mixed to unmixed decays known as the r ratio,

$$r = \frac{\int_0^\infty P_{mix}(t)dt}{\int_0^\infty P_{unmix}(t)dt} = \frac{(\Delta m)^2 + (\Delta\Gamma/2)^2}{2\Gamma^2 + (\Delta m)^2 - (\Delta\Gamma/2)^2}. \tag{1.70}$$

With $x = \Delta m/\Gamma$ and assuming $\Delta\Gamma$ can be neglected [13],

$$r = \frac{x^2}{2 + x^2}. \tag{1.71}$$

ARGUS found $r = 0.21 \pm 0.08$. When x is small, the oscillation period is much larger than the B lifetime and only a small fraction of B^0s will mix before decaying. In this
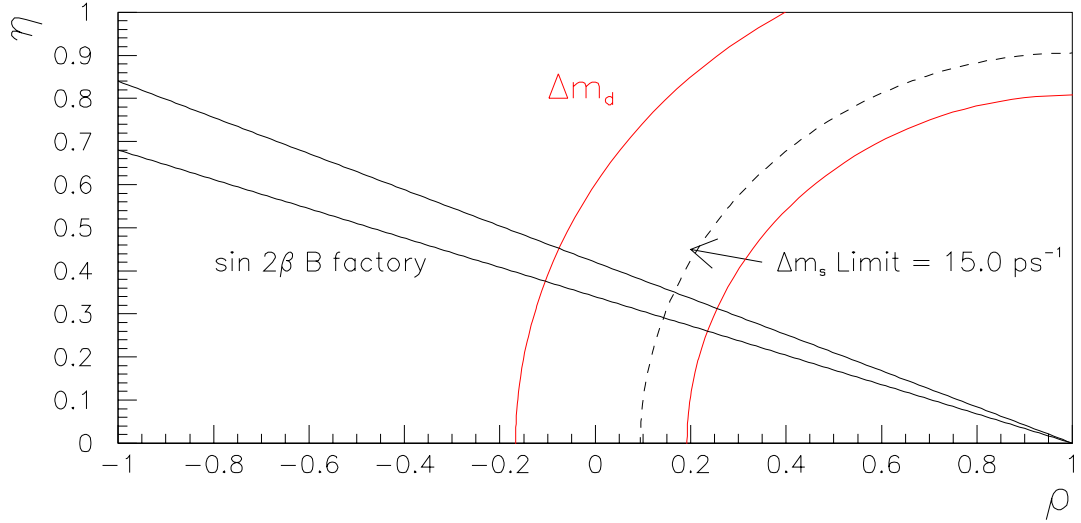
Figure 1.8: B factory measurements of $\sin 2\beta$ will be orthogonal to mixing measurements. The plot assumes $\sin 2\beta = 0.70 \pm 0.06$.

regime, dr/dx is large and thus the r measurement can be used to extract x or Δm_d. As x increases, $r \to 1.0$ since one lifetime covers many oscillation periods and any B^0 is almost equally likely to decay as mixed or unmixed. Therefore, r loses sensitivity to Δm. Current limits on Δm_s suggest that this is the case for $B_s^0 - \bar{B}_s^0$ mixing.

More recently, time dependent $B_d^0 \bar{B}_d^0$ mixing analyses have been performed at the Z^0 pole by SLD [22, 23, 24] and the four LEP experiments: ALEPH [25], DELPHI [26], L3[27], and OPAL [28, 29, 30]. CDF has also produced $B_d^0 - \bar{B}_d^0$ mixing results [31] using $p\bar{p}$ collisions at the Tevatron. For a time dependent analysis the strategy is generally to measure the fraction of B^0 mesons which decay as mixed as a function of the decay proper time. For a pure B^0 sample the *mixed fraction* is expected to be,

$$\text{Mixed Fraction} \quad = \quad \frac{P_{mix}(t)}{P_{mix}(t) + P_{unmix}(t)}, \qquad (1.72)$$

$$= \quad \frac{1}{2}(1 - \cos \Delta mt).$$

The mixing frequency can then be extracted directly by fitting the data mixed fraction to the expected function taking into account backgrounds, mistag rates and proper time resolution. So there are three essential ingredients to a time dependent mixing analysis:

1. Measure the B decay proper time.

2. Tag the b quark flavor at production.

3. Tag the b quark flavor at decay.

At the Z^0 pole, the Z^0 decays to $b\bar{b}$ pairs roughly 15% of the time. Due to the large Z^0 mass, B hadrons are produced with a large boost, $< \beta\gamma >\approx 6$. Given that the average B lifetime is about 1.5 ps, the average B decay length turns out to be 2-3 mm. Therefore, using the precise vertex detectors found at e^+e^- colliders, the B hadron decay position can be located as a secondary vertex separated from the interaction point. Decay length resolution down to about 100 μm is possible. The B momentum must be determined independently. Unlike $\Upsilon(4S)$ decays, the Bs produced at the Z^0 exhibit a distribution of momenta described by the fragmentation function. Combining the decay length and boost measurements the decay proper time can be calculated, $t = L/\beta\gamma c$.

To determine whether mixing has occurred, the b quark flavor must be tagged at production and decay. These are commonly referred to as the initial state tag and the final state tag respectively. Many techniques have been developed for this purpose as described in the references given above. The final state tags are obtained from examining the B decay products. The most common technique, which is adopted in this thesis, is to locate a lepton produced in the B decay. As discussed in chapter 4, the charge of the lepton tags the charge, and thus the flavor, of the decaying b quark. Another common technique is the reconstruction of a $D^{(*)\pm}$ decay vertex that tags the B^0 meson through the process $B_d^0 \rightarrow D^{*-} X$. Charged kaons may also be used as a final state tag by exploiting the dominant $b \rightarrow c \rightarrow s$ quark decay chain which often results in the production of a K^-.

When the final state of a B meson has been tagged and it's proper time reconstructed, we refer to this as the *tagged B*. It resides in the *tagged* hemisphere. The initial state tag then generally depends on the b quark produced in the *opposite* hemisphere. The Z^0 decays to a $b\bar{b}$ pair so there is generally a b hadron in the opposite hemisphere. Furthermore, mixing in the opposite hemisphere is independent of mixing in the tagged hemisphere. Therefore, the opposite hemisphere b quark flavor can

be used as a reference to determine if the tagged B has mixed. In general, any technique used for final state tagging may also be used for initial state tagging. However, most experiments select initial state tags that have large efficiencies since the efficiency to select B decays and reconstruct their proper time in the tagged hemisphere is frequently small. The most common initial state tag is the *jet charge* technique. Jet charge or hemisphere charge can be defined in various ways but essentially the technique attempts to determine the b quark charge by forming a momentum weighted track charge for all tracks in the hemisphere. Jet charge is utilized in this analysis and is described in more detail in section 4.8.2. High momentum leptons generally provide a cleaner tag of the initial state but with much lower efficiency. Leptons are frequently used when available.

At SLD we have the great advantage of a longitudinally polarized electron beam. As described in section 1.3, parity violation at the $Z^0 \to b\bar{b}$ vertex results in a strong polarized forward-backward asymmetry. Therefore, the initial state flavor of b quarks can be tagged with high purity and essentially 100% efficiency simply based on the b flight direction and the sign of the polarization. This technique is described in more detail in section 4.8.1.

CDF has developed a technique called same side tagging (SST). The idea behind SST is to use correlations between tracks produced in the b hadronization process to tag the initial state b flavor. For example, when a b quark pulls a $d\bar{d}$ pair out of the vacuum to become a $\bar{B}_d^0$ the remaining d quark often forms a π^-. The charge of the fragmentation pion thus tags the initial b flavor. In addition, pions from strong decays of excited B mesons can also be used as an initial state tag since the B^* decays almost instantaneously.

B_d^0 mixing is now well established and precise measurements of Δm_d have been performed. Figure 1.9 shows the results of measurements from the four LEP experiments, CDF, and SLD. The world average value for Δm_d has been calculated by the LEP B oscillations working group [32] to be $\Delta m_d = 0.477 \pm 0.017 \text{ps}^{-1}$.

Similar techniques can be applied to $B_s^0 - \bar{B}_s^0$ mixing. However, several factors combine to make this a much more difficult measurement experimentally. First, the B_s^0 production fraction is only about 10% as compared to 40% for B_d^0 and B^+ at the
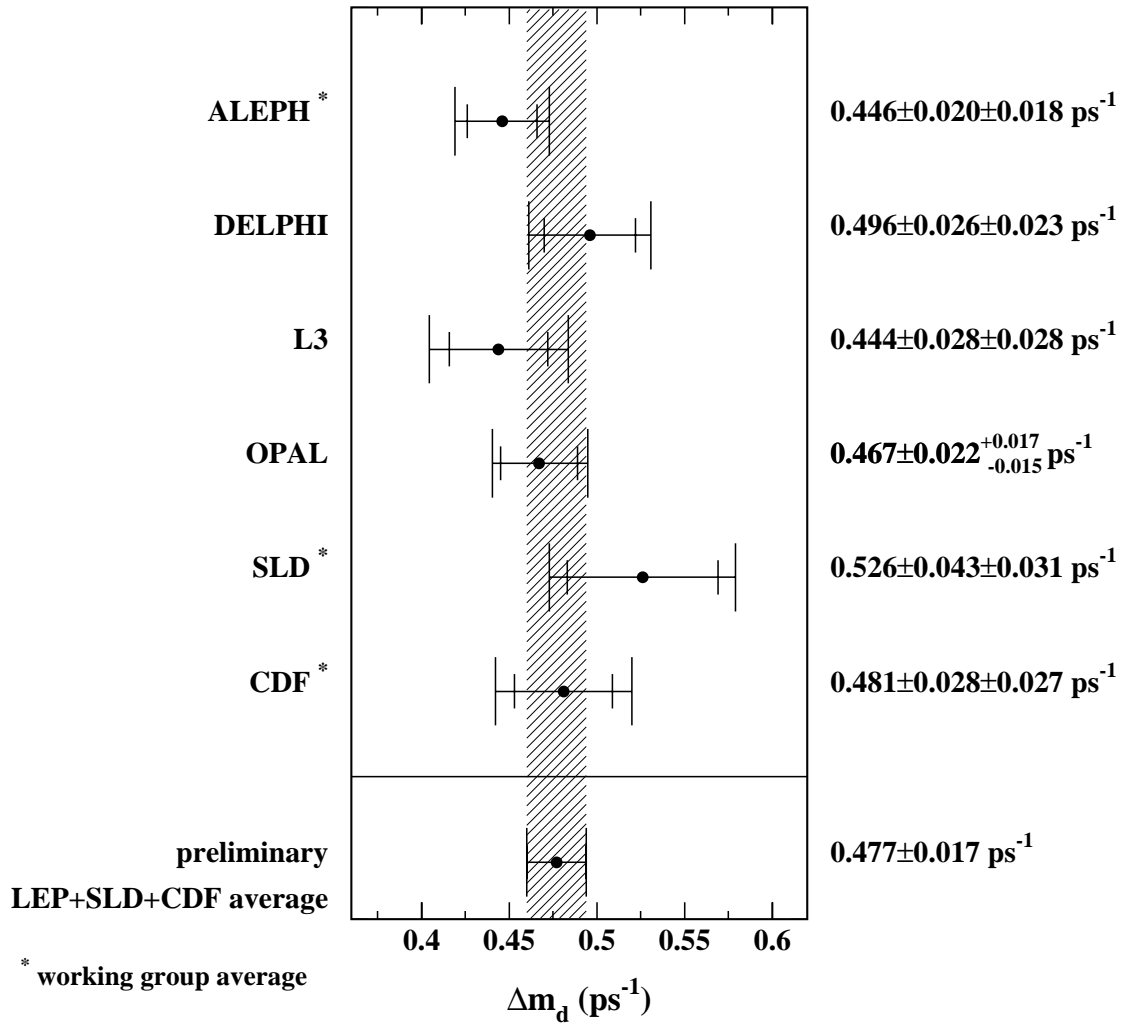
Figure 1.9: The world average value of Δm_d as derived by the LEP B Oscillations working group as of May 1999.

Z^0 pole. Therefore, the mixing signal must be extracted from a large background. Second, Δm_s is expected to be many times larger than Δm_d. From equation 1.68 we expect $\Delta m_s/\Delta m_d \approx 1/\lambda^2 \approx 20$. Therefore, proper time resolution can become a limiting factor when the oscillation period becomes comparable to the resolution. Only lower limits have been placed on Δm_s thus far. Figure 1.10 shows the combined *amplitude fit* for LEP experiments ALEPH [33, 34, 35], DELPHI [36], and OPAL [37]. The amplitude fit technique will be explained in great detail in chapter 5. Essentially, the plot shows the normalized fourier amplitude of the mixing signal as a function of frequency. We expect to find a peak in the amplitude at the true value of Δm_s. One notices that the uncertainty on the amplitude measurement grows as frequency increases. This effect is due to imperfect proper time resolution and limits the frequency range in which mixing can be resolved. This particular amplitude fit suggests that $\Delta m_s < 11.5$ ps^{-1} can be excluded at 95% CL.

Although Δm_s has not been measured there are indications that a measurement may be just around the corner. When the the LEP amplitude fit above is combined with results from CDF [38] and SLD [39], the 'bump' at ~ 15.0 ps^{-1} becomes even more suggestive. However, the significance is not great enough to claim a measurement. Furthermore, by using other measurements and constraints ($|V_{ub}/V_{cb}|$, $|\epsilon_K|$, and Δm_d), it is possible to obtain a SM 'prediction' for Δm_s [18]. The result is that Δm_s is expected to be between 12.0 and 17.6 ps^{-1} at 1σ and less than 20 ps^{-1} at 95% C.L. as shown in figure 1.11.
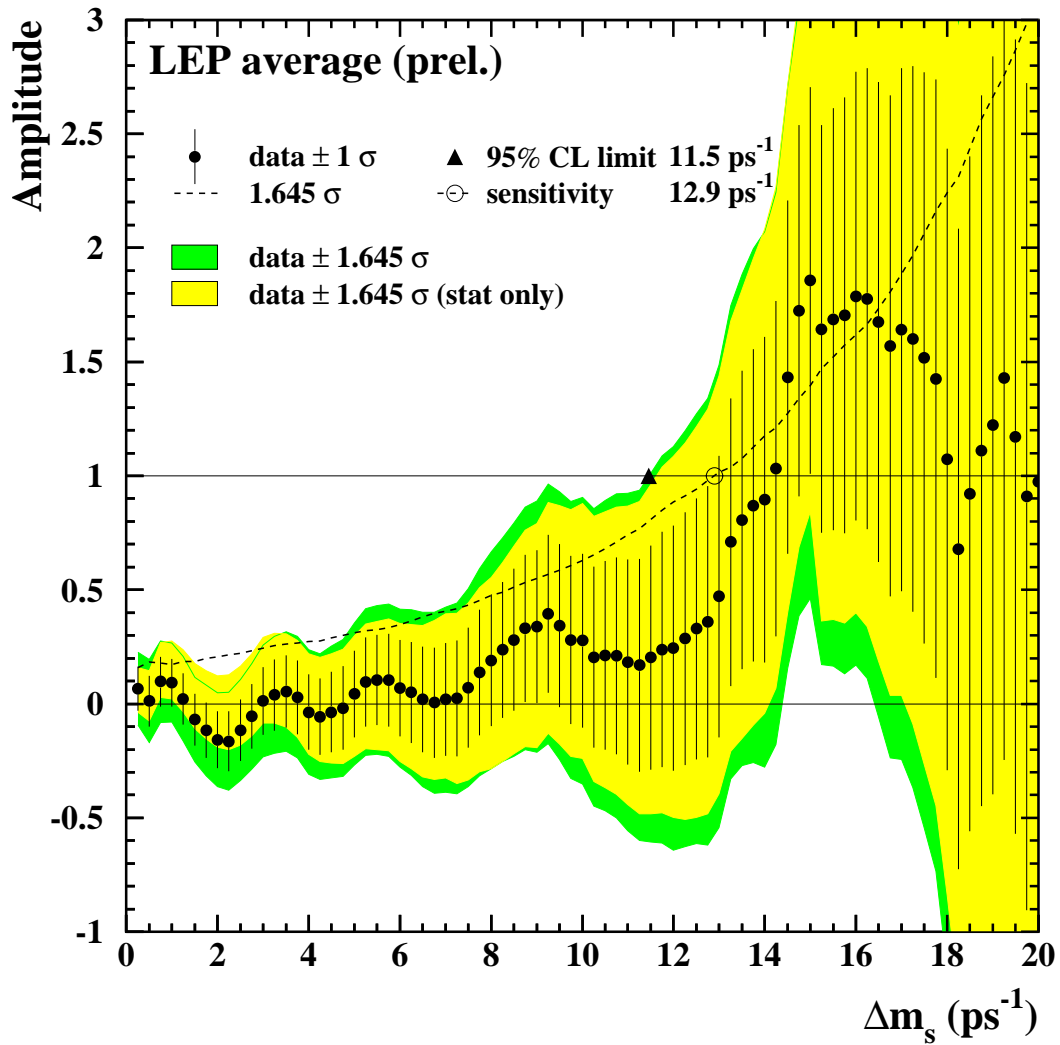
Figure 1.10: LEP combined amplitude fit for $B_s^0 - \bar{B}_s^0$ mixing.
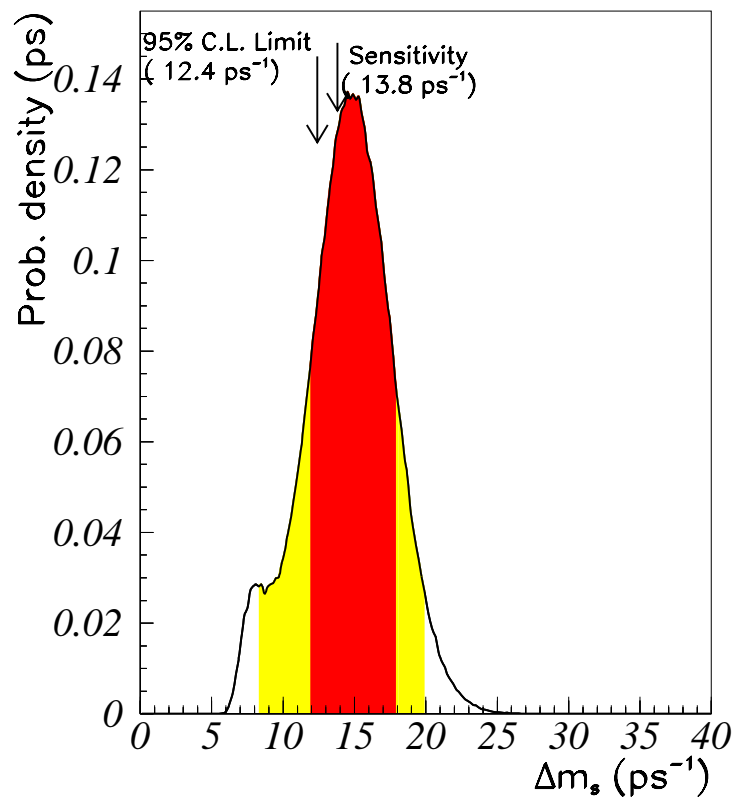
Figure 1.11: Standard model expectation for Δm_s.

Chapter 2

Experimental Apparatus

The data presented in this thesis was collected between 1996 and 1998 by the SLD experiment at SLAC. The SLD detector observes the decays of polarized Z^0 bosons produced by the SLC. This chapter will briefly describe several aspects of the SLC including the polarized source, accelerator operation, and the beam polarization measurement. Finally, the various subsystems of the SLD detector will be discussed.

2.1 Stanford Linear Collider

The SLC is an e^+e^- collider located at SLAC in Palo Alto, California. SLC is the first and only linear collider. It collides longitudinally polarized electrons with unpolarized positrons at a center-of-mass energy of 91.2 GeV, the mass of the Z^0 boson. The collision rate is 120 Hz.

2.1.1 Polarized Source

One of the unique features of the SLC is the polarization of the electron beam [40] that greatly enhances the physics potential of the experiment. Polarized electrons are obtained by photoemission from a *strained* GaAs photocathode as shown in figure 2.1. The process begins with two Nd:YAG pumped Ti:sapphire lasers producing linearly polarized light. Two 2 ns pulses are produced, separated by about 60 ns.
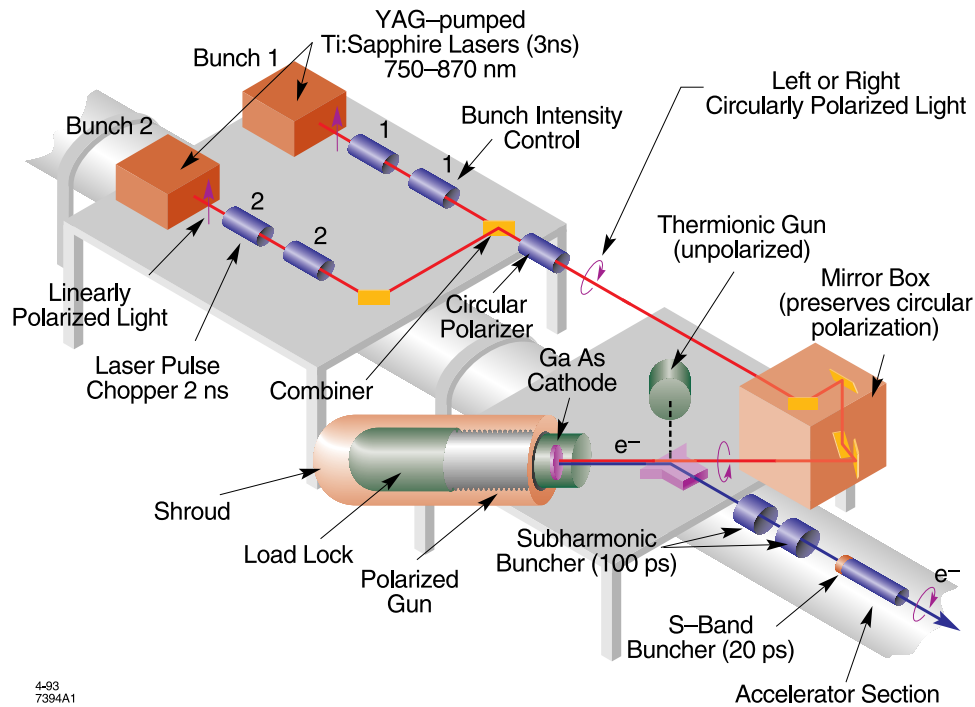
Figure 2.1: Schematic view of the polarized source.

As described shortly, the two laser pulses produce two electron bunches. One will be used for collisions at the interaction point while the other is directed onto a target to produce the positron bunch for the next cycle.

The laser pulses are circularly polarized by a linear polarizer followed by a CP Pockels cell operated at quarterwave voltage. The helicity of the laser pulse can be flipped by changing the sign of the high voltage applied to the CP Pockels cell. A pseudo-random number generator determines the polarity of the high voltage which is varied at a rate of 120 Hz, the SLC collision rate. Small phase shifts are known to occur in the transport optics to the photocathode. Therefore, a PS Pockels cell is included to make small adjustments to ensure that the laser pulses are circularly polarized at the photocathode.

The polarized laser pulses are directed onto the GaAs photocathode. The GaAs has been strained by growing a 0.1 μm layer on GaAsP. The result is that the degeneracy of the j=3/2 valence band is split by about 50 meV as shown in figure 2.2. By properly tuning the energy of the incoming laser pulses, a particular spin state
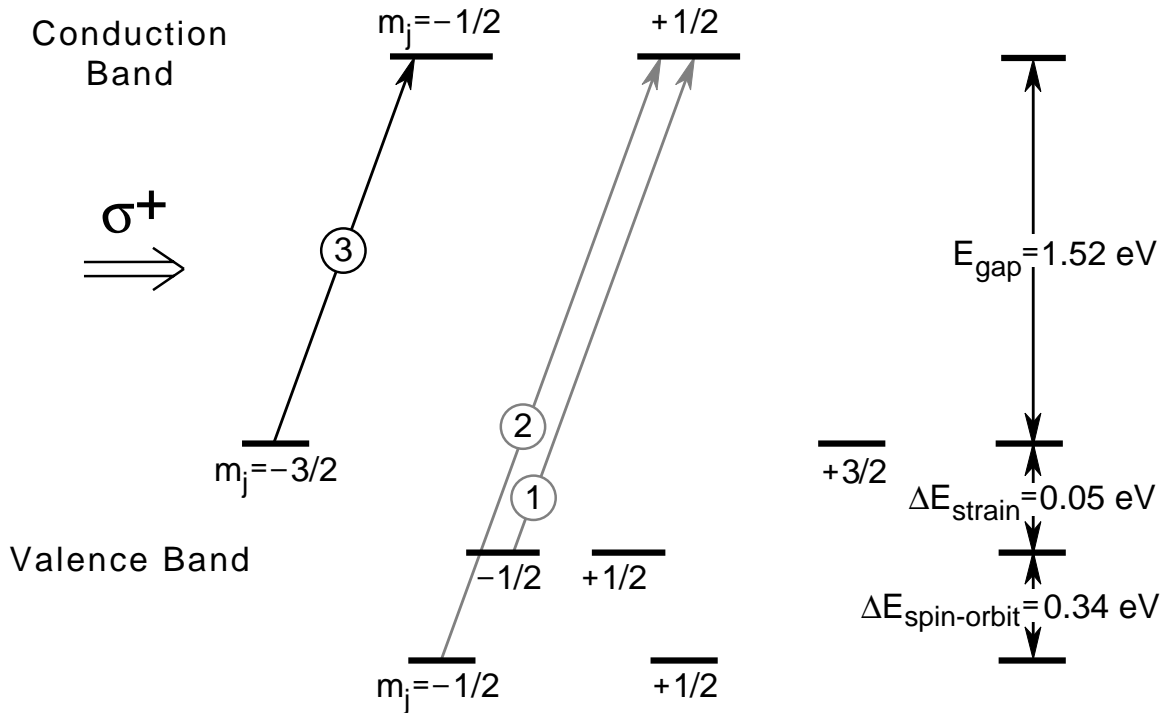
Figure 2.2: The energy levels of strained GaAs. The relative Clebsch-Gordon coefficients for each transition is indicated on the arrows.

in the conduction band can be populated due to conservation of angular momentum. For example, right handed photons excite transitions to the $m_j = -1/2$ level in the conduction band. The extracted electrons from the conduction band should have the same helicity as the photon since they emerge in the opposite direction. At the source, a typical electron bunch contains about $7\text{-}8 \times 10^{10}$ particles [41] with a maximum polarization of $\sim 80\%$.

2.1.2 The Accelerator

Figure 2.3 shows the layout of the SLC [42]. Longitudinally polarized electron bunches emerging from the source are accelerated to 1.2 GeV before entering the damping rings. Maintaining the polarization of the electron beam all the way to the interaction point requires several manipulations of the spin direction. In the linac-to-ring (LTR) transport line, superconducting solenoids rotate the spin until it
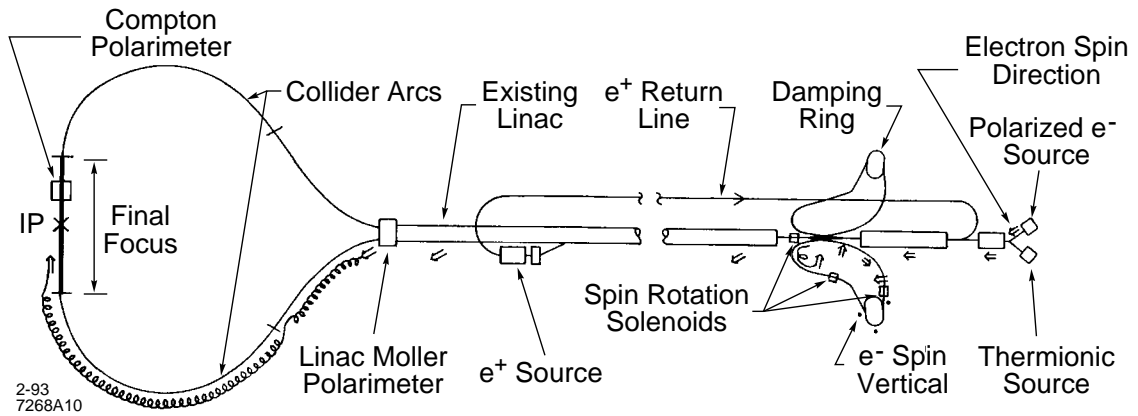
Figure 2.3: Layout of the SLC.

is transverse to the horizontal plane and can be stored in the damping ring without depolarization. The two electron bunches are stored in the 35 m circumference damping ring for one accelerator cycle or 1/120 s where they are cooled by synchrotron radiation to reduce beam emittance. Positron bunches created in previous cycles are simultaneously cooled in the positron damping rings for 2 cycles.

At the beginning of a cycle, both electron bunches and one positron bunch are ejected from their respective damping rings to the ring-to-linac (RTL) transport. At this stage a bunch compressor reduces the length of the bunch from 6-9 mm to about 1 mm [43]. The polarization direction of the electrons remains vertical during extraction from the damping ring and acceleration by the 2946 meter linac. Acceleration in the linac is provided by a series of 230 67 MW S-Band klystrons. The accelerating gradient is about 20 MeV/m. The positron and leading electron bunches are accelerated to an energy of 46.6 GeV while the trailing electron bunch is accelerated to only 30 GeV before branching off to the positron production target.

At the end of the linac the electron and positron bunches are diverted by a dipole into the north and south arcs respectively. The arcs guide the two beams to the IP by a series of 23 achromats consisting of 20 dipole magnets each. A pair of 'spin bumps' are introduced by the achromats in the last third of the electron arc to produce longitudinal electron polarization at the IP. Synchrotron radiation losses of about 1 GeV are expected in the arcs. This is compensated for by accelerating the beams

above $m_Z/2$ in the linac. The final focus optics just before the IP increases the luminosity by reducing the transverse dimensions of the beam. In the 1997-98 runs, spot sizes as small as 1.5×0.65 μm were obtained. Typical bunch sizes at the IP are about 4×10^{10} [44]. After passing through the IP, ejection transport lines lead to beam dumps.

The second bunch of electrons is directed onto a water cooled tungsten target to produce positrons. Positrons with energy between 2 and 20 MeV are collected and accelerated to 200 MeV by the linac back towards the damping rings. The positron bunches are cooled in the damping ring for 2 cycles before being extracted. With the injection of two new electron bunches, the next cycle begins.

The SLC luminosity has been steadily growing over time. In the 1997-98 run the luminosity increased by more than a factor of 3 to bring SLC within a factor of 2 of the initial design luminosity. Peaks of around 300 Z^0s per hour or 3×10^{30} cm^{-2}s^{-1} were obtained. A record week of 21,000 Z^0s was recorded in April 1998. The analysis presented in this thesis uses the 50k Z^0s collected in 1996 plus the 350k collected in the 1997-98 run.

2.1.3   Compton Polarimeter

Many of the physics analyses performed at SLAC rely heavily on the electron beam polarization. Section 2.1.1 described how the polarized electron bunches are created. However, for a physics analysis, the important parameter is the polarization at the interaction point. Due to the bunch width in phase space and spin manipulations in the accelerator, the polarization will be degraded with respect to that at the source. Therefore, it is crucial that the polarization be monitored precisely during the accumulation of data. This task is accomplished by the Compton polarimeter [45] shown in figure 2.4.

The Compton polarimeter is located downstream of the SLC interaction point. Electrons not involved in collisions at the SLC IP proceed to the 'Compton IP' where they encounter circularly polarized laser pulses from a Nd:YAG laser. The 532 nm laser has a repetition rate of 17 Hz and fires on every 7th cycle of the SLC. It is
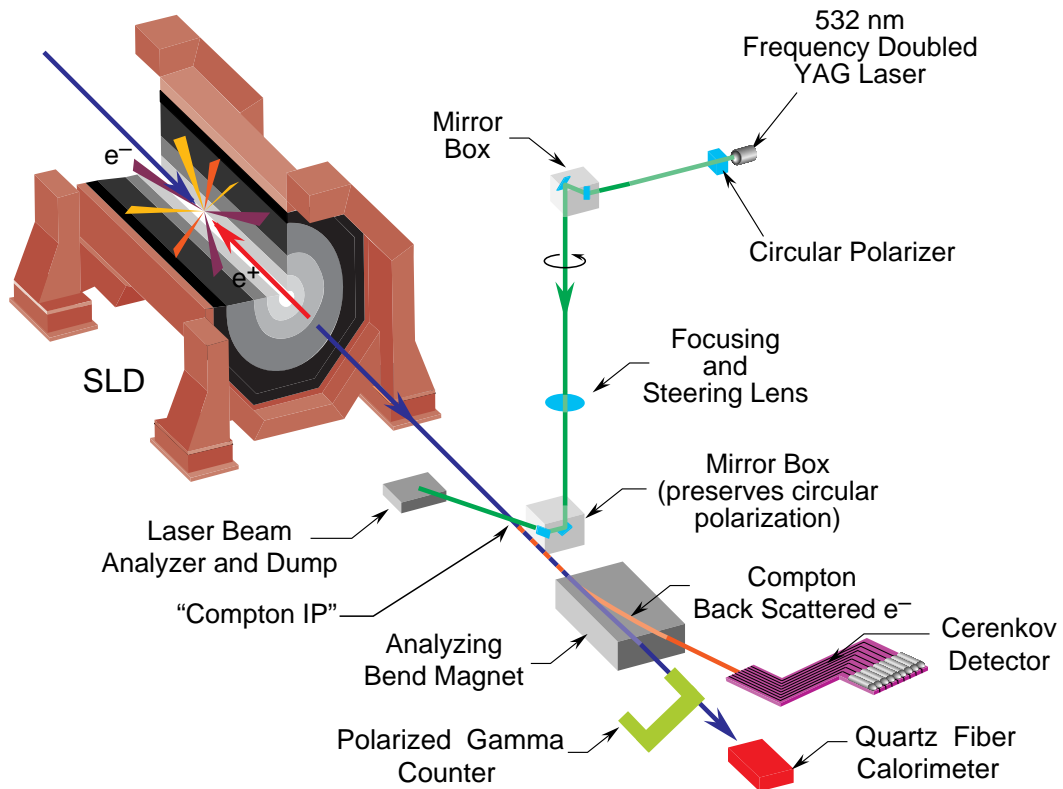
Figure 2.4: Schematic view of the Compton Polarimeter.

polarized with a linear polarizer followed by a series of PS and CP Pockels cells similar to the arrangement described for the polarized source. The Compton back scattered electrons lose energy in the photon collisions and are separated out by an analyzing bend magnet. The energy distribution of the scattered electrons is then measured by a 9 channel Cherenkov detector (CKV). This device consists of an airtight vessel filled with a Propane gas radiator. The nine channels are instrumented with phototubes and segmented transverse to the beam. Cherenkov photons from the Compton scattered electrons are detected by the phototubes. The transverse segmentation provides the energy measurement [46].

The polarized Compton cross section is given in terms of the unpolarized cross section by,

$$\sigma(y) = \sigma_0(y)[1 + P_e P_\gamma A(y)] \tag{2.1}$$

where P_e and P_γ are the electron and photon polarizations respectively. $A(y)$ is the

1992	P_e	=	0.224	$\pm$	0.006	
1993	P_e	=	0.626	$\pm$	0.012	
1994-95	P_e	=	0.772	$\pm$	0.005	
1996	P_e	=	0.765	$\pm$	0.005	
1997	P_e	=	0.733	$\pm$	0.008	Prel.
1998	P_e	=	0.731	$\pm$	0.008	Prel.

Table 2.1: The luminosity weighted polarization at SLC by year.

Compton asymmetry function and $y = E'/E_0$. The polarization measurement is made by measuring the following asymmetry,

$$\frac{N_i^{\rightarrow\rightarrow} - N_i^{\rightarrow\leftarrow}}{N_i^{\rightarrow\rightarrow} + N_i^{\rightarrow\leftarrow} - 2N_i^{\text{off}}} = a_i P_e P_\gamma \qquad (2.2)$$

The N_i are the numbers of Compton scattered electrons in channel i of the Cherenkov detector for parallel and opposite configurations of the electron and photon helicities. N_i^{off} reflects the backgrounds measured with the laser off. Finally, a_i represents the analyzing power for channel i. Typically, about one thousand backscattered electrons are detected per pulse with a channel occupancy of about 100. The typical signal to noise ratio in each channel is about 5:1. P_γ is measured on both sides of the compton IP by photodiode measurements of the amount of left and right polarized light.

The measured asymmetry provides nine independent measurements of P_e, one for each Cherenkov channel. However, the energy distribution of the Compton scattered electrons is characterized by the kinematic edge at 17.4 GeV (180° backscatter in the center-of-mass frame) and the zero-asymmetry point at 25.2 GeV (90° backscatter in the center-of-mass frame). Detector position scans precisely locate the kinematic edge in channel 7. This channel is used to make the polarization measurement while the others are used as cross checks. The statistical precision obtained in a 3 minute run is typically $< 2\%$. The luminosity weighted polarization is listed by year in table 2.1 [46].

Figure 2.5 shows the measured beam polarization at SLC as a function of time. Peak polarizations of $\sim 77\%$ were obtained at the IP from 1994-1996. The 1997-98 run saw substantial increases in luminosity but the polarization was slightly degraded. The average polarization over the 1997-98 run was 73%.
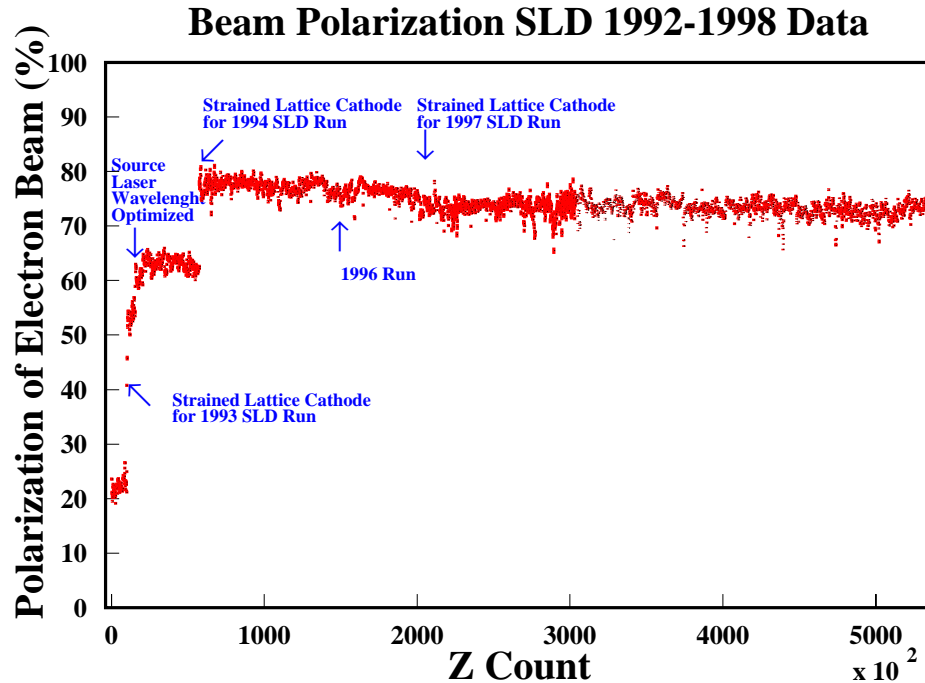
Figure 2.5: The measured SLC beam polarization versus time.

A series of other polarization measurements have been made as a cross check of the Compton polarimeter. The Quartz Fiber Calorimeter (QFC) and Polarized Gamma Counter (PGC) both measure the electron beam polarization by detecting the compton backscattered photons. However, both of these techniques require dedicated electron beam only operation. The preliminary QFC and PGC data analysis agrees with the CKV to $\sim 1\%$. Finally, the positron beam is assumed to be unpolarized but this was first checked experimentally after the 1998 run. The result was found to be $P_P = -0.02\% \pm 0.07\%$, consistent with 0.

2.2 SLAC Large Detector

The e^+e^- collisions produced by the SLC are observed and recorded by the SLAC Large Detector (SLD) which surrounds the SLC interaction point as shown in figure 2.6. The SLD is a general purpose detector designed to study decays of the Z^0
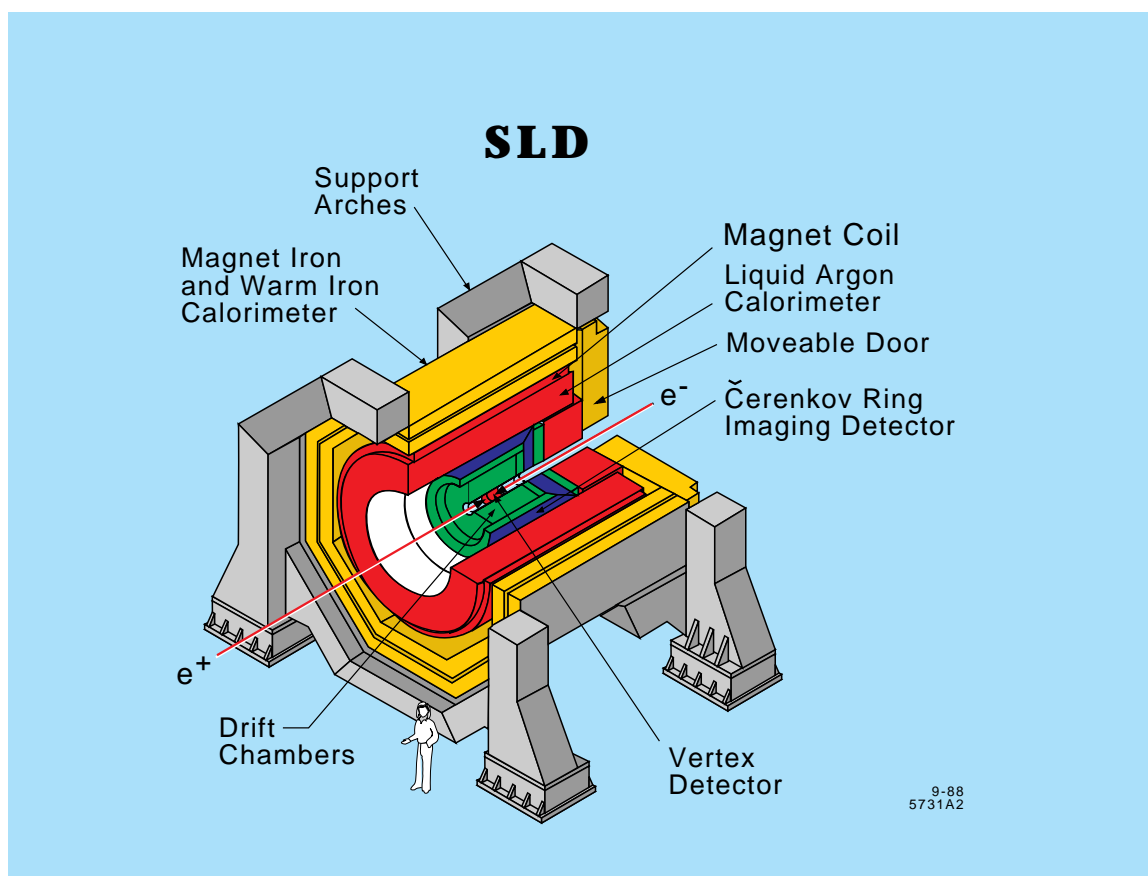
Figure 2.6: The SLD detector.

boson. It is composed of several detector subsystems. Charged particle tracking is performed by the central and endcap drift chambers in conjunction with a precise CCD pixel vertex detector. A Cherenkov ring imaging detector is located outside the drift chambers to provide particle identification. Calorimetry is performed by the liquid Argon calorimeter which includes both electromagnetic and hadronic sections. Finally the warm iron calorimeter is responsible for muon identification and tracking. The SLD magnet coil provides a 0.6 T magnetic field along the axis of the detector. Figure 2.7 is a cross sectional view of one SLD quadrant showing the relative locations of each subsystem. Each of the subsystems was utilized to some extent in this analysis and will, therefore, be described in some detail.
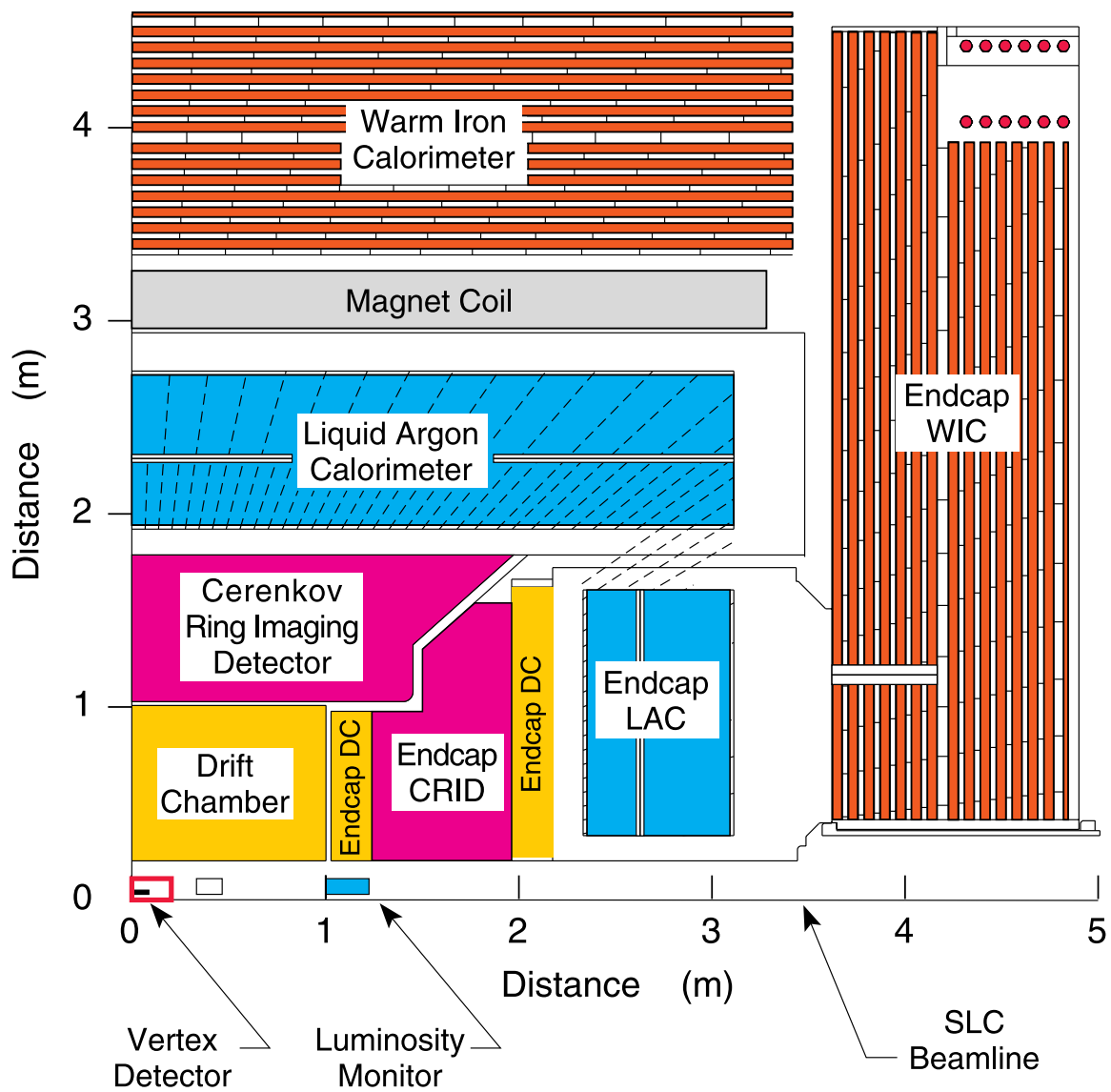
Figure 2.7: A cutaway view showing one quadrant of the SLD detector.

VXD3
(SLD)

1-97
7934A1
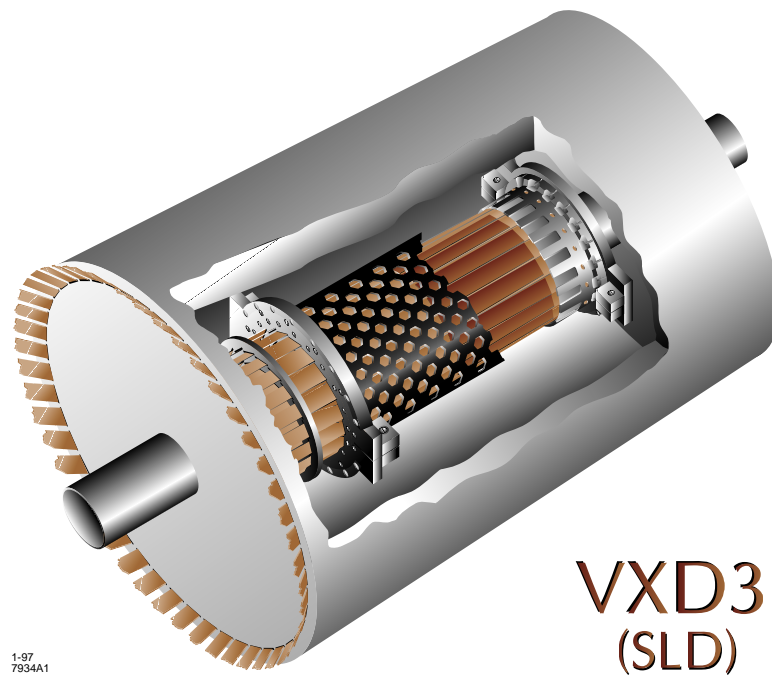
Figure 2.8: Cut-away drawing of the VXD3 detector.

2.2.1 VXD3

The vertex detector is the detection layer closest to the beamline and is responsible for precise tracking information near the interaction point (IP). For B physics, quality vertexing is essential for locating the B decay position and separating secondary tracks from those originating at the IP. In January 1996, SLD replaced the existing vertex detector, VXD2, with an improved model. Like it's predecessor, VXD3 [47] utilizes Charge Coupled Devices (CCDs) as the active element. The upgrade was possible due to advancements in CCD technology that allowed much larger devices of custom design.

The CCDs designed for VXD3 have an active area of 80×16 mm^2 each. The individual pixel size is 20×20 μm^2 which corresponds to 800 pixels horizontally and 4000 vertically. They are mounted on thin beryllium substrates which have kapton/copper flex circuits bound to both sides. The flex-circuits cover the full area of the substrate and have 5 cm 'pigtail' extensions for connecting to external micro-connectors. CCDs are attached to the flex circuits and wire bonded to circuit traces

CCD Fiducials   Flex-Circuit Fiducials

Outer CCD

Pigtail (Kapton/ Copper stripline)

Inner CCD

Beryllium substrate

North End   South End

4–97   8262A11
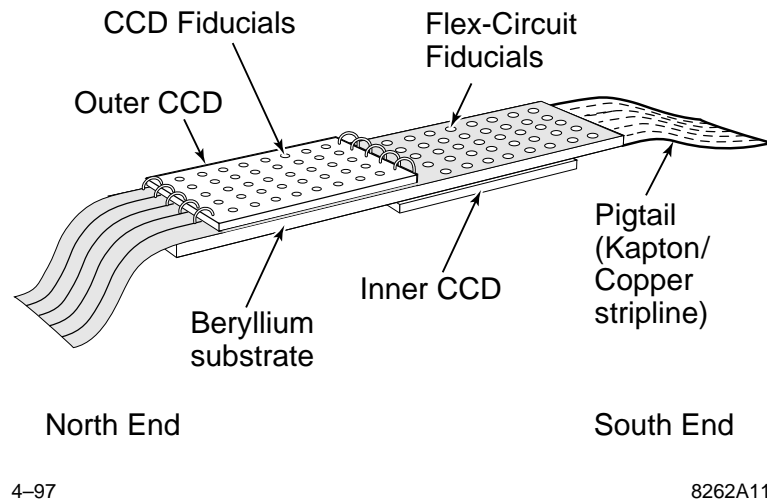
Figure 2.9: Basic 2 CCD Ladder Design.

at the narrow end to form 'ladders' (see figure 2.9). Each ladder holds two CCDs on opposite sides. Notice that this design allows the active region to extend fully to the long edge of the ladder with all external circuitry located along the short edges. The ladders can, therefore, be placed directly side-by-side in the final structure.

The CCD-ladder assemblies are attached to three, concentric beryllium annuli to form radial layers. Due to constraints from the beampipe radius at 23.2 mm and concerns over background levels, the first layer is located at an average CCD radius of 28.0 mm. It consists of 12 ladders mounted in a 'shingled' design with a cant angle of 10 degrees so that there is a small region of overlap (300 μm to 1 mm) between neighboring CCDs (see figure 2.10). This technique allows full azimuthal coverage in each radial layer. As a result, we expect ≥ 3 VXD hits per track which allows stand alone tracking and improved overall tracking efficiency.

The third layer, consisting of 20 ladders, was placed at an average CCD radius of 48.3 mm. This position was chosen to provide the maximum lever arm for track extrapolation to the IP while maintaining the full polar angle coverage allowed by the CDC ($|\cos \theta| \leq 0.85$). Large $\cos \theta$ coverage is important to analyses that depend on the polarized forward-backward asymmetry which is strongest at large angles.

The second layer contains 16 ladders at an average radius of 38.2 mm and cant
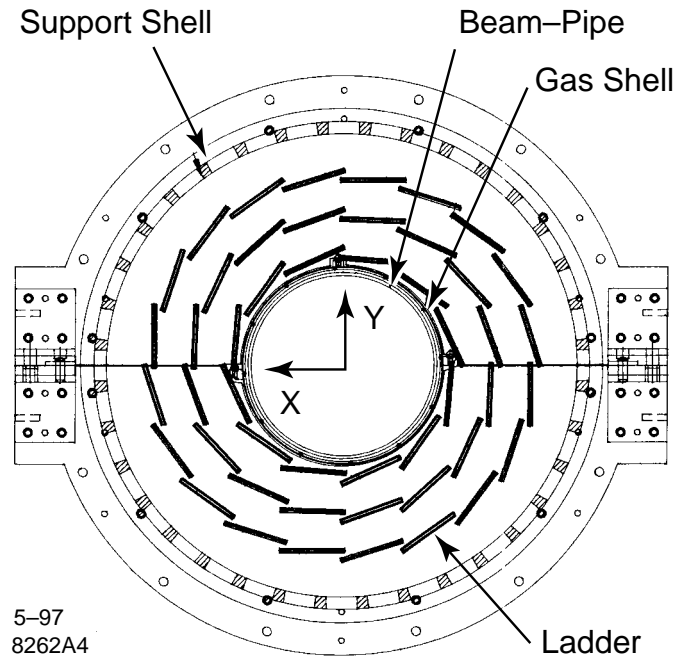
Figure 2.10: Cross-section $(r\phi)$ view of VXD3.

angle of 9 degrees. This layer is approximately half-way between layers 1 and 3 so that an adequate lever arm is still possible in the event of lack of data from layers 1 or 3.

The three annuli are clamped to a beryllium support structure. This structure was required to have high rigidity and low mass to minimize multiple scattering that would compromise impact parameter resolution. Beryllium was chosen for the support structure, as well as the ladder substrates and annuli, due to its high elastic modulus $(44.0 \times 10^6$ psi) and long radiation length (35.3 cm). The thickness of the ladder structure is only $0.4\%X_0$ compared to $1.15\%X_0$ for VXD2.

The entire structure is located in a low mass, foam cryostat for temperature regulation. The detector is cooled with Nitrogen gas to an operating temperature of around 185 K. Low temperature operation is necessary to reduce the effects of radiation displacement damage in the bulk of the silicon. This type of damage can cause the development of electron trapping centers that capture electrons as they traverse the device. The increase in charge transfer inefficiency is greatly reduced by operating

at low temperatures. During the 1996 run, VXD3 was operated at around 220 K. However, due to some initial non-standard beam tuning with high emittance beams and no magnetic field, layer 1 experienced significant radiation damage resulting in an efficiency loss of around 15%. It was found that lowering the temperature to 185 K restored operation to pre-damage performance levels. Therefore, VXD3 was operated at this lower temperature during the 97 and 98 runs.

In total, VXD3 consists of 48 ladders equipped with 96 CCDs of 3.2 million pixels each, or 307 million pixels in all. In order to measure the charge deposited in each pixel, the CCD is divided into four regions with an analogue output node in each of the four corners (384 total). Individual pixel charges are moved to the output nodes by a series of I clock and R clock pulses. The I clocks transfer charge, row to row, to the readout register where R clock pulses then move the charge to the output nodes. The R clock operating frequency is 5 MHz resulting in a total readout time of about 0.2 sec or 26 beam crossings at 120 HZ. In the 97-98 run a maximum luminosity of about 300 Z/hr or 1450 beam crossings per Z was achieved, so the rather long VXD3 readout time is adequate. However, each VXD event will contain integrated background from 26 beam crossings that must be rejected in the clustering and track linking stages. Even with these additional hits, the pixel occupancy is only a few times 10^{-5}.

The analogue outputs are transferred by the pigtails mentioned above to 50 cm long flex-circuits that lead out of the cryostat to 16 front-end (F/E) electronics boards. The F/E boards are responsible for amplifying and shaping the analogue CCD outputs as well as digitization using 8-bit flash ADCs. The multiplexed and serialized digital data is then carried by 50 m fiber optic cables to FASTBUS data acquisition modules in the SLD counting house.

The ultimate performance of the vertex detector depends on our knowledge of the detector geometry and alignment. The first pass geometry was produced by an optical survey of VXD3 to measure the CCD shapes and estimate the gravitational sag of the individual ladders. This survey was successful in establishing the geometry to within 1 pixel. Further internal alignment was performed by looking at tracks produced in hadronic Z^0 events. Three types of hit vectors were considered at this
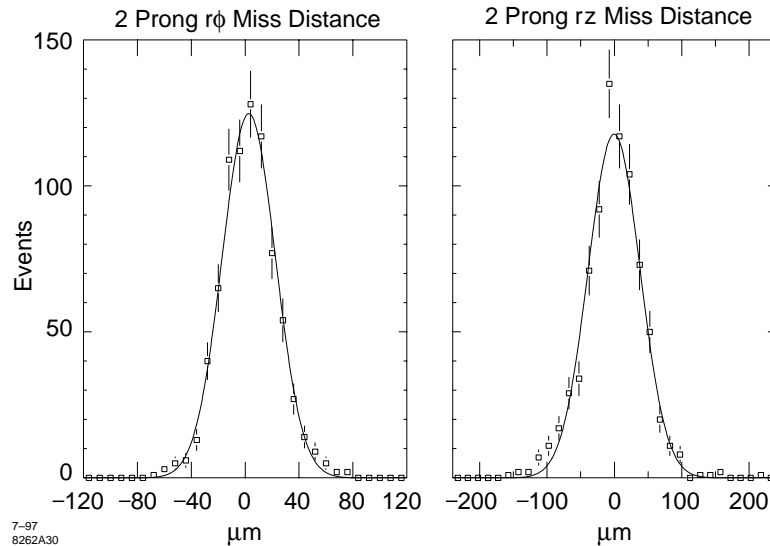
Figure 2.11: Mu-pair miss distance in $r\phi$ and rz projections.

stage:

1. **Doublets**: tracks that pass through both CCDs on a given ladder.

2. **Shingles**: tracks that pass through the overlapping region of two neighboring CCDs in the same layer.

3. **triplets**: tracks with hits in all three layers.

After internal alignment, the detector can be aligned with respect to the CDC by again looking at tracks in hadronic Z^0 decays and comparing the VXD hit vectors with CDC tracks extrapolated to the VXD region. This global alignment is performed after any known adjustments to the VXD3 position have been made. The degree of internal alignment can be assessed by measuring the two track miss distance in $Z \to \mu^+\mu^-$ events as in figure 2.11. The data suggest a single track impact parameter resolution of 14 μm in $r\phi$ and 26.5 μm in rz.

2.2.2 Drift Chamber

The drift chambers lie just outside the vertex detector and comprise the second stage of SLD's charged particle tracking system. The central drift chamber (CDC) is a

cylindrical section extending from 0.2 m to 1.0 m in radius and from -1.0 m to +1.0 m in z as shown in figure 2.7. It provides coverage for polar angles up to $|\cos\theta| < 0.85$. There are also two endcap drift chamber sections. The endcap tracking systems have not been utilized in this analysis so only the CDC will be discussed in detail [48].

When a charged particle traverses material, it suffers energy losses due to the ionization of atoms in the material through electromagnetic interactions. The principle behind drift chambers is to use the electrons liberated by the ionization process to track the charged particle. The cylindrical volume of the CDC is filled with a gas mixture consisting of 75% CO_2, 21% Argon, 4% Isobutane, and 0.2% water [49]. CO_2 was selected due to it's slow electron drift velocity that allows the resulting charge waveforms to be accurately sampled by the SLD electronics. It also has a low diffusion coefficient which is essential for good resolution. Isobutane was added as a quencher while the Argon produces the required gain. Water is included to reduce the effects of wire aging.

The CDC is divided radially into ten *superlayers*. Each superlayer is further subdivided azimuthally into *cells* measuring roughly 6 cm wide and 5 cm high. Each cell is instrumented with a series of wires running approximately parallel to the beam axis. Figure 2.12 shows the arrangement of sense wires, guard wires and field shaping wires in a typical cell. The guard and field shaping wires are made of 150 μm gold coated aluminum and are held at high voltage so that ionized electrons will drift onto the sense wires. The guard wires are set at 3027 V and surround the sense wires to focus the drifting electrons and provide uniform charge amplification. The gas gain is approximately 10^5. The high voltage on the field shaping wires varies with position with an average of 5300 V. The mean drift field produced by this arrangement is 0.9 kV/cm. The eight sense wires per cell are made of 25 μm gold-coated tungsten and are separated by 5 mm. A minimum ionizing particle passing through the CDC is expected to liberate about 16 electrons per sense wire resulting in a total charge at the sense wires of about 3×10^6 electrons.

The location of ionization sites is determined from the waveforms produced by the deposited charge at each end of the sense wires. These waveforms are sampled at 119 MHz by Analog Memory Units. The time of the leading edge of a pulse can be used
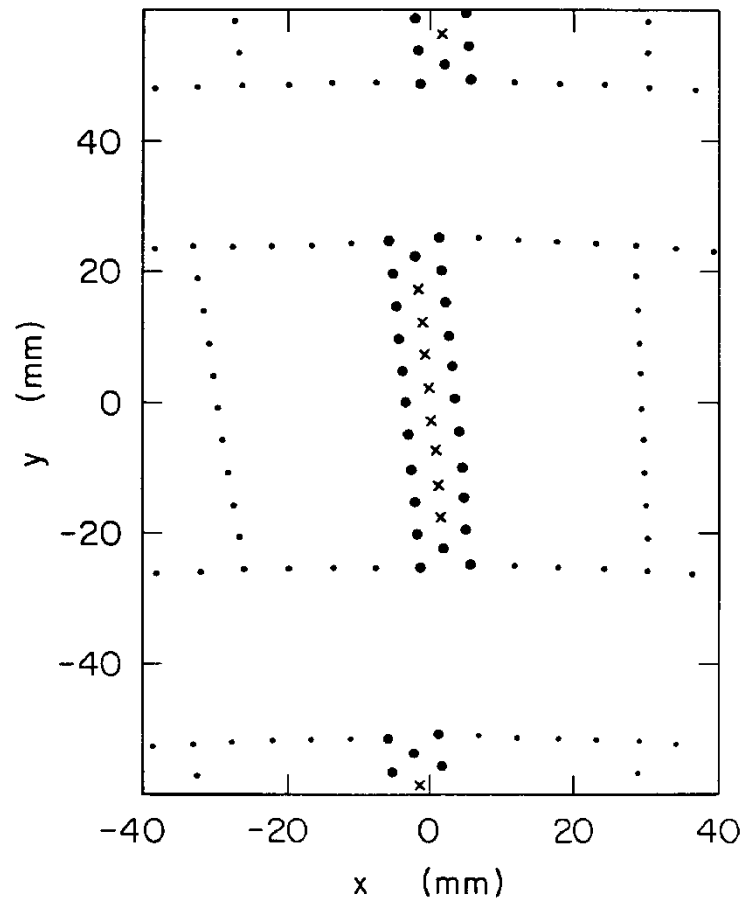
Figure 2.12: Wire layout in a single cell of the CDC. The 8 sense wires (x's) are surrounded by a grid of guard wires (bold dots). The field shaping wires are shown as dots.

to determine the distance of the hit from the sense wire. This requires an accurate knowledge of the drift field as well as the temperature and pressure of the gas which all affect the electron drift velocity, v_d. Given the drift time and trajectory predicted from the drift field and 0.6 Tesla SLD B field, the hit position can be located in xy. The nominal drift velocity is about 7.9 μm/ns and is used to locate initial hit positions. This estimate is refined run-by-run by allowing v_d to vary in the track fitting routines. Variations in v_d can be as large as 2%. The position of the hit along z is determined from the ratio of pulse heights at each end of the wire. This charge division technique is accurate to about 5 cm. Multiple hits on a single wire produce

several pulses in the waveform. The sampling rate used allows us to resolve hits whose drift distances are separated by $\sim$ 1 mm with good efficiency.

The 10 superlayers of the CDC alternate between axial layers where the wires run parallel to the beam axis and pairs of stereo layers with stereo angles of $\pm$ 41 mrad with respect to the beam axis. There are 4 axial layers separated by three stereo double layers. The purpose of the stereo layers is to resolve ambiguities in the xy hit positions. Note that the procedure described above cannot determine on which side of a given wire the hit occurred.

Track reconstruction occurs offline beginning with the time and charge information from each sense wire. The track fitter performs a detailed track swim taking into account fluctuations in the magnetic field, multiple scattering and energy loss. The intrinsic hit resolution is found to be $\sim$ 100 μm in regions of uniform field. The 0.6 T axial B field at SLD allows us to measure the track momentum transverse to the beamline from the track curvature. The momentum resolution of the CDC can be characterized by,

$$(dp_t/p_t^2)^2 = 0.0050^2 + (0.010/p_t)^2 \tag{2.3}$$

where p_t is measured in GeV/c.

Tracks found in the CDC are then extrapolated to the VXD for linking. A search for matching VXD hits is performed starting in the outer layers where backgrounds are low. Tracks are fixed at any matching hits and the resulting track is extrapolated to the inner VXD layers. A successful link is required to have at least 2 VXD hits. Finally, a combined VXD-CDC track fit is performed taking into account multiple scattering effects. In high momentum $Z^0 \rightarrow \mu^+\mu^-$ events the track linking efficiency is estimated to be greater than 99.8% [47]. The combined VXD-CDC impact parameter resolutions can be parametrized by,

$$\sigma_{r\phi} = 14.0 \oplus \frac{33}{p\sin^{3/2}\theta}\mu\text{m} \tag{2.4}$$

$$\sigma_{rz} = 26.5 \oplus \frac{33}{p\sin^{3/2}\theta}\mu\text{m} \tag{2.5}$$
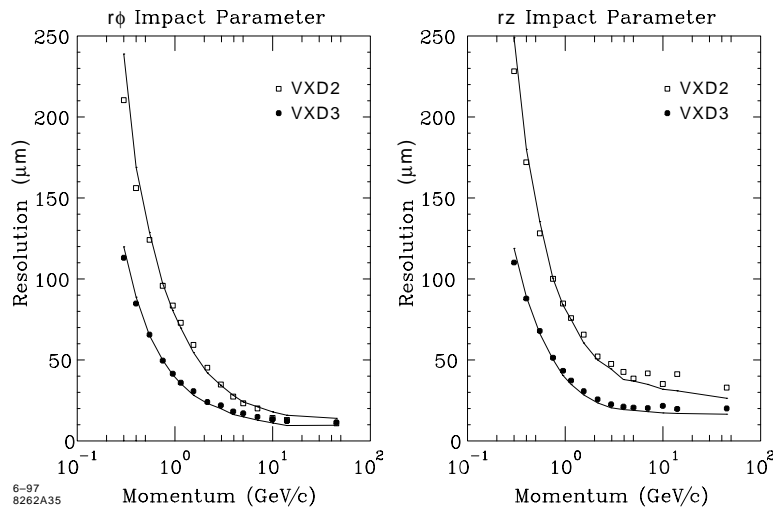
Figure 2.13: VXD3 impact parameter resolution for tracks at $\cos\theta = 0$ as a function of momentum. The solid lines are MC simulations.

2.2.3 CRID

When a charged particle passes through material at a velocity greater than the speed of light in that medium, it emits radiation known as Cherenkov radiation. The effect is similar to the shock waves produced by objects travelling faster than the speed of sound. A coherent wavefront is produced at an angle θ_C with respect to the flight direction determined by the particle velocity,

$$\cos\theta_C = \frac{1}{\beta n} \tag{2.6}$$

where n is the index of refraction of the medium [50]. The radiation is distributed uniformly in azimuth thus forming a ring in the plane perpendicular to the particle momentum. The angle of the Cherenkov radiation allows us to determine the velocity of the charged particle. Combined with a momentum measurement, the mass of the particle and, therefore, it's identity can be determined.

Charged particle identification is performed at SLD by the Cherenkov ring imagining detector (CRID). The position of the CRID in SLD is shown in figure 2.7. It is composed of barrel and endcap sections located between the drift chambers and the liquid Argon calorimeter. The barrel CRID provides coverage for the angular region $|\cos\theta| < 0.68$.
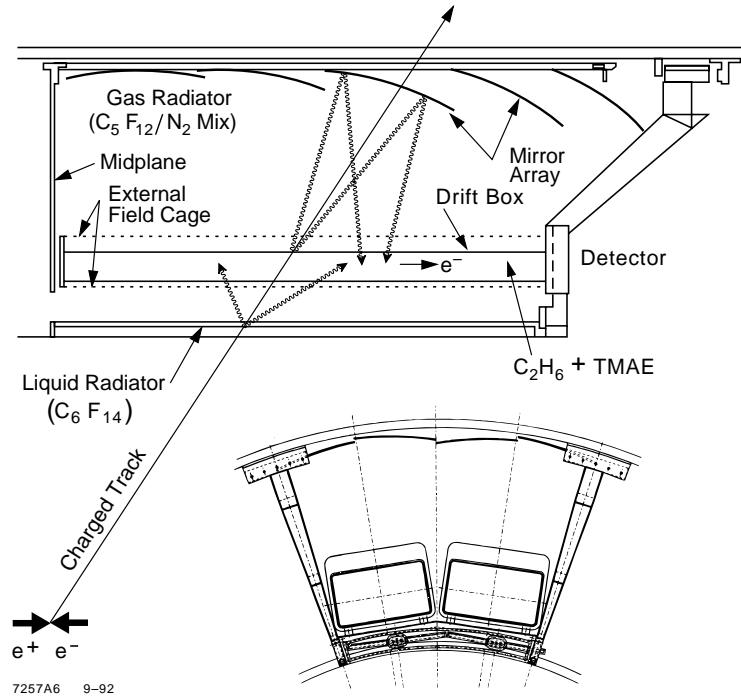
Figure 2.14: Schematic diagram of the barrel CRID.

The barrel CRID employs two separate radiators as shown in figure 2.14 so that particles can be identified over a wide momentum range. There is a liquid C_6F_{14} radiator ($n = 1.2176$) contained in 1 cm thick trays [51]. Also, the volume of the detector vessel is filled with a 76% C_5F_{12} ($n = 1.0017$), 24% N_2 ($n = 1.00032$) gas mix. For particles with $\beta = 1$, the expected Cherenkov angles are expected to be $3.04°$ and $38.5°$ for the gas and liquid radiators respectively. This combination of radiators provides efficient $\pi/K/p$ identification in hadronic Z^0 decays from $\sim$ 0.3-46 GeV/c [52].

The Cherenkov photons are detected by means of time projection chambers (TPCs) consisting of drift boxes connected to multiwire proportional chambers (MWPCs) as shown in figure 2.15. There are a total of forty TPCs in the barrel. They are spaced in ten azimuthal sectors with two TPCs on each side of the detector midplane. The inner and outer surfaces of the TPCs have windows made of UV transmitting quartz. Photons from the liquid radiator pass directly through the inner TPC window. An array of 400 spherical mirrors is positioned along the outer wall of the vessel to focus

photons from the gas radiator back onto the outer TPC window. Inside the TPCs is a mixture of 85% C_2H_6 and 15% CO_2. In addition, there is a small concentration ($\sim 0.1\%$) of a complex organic gas molecule, Tetrakis(diMethylAmino)Ethylene (TMAE), which has a large photoionizing cross section in the 170-220 nm region. The individual Cherenkov photons entering the TPCs interact with the TMAE to produce photoelectrons.

A double field cage consisting of 1600 field shaping wires and 163 corona preventing wires is located on the inside and outside of the TPCs. It produces a uniform electric field of roughly 400 V/cm along the axis of the detector. The photoelectrons, therefore, drift toward the MWPCs. The operation of the MWPCs is similar to that of the CDC described above. There are ninety-three 7 μm carbon anode wires per detector with readout amplifiers at each end. The 3 dimensional location of the point of origin of the photoelectron is approximated by the drift time (z-coordinate), address of the wire hit (x-coordinate), and charge division along the wire (y-coordinate). The photoelectron production point is measured to a precision of roughly $1 \times 1 \times 2$ mm in x, y, and z. The average number of hits per ring in hadronic decays is about 12.8 and 9.2 for the liquid and gas radiators respectively. The Cherenkov angle resolution is about 16 and 4.5 mrad for the liquid and gas radiators.

A likelihood is calculated for each charged track for the π, K, and p hypotheses [53]. The calculation takes into account both liquid and gas radiator information and is able to give smooth behavior at the thresholds. Particle identification is then made by considering differences in the $-\log \mathcal{L}$ for the various hypotheses. The π/K/p identification matrix is plotted in figure 2.16.

2.2.4   Liquid Argon Calorimeter

The SLD liquid Argon calorimeter (LAC) [54, 55] is located between the CRID and the magnet coil as diagrammed in figure 2.7. It is composed of a 6 meter long cylindrical barrel which extends from 1.77 to 2.91 meters in radius and is closed by two endcap sections. The endcaps extend from 0.33 to 1.60 m in radius and from 2.32 to 3.1 m along z. The barrel section covers the angular region $\theta \geq 33°$ while the
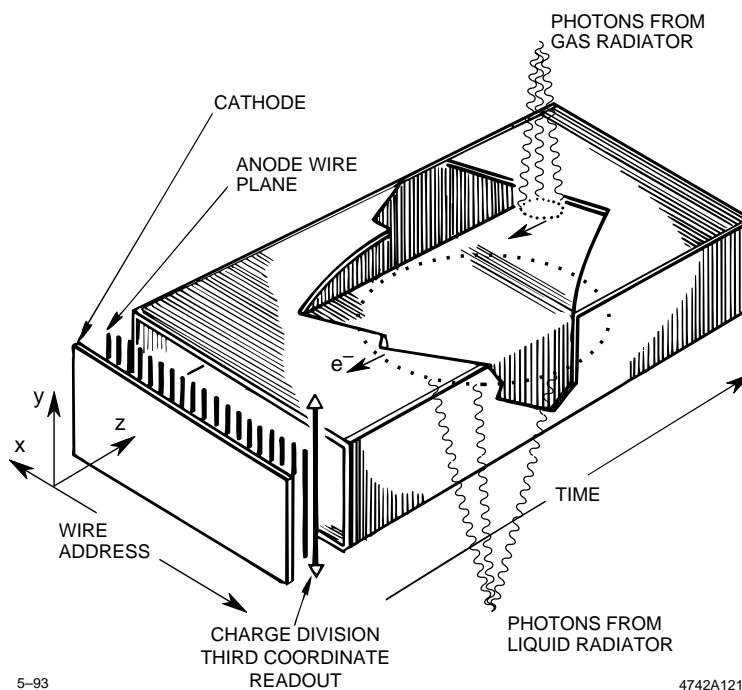
Figure 2.15: Diagram of the CRID time projection chamber design.

two endcaps cover $8° \leq \theta \leq 35°$. The calorimeters are responsible for measuring the energies of particles produced in Z^0 decays.

The basic structural units of the LAC are the electromagnetic and hadronic *modules*. The LAC barrel is divided into 3 segments of about 2 meters each along the beam axis. Each segment contains 48 EM and 48 hadronic modules spaced evenly around the azimuth with the hadronic modules stacked radially on the EM modules. The endcaps are constructed of 16 wedge shaped modules, each containing EM and hadronic components. The barrel and endcap modules are contained within 3 distinct vacuum insulated cryostats that use liquid nitrogen to cool the Argon. The modules within each cryostat share a common liquid Argon volume.

As shown in figure 2.17, the individual modules consist of layers of lead sheets and segmented lead tiles that are separated and electrically isolated by plastic spacers. The gaps between sheets and tiles are filled with pure liquid Argon. EM and hadronic showers, originating primarily in the lead, deposit ionization in the liquid Argon as they traverse the calorimeter. This ionization is collected by the lead tiles which are
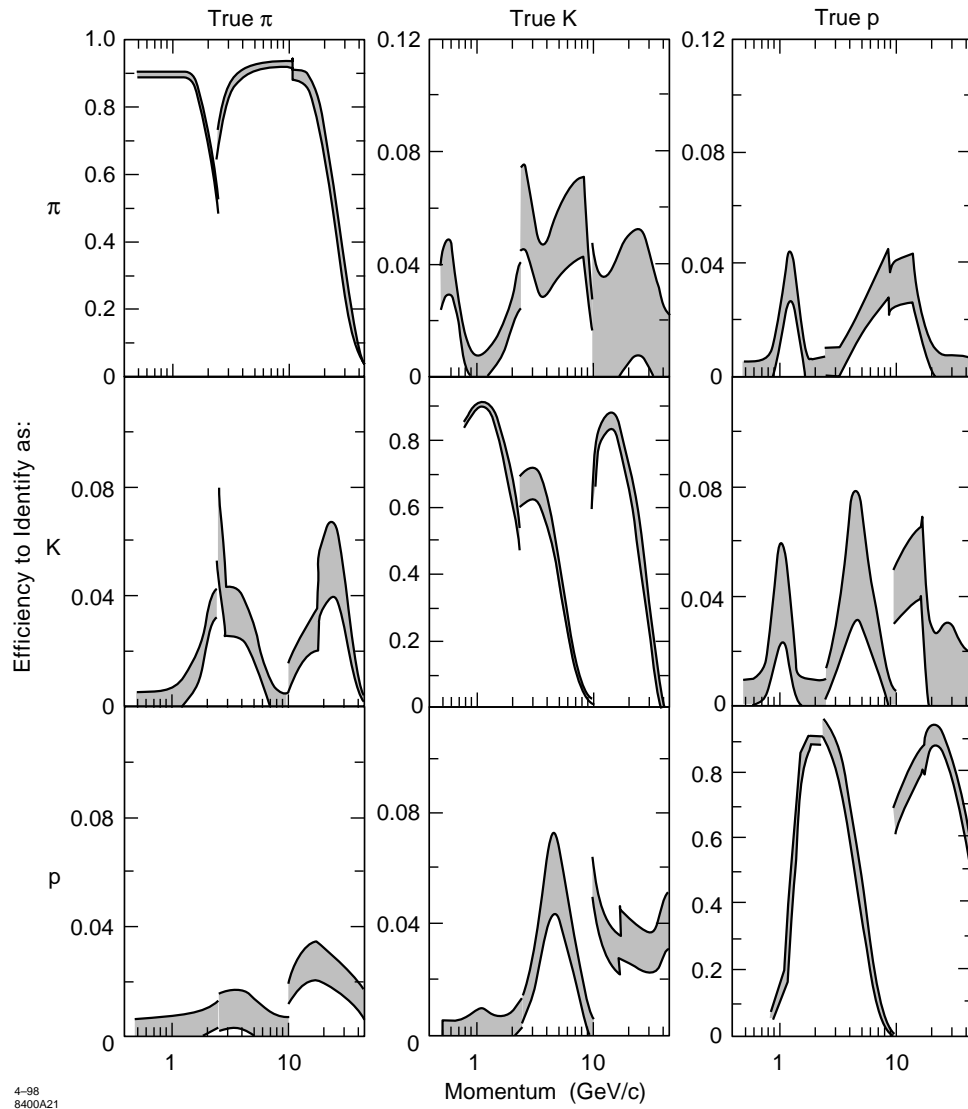
Figure 2.16: The CRID particle identification efficiency matrix. The diagonal elements represent the efficiency versus momentum to correctly identify $\pi/K/p$. The off-diagonal elements are the misidentification efficiencies. Note the difference in scale.
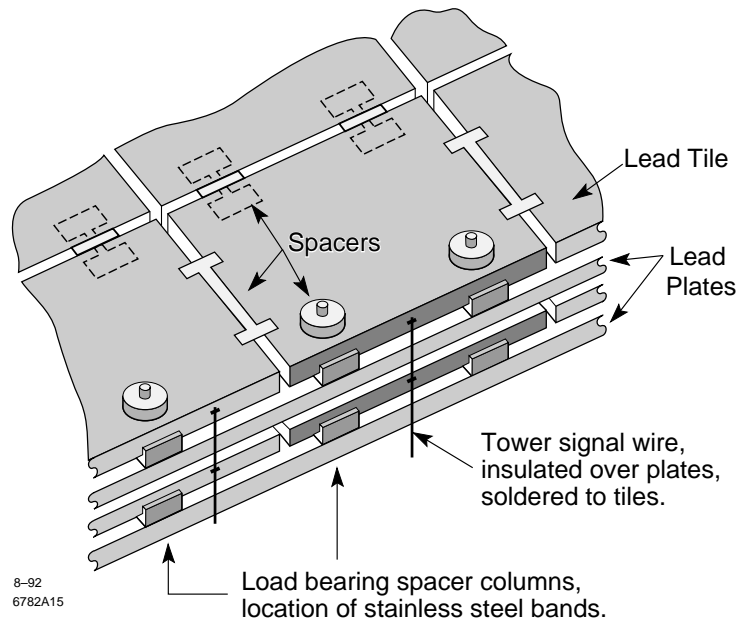
Figure 2.17: Detail of a hadronic module in the LAC barrel.

maintained at about -2000 V with respect to the grounded sheets. Thus the lead tiles act as charge collecting electrodes as well as providing high density material to absorb energetic particles. This design allows a more compact size. The ionization produced in the Argon is roughly proportional to the shower energy at that depth. Therefore, the LAC acts as a sampling calorimeter.

Projective towers are formed by linking tiles in adjacent layers with signal wires as in figure 2.17. These towers are constructed such that they project back in the direction of the interaction point, each tower presenting a roughly equal solid angle to particles coming directly from the IP. In this manner, each tower should measure approximately equal fractions of the event energy and provide uniform angular resolution of shower position, independent of the z coordinate. The EM layers are segmented into 192 towers in azimuth thus providing a resolution of $\delta\phi \sim 33$ mrad. The tower width in the z direction varies as a function of z so that $\delta\theta$ varies from 21 to 36 mrad. The hadronic layers are more coarsely segmented with 32 towers in z and 96 in azimuth.

In the EM modules, the lead plates and tiles are 2.0 mm thick and are separated by
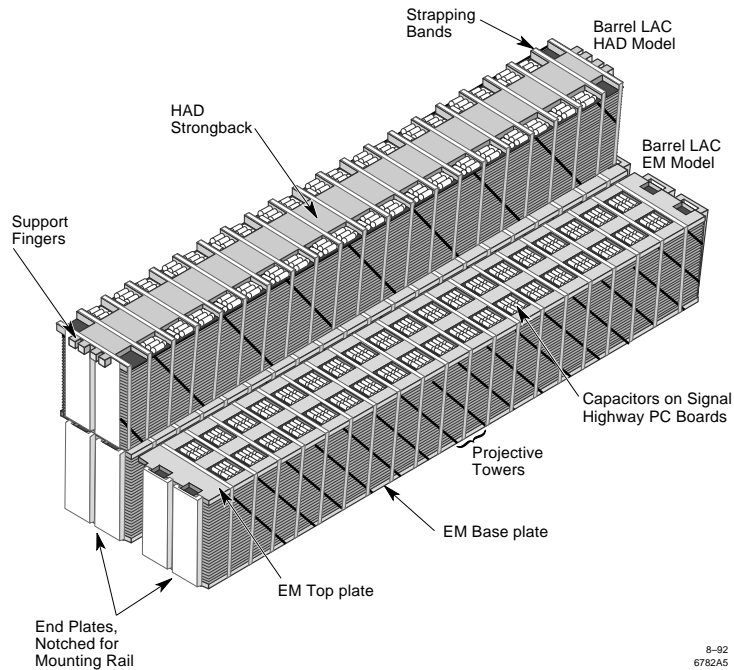
Figure 2.18: LAC barrel modules.

2.75 mm of Argon. The dE/dX sampling fraction for a minimum ionizing particle is, therefore, about 18%. A unit cell is defined as 2 layers of lead and 2 layers of Argon which corresponds to 0.751 X_0 of material. The EM calorimeter is longitudinally divided into two separate readout sections, EM1 and EM2, that are constructed of 8 and 20 unit cells respectively. This division allows us to monitor longitudinal shower development which is particularly useful in discriminating between electrons and pions. The two EM layers provide 21 radiation lengths total and, therefore, are sufficient for containing electrons up to 50 GeV with only 1-2% leakage. The LAC EM energy resolution is measured to be,

$$\sigma_E/E = 15\%/\sqrt{E(\text{GeV})}. \tag{2.7}$$

The lead sheets and tiles in the hadronic modules are increased in thickness to 6.0 mm while the Argon layers remain at 2.75 mm. The dE/dX sampling fraction thus drops to 7%. As in the EM calorimeter, the hadronic calorimeter is divided into two radial sections, HAD1 and HAD2, each composed of 13 unit cells. Each hadronic

LAC section	Cell Count	Cell X_0	Section X_0	Cell λ	Section λ
EM1	8	0.75	6.0	0.030	0.24
EM2	20	0.75	15.0	0.030	0.60
HAD1	13			0.077	1.00
HAD2	13			0.077	1.00

Table 2.2: LAC Longitudinal Segmentation

layer represents 1 interaction length, λ. This information is summarized in table 2.2. For hadronic showers, the energy resolution is about,

$$\sigma_E/E = 60\%/\sqrt{E(\text{GeV})}. \tag{2.8}$$

The analysis of LAC data will be discussed in more detail in section 4.7.2.

2.2.5 Magnet Coil

The SLD magnet coil [48] is located between the LAC and the WIC. It provides the 0.6 T solenoidal magnetic field used by the tracking systems to determine the charge and momentum of charged tracks. The coil is formed from 5 cm × 7 cm rectangular aluminum conductor. It is wound in four 27 turn layers to produce a cylindrical coil that is 5.9 meters in diameter, 6.4 meters long and 29 cm thick. The iron for the magnetic flux return is provided by the WIC, to be described in the next section.

The power supply provides 6600 Amps at 750 volts through the coil. The field produced can be expressed as,

$$B_r = B_r^0 \frac{rz}{r_0 z_0} \tag{2.9}$$

$$B_z = B_z^0 + 0.5 B_r^0 \left(\frac{r^2 - 2z^2}{r_0 z_0} \right) \tag{2.10}$$

where $B_r^0 = 0.0214$ T, $B_z^0 = 0.6$ T, $r_0 = 1.2$ m, and $z_0 = 1.5$ m. The magnet is water cooled at about 50 l/s to dissipate the 5 MW of power produced.

2.2.6 Warm Iron Calorimeter

The warm iron calorimeter (WIC) [48, 56] is the outermost section of the SLD detector. It is responsible for absorbing any hadronic shower tails that are able to

penetrate the LAC as well as muon identification and tracking. The WIC is located outside the magnet coil and provides the iron necessary for magnetic flux return. Like most subsystems, the WIC is formed by a barrel section and two endcaps, as shown in figure 2.7, for nearly complete solid angle coverage (99.2%). However, the WIC also employs 45° chambers due to a gap in coverage in this region. In this analysis, the WIC was used for muon tracking and identification only in the barrel region.

The WIC barrel is 6.8 meters long and extends from 3.3 to 4.5 m in radius with an octagonal cross section. The eight octants are each formed by two *coffins* of 54 cm height and 315-360 cm width. Each coffin is made up of seven 5 cm thick iron plates separated by 3.2 cm gaps. The gaps are filled by plastic limited-streamer tubes known as Iarocci tubes which form the active elements of the WIC. At $\theta = 90°$, the iron is 71 cm thick or about 4 absorption lengths.

The structure of the Iarocci tubes is indicated in figure 2.19. Each tube is actually a module of extruded plastic which is divided into eight cells. The 9×9 mm cells contain a 100 μm Be-Cu wire at 4.75 kV and are filled with a gas mixture of 88% CO_2, 9.5 % Isobutane, and 2.5% Argon. The inner wall of the cells is coated with a conductive graphite paint. A charged particle passing through the cell will ionize atoms of the gas mixture. The free electrons are accelerated by the high voltage wire and thus produce more ionization in collisions with the gas. The resulting avalanche is called a streamer.

Individual Iarocci tubes are combined to form chambers by attaching them to sheets of glassteel, a material similar to G-10. The number of tubes per chamber varies with location in the WIC, the maximum being 14. The glassteel is coated on both sides with 25 μm of copper which is etched in strip and pad configurations. Streamers in the Iarocci tubes produce a signal in the copper due to the conductive graphite coating inside the cells. Therefore, the strips and pads act as the readout electrodes. Generally, a ground plane and a layer of strips running parallel to the wire direction is attached below the tubes and a layer of pads is located above.

The rectangular pads in the layers of each coffin are daisychained together to form projective towers. These towers are constructed to point back to the interaction point such that they continue the tower structure initiated in the LAC. This double tower
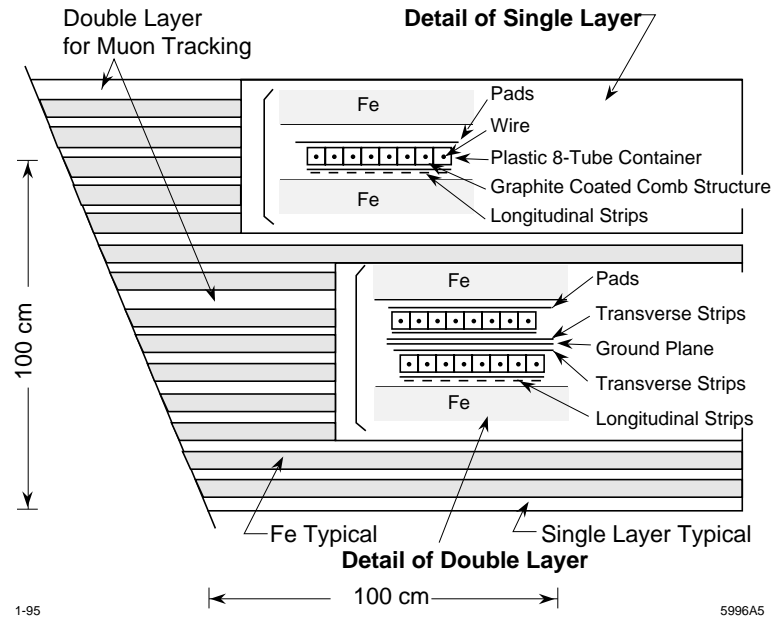
Figure 2.19: Detail of the WIC showing the layers of iron and Iarocci tubes.

structure provides the WIC calorimetry information. However, the energy resolution is fairly poor $(\sim 80\%/\sqrt{E(GeV)})$ so that the WIC pads are not used in the SLD event reconstruction. The strip electrodes provide the muon tracking information. In the WIC barrel, most strips are oriented parallel to the wire direction or along the z axis. Therefore they can only provide particle tracking in the $r\phi$ plane. To locate muons in three dimensions a double layer of tubes is located at the top of each coffin as shown in fig 2.19. One layer of tubes is equipped with longitudinal strips and pads while the other has strips longitudinal and transverse to the wire direction. Therefore, two space points are located along the muon track. The use of the WIC in muon identification will be described in more detail in section 4.6.2.

The WIC endcaps consist of two octagonal layers. The inner endcap layer is constructed of three horizontal sections and is 4.5 m in width. The outer endcap is 3.9 m in width and is constructed of two vertical sections. The structure of these layers is nearly identical to the barrel coffins: seven 5 cm iron plates separated by 3.2 cm gaps instrumented with Iarroci tubes. The tubes in the inner section run horizontally while those in the outer section are vertical. As in the barrel, there

	Tubes	X Strips	Y Strips	Towers
Barrel	40336	35312	21120	4416
45° Chambers	11264	11264	3840	NA
Endcaps	26752	23532	6400	3872
Total	78352	70128	31360	8288

Table 2.3: WIC Readout Channel Counts

are double layers located between sections and outside the outer section for muon tracking. The WIC readout channel counts are summarized in table 2.3.

2.2.7 Luminosity Monitor

Two silicon-tungsten sampling calorimeters [57] provide coverage at very small angles at SLD. The Luminosity Monitor and Small Angle Tagger (LMSAT) is mounted around the beamline with the front face 101 cm from the IP. It covers the angular region between 28 and 68 mrad. The Medium-Angle Silicon Calorimeter (MASC) is located 31 cm from the IP and covers 68-190 mrad. An identical pair of calorimeters is located on each side of the IP.

The LMSAT and MASC are both formed from alternating layers of tungsten plates and 300 μm silicon chips mounted on G-10 circuit boards. The silicon is divided transversely into ~ 1 cm^2 cells to provide angular information. The LMSAT is composed of 23 layers, the first 6 are ganged together to form EM1 and the last 17 form EM2. Each layer is 0.86 X_0 thick. The cells are connected to form projective towers, similar to the grouping of the lead tiles in the LAC. The MASC is composed of 10 layers, the first 3 forming EM1 and the remaining seven forming EM2. The MASC layers are 1.74 X_0 each.

The LMSAT is able to act as a luminosity monitor for the SLC by counting small angle bhabha events $(e^+e^- \rightarrow e^+e^-)$. The cross section for this process is well known and has very little interference from the Z^0 at small angles. We expect about 4 Bhabhas in the LMSAT per hadronic Z^0. The integrated luminosity can be measured to about 3%.

Run 34356, EVENT 3541
28-MAY-1996 13:17
Source: Run Data   Pol: R
Trigger: Energy CDC Hadron WAB
Beam Crossing   1539771121
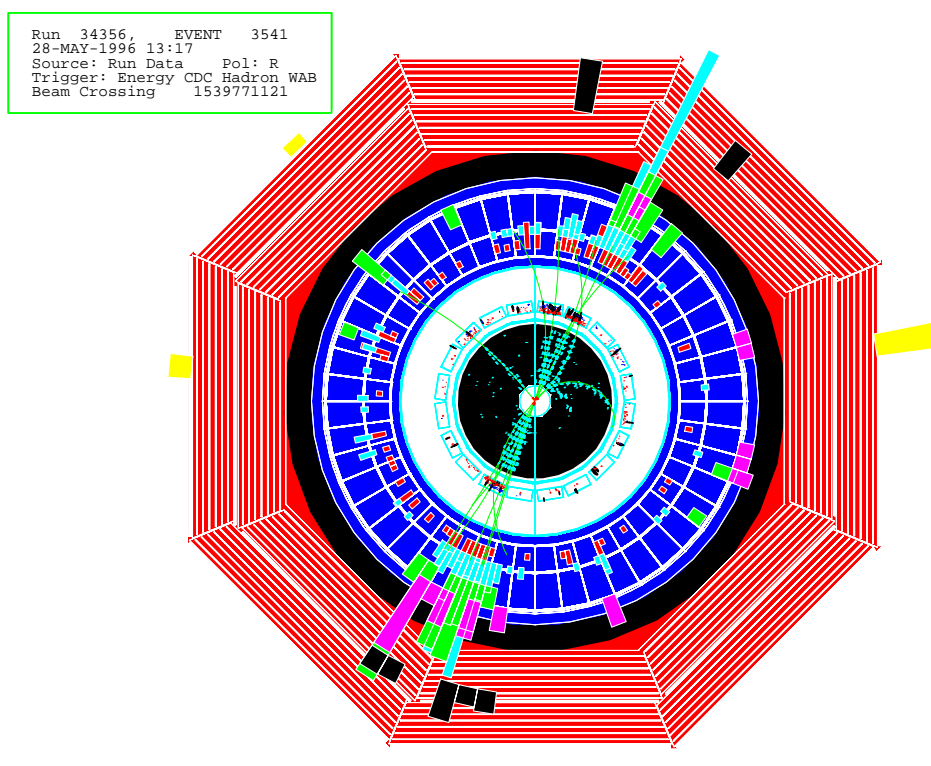
Figure 2.20: A typical 2 jet hadronic event in the SLD detector as seen along the beam axis.

Chapter 3

Monte Carlo

This analysis makes extensive use of simulated data called Monte Carlo (MC). This technique attempts to 'create' individual events in as much detail as the true data. Beginning with the initial electron-positron interaction, the MC generates physics events by randomly sampling the relevant cross sections, decay widths, lifetime distributions and so forth expected in our current understanding of particle physics. Of course, not all of particle physics is well understood at this point so phenomenological models are called upon when necessary. Ultimately, the data produced by a high energy physics experiment consists of the signals generated in the detector subsystems. Therefore, MC generation includes a complex description of the interaction of the final state particles with the detector. In the limit of a large number of MC events, we expect the simulated distributions to match those in the true data.

The creation of MC data at SLD proceeds in three main steps: beam simulation, event generation, and detector response. The SLC collides positrons with longitudinally polarized electrons so the beam simulation stage is relatively simple. The output of this stage is a center of mass energy, electron beam polarization, and interaction point. Random fluctuations in these quantities are allowed within a predefined range. The event generation and detector simulation are significantly more complex. The next two sections will describe these processes in more detail.

The MC data was used throughout this analysis to optimize the analysis technique, tune the selection cuts and evaluate the effectiveness of the analysis. Therefore, it
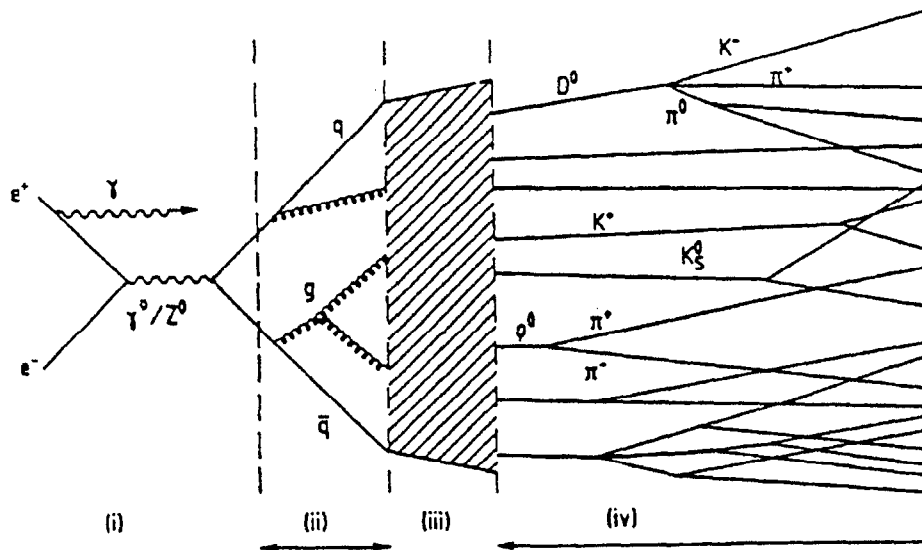
Figure 3.1: Stages of event generation

is important to make sure the MC well simulates the data. The following chapter describing the analysis will contain frequent data/MC comparisons.

3.1 Event Generator

The results of the beam simulation provide the input to the next stage: event generation. At SLD, the JETSET 7.4 [58] event generator is used to create physics events. The fundamental stages of event generation are shown schematically in figure 3.1.

Stage (i) represents the electron-positron interaction including initial state radiation as well as hard scattering. Although the electron and positron are elementary particles, a parton distribution function $f_e^e(x)$ is introduced. It represents the probability that the electron taking part in the hard scattering does so with a fraction x of it's original energy. The rest is radiated as initial state photons.

At SLD, the hard scattering process of most interest is,

$$e^+e^- \rightarrow \gamma/Z^0 \rightarrow q\bar{q} \tag{3.1}$$

The matrix elements involved in this interaction are calculable in the current electroweak theory. The final state quark flavor is chosen at random according to the relative couplings and CM energy. The quark angular distributions are also included.

Stage (ii) describes the final state radiation from the $q\bar{q}$ pair. Both the initial and final state radiation processes are simulated using a *parton shower* technique. This process describes the emission of photons and gluons from charged and colored partons respectively. It is responsible for the overall topology of the event. Hard gluon radiation frequently results in multijet events. The parton showers are built up from the individual branchings $e \to e\gamma$, $q \to qg$, $q \to q\gamma$, $g \to gg$, and $g \to q\bar{q}$. Each is characterized by a splitting kernel $P_{a \to bc}(z)$ which is an approximation to the matrix element calculations with simplified kinematics, interference and helicity structure. The variable z is the momentum fraction of particle a that is carried away by particle b.

Stage (iii) of figure 3.1 represents *hadronization*. Also known as *fragmentation*, hadronization is the process which transforms the colored partons into colorless hadrons. The process we are mainly interested in is $Z^0 \to q\bar{q}$ where the quarks emerge back to back with energies equal to half the Z^0 mass. As the quarks move apart the color force between them grows. Eventually the energy density is great enough to create new $q\bar{q}$ pairs from the vacuum which combine with the original partons into colorless hadrons as shown schematically in figure 3.2.

As suggested by the shaded region in figure 3.1, the hadronization process is not well understood. At short distances, quarks become asymptotically free so that calculations may be performed with perturbative QCD. But fragmentation involves interactions where the color force is large which is precisely the region where perturbative QCD breaks down. Therefore, only phenomenological models exist to describe fragmentation. The JETSET package employs a fragmentation model called the LUND string fragmentation [59]. The string fragmentation model describes the quark interaction as a 'color flux tube' with uniform energy density (~ 1 GeV/fm) being stretched between the two quarks. Therefore, the potential grows linearly as the quark separation increases. When the string breaks, a new $q'\bar{q}'$ pair is formed. Further string breaks are possible until only on shell hadrons remain.
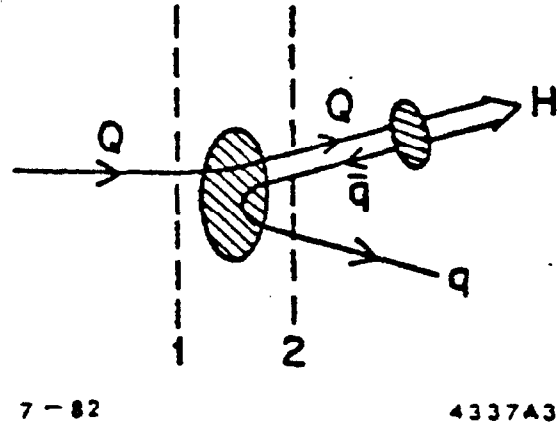
Figure 3.2: Heavy quark fragmentation.

The LUND model treats the production of new $q'\bar{q}'$ pairs as a form of quantum mechanical tunneling so that the likelihood of pulling a particular quark flavor from the vacuum depends on mass. The suppression of heavy quark production is in the approximate ratio

$$u : d : s : c :\approx 1 : 1 : 0.3 : 10^{-11}. \tag{3.2}$$

The fraction of the total momentum taken by each new particle is determined by the fragmentation function. Symmetry considerations in the LUND scheme result in the 'LUND symmetric fragmentation function' which contains two free parameters that must be tuned to the data. For heavy quark fragmentation (b and c) the Peterson *et al.* [60] parametrization was found to give a better description of the data. In this model the fragmentation function of heavy quarks Q is given by,

$$\mathcal{D}_Q^H(z) = \frac{N}{z(1 - \frac{1}{z} - \frac{\epsilon_Q}{1-z})^2} \tag{3.3}$$

where z is the fraction of the initial heavy quark momentum retained by the heavy hadron, $z = (E + p_{||})_{\text{hadron}}/(E + p)_{\text{quark}}$. The single parameter ϵ_Q is expected to be approximately the ratio of effective quark masses m_q^2/m_Q^2. The normalization N is
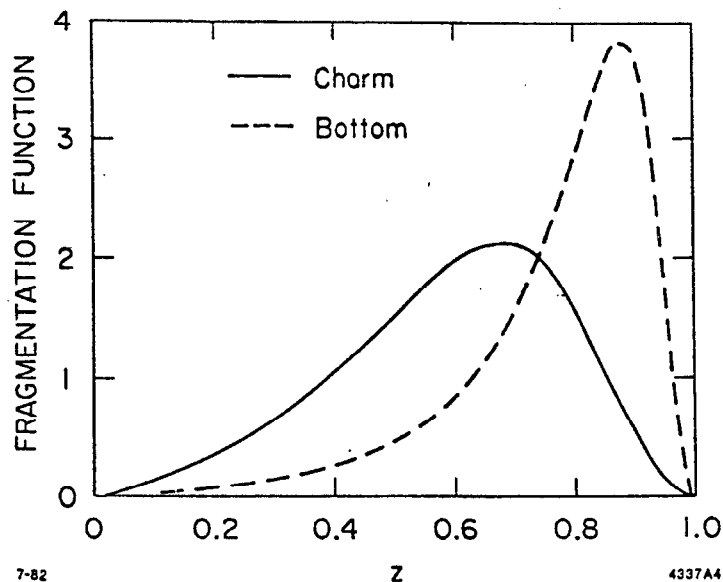
Figure 3.3: Bottom and charm quark fragmentation functions in the peterson parametrization.

determined by summing over all hadrons containing Q,

$$\sum \int_0^1 dz \, \mathcal{D}_Q^H(z) = 1. \tag{3.4}$$

For b quarks this function is sharply peaked at large z as shown in figure 3.3. This behavior is expected since attaching a light quark $\bar{q}$ or diquark qq (for baryon production) should only slightly decelerate the heavy quark. Thus the resulting heavy hadron has nearly the same energy as the initial heavy quark.

Stage (iv), the final step in the event generation, simulates the decays of unstable hadrons produced in the fragmentation process. The decays are governed by tables of decay modes and branching ratios. Of particular importance to this analysis are the B decays. The B meson decay modes have been tuned to reproduce the spectra and multiplicities of leptons, charmed hadrons, pions, kaons, and protons at the $\Upsilon(4S)$ according to the CLEO B decay model [61]. The CLEO model uses its own separate lists of particle masses and widths together with a complete listing of branching ratios. The CLEO lifetime values are ignored in favor of LUND's. Semileptonic

Parameter	B_d^0	B_s^0	B^+	Λ_b
Production Fraction	40.6	11.4	40.6	7.4
Lifetime (ps)	1.55	1.57	1.64	1.22
$\mathcal{B}(b \to l)$	11.0	11.0	11.0	10.5
$\mathcal{B}(b \to c \to l)$	10.5	8.2	7.5	5.0
$\mathcal{B}(b \to \bar{c} \to l)$	1.7	1.78	1.7	1.4
Δm_d (ps^{-1})	0.484	-	-	-
Δm_s (ps^{-1})	-	10.0	-	-

Table 3.1: Important Monte Carlo parameters.

decays follow the ISGW model [62]. The remaining unstable hadrons are decayed by the default JETSET except for the semi-stable K_s^0, Σ^+, $\Xi^{0,-}$, Λ, and Ω^-. These particles are decayed later by the detector simulation to account for the B field and detector interactions.

3.2 Detector Simulation

The event generator described above creates individual events given our best knowledge of elementary particle physics. However, the data in a high energy physics experiment consists of the signal produced by final state particles interacting with our detector. Therefore, the next step of MC production is the detector simulation. SLD uses the GEANT 3.21 package [63, 64] produced at CERN to simulate the detector response. Given the large size and complexity of the SLD, it is no easy task to predict the outcome of high energy particle interactions. We must take into account the active detector components which generate the observed signals as well as interactions with the passive material in the support structure, electronics, cabling, plumbing and so forth. Therefore, the simulation includes a detailed description of the detector geometry including material properties and detector elements. The other inputs at this stage are the final particles produced by the event generator along with details of the field configuration.

GEANT is responsible for tracking the particles produced by the event generator through the detector volume taking into account the interactions with matter and

the magnetic field. Simulating a given discrete interaction requires sampling the total cross section to evaluate the probability of the process occurring. After interaction, the differential cross section is sampled to generate the final state. GEANT currently includes descriptions of e^+e^- pair production and annihilation, Compton scattering, the Photoelectric effect, Bremsstrahlung, generation of Cherenkov light, synchrotron radiation, δ ray production and decay in flight. Quasi-continuous processes such as dE/dx energy loss and multiple scattering are included by computing mean values of the characteristic quantities. Interactions of hadrons with nuclei are simulated with the GHEISHA hadron shower generator. Each particle is tracked through the detector until it is absorbed in an interaction, exits the detector, or falls below its energy threshold.

The output of the detector simulation is a set or raw data banks that are essentially identical to the real data. In general, the MC data describes the real data quite well. However, there remain several discrepancies which are corrected at a later stage. The first is called the tracking efficiency correction. The charged track multiplicity in the Monte Carlo turns out to be slightly larger than that in the data. In the MC, the average track multiplicity per event is 15.08 while it is only 14.54 in the data [65]. Therefore, we randomly toss out about 3.3% of the charged tracks in the MC based on a parametrization of the data/MC disagreement in the track p_T, $\cos\theta$ and ϕ distributions. Figure 3.4 shows the event charged track multiplicity before and after the correction.

The charged track resolution is also smeared to match impact parameter distributions in the data. Comparing the z coordinates of tracks at the point of closest approach to the beam axis, it was found that the data distribution has a core width slightly larger than that in the MC. A track $p_\perp$ dependent smearing is, therefore, applied to the MC. After smearing, the z coordinate of the IP is recalculated.

Finally, if we want the MC data to be directly comparable to the real data we must take into account the time dependent run conditions. Concessions are made for noisy running periods, broken wires, hot calorimeter chambers, etc. In addition, beam related backgrounds are simulated by studying background events in the data. These background events are overlayed on the MC hadronic events to reproduce noisy

Tracking Efficiency Corrections

ID	102
Entries	187497
Mean	15.08
RMS	4.460

Before Eff. Correction
Data mean = 14.54

Track Multiplicity

ID	103
Entries	187497
Mean	14.55
RMS	4.368

After Eff. Correction

Track Multiplicity
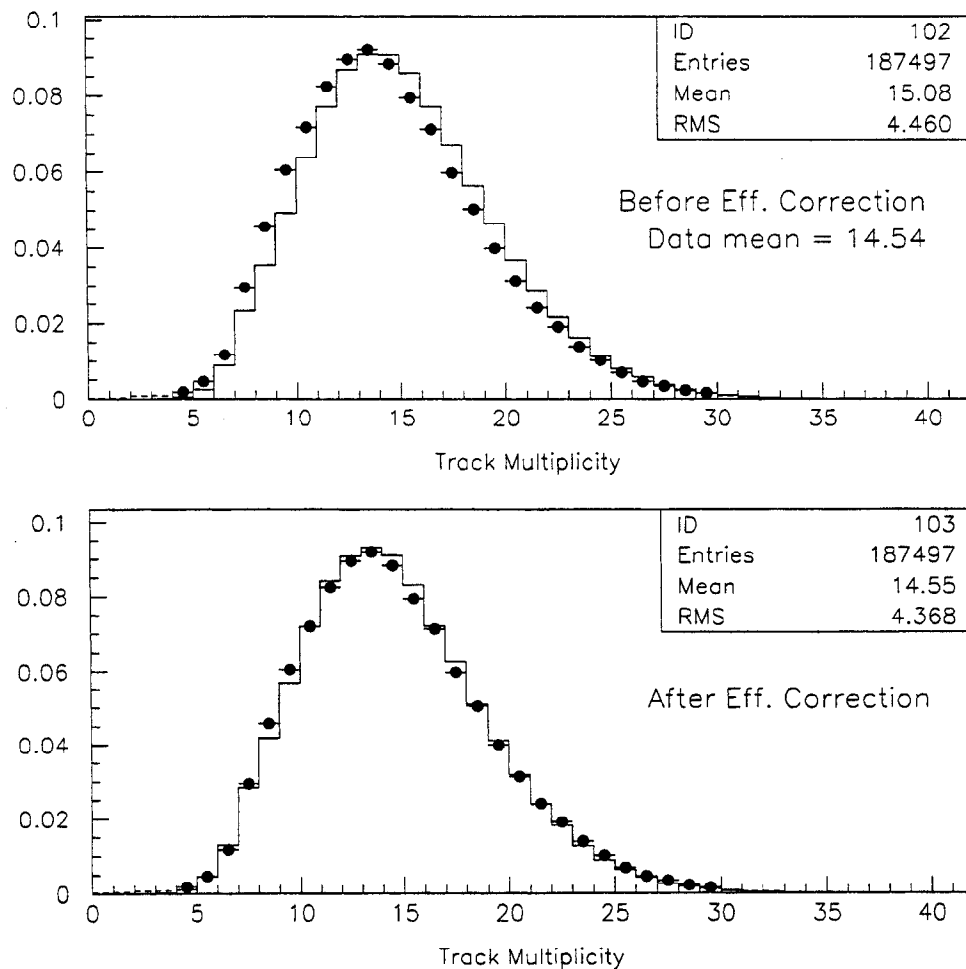
Figure 3.4: Results of the tracking efficiency correction. The points are the data while the histograms are the MC before and after the correction. The histogram statistics refer to the Monte Carlo.

beam conditions. Eventually, very good agreement is attained between the SLD data and MC.

Chapter 4

Event Selection and Reconstruction

This chapter begins with the basics of event selection and reconstruction at SLD. A brief description of the data acquisition triggers and hadronic event selection used to isolate $Z^0 \rightarrow q\bar{q}$ events will be given. Jet formation and determination of the interaction point (IP) will be described. Finally, there is a discussion of the time dependent analysis of $B^0\bar{B}^0$ mixing broken into the three main components: the initial state flavor tag, the final state flavor tag, and the determination of the B decay proper time.

4.1 Triggers and Filters

The SLC collides e^- and e^+ bunches at a rate of 120 Hz. However, only a small fraction of collisions result in the production of a Z^0 boson. The peak luminosities for the 1998 run reached $\sim$ 300 Z^0/hr or 0.08 Hz. Therefore, the majority of beam crossings at the SLC result in uninteresting backgrounds events. So it would be impractical and unnecessary to record the data produced by each collision to tape. Furthermore, the time required to readout the entire detector system is about 66 ms [66] where the time between beam crossings is only about 8 ms. So it is, in fact, impossible to record the data produced by each collision. Therefore, SLD employs a

set of *triggers* [67] in order to flag interesting events to be recorded for later analysis.

During data acquisition, if the conditions for a given trigger are met, the event is read out and written to tape. The three triggers primarily responsible for signaling hadronic Z^0 decays are the *Energy, Track,* and *Hadron* triggers. The Energy trigger is satisfied when the sum of energies in all LAC towers above a certain HI threshold is ≥ 12 GeV. The HI tower thresholds are 60 ADC counts in the EM sections and 120 ADC in the HAD sections. The conversion between ADC counts and energy for the trigger calculations are 524 MeV/128 ADC and 1384 MeV/128 ADC in the EM and HAD sections respectively. This energy sum is denoted E_{HI}. There is also a veto when the number of LAC hits above the LO threshold is greater than 1000.

The Track trigger requires ≥ 2 well separated ($> 120°$) CDC tracks. There is a veto on CDC cell counts greater than 275. A DC cell is counted as hit if at least 5 of the 8 wires in the cell were hit. This trigger was rate limited to 10 triggers every 100 seconds to prevent excessive dead time during noisy beam conditions.

The Hadron trigger is a combination of the Energy trigger with CDC information. It requires ≥ 4 GeV in the LAC plus ≥ 1 CDC track.

The selection of hadronic events is further enhanced by the application of the PASS1 filter [67]. This filter requires $E_{HI} > 15$ GeV with at least 10 EM clusters contributing. In addition, E_{LO} is defined to be the LAC energy in towers above the LO threshold. The LO thresholds are 8 ADC in the EM sections and 12 ADC in the HAD sections. E_{LO} is required to be < 140 GeV. This cut is intended to reduce backgrounds from SLC muons that produce many low energy hits. Finally, we require

$$E_{HI} > 1.5 \times (E_{LO} - 70). \tag{4.1}$$

All events that pass the PASS1 filter go on to the standard SLD event reconstruction in PASS2.

It is vital that the triggers be highly efficient. Z^0 decays which fail to set at least one trigger will not be recorded and the data is lost. The combined trigger and selection efficiencies for hadronic events can be estimated by comparing the number of wide angle Bhabha (WAB) events to the number of selected hadronic events using the known WAB/hadronic cross section ratio. The results suggest an efficiency of

92% overall and 95% for events well contained in the SLD barrel region [68].

4.2 IP Determination

The first step of the event analysis is finding the precise location of the primary Z^0 decay vertex [69]. The primary vertex is important in this analysis for determining the B decay length as well as discriminating between primary and secondary tracks. One technique for locating the primary vertex would be to fit all tracks in each event consistent with the luminous region to a common vertex. However, the small size and stability of the SLC interaction point allows us to make a more accurate determination by averaging over many sequential events. During the 97-98 run, spot sizes as small as 1.5×0.65 μm in the xy plane were obtained [44]. Furthermore, the beam feedback mechanism used to stabilize collisions indicates that the transverse movements in the interaction point are stable within ~ 6 μm over periods of 20-30 events. Therefore, the transverse location of the primary vertex can be located by averaging over many sequential events. Unfortunately, the longitudinal bunch size at SLC is much longer, about 700 μm, so that the best estimate of the z coordinate comes from individual event analysis.

The procedure is to divide the data into segments of 20-30 events where no major changes in the primary vertex location occurred as suggested by the beam corrector magnets. A trial IP position is chosen and all tracks with VXD hits that pass within 3σ of the trial IP are fit to a common vertex. The IP fit result is then taken as the new trial IP and the fit is repeated. This procedure continues until it converges. The fit $\chi^2/d.o.f$ is required to be less than 1.3. The total uncertainty in the transverse position of the IP is composed of ~ 3 μm from the fit, ~ 1 μm from the SLC luminous region, and about 6 μm from beam movement. Added in quadrature we obtain about 7 μm (5 μm for 98) total [52].

The IP z position must be determined on an event-by-event basis. The point of closest approach to the transverse IP position is determined for each track with a VXD hit. The z coordinate at this point is called z_{POCA}. Tracks with $r\phi$ impact parameters less than 500 μm that pass within 3σ of the IP are then selected and their

z_{POCA} positions are averaged to locate the IP z coordinate. The uncertainty in the z position is about 20 μm depending on the type of event. The $b\bar{b}$ events have poorer resolution due to the presence of displaced secondary vertices.

4.3 Hadronic Event Selection

The next step of the analysis is to identify the hadronic decays $Z^0 \to q\bar{q}$ where the Z^0 decays into quark pairs. The main backgrounds consist of leptonic Z^0 decays and beam related backgrounds. The leptonic decays can be rejected by placing a cut on the number of tracks in the event. For $Z^0 \to \mu^+\mu^-$ we expect only two final state tracks. $Z^0 \to e^+e^-$ may produce a few more due to Bremsstrahlung but the multiplicity should be small. $Z^0 \to \tau^+\tau^-$ decays can produce up to six tracks. Therefore, we require ≥ 7 well measured CDC tracks per event where a well measured track has momentum transverse to the beam direction $p_\perp > 200$ MeV/c and passes within 5 cm of the IP at the point of closest approach to the beam axis. Also, the total energy of these charged tracks is required to be at least 18 GeV to reject beam related backgrounds. Finally, we require at least 3 tracks with VXD hits.

Detector acceptance is also considered by evaluating the event *thrust* axis, $\hat{T}$, which is intended to provide an indication of the energy flow direction of the event. The thrust axis is located by maximizing the following quantity T,

$$T = \frac{\sum^i |\hat{T} \cdot \vec{E}_i|}{\sum^i |\vec{E}_i|} \tag{4.2}$$

where the $\vec{E}_i$ represent the energies and directions of final state particles determined from calorimeter clusters. To ensure that the event is well reconstructed in the vertex detector, we require $|\cos\theta_T| < 0.85$. In general, $\hat{T}$ is a good indicator of the initial quark directions. This will be important for initial state flavor tagging to be described in section 4.8. After hadronic event selection, we are left with about 309,500 events in the 96-98 data out of an estimated 400 k hadronic Z^0 decays. Figure 4.1 shows several of the quantities considered in the hadronic selection for the data (points) and $q\bar{q}$ MC (histograms). The disagreement in the two CDC track plots at low track multiplicity is due to the lack of leptonic decays in the $q\bar{q}$ MC.
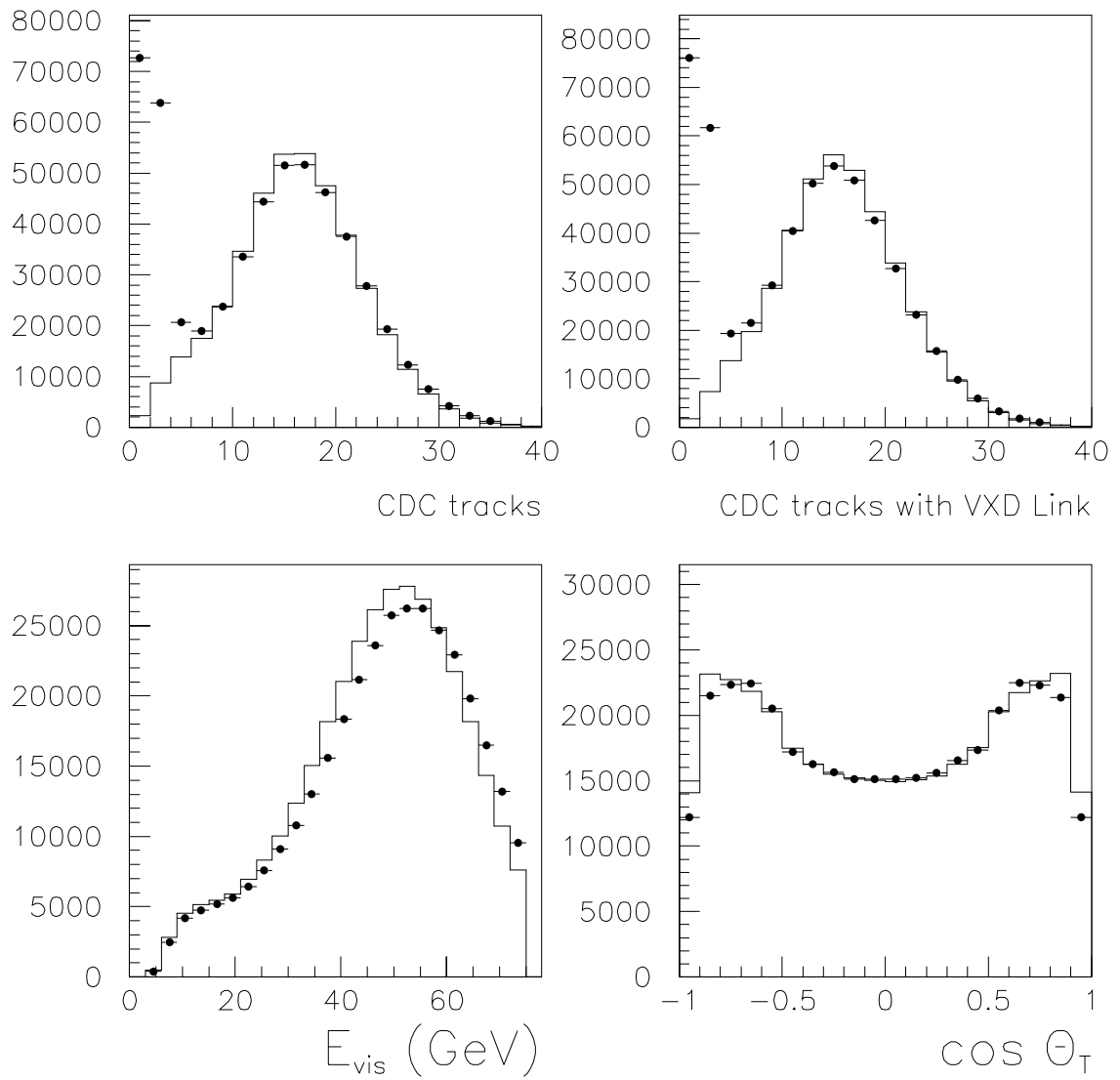
Figure 4.1: Data (point) and MC (histogram) distributions of quantities considered in hadronic event selection.

4.4 Jet Reconstruction

In $Z^0 \to q\bar{q}$ decays, the initial partons are produced with large energies due to the large Z^0 mass. Hard gluon radiation can result in the presence of three or more partons. The resulting hadrons tend to be highly boosted so that their decay products are grouped into distinct *jets* of particles. The concept of jets is very useful for describing the overall shape of an event but the jet is not, however, a well defined object. Many algorithms exist for the reconstruction of jets in an event.

In this analysis, jets are formed from the reconstructed charged tracks using the YCLUS algorithm [70]. The technique begins by forming the scaled invariant mass of all two-track combinations,

$$y_{ij} \equiv \frac{M_{ij}^2}{E_{vis}^2} = \frac{2E_i E_j (1 - \cos\theta_{ij})}{E_{vis}^2} \tag{4.3}$$

assuming the individual tracks are massless. E_{vis} is the total visible energy in the event. The two tracks resulting in the smallest y_{ij} are combined into a single *cluster*. This process is repeated with the remaining tracks and clusters until all y_{ij} are greater than an input parameter y_{cut}. The remaining clusters then represent the final reconstructed jets.

The average number of jets constructed per event depends on the parameter y_{cut}. As y_{cut} increases, fewer jets are resolved. Ideally we would like for the number of jets to equal the number of initial state partons. Since this is not possible to determine, the user must select a value of y_{cut} appropriate to the particular analysis. The jet structure is involved in several aspects of this analysis that have influenced the particular value of y_{cut} selected. First, the jet axis represents the B hadron flight direction in the determination of the lepton p_T. Small values of y_{cut} (more jets) tend to provide better resolution on the B flight direction. However, only tracks contained in the B jet are used for vertexing and boost calculations. It was determined that these algorithms prefer larger values of y_{cut} where we obtain fewer jets with more tracks. Therefore, a medium value was eventually selected, $y_{cut} = 0.07$. This value results in an average of 2.2 jets per event with a 35 mrad resolution on the B hadron flight direction. Jets in this analysis are required to pass several loose quality cuts. The
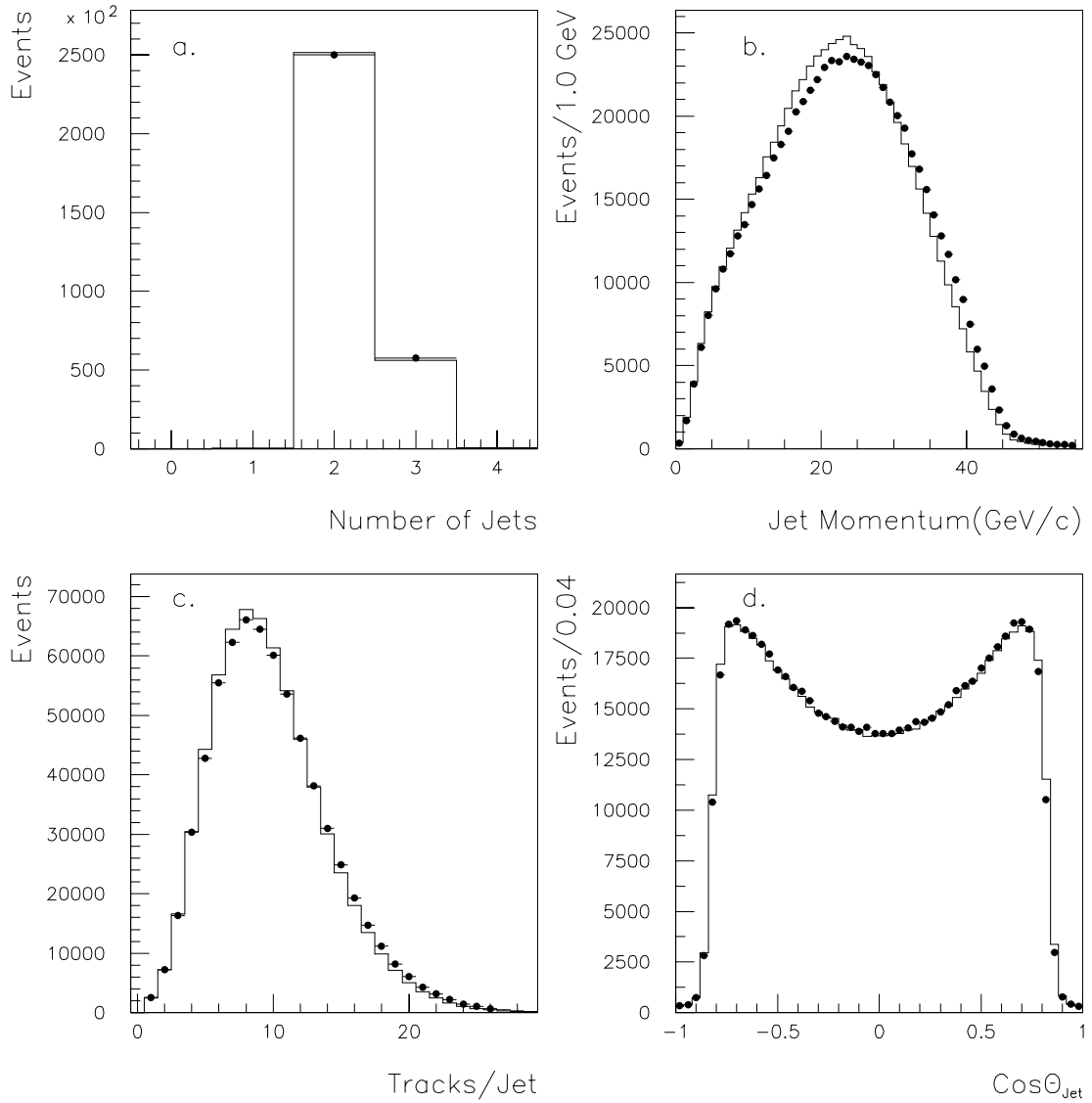
Figure 4.2: Characteristics of jets in the 96-98 data and MC. Plot (a) shows the number of jets reconstructed per event. Plot (b) is the jet momentum calculated from the momenta of assigned charged tracks. The number of tracks per jet and the jet polar angle are shown in figures (c) and (d) respectively.

jet is required to include ≥ 3 tracks and have momentum between 5 and 50 Gev/c. Finally, the jet $|\cos\theta|$ is required to be less than 0.8. Several jet quantities are plotted in figure 4.2.

4.5 Charged Track Selection

To assure that only well reconstructed tracks go into the following vertex calculations, we begin by classifying tracks in two categories, *Quality* and *OK*. The *Quality* tracks are required to have ≥ 23 CDC hits, momentum transverse to the beam axis $p_\perp > 250$ MeV/c, a $\chi^2/d.o.f$ of CDC track fit < 8.0, and a $\chi^2/d.o.f$ of combined CDC/VXD fit < 8.0. In addition, we require the radius of the first CDC hit < 39.0 cm, 2-D impact parameter in $r\phi < 1.0$ cm, at least 2 VXD hits, and distance of closest approach to the IP in $z < 1.5$ cm. *OK* tracks are required to have momentum transverse to the beam axis $p_\perp > 200$ MeV/c and $\sqrt{\sigma_{r\phi}^2 + \sigma_{rz}^2} < 0.07$ cm.

In the selected semileptonic events, the number of *Quality* tracks per hemisphere ranges from approximately 1 to 20 with an average of 7.6. The average number of *OK* tracks is about 0.8 per hemisphere. The track quality cuts are summarized in table 4.1. Figure 4.3 shows the distributions of some basic track quantities in the 96-98 data and MC.

4.6 Final State Tag

We now begin the analysis of $B^0\bar{B}^0$ mixing. In order to describe the procedure in approximately the same order it occurs in the analysis, we will begin with the final state tag that is used to determine the flavor of the b quark at decay. The method described in this thesis exploits the properties of semileptonic B decays, $B \to l^-\bar{\nu}_l X$. This is a weak charged current decay mediated by the W boson as shown in figure 4.6. The sign of the lepton charge is the same as that of the decaying b quark. Therefore, the lepton charge provides an unambiguous tag of the b quark decay flavor.

The analysis begins by selecting a sample of leptons (e and μ) using standard SLD lepton identification schemes described in detail below. Next, a sample enriched in B
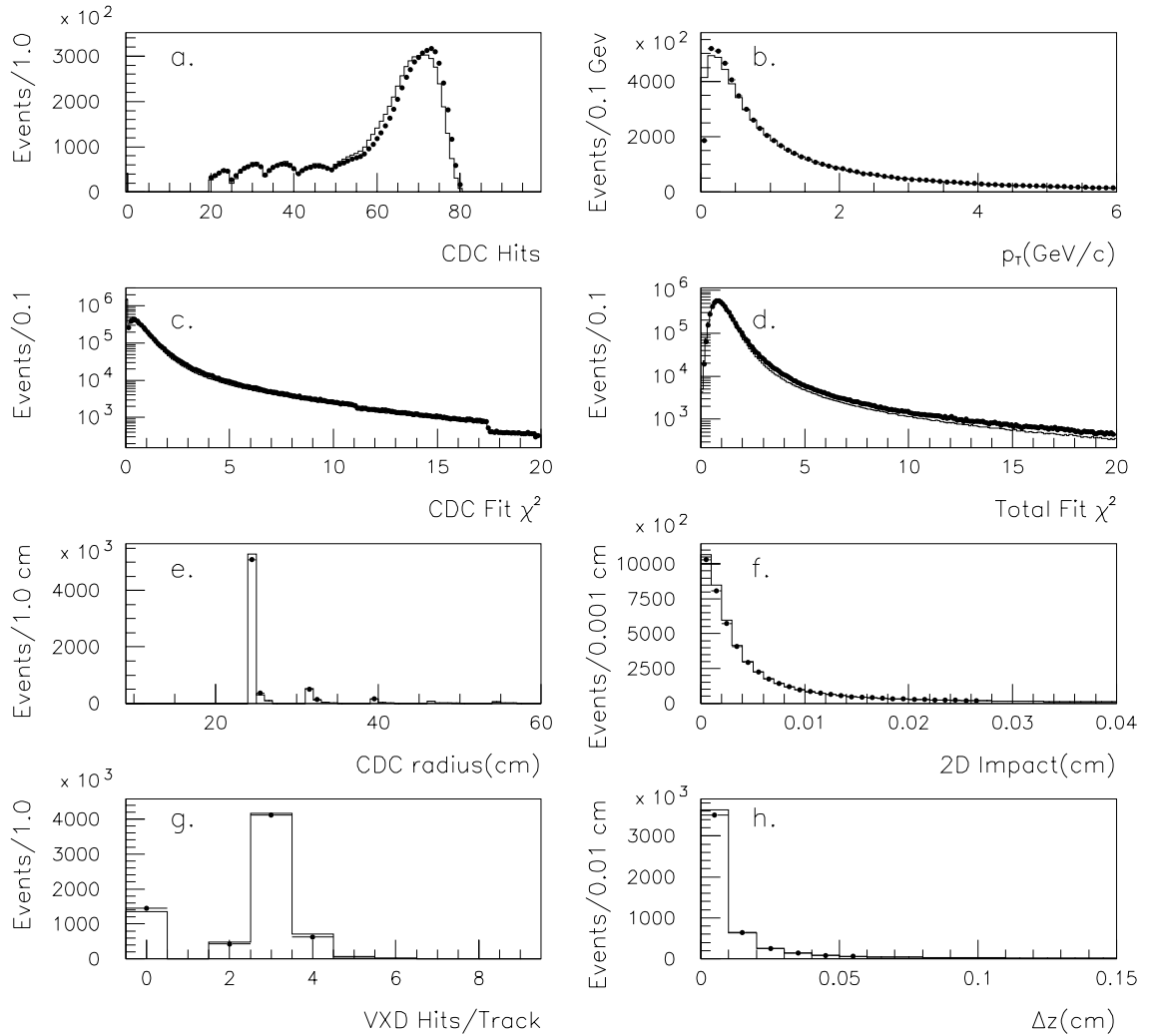
Figure 4.3: Basic track quantities in the 96-98 data and MC. The plotted distributions are: number of CDC hits (a), the momentum transverse to the beam direction (b), CDC fit $\chi^2/d.o.f$ (c), combined VXD/CDC fit $\chi^2/d.o.f$ (d), radius of the first CDC hit (e), 2D impact parameter to the IP (f), the number of VXD hits per track (g), and the track-IP distance in z at the point of closest approach to the IP (h).

Track Parameter	Cut
Quality Tracks	
CDC track	$\chi^2/d.o.f < 8$
CDC + VXD track	$\chi^2/d.o.f < 8$
CDC hits	≥ 23
$p_\perp$	> 250 MeV/c
radius of first CDC hit	< 39.0 cm
2D impact parameter in $r\phi$	< 1.0 cm
Distance to IP in z at POCA to beam	< 1.5 cm
VXD hits	≥ 2
OK Tracks	
$p_\perp$	> 200 MeV/c
$\sqrt{\sigma_{r\phi}^2 + \sigma_{rz}^2}$	< 0.07 cm

Table 4.1: Track quality cuts.

decay leptons is produced by examining the momentum of the lepton transverse to the B flight direction.

4.6.1 Electron Identification

The identification of electrons at SLD combines information from the LAC, CDC, and CRID. The identification efficiency and purity are optimized by using a neural net (NN) algorithm [71] to obtain the maximum information from the relevant variables. NNs are ideal for this application because large numbers of statistically correlated variables may be used as inputs. Therefore, it is possible to use all the relevant information rather than relying on several specific cuts.

The CDC tracks are first grouped in 4 momentum bins: $1 \rightarrow 2.5$ GeV, $2.5 \rightarrow 4$ GeV, $4 \rightarrow 8$ GeV and > 8 GeV. Two separate NNs are created for each momentum bin. The first contains information from the LAC and the CRID. The second NN is constructed with LAC information only when the CRID data is not available. The variables used as input to each NN are:

- P_{ext}/P_{max}

  where P_{ext} is the momentum of the CDC track extrapolated to the LAC barrel
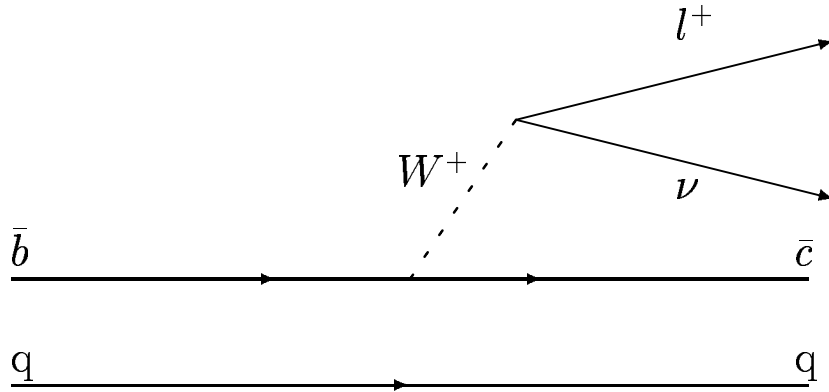
Figure 4.4: A semileptonic B decay in the spectator model. The sign of the charge of the lepton is the same as that of the decaying b quark.

and P_{max} is the maximum momentum of the track's momentum bin.

- $|\sin\theta|$

  the polar angle of incidence of the track on entering the LAC. The polar angle determines the path length of the track while traversing a LAC layer. Therefore, the angle modifies the expected signal and sampling fraction.

- $(EM/P_{ext} - 1)/\sigma$

  is the normalized energy-momentum match between the CDC and the LAC. Recall that the LAC is composed of 2 electromagnetic calorimeter layers, EM1 and EM2, followed by two hadronic layers, HAD1 and HAD2. EM is just the sum of cluster energies in the two EM layers associated with the given electron candidate track. The parameter σ represents the combined track momentum and LAC energy resolutions.

  EM1 and EM2 represent 6 and 15 radiation lengths respectively. Therefore, we expect an electron to deposit essentially all of its energy in the EM sections and thus $EM/P_{ext} - 1$ should be sharply peaked at 0 for electrons. By contrast,

EM1 and EM2 represent only 0.84 hadronic interaction lengths so we obtain a wide, mostly negative distribution for charged pions, the largest background.

- EM1/EM describes the longitudinal shower shape. For a purely electromagnetic shower, most of the energy is deposited in the first layer.

- $EM1(1 \times 1)/EM1(3 \times 3)$,

  $EM1(2 \times 2)/EM1(3 \times 3)$,

  $EM2(2 \times 2)/EM1(3 \times 3)$

  describe the transverse shower shape. The first is the energy contained in the central tower of the associated LAC cluster in EM1 divided by the energy in a 3×3 grid. The other variables are defined analogously.

- $HAD1/P_{ext}$ measures the amount of hadronic showering present.

- $\Delta\phi \equiv \phi_{track} - \phi_{cluster}$

  $\Delta\theta \equiv \theta_{track} - \theta_{cluster}$

  are the θ and ϕ residuals from the extrapolated track and the EM2 cluster centroid. They describe the quality of the track cluster association. The widths of the EM2 cluster centroid in θ and ϕ are also considered.

- $L_e - L_\pi$ is the CRID log-likelihood difference between the electron and pion hypotheses for the lepton candidate track. Only information from the gas radiator is used to further eliminate $\pi^{\pm}$ background. Electrons and pions are efficiently separated in the 2-5 GeV range.

The NN code consists of a three layer feed-forward architecture built with the JETNET 3.1 package [72]. The output is a continuous distribution ranging from 0 to 1 where 1 is most like an electron. A cut was placed on the NN output at 0.96 for electron identification. Selected electrons are also required to be *Quality* tracks with total momentum greater than 1 GeV/c and $|\cos\theta| < 0.71$ so that the track is well contained in the LAC barrel. The $b\bar{b}$ Monte Carlo indicates an electron purity of 75% with an efficiency of 59%. The misidentified electrons consist of 20% pions,

4% kaons, and 1% protons. The $e - \pi$ separation of the technique was tested on $\pi^{\pm}$ samples from K_S^0 decays, as well as $e^{\pm}$ samples from γ-conversions and wide angle Bhabhas. The results match the MC predictions well.

4.6.2 Muon Identification

Muons are identified at SLD primarily by the WIC. Recall that the WIC is the outermost layer of the SLD detector. Between the IP and the WIC there is about 3.5 interaction lengths of material and the WIC itself consists of 4 interaction lengths. Therefore, only highly penetrating particles are likely to produce hits in the WIC. Muons are able to penetrate more material than most charged particles for two reasons. First, they are leptons and, therefore, do not experience strong interactions like the pions and kaons. Second, muons are heavy enough that, unlike electrons, they lose little energy to bremsstrahlung. Unfortunately, far more pions and kaons are produced in hadronic events at SLD and they can form a significant background to muon identification. To help reduce these backgrounds, CRID information is employed to reject identified pions and kaons. The WIC stage of the identification is described more fully in reference [56] while the more recent CRID analysis is described in [73]. Both analyses will be summarized here.

Muon identification begins by extrapolating reconstructed tracks in the CDC to the WIC surface. The CDC track is required to have $p_{tot} > 2$ Gev/c. The track error matrix is also extrapolated taking into account multiple scattering effects. All WIC hits within 4σ of the extrapolated track position are identified where σ represents the track error combined in quadrature with a 2 cm error to account for the uncertainty in the hit locations. The identified WIC hits for each track are then grouped into one or more *subpatterns* that consist of hits in successive WIC layers that may represent the passage of a charged particle. Various *patterns* are then formed by selecting one subpattern from each group of hits.

The WIC fitter is then called upon to determine the parameters of the best fit tracks for each hit pattern. For a given set of track parameters, a track is formed and extrapolated through the WIC. A χ^2 is calculated by comparing the extrapolated

track to the WIC hits. The track parameters are varied iteratively until the minimum χ^2 is obtained. Patterns with a minimum χ^2 per degree of freedom greater than five are rejected.

The next step is to match the best fit tracks in the WIC to the extrapolated CDC tracks. Note that the WIC fitter output parameters, p_i, are referenced to a coordinate system with origin at the extrapolated CDC track position. Therefore, the parameters p_i, represent two position offsets and two directions resulting in four degrees of freedom. However lack of hits in a given dimension can reduce the number of degrees of freedom. Again, a χ^2 test is performed to determine the match quality.

$$\chi^2 = \frac{1}{n} \sum_{i,j}^{n} p_i W_{ij} p_j \tag{4.4}$$

where, W is the inverse of the sum of the WIC fit and CDC extrapolation error matrices, p_i are the track fit parameters and n is the number of degrees of freedom. Patterns producing a matching χ^2 greater than 6 are rejected.

Matches passing the above χ^2 cut are likely to be muons. However, it is possible that several CDC tracks match the same set of WIC hits or a single CDC track matches several sets of WIC hits. In these cases, the match with the greater number of degrees of freedom is selected. If both matches have the same number of degrees of freedom, a quality factor, Q is constructed,

$$Q = \chi^2 - A \cdot N \tag{4.5}$$

where χ^2 is the matching χ^2 and N is the number of WIC hits. A is an input parameter and is set at 0.1. The CDC-WIC match with the smallest Q is selected. The quality factor, therefore, favors matches with a large number of hits. The remaining tracks are considered muon candidates.

Once hits in the WIC are linked to CDC tracks, the CRID particle ID information relating to those tracks can be applied. The CRID is very helpful in eliminating several of the major sources of background. First is the *punch through* background from kaons and pions that are able to penetrate the LAC and reach the WIC. If these tracks can be identified as hadrons, they can be eliminated. Second, are the muons produced by the *decay in flight* of pions or kaons in the detector. If the muon is produced nearly

collinear with the decaying hadron, a WIC-CDC match is likely. Therefore, the WIC actually detects a muon but the linked CDC track was produced by a hadron. The CRID can also be used to eliminate this type of confusion.

For muon identification, only information from the gas radiator is considered. The CRID results for a given track are presented as log Likelihood values for the various particle hypotheses. In this analysis, the CRID is used in pion and kaon rejection mode. That is, cuts are placed on $\log \mathcal{L}_\mu - \log \mathcal{L}_\pi$ (pion rejection) and $\log \mathcal{L}_\mu - \log \mathcal{L}_K$ (kaon rejection). Muons are effectively separated from pions in the 2-5 GeV range and from kaons in the 2-15 GeV range.

The final muon selection cuts are based on the following variables:

- The probability for a muon track to not leave hits in the WIC layers missed by the muon candidate. This quantity takes into account the average efficiency of the WIC layers.

- The number of layers missed by the muon candidate in the last 4 and 6 WIC layers.

- The CDC-WIC matching χ^2

- The number of hits in the WIC pattern associated with the muon candidate.

- Quality factor Q

- $\log \mathcal{L}_\mu - \log \mathcal{L}_\pi$ and $\log \mathcal{L}_\mu - \log \mathcal{L}_K$

The specific cut values have been optimized separately for tracks with and without CRID information as well as in eight total momentum regions, resulting in sixteen sets of cuts. In addition, allowances have been made for the $\cos \theta$ region between 0.6 and 0.7 where we expect differences in the WIC and CRID performance for geometrical reasons. Muon identification falls off rapidly after $|\cos \theta| \approx 0.6$ due to a decrease in the WIC acceptance at the edge of the barrel. Tables of these cut values can be found in reference [73]. Muon candidates are required to be *Quality* tracks with $p_{tot} > 2.0$ GeV/c. In the angular region $|\cos \theta| < 0.6$, the $b\bar{b}$ Monte Carlo indicates an identification efficiency of 80% with a purity of 92%.

4.6.3   Lepton Selection

After identifying lepton tracks we proceed to select those that were likely to have been produced in B decays. In this analysis, initial lepton selection is critical for several reasons. First, the charge of the lepton track will be used to determine the flavor of the decaying B hadron. As discussed previously, the sign of the lepton charge is the same as that of the b quark in B semileptonic decays. Second, because we are assuming the lepton was produced in the B decay, it is reasonable to assume that the B decay vertex lies somewhere very near the lepton track. Therefore, we will reconstruct the decay vertex along the lepton track as described in section 4.7.1. So the selected lepton determines both the final state tag and the decay position which are essential ingredients of a time dependent mixing analysis.

The most significant background comes from leptons produced in cascade charm decays. For these leptons, the sign of the charge is opposite that of the final state b quark thus producing the wrong tagging information. For a random background we would still expect the final state tag to be correct at around 50%. Therefore, the $b \rightarrow c \rightarrow l^{\pm}$ background functions as an 'anti-signal' which is particularly damaging. Other backgrounds include leptons produced in $c\bar{c}$ and uds events as well as fake leptons.

A common technique for identifying B decay leptons is to place a cut on the momentum transverse to the B flight direction or p_T. In general, leptons produced in B decays have large p_T as well as total momentum, p_{tot}, due to the B's large mass. In this analysis, we use the jet axis to approximate the B hadron flight direction. Selected jets are required to have ≥ 3 tracks and total momentum between 5 and 50 GeV. As mentioned earlier, the resolution on the B flight direction provided by the jet axis is about 35 mrad.

The p_T of each *Quality* identified lepton track is calculated with respect to the nearest jet direction. Monte Carlo studies show that a p_T cut at 0.8 GeV/c provides the optimum combination of efficiency and purity for identifying B decay tracks. The Monte Carlo indicates that 67% of true leptons produced directly in B decays pass this p_T cut. Only 22% of leptons from cascade charm decays pass the cut as well as 24% and 13% of leptons from $c\bar{c}$ and uds decays respectively. Those tracks with

Source	Fraction(%)
$b \rightarrow e^{\pm}$	39.5
$b \rightarrow \mu^{\pm}$	37.2
$b \rightarrow c \rightarrow e^{\pm}$	6.2
$b \rightarrow c \rightarrow \mu^{\pm}$	6.1
$b \rightarrow \bar{c} \rightarrow e^{\pm}$	1.2
$b \rightarrow \bar{c} \rightarrow \mu^{\pm}$	1.2
$b \rightarrow \tau \rightarrow e^{\pm}$	1.0
$b \rightarrow \tau \rightarrow \mu^{\pm}$	0.8
$c \rightarrow e^{\pm}$	0.1
$c \rightarrow \mu^{\pm}$	0.1
π, K, $\gamma \rightarrow e^{\pm}$	0.3
π, K, $\gamma \rightarrow \mu^{\pm}$	0.3
fragmentation $e^{\pm}$	0.2
fragmentation $\mu^{\pm}$	0.0
π	3.7
K	1.4
p	0.5

Table 4.2: Identity and origin of selected lepton candidates in the $b\bar{b}$ MC.

p_T less than 0.8 GeV/c are discarded as lepton candidates. We also require that the lepton total momentum be greater than 1 GeV/c for electrons and 2 GeV/c for muons and that the lepton $|\cos\theta| < 0.71$. Finally, we require that the track not be consistent with a γ-conversion. Only one lepton is selected per jet. In the event that more than one high p_T lepton is identified, the one with the largest elliptical momentum,

$$p_T^2 + (p_{tot}/15)^2 \qquad (4.6)$$

is selected. A total of 16,601 high p_T leptons are selected in the 96-98 data. The p_T spectra of identified electrons and muons are shown in figure 4.5. Note that the $B \rightarrow l^{\pm}$ purity grows as p_T increases and that the $B \rightarrow c \rightarrow l^{\pm}$ component is greatly reduced by the cut at 0.8 GeV/c. The results of the lepton selection in $b\bar{b}$ events are given in table 4.2. The average correct tag probability is $\sim 85\%$.
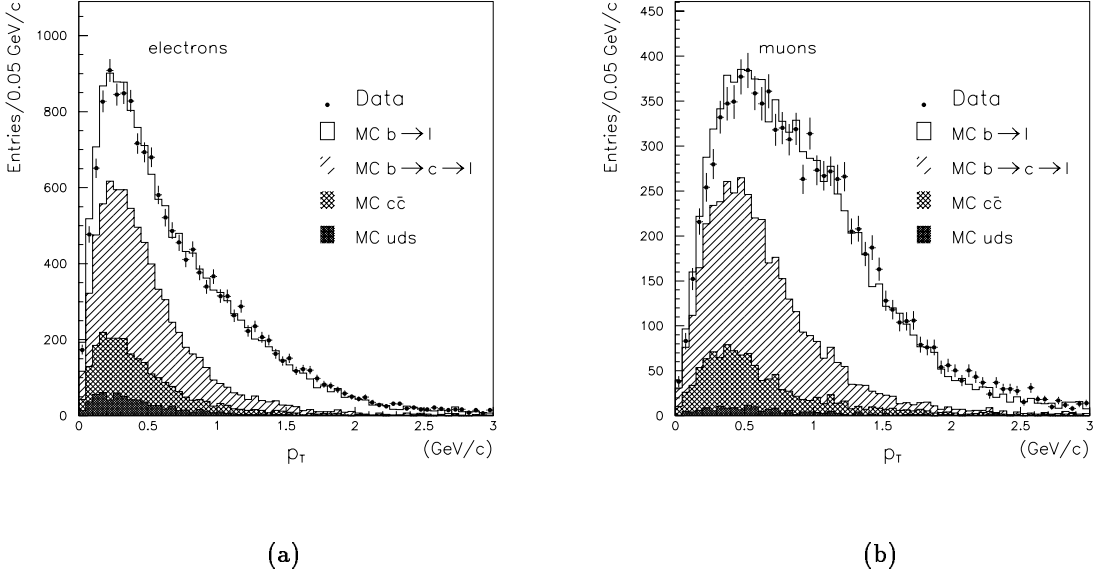
Figure 4.5: Electron (a) and muon (b) p_T distributions in the data and MC.

4.7 Proper Time Reconstruction

The proper time of the B decay is estimated by first reconstructing the B decay length using a statistical technique that exploits the topology of semileptonic B decays and the selected high p_T lepton. The relativistic boost, $\beta\gamma = p_B/m_B$, is then determined by attaching charged tracks to the decay vertex and assigning some component of the LAC EM cluster energy. The decay proper time can then be calculated as $t_{rec} = L/\beta\gamma c$.

4.7.1 Decay Length

A p_T cut at 0.8 GeV/c produces a relatively pure sample of B decay leptons but the efficiency is, unfortunately, rather low. Therefore, to maintain adequate statistics, a novel vertexing technique was developed for this analysis that provides high efficiency with good decay length resolution once the initial high p_T lepton is selected [74, 75]. The method relies on the fact that the lepton track should pass near the true B decay
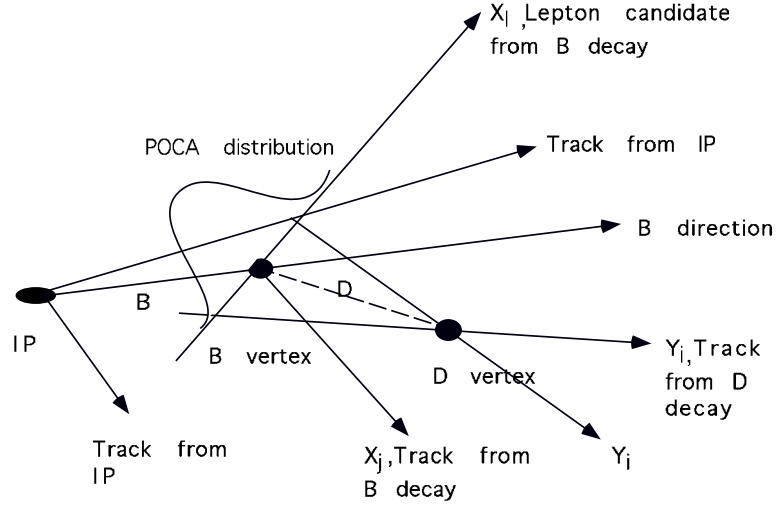
Figure 4.6: A typical B Semileptonic Decay

position assuming that a B decay lepton was selected. We can expect miss distances on the order of the multiple scattering term of the impact parameter resolution, $33/p\sin^{3/2}\theta\ \mu m$. Statistical properties of B semi-leptonic decays are then exploited to locate the B vertex along the lepton track.

Figure 4.6 shows the topology of a typical semileptonic B decay. Tracks produced directly in the B decay are labelled X_i while those from the cascade charm decay are labelled Y_i. The hemisphere also contains fragmentation tracks from the interaction point. The intersection, or point of closest approach (POCA), of a B decay track, X_i, with the lepton should locate the true B vertex within the small track reconstruction errors. However, it is impossible to determine exactly which tracks were produced in the B decay. If a track produced in the cascade charm decay is intersected with the lepton, the POCA will be offset from the true B decay position by an amount δL_{vtx}. This offset is due to the finite lifetime of the D meson,

$$\delta L_{vtx} = \frac{p_T}{p_{\parallel}} \cdot L_D \tag{4.7}$$

where p_T and $p_{\parallel}$ are the transverse and parallel components of the track momentum with respect to the D flight direction and L_D is the D decay length. For small L_D,

the POCA still provides a good estimate of the B vertex position. On average, the D decay length relative to the B decay position is ~ 1 mm. MC studies show that the average distance from the POCA to the true B vertex is about 200 μm for B decay tracks and 260 μm for D decay tracks.

On average, there are about 5.5 other *Quality* tracks (as defined in table 4.1) per jet after lepton selection. Generally, there are about three D decay tracks for every B track. This analysis uses a statistical method in which the point of closest approach to the lepton is calculated for each *Quality* track in the hemisphere. The B decay vertex is then reconstructed as,

$$\vec{X}_{vtx} = \frac{\sum W_i \vec{X}_i}{\sum W_i} \tag{4.8}$$

where $\vec{X}_i$ is the vector from the IP to the POCA for track i and W_i is the product of four weighting functions employed to enhance the contribution from B decay tracks with respect to tracks from the D decay or interaction point. In this way, we are able to use all the hemisphere tracks without making any cuts to select B decay tracks.

The true B vertex should be located near the POCAs of the secondary tracks in the hemisphere. The secondary tracks are those that are produced in the B decay or downstream (not from fragmentation). Therefore, the first weight is a function of the normalized 3-D impact parameter, σ_3, which is given by the distance of closest approach of the track to the IP divided by an error determined from the track and IP errors. The σ_3 parameter indicates whether the track is consistent with passing through the interaction point. Due to the long lifetimes of the B and D mesons, secondary tracks tend to have larger impact parameters than fragmentation tracks as shown in figure 4.7. The following function represents the secondary track probability as a function of $x = \sigma_3/A_2$,

$$W_1(x) = \frac{x}{x + A_1}(1 - e^{-x^2}). \tag{4.9}$$

This function provides a larger weight for those tracks with large σ_3. The parameters A_1 and A_2 were determined from the Monte Carlo to be 0.5 and 4.0 respectively.

The second weighting function makes use of the information contained in the jet axis direction. MC studies show that the jet axis is a good indicator of the B hadron
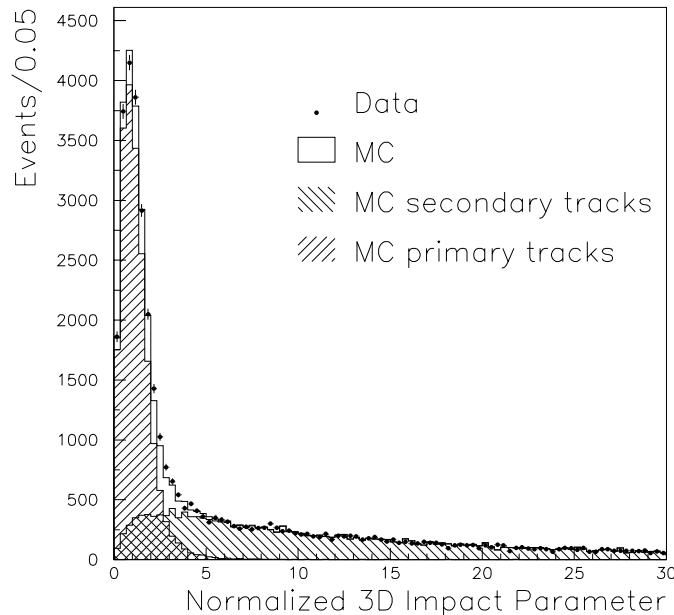
Figure 4.7: The normalized 3D impact parameter in the 96-98 data and MC. The MC histograms show that secondary tracks tend to have larger normalized impact parameters.

flight direction. Therefore, the lepton-jet intersection should provide a reasonable approximation to the true B decay position. Secondary tracks originating in the B decay should, therefore, intersect the lepton near the lepton-jet intersection while fragmentation tracks are likely to produce a larger offset. So individual track POCAs are weighted by a function depending on the angular difference between the track POCA and the lepton-jet intersection, α. For secondary tracks, the $\sin \alpha$ distribution is sharply peaked st small angles with an average of about 0.1. For fragmentation tracks, $\sin \alpha$ is randomly distributed with average about 0.5. The weighting function is given by,

$$W_2 = e^{-\sin \alpha / B}. \tag{4.10}$$

This function enhances the significance of tracks that intersect the lepton near the lepton-jet intersection. The parameter B is set to 2.5.

Tracks from the B decay are further enhanced by considering the distance of closest approach (DOCA) of the track to the lepton. If the lepton was actually produced in the B decay, then we expect the DOCA of other B decay tracks to be due mainly to tracking errors. The D decay products will likely have larger DOCAs due to the lifetime of the D meson. Therefore, W_3 is given by,

$$W_3 = e^{-(DOCA/C)^2}. \tag{4.11}$$

The parameter C is set to 50 μm, the average DOCA of B tracks to the lepton. The average DOCAs for D decay and fragmentation tracks are 65 and 100 μm respectively.

The final weight is determined from the lepton-track opening angle λ and the $\chi^2/d.o.f.$ of the track reconstruction,

$$W_4 = \left(\frac{\sin\lambda + D_1}{\sin\lambda + D_2}\right) \cdot \left(\frac{1}{\chi^2/d.o.f. + D_3}\right) \tag{4.12}$$

The first term reflects the fact that the position of the POCA becomes more uncertain as the lepton-track opening angle decreases. By choosing $D_1 = 0.001$ and $D_2 = 0.1$, the first term is approximately $\sin\lambda$ for small λ and increases to approximately 1 as λ increases. Therefore, more weight is given to tracks with large opening angles to the lepton where the POCA is more easily determined.

The second term simply accounts for tracking errors by giving more weight to those tracks that are well measured and thus have a low value of $\chi^2/d.o.f.$ The final parameter $D_3 = 0.1$ prevents the term from becoming too large in the case of very small $\chi^2/d.o.f.$

The combined weights enhance the secondary track contribution by a factor of about 30 over the fragmentation tracks. The B decay length is calculated as the distance between the interaction point and the reconstructed B vertex. Events where only 1 other track was available for vertexing are rejected, resulting in a vertex reconstruction efficiency of $\sim 96\%$. In the rare event ($\sim 0.1\%$) that more than 1 high p_T lepton vertex is located in a single hemisphere, the one producing the largest decay length is selected. At this stage, we are left with a total of 15,845 lepton candidates consisting of 7227 muons and 8618 electrons.
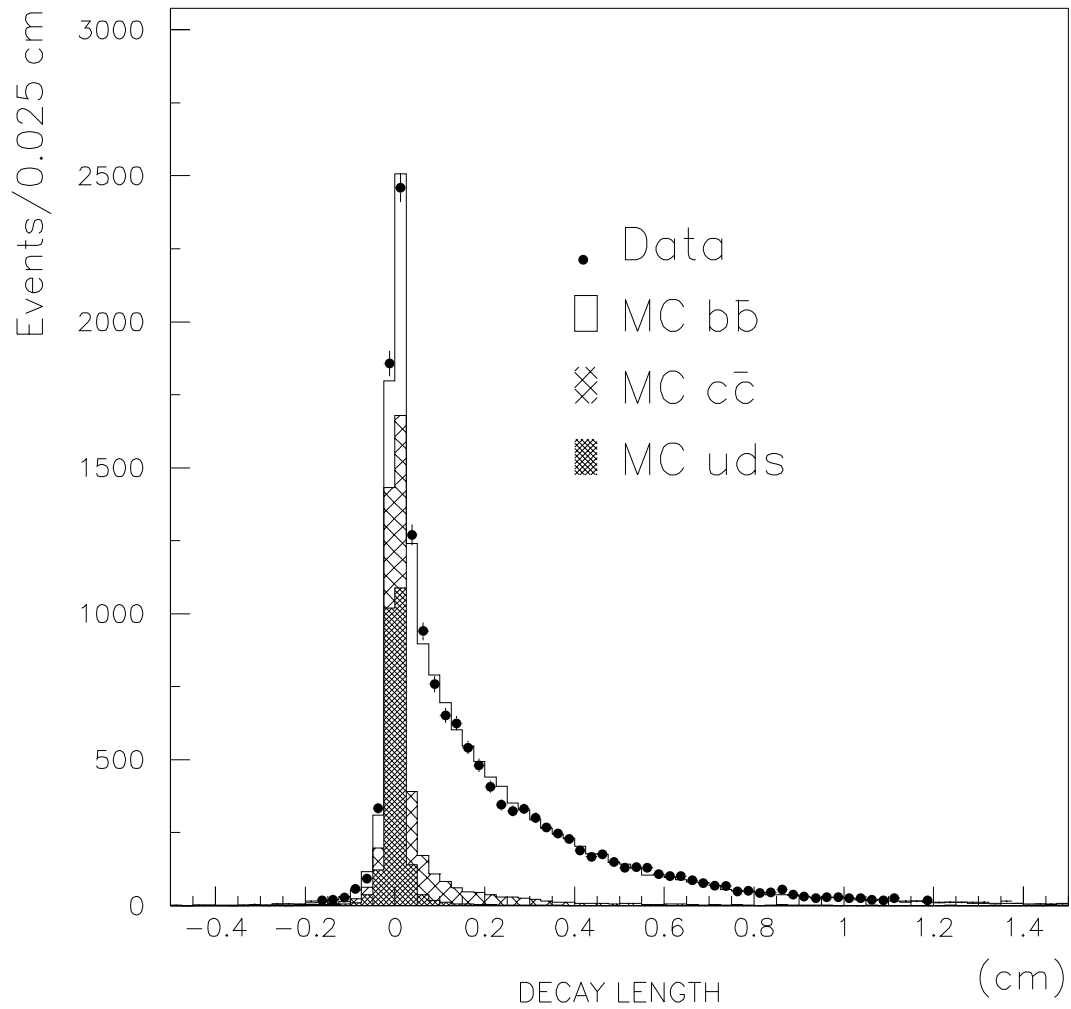
Figure 4.8: Distribution of reconstructed decay lengths in the data and MC. The data and MC histograms show that the $c\bar{c}$ and *uds* backgrounds are concentrated at small decay length. The negative decay lengths imply that the reconstructed vertex is behind the IP with respect to the jet axis.

The results of this procedure are shown in figures 4.8 and 4.9. Figure 4.8 compares the fully reconstructed decay length distribution in the data and MC. There is good overall agreement between the two. Note that the $c\bar{c}$ and uds backgrounds tend to be concentrated at small decay lengths as we would expect. The average B decay length is about 2 mm.

Figure 4.9 shows the decay length residual, $L_{rec} - L_{true}$, for the $B \rightarrow l^{\pm}$ and $B \rightarrow c \rightarrow l^{\pm}$ signal components. We see that when a true B decay lepton is selected, the residual is centered around 0 as expected. A two gaussian fit indicates a core width of 125 μm and a tail width of 520 μm. The core fraction is about 62%. When a lepton from the cascade charm decay is selected, however, the residual develops a large positive tail. We have essentially reconstructed the D vertex and so the B decay length tends to be overestimated. A two gaussian fit results in a core width of 190 μm and tail width of 840 μm. The tail represents about 52% and is centered significantly above 0.

The results above describe the *average* decay length resolution that can be obtained with this method. However, for any given event, we have more information that allows us to estimate the uncertainty in the decay length for that event. The idea is to consider the POCA for each track in the hemisphere as a statistically independent measurement of the B decay vertex. The weighted RMS spread in the POCA positions can then be interpreted as the uncertainty in the vertex position. The POCA RMS can be calculated in each dimension as,

$$\sigma_x = \sqrt{\langle x^2 \rangle - \langle x \rangle^2} \tag{4.13}$$

where the brackets represent the weighted average using the same weights applied above and x is the x-coordinate of the individual POCAs. Note that $\langle x \rangle$ is just the x-coordinate of the reconstructed B vertex. The uncertainty in the total decay length can now be computed by,

$$\sigma_{vtx} = \sqrt{\sigma_x^2 + \sigma_y^2 + \sigma_z^2} \tag{4.14}$$

The interpretation of σ_{vtx} is very simple. The more closely the individual track POCAs are grouped along the lepton track, the better the decay length resolution. The σ_{vtx} distribution also gives us a check of the decay length resolution inferred from
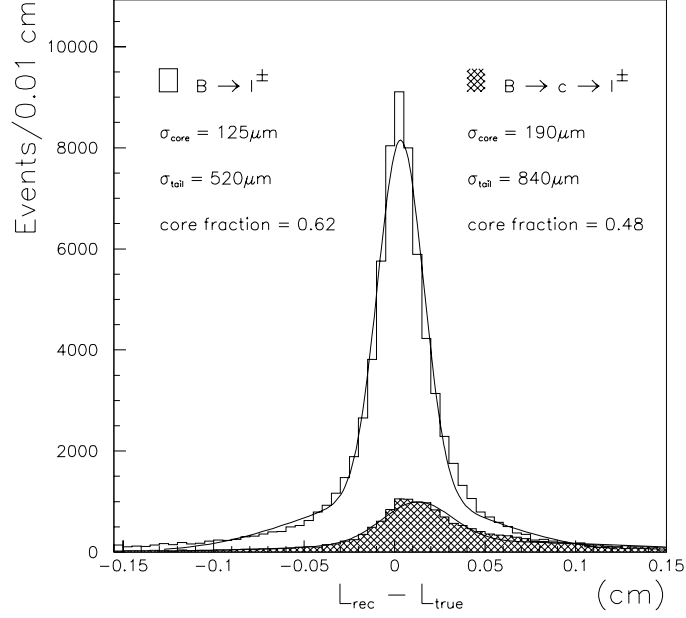
Figure 4.9: The average decay length residuals $L_{rec} - L_{true}$ for $B \to l^{\pm}$ events and $B \to c \to l^{\pm}$ events.

the MC. Figure 4.10 compares the σ_{vtx} distributions in the data and MC. The good agreement implies that the resolution in the data is well simulated by the MC. This information will be used to improve our sensitivity to B_s^0 mixing in the likelihood fit procedure to be described in chapter 5.

4.7.2 Boost

The vertexing method described above provides an estimate of the B decay length and position. To determine the proper time of the decay, we must still estimate the relativistic boost of the B hadron, $\beta\gamma = p_B/m_B$. The boost reconstruction used in this thesis is called the *fragmentation method* [76]. The procedure is to estimate the amount of energy in the jet or hemisphere that is due to fragmentation particles. The
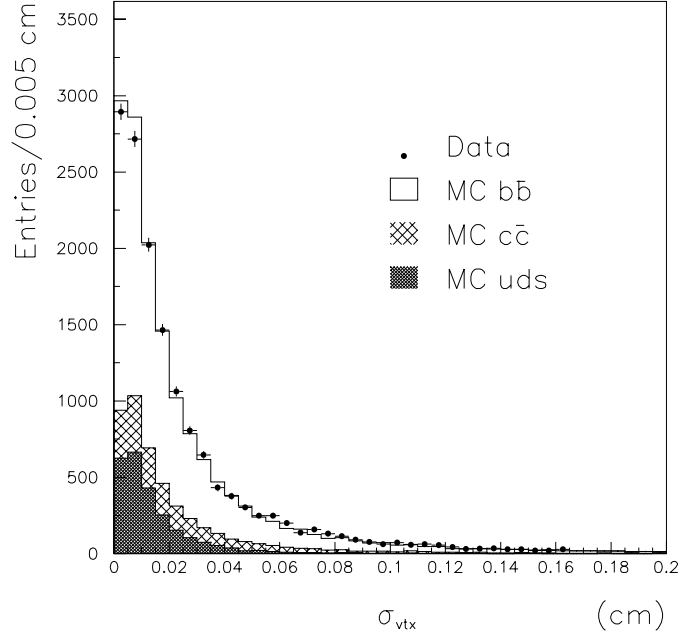
Figure 4.10: The distribution of the estimated vertex resolution σ_{vtx} in the data and MC.

B energy is then simply,

$$E_B = E_{jet/hemi} - E_{frag} \tag{4.15}$$

where $E_{jet/hemi}$ is the total energy of the jet or hemisphere containing the lepton and $E_{frag} = E_{frag}^0 + E_{frag}^{\pm}$ is the fragmentation energy. $E_{frag}^{\pm}$ is determined by classifying each charged track as primary or secondary based on tracking and vertex information. E_{frag}^0 is estimated from cluster energies in the LAC.

The first step in determining the B energy is to find the total energy in the jet containing the lepton candidate. Because we are dealing with Z^0 decays, we know that the total energy in the event is equal to m_Z. In two jet events we assume that a $b\bar{b}$ quark pair was produced back-to-back in the decay. Therefore, the energy per jet is simply $E_{jet} = m_Z/2$. In three jet events we can use the jet directions to estimate

the energy in each jet by energy and momentum conservation. The result is,

$$E_{jet}^{1,2,3} = m_Z \frac{\sin\theta_{23,13,12}}{\sin\theta_{12} + \sin\theta_{13} + \sin\theta_{23}} \tag{4.16}$$

where θ_{ij} is the angle between jets i and j. For the small fraction of four jet events, we divide the event into two hemispheres and treat it as a 2 jet event.

To estimate $E_{frag}^{\pm}$, we need to determine which tracks in the jet/hemisphere were produced at the IP and which are secondary tracks that should be attached to the B vertex. It was found that the boost calculation is improved by including both *Quality* and *OK* tracks at this stage. To classify each track as primary or secondary, we consider two quantities. First, we determine how close each track comes to the B vertex. Figure 4.11 shows the relevant variables. A vertex axis is formed by connecting the IP to the reconstructed B vertex or *seed* vertex. For each track, we calculate the longitudinal and transverse distances of the track to the vertex axis at the point of closest approach. The parameter t is required to be less than 0.1 cm to reject tracks clearly not associated with the B decay chain. The longitudinal distance L, divided by the decay length D, is plotted for primary and secondary tracks in figure 4.12. The two are clearly separated.

The second factor to consider is the normalized 3-D impact parameter, σ_3. Recall that the vertexing procedure described above used σ_3 as the basis for one of the track weighting functions. It is equal to the 3 dimensional distance of closest approach of the track to the IP divided by the track and IP errors. Therefore, σ_3 tells us if the track is consistent with passing through the interaction point. Figure 4.7 shows the difference in the σ_3 distributions for primary and secondary tracks.

The L/D and σ_3 information is combined to form a variable ρ,

$$\rho^2 = \left(\frac{L/D}{0.4}\right)^2 + \left(\frac{\sigma_3}{2.5}\right)^2 \tag{4.17}$$

MC studies suggest that the maximum efficiency and purity is obtained by placing a cut on ρ^2 at 1.55. Essentially, we are making an elliptical cut in the L/D - σ_3 plane. Tracks with $\rho^2 > 1.55$ are classified as secondary tracks and are attached to the B vertex. The remaining tracks are assumed to be from fragmentation. The MC indicates a purity of 91% and efficiency of 96% for secondary track identification.
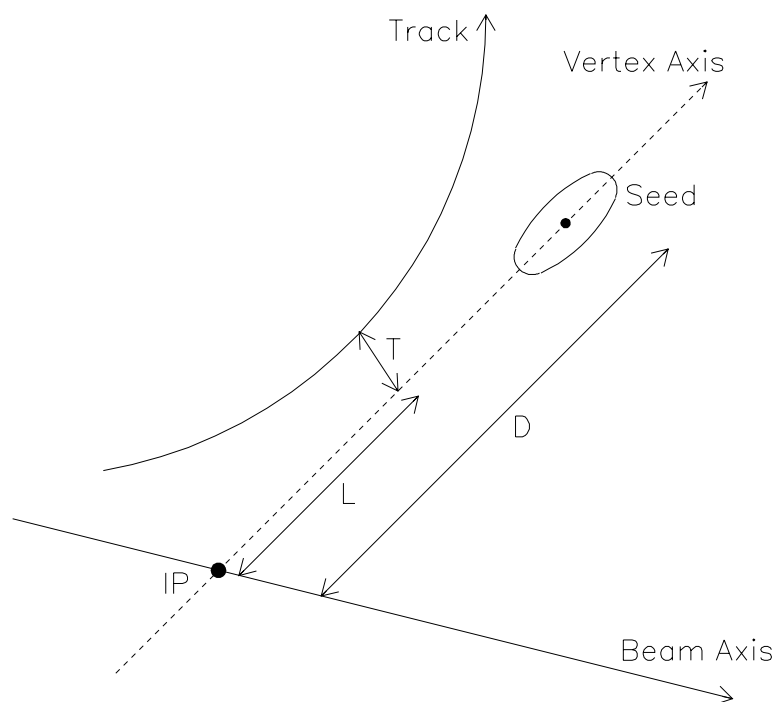
Figure 4.11: Schematic diagram showing the L and D parameters that determine whether a given track will be attached to the B vertex.
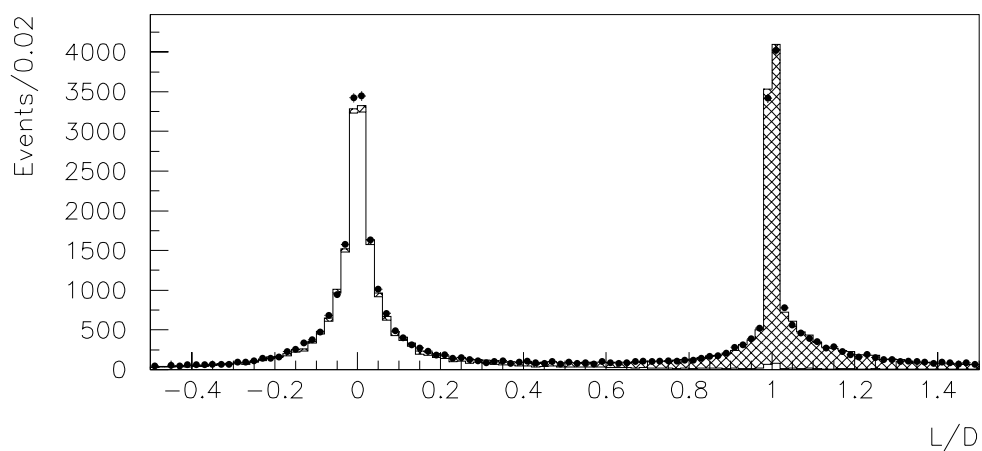
Figure 4.12: The L/D distributions in the data (points) and MC. The MC shows separation between the fragmentation tracks and secondary tracks.

On average, about 4.25 tracks are attached to the vertex in addition to the lepton. Vertices with fewer than 2 attached tracks ($\sim$ 2.5%) are rejected. The charged B energy distribution ranges from 0 to 45 GeV with an average of about 18 GeV. When all the correct secondary tracks are selected (and no others) the resolution on $E_B^\pm$ is about 2%. This is true for about half of the reconstructed vertices. The remaining vertices have an $E_B^\pm$ resolution of about 25% as we would expect if 1 track out of about four is missed.

$E_{frag}^\pm$ can now be easily computed. The energy of each track in the jet or hemisphere is calculated from the track momentum assuming the pion mass. If the track is an identified lepton, we use the appropriate e or μ mass. $E_{frag}^\pm$ is just the sum of the energies of all tracks in the jet or hemisphere minus the energies of those tracks attached to the B vertex,

$$E_{frag}^\pm = E_{jet/hemi}^\pm - E_B^\pm. \tag{4.18}$$

The above procedure for attaching tracks to the B vertex also allows us to reconstruct the B hadron charge. The vertex charge, Q_{vtx}, is just the sum of the charges of tracks attached to the seed vertex. Note that we have not attempted to distinguish between tracks produced in the B and D decays. All non-fragmentation tracks should ideally be attached to the seed vertex and, therefore, give the correct B hadron charge. Figure 4.13 shows the distribution of reconstructed vertex charges in the data and MC. The MC histograms are divided into the charged and neutral components to show the purity of the charge reconstruction. About 52% of neutral Bs are reconstructed with $Q_{vtx} = 0$ as opposed to 21% of charged Bs. In the $Q_{vtx} = 0$ sample, the neutral to charged ratio is about 3.2:1 as compared to 1.2:1 in the total sample. In this analysis, all vertex charges are retained in the final sample. The maximum likelihood fit, however, uses Q_{vtx} to estimate the sample fraction for each event.

Next, we must account for the neutral energy. In a B semileptonic decay, a neutrino is produced which will, of course, go undetected. One of the advantages of the fragmentation method is that no direct estimate of the neutrino energy needs to be made. We are only required to estimate E_{frag}^0, the neutral fragmentation energy. We depend on the LAC to detect energy from neutral particles.
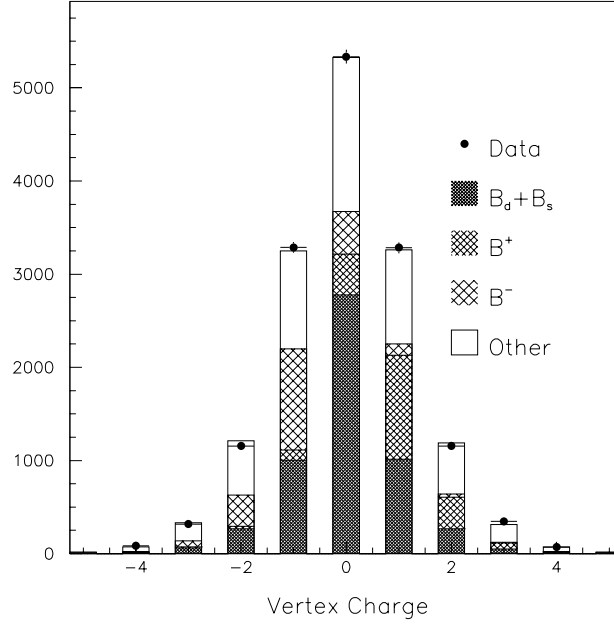
Figure 4.13: The reconstructed vertex charge in the data and MC.

For the boost calculation, we must first identify the 'neutral' LAC clusters. As described above, all CDC tracks are classified as B decay tracks or fragmentation from which we calculate $E_B^{\pm}$ and $E_{frag}^{\pm}$. We assume that these quantities account for the energy of the stable charged particles produced in the event. However, charged particles tracked by the CDC can also produce LAC clusters either through direct interaction with the calorimeter or through decay products created by interactions with the detector. To avoid double counting of energy, each LAC cluster is checked for a track association. The *track-cluster association* procedure is to extrapolate CDC tracks to the LAC surface and search for clusters in the vicinity of the track taking into account the track errors and cluster widths. For each track within 4 $\sigma_{clus\theta}$ and $\sigma_{clus\phi}$ of a given cluster, a likelihood parameter is calculated,

$$L = exp\left[-\frac{1}{2}\left(\frac{(\theta_{trk} - \theta_{clus})^2}{\sigma_{trk\theta}^2 + \sigma_{clus\theta}^2} + \frac{(\phi_{trk} - \phi_{clus})^2}{\sigma_{trk\phi}^2 + \sigma_{clus\phi}^2}\right)\right] \qquad (4.19)$$

where θ_{clus} and ϕ_{clus} are the energy weighted average position of hit towers in the

cluster. The parameters $\sigma_{clus\theta}$ and $\sigma_{clus\phi}$ are the energy weighted RMS widths of the clusters in θ and ϕ taking into account the spread in hit towers and the individual tower widths. The coordinates θ_{trk} and ϕ_{trk} are the extrapolated position of the track at the LAC surface while $\sigma_{trk\theta}$ and $\sigma_{trk\phi}$ are the track errors at that point. If $L > 0.01$, the track is associated with the cluster. The association procedure allows a cluster to be associated with more than one track, but each track can only be associated with one cluster. Those clusters not associated with a charged track are assumed to have been produced by neutral particles. Therefore, we will only be dealing with the unassociated clusters.

In principle, every CDC track should produce some LAC energy and, therefore, be associated to a LAC cluster. Figure 4.14 shows the fraction of charged tracks that have a cluster association as a function of the track momentum. The association procedure works well for high momentum tracks but below a few GeV/c the association efficiency begins to drop. For B hadron decays, the average charged track momentum is around ~ 2 GeV/c.
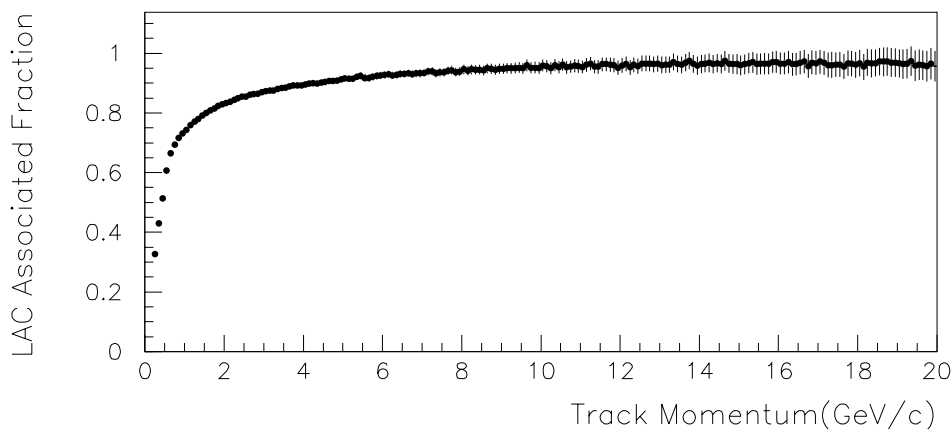
Figure 4.14: The fraction of CDC tracks associated with LAC clusters in the 1996-1998 Data. The associated fraction varies with momentum and drops sharply for low momentum tracks.

The next step is the application of an energy scale. The raw data from the LAC is reported in the *mip* scale. That is, the conversion from ionization produced in the liquid Argon to GeV assumes that a minimum ionizing particle was responsible for

the signal. Of course, the LAC response to EM and hadronic showers will be quite different from that of minimum ionizing particles. Therefore, each cluster must be identified as EM or hadronic and an appropriate scale factor must be applied to the raw energy to account for the difference in response.

Recall that the LAC is divided longitudinally into four layers. There are two EM layers followed by two hadronic layers as described in section 2.2.4. The distinction between EM and hadronic clusters is made by considering the shape of the energy deposition in the LAC layers. Given that EM1 and EM2 make up 21 radiation lengths, we expect photons and electrons to deposit most of their energy in EM1 and the rest in EM2. Hadrons, on the other hand, should pass through the EM layers more easily and deposit more energy deeper in the LAC. For this analysis, EM clusters were selected by requiring,

$$\frac{EM1 + EM2}{E_{raw}} > 0.6. \tag{4.20}$$

The remaining clusters are assumed to be hadronic. E_{raw} is then scaled by the appropriate factor, e/μ or π/μ, for EM and hadronic clusters respectively [77]. Note that this cut has been optimized for the unassociated clusters alone since the associated clusters are not used in the boost calculation.

At this point, we have divided the calorimeter clusters into four groups,

- Unassociated EM

- Associated EM

- Unassociated Hadronic

- Associated Hadronic

Figure 4.15 shows the actual particle content of each group according to the MC. If more than one MC particle contributes to the cluster, the highest energy contributor is chosen as the cluster 'parent'. The two associated categories are dominated by charged particles as we would expect and, therefore, can be ignored for the boost calculation. The unassociated EM also behaves as expected, being dominated by photons. The unassociated hadronic component, however, shows a large contamination of $\pi^{\pm}$. These
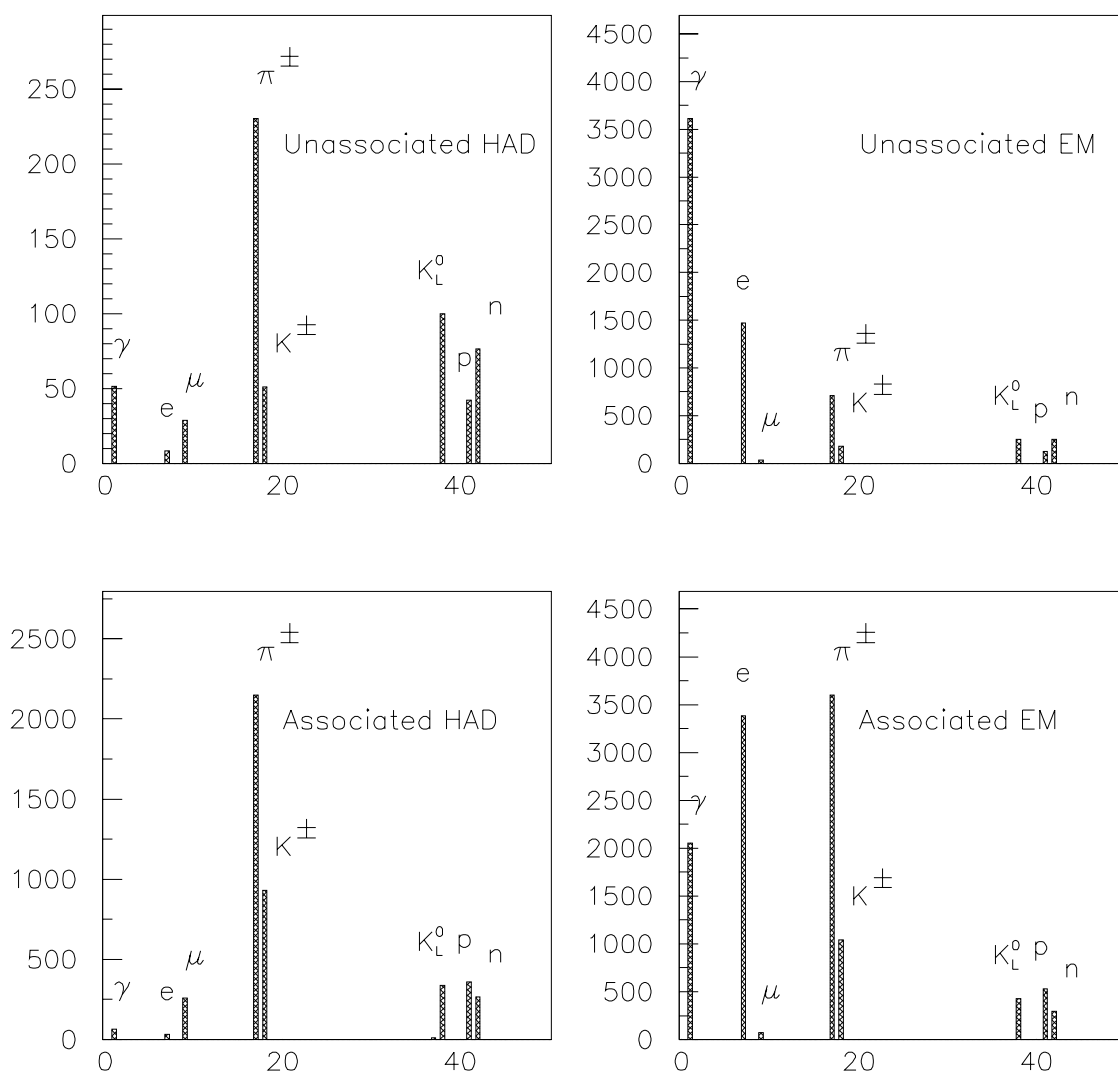
Figure 4.15: The MC particle content of the various cluster categories weighted by raw energy.

are mainly low energy tracks that failed the track-cluster association. As a result, the unassociated hadronic clusters are also ignored in the neutral energy sum leaving only the unassociated EM component.
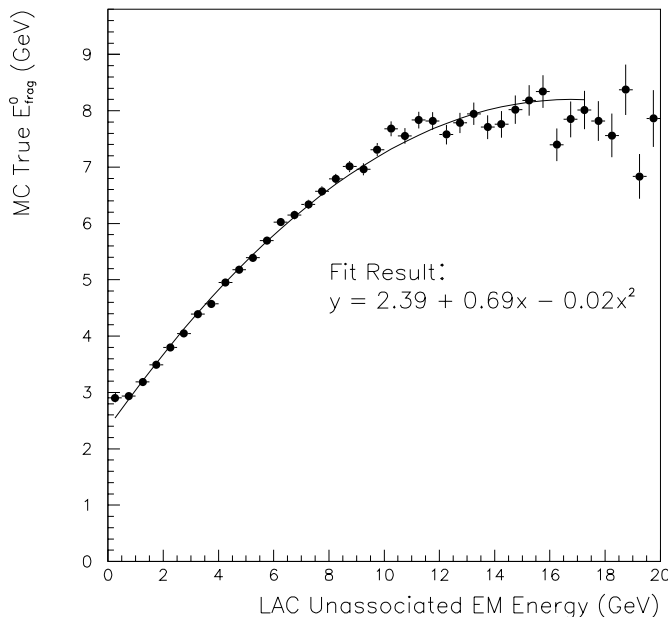
Figure 4.16: The correlation between the LAC unassociated EM energy and the true MC E^0_{frag}.

Once the neutral clusters have been identified and the appropriate energy scale applied we can attempt to form the neutral fragmentation energy, E^0_{frag}. At this point, we have not determined what fraction of the LAC neutral energy is from the B and what fraction is from fragmentation. Ideally, we would like to assign each cluster to either the B decay or fragmentation as we did with the charged tracks. However, the spatial resolution in the LAC is not sufficient to make this distinction. Therefore, we are forced to use Monte Carlo to parametrize E^0_{frag} in terms of the unassociated EM energy. We simply consider those clusters angularly closest to the jet axis containing the lepton and perform a fit of the true E^0_{frag} to the unassociated EM energy in the LAC. Figure 4.16 shows the result. Admittedly, the LAC unassociated EM energy
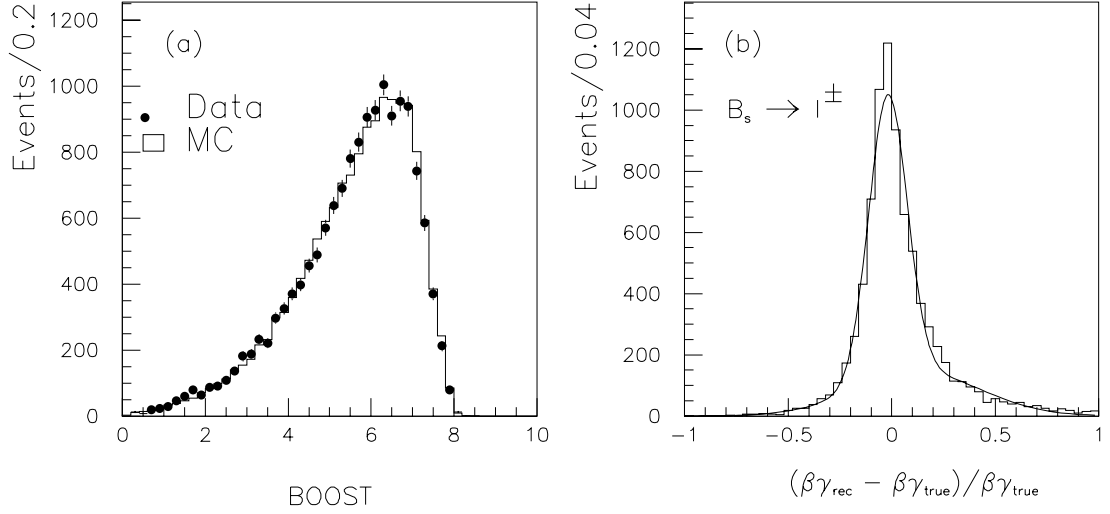
Figure 4.17: Plot (a) is the reconstructed boost distribution in the data and MC. Plot (b) shows the relative boost residual for $B_s \to l^{\pm}$ decays.

should include both the B and fragmentation components. However, figure 4.16 shows that there is some correlation to E_{frag}^0.

Using the fitted value of E_{frag}^0, the B energy is calculated by equation 4.15. The B boost is then determined by,

$$\beta\gamma = \frac{p_B}{m_B} = \frac{\sqrt{E_B^2 - m_B^2}}{m_B} \qquad (4.21)$$

where m_B is assumed to be 5.3 GeV. Figure 4.17(a) compares the distributions of the reconstructed boost in the data and MC. Figure 4.17(b) is the relative boost residual for the B_s^0 decays. A two gaussian fit yields $\sigma_{core} = 9\%$ and $\sigma_{tail} = 30\%$ with a core fraction of 66%.

The proper time of the B decay can now be easily calculated from the decay length and boost using,

$$t = \frac{L}{\beta\gamma c} \qquad (4.22)$$

where the determination of L and $\beta\gamma$ were described in the previous sections. Figure 4.18 compares the reconstructed proper time distributions in the data and MC. The negative proper times are the result of negative decay lengths produced when the

vertex is reconstructed behind the IP with respect to the jet axis direction. Events with $t_{rec} < 0$ are removed in the likelihood fit.

The proper time residual $t_{rec} - t_{true}$ is plotted for the MC in figure 4.19. A two gaussian fit yields a core width of 0.17 ps and a tail width of 0.68 ps for $B \to l^{\pm}$. The core fraction is 61%. The $B \to c \to l^{\pm}$ plot shows a large positive tail due to the overestimation of the decay length. The core width is 0.24 ps while the tail width is 0.87 ps. The core fraction is 48%.

4.7.3 Topological Vertexing

The statistical vertexing technique described above was developed for the specific needs of a semileptonic analysis. It requires the detection of a quality, high p_T lepton track but is then able to reconstruct a vertex with very high efficiency. The topological approach described in this section is a more general vertexing scheme which does not rely on any specific decay mode or topology. The basic idea is to use the track helix parameters and error matrix to describe each charged track as a 'gaussian probability tube'. By summing the track probability functions in 3-D space, vertices should appear as regions of high overlap probability [78, 79]. Topological vertexing is included in this analysis primarily in the $b\bar{b}$ event tag and initial state flavor tags to be described below.

Figure 4.20 illustrates the construction of the track probability functions, $f_i(\vec{r})$. The z axis is the beam axis with the positive direction given by the direction of the e^+ beam. The x' and y' axes are determined for each track by orienting y' such that the projection of the track momentum onto the xy plane at the distance of closest approach to the z axis is parallel to y'. In this new coordinate system the track probability functions are defined by,

$$f_i(\vec{r}) = \exp\left\{ -\frac{1}{2}\left[\left(\frac{x' - (x'_0 + \kappa y')}{\sigma_T}\right)^2 + \left(\frac{z - (z_0 + \tan(\lambda)y')}{\sigma_L}\right)^2 \right] \right\} \qquad (4.23)$$

where σ_T and σ_L are the track position errors in the transverse and longitudinal directions to the beam axis at the point of closest approach to the axis. The parameter κ accounts for the track curvature in the xy plane due to the detector magnetic field. It is a function of the track momentum, charge, and field strength. The angle between
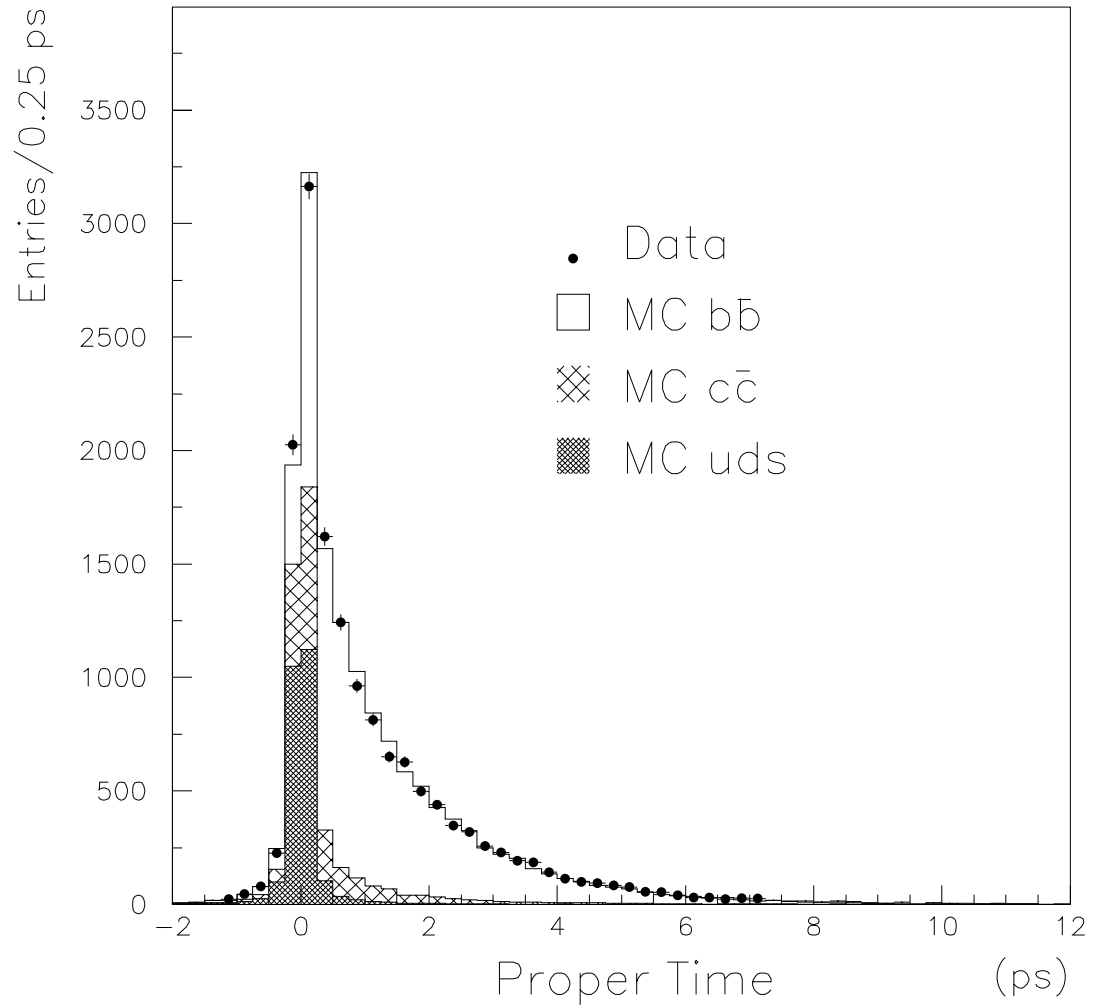
Figure 4.18: The reconstructed proper time distribution for the data (points) and MC (histograms). The $c\bar{c}$ and *uds* backgrounds are concentrated at small proper time.
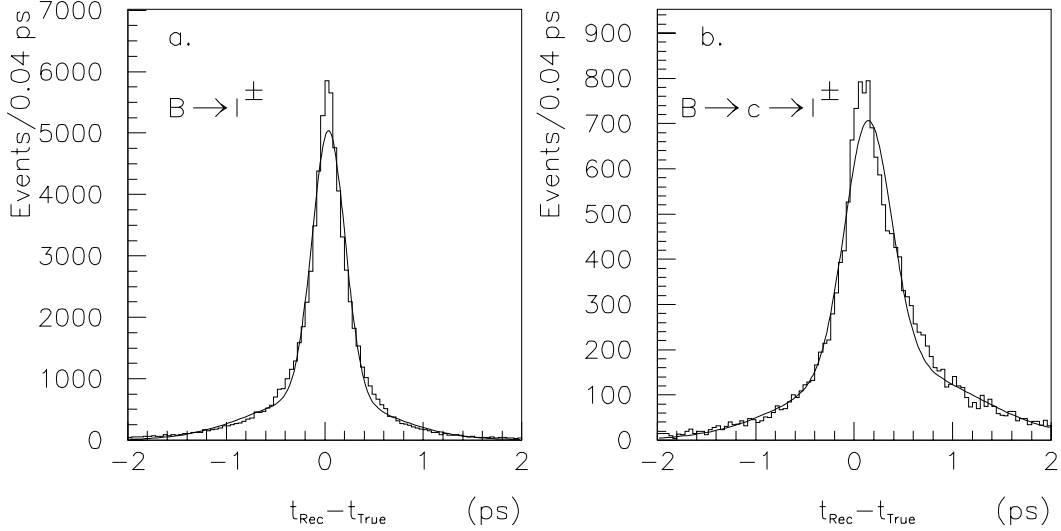
Figure 4.19: The average proper time residuals for $B \to l^{\pm}$ decays (a) and $B \to c \to l^{\pm}$ decays (b).

the track momentum and the positive y' axis is denoted λ. The $\tan(\lambda)y'$ term in the second exponential accounts for the track propagation along the z direction.

A probability function $f_0(\vec{r})$ is also included to describe the probable position of the interaction point. $f_0(\vec{r})$ is represented by an unnormalized gaussian ellipsoid centered at the origin. The widths of the ellipsoid are determined by the uncertainty in the IP position, $\sigma_x = \sigma_y = 7 \ \mu m$ and $\sigma_z = 70 \ \mu m$. In the rest of the procedure, $f_0(\vec{r})$ will be treated exactly like the other track probability functions. The track probability functions projected into the xy plane are shown for a typical $Z^0 \to b\bar{b}$ MC event in figure 4.21(a).

The physical vertices should occur in the overlap regions of at least two tracks. Therefore, the volume of 3-D space that must be searched can be greatly reduced by first locating the maxima of the two-track products $f_i(\vec{r})f_j(\vec{r})$. These maxima can be calculated analytically and will be denoted $\vec{r}_{ij}$. For a jet or hemisphere of N tracks, there will be $\frac{1}{2}N(N+1)$ such maxima. This number can be further reduced by requiring both tracks to pass a χ^2 test based on the consistency with the two track maximum $\vec{r}_{ij}$. That is, we require $\chi^2 < \chi_0^2$ for each track where χ^2 is the distance
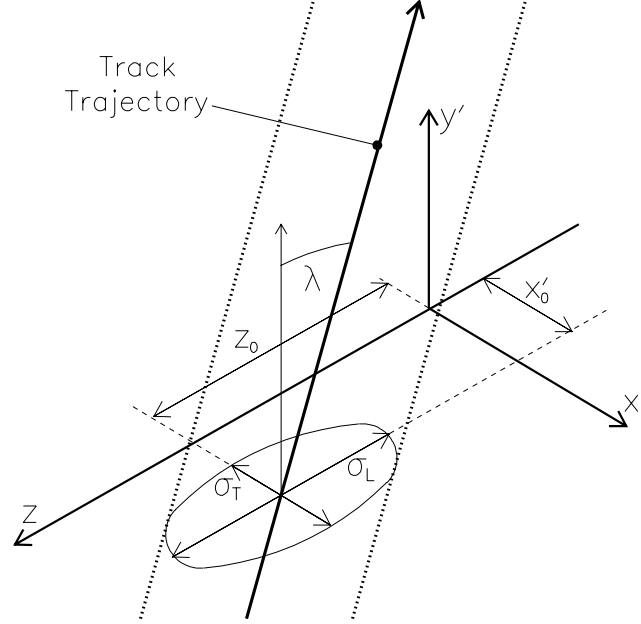
Figure 4.20: Parametrization of the Gaussian tube $f_i(\vec{r})$ for each track i.

squared from the track to $\vec{r}_{ij}$ divided by the track error and χ_0^2 is an input parameter.

Once the probable vertex regions are identified from the two-track maxima, a total vertex probability function can be constructed and maximized in these regions. The relative probability of a vertex at $\vec{r}$ is expressed as,

$$V(\vec{r}) = \sum_{i=0}^{N} f_i(\vec{r}) - \frac{\sum_{i=0}^{N} f_i^2(\vec{r})}{\sum_{i=0}^{N} f_i(\vec{r})}. \tag{4.24}$$

Note that for a single track or IP, no vertices are possible and $V(\vec{r})$ is 0. Similarly, in regions where only one $f_i(\vec{r})$ is significant, $V(\vec{r}) \approx 0$. Therefore, the second term ensures that $V(\vec{r})$ is only significant in regions of high track overlap probability. Figure 4.21(b) shows $V(\vec{r})$, also projected into the xy plane. The IP and a single secondary vertex are clearly visible.

For each two-track maximum $\vec{r}_{ij}$ the nearest maximum in $V(\vec{r})$ is located by an iterative procedure. The set of adjusted maxima $\vec{r}_{ij}$ is then subjected to a clustering
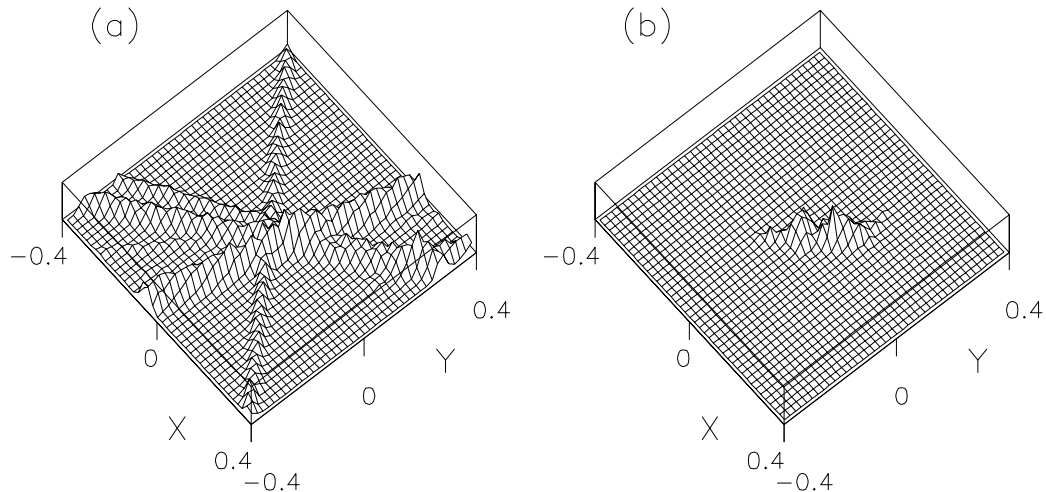
Figure 4.21: Figure (a) shows the track functions $f_i(\vec{r})$ projected into the xy plane. Figure (b) is the vertex function $V(\vec{r})$.

procedure that will produce the final reconstructed vertices. We begin with the maximum that produces the largest value of $V(\vec{r})$ and merge in all other maxima which are *unresolved*. Two locations $\vec{r}_1$ and $\vec{r}_2$ are considered resolved if,

$$\frac{\min\{V(\vec{r}) : \vec{r} \in \vec{r}_1 + \alpha(\vec{r}_2 - \vec{r}_1),\ 0 \le \alpha \le 1\}}{\min\{V(\vec{r}_1),\ V(\vec{r}_2)\}} < R_0. \qquad (4.25)$$

The numerator represents the minimum value of $V(\vec{r})$ along the line joining $\vec{r}_1$ and $\vec{r}_2$. The denominator is simply the smaller of $V(\vec{r}_1)$ and $V(\vec{r}_2)$. R_0 is a tuneable input parameter in the range 0 to 1 and determines the number of vertices that will be resolved. This procedure continues until all remaining adjusted maxima $\vec{r}_{ij}$ are resolved from every maximum in the cluster.

If any maxima remain, the one producing the largest value of $V(\vec{r})$ is selected to begin a new cluster and the above clustering procedure is repeated. The process continues until all maxima $\vec{r}_{ij}$ are included in a cluster. The resulting clusters will become the final reconstructed vertices.

Finally, all tracks must be assigned to a unique vertex. Recall that the maxima $\vec{r}_{ij}$ were determined for all two-track combinations. In the clustering process, the set

of maxima involving a given track may be divided among several clusters making the track assignment ambiguous. Therefore, for each cluster, all associated tracks are fit to a common vertex position. The track with the largest χ^2 contribution is removed if $\chi^2 > \chi_0^2$ where χ_0^2 is the input parameter described above. This process is repeated while two or more tracks remain until all tracks associated with each cluster pass the χ^2 cut. Note that this procedure allows for isolated tracks that are not associated with any cluster.

If track ambiguities persist, the tracks in the vertex with the largest $V(\vec{r}_{ij})$ are fixed in that vertex and removed from others. This procedure is repeated for the remaining vertices in decreasing order of maximum $V(\vec{r}_{ij})$. All non-isolated tracks should now be uniquely assigned to a vertex. The final vertices are located by performing a χ^2 fit to a common location for all tracks associated with the vertex.

One final step is performed to determine the origin of the isolated tracks. We begin by forming a vertex axis from the IP to the reconstructed secondary or *seed* vertex as shown schematically in figure 4.11. For each isolated track, the point of closest approach to the vertex axis is located. The parameter T is defined to be the transverse distance from the vertex axis to the track at the point of closest approach. L is the longitudinal distance from the IP to the point of closest approach along the vertex axis. Isolated tracks passing $T < 0.1$ cm are assumed to be associated with the B decay chain. Those with $L/D > 0.3$ are taken to be secondary tracks while the rest are assumed to be primary. The inclusion of the isolated tracks does not alter the vertex positions determined above.

4.7.4   The $b\bar{b}$ Tag

The inclusion of the topological vertices in this analysis is mainly to reject $c\bar{c}$ and *uds* backgrounds. In the the previous B_d^0 mixing analyses, these backgrounds were easily removed by making cuts on the reconstructed proper time (see figure 4.18). Given the long oscillation period for B_d^0 mixing, little information was lost. For B_s^0 mixing, however, the oscillation frequency is much larger so that we cannot afford to make the proper time cut. Therefore, the topological vertex information is used to

construct a vertex mass that functions as a $b\bar{b}$ tag.

The vertex mass, M, is calculated by forming the invariant mass of all charged tracks included in the topological vertex where each track is assumed to have the pion mass. This procedure does not include the neutral decay products but we are able to make a correction based on the missing p_T in the vertex. Assuming the B hadron momentum direction is given by the vertex axis, the missing p_T is just the total charged track momentum transverse to the B flight direction. It represents the minimum momentum of the neutral decay products consistent with conservation of momentum at the B vertex. The direction of the vertex axis is varied within the 1σ errors on the IP and vertex positions so that the minimum missing p_T is determined. This ensures that background uds and $c\bar{c}$ events do not obtain a large p_T corrected mass due to random fluctuations in the measured p_T. The p_T-added mass can then be defined as,

$$M_{p_T} = \sqrt{M^2 + p_T^2} + |p_T|. \tag{4.26}$$

Figure 4.22 shows the p_T-added mass distribution in the data and MC for those events with secondary topological vertices. Topological vertices were located in about 79% of the lepton candidate hemispheres and 76% of opposite hemispheres. Since a $b\bar{b}$ event produces a B hadron in both hemispheres, a high mass vertex in either hemisphere tags $b\bar{b}$ events. The uds and $c\bar{c}$ backgrounds are concentrated in the low mass region. Note that the charm distribution has a sharp cutoff at ~ 2 GeV/c^2, near the D meson mass.

A B decay vertex can also be tagged by the presence of tracks with large impact parameters. Due to the long lifetime of B hadrons, tracks produced in B decays typically have larger impact parameters to the IP. Therefore, this analysis also considers the number of *significant* tracks where a significant track is defined to be a *Quality* track with normalized 3-D impact parameter greater than 3.0. The quality track cuts were described in section 4.5.

Finally, the $b\bar{b}$ tag requires that there be a topological vertex with p_T-added mass greater than 1.8 GeV/c^2 in either hemisphere or at least three significant tracks in the event. About 70% of all events with a high p_T lepton candidate pass the $b\bar{b}$ tag. According to the Monte Carlo, about 93% of the $b\bar{b}$ events pass the tag producing
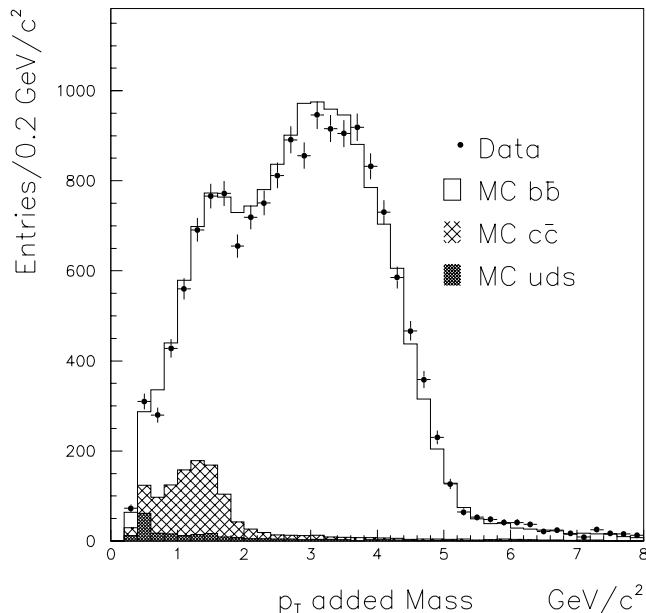
Figure 4.22: The p_T-added mass distribution for events containing topological vertices. Note that much of the *uds* background does not contain a secondary topological vertex.

final purities of 92.5% $b\bar{b}$, 5.7% $c\bar{c}$, and 1.8% *uds*. The efficiency of the tag varies with proper time and drops off at small proper time. Unfortunately, it is difficult to tag B's with high efficiency and purity near the IP.

4.8   Initial State Tag

We now turn to the initial state flavor tag. Recall that we must know the b quark flavor (b or $\bar{b}$) at production and decay to determine whether mixing has occurred. The charge of the lepton in the semileptonic B decays tags the final state flavor as described above. The main component of the initial state flavor tag is the polarized forward-backward asymmetry of the b quark. We also include a standard jet charge technique using charged tracks in the opposite hemisphere. Finally, several other tags derived from topological vertexing will be included.

4.8.1 Polarization

At SLD, the longitudinal electron beam polarization provides a pure and highly efficient method of tagging the initial state quark flavor by exploiting the large polarized forward-backward asymmetry of the b quark. Recall from section 1.3 that in the process $e^+e^- \to Z^0 \to b\bar{b}$, the differential cross section has the form,

$$\frac{d\sigma^b(P_e)}{dz} \propto (1 - A_eP_e)(1 + z^2) + 2A_b(A_e - P_e)z \equiv \sigma^b(z) \qquad (4.27)$$

where $z = \cos\theta$ is the angle between the incident electron direction and the final state fermion and P_e is the electron beam polarization (P_e is negative for left-handed polarization). A_e and A_b are determined from the vector and axial vector coupling constants of the fermion to the Z^0 and express the degree of parity violation at the Z^0 vertex. Due to this parity violation, there is an asymmetry in the directions of the emerging fermions. For $P_e < 0$, the b quark tends to be emitted in the positive or e^- beam direction and the $\bar{b}$ in the backward direction. Using the differential cross section above, we can form the forward-backward asymmetry as a function of P_e and z,

$$\tilde{A}^b_{FB}(z, P_e) = \frac{\sigma^b(z) - \sigma^b(-z)}{\sigma^b(z) + \sigma^b(-z)} \qquad (4.28)$$

$$= 2A_b \left(\frac{A_e - P_e}{1 - A_eP_e} \right) \left(\frac{z}{1 + z^2} \right).$$

$\tilde{A}^b_{FB}$ tells us the number of b quarks emitted at angle z minus the number emitted at $-z$ divided by the sum for beam polarization P_e. Note that $\tilde{A}^b_{FB}$ is antisymmetric in z and that the asymmetry is stronger for left handed electrons.

In this analysis, the thrust axis is used to estimate the initial directions of the $b\bar{b}$ quark pair. For each selected lepton, the thrust axis is signed by the momentum direction of the reconstructed B vertex. The probability that the initial state quark was a b can then be calculated as,

$$P^{pol}_b = \frac{1}{2}(1 + \tilde{A}^b_{FB}) \qquad (4.29)$$

using the signed thrust axis and the measured event polarization. For the calculation, we assume $A_b = 0.935$ and $A_e = 0.15$. The uncertainty in these values will be
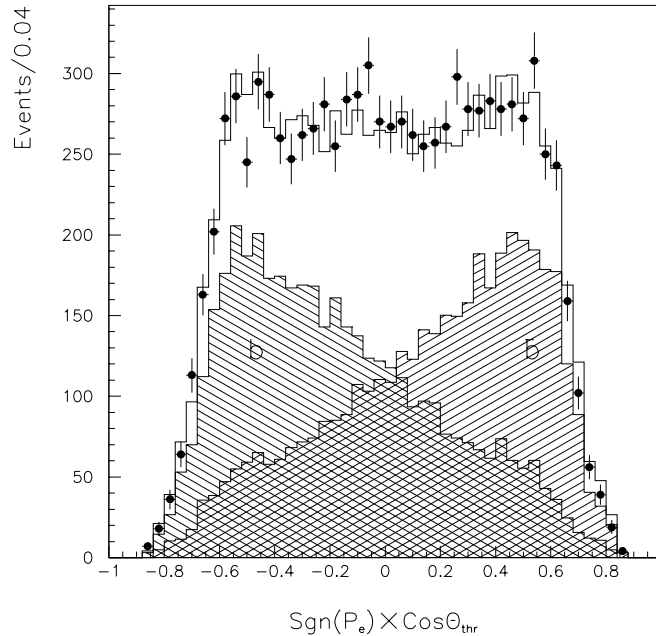
Figure 4.23: The polarization signed thrust angle for the data and MC. The MC histograms show the separation between b and $\bar{b}$ quarks. For negative polarization, the b quark tends to scatter in the forward direction.

considered as systematic errors. Figure 4.23 shows the excellent data/MC agreement for the polarization signed thrust axis distribution. The MC histograms show the separation obtained in the b and $\bar{b}$ samples.

The purity of the polarization tag varies with thrust angle and beam polarization. Unfortunately, lepton identification requires $|\cos\theta_{lepton}| < 0.71$ which reduces the purity of the tag by removing those events at large angles where the asymmetry is the strongest. For the average beam polarization of $P_e = 73\%$ in the data, the polarization tag has an average purity of 69% for this analysis. The tag is unavailable only for events with very low beam polarization. A cut on $|P_e|$ at 40% removes $\sim 3\%$ of the remaining events.

4.8.2 Jet Charge

The second method employed to tag the initial quark flavor is the *jet charge* technique. In a $Z^0 \rightarrow b\bar{b}$ decay the two quarks emerge back to back, usually forming two distinct jets. The jet charge method exploits the fact that the two quarks are opposite in charge. The final charged tracks from the B decay should carry this charge information. Also, B decay tracks tend to be higher in momentum than those from fragmentation. Therefore, we form a momentum-weighted track charge as follows,

$$Q_{jet} = \sum q_i \mid \vec{p_i} \cdot \hat{T} \mid^{\kappa} \qquad (4.30)$$

where the sum is over all tracks with charge q_i and momentum $\vec{p_i}$ in the hemisphere. These tracks are required to have total momentum $p < 50$ GeV/c, momentum transverse to the beam direction $p_{\perp} > 0.15$ GeV/c, 2 dimensional impact parameter to the IP $\delta < 2$ cm, distance between the IP and point of closest approach to the beam axis $\Delta z < 10$ cm and $\mid \cos\theta \mid < 0.87$. $\hat{T}$ is the thrust axis and κ is chosen to maximize the separation between b and $\bar{b}$ in the MC. For this analysis κ is set to 0.5.

In this analysis hemispheres are used in place of jets. For each hemisphere containing a lepton, the Q_{jet} is calculated for the opposite hemisphere defined by the thrust axis. The opposite hemisphere is chosen so that there will be no correlation between the final state tag and the initial state tag. If the tagged hemisphere was used, the presence of the high p_T lepton would bias the jet charge calculation. Figure 4.24 compares the data and Monte Carlo jet charge distributions as well as the $b\bar{b}$ separation in the Monte Carlo.

The jet charge technique has an efficiency of nearly 100%. The purity of the tag depends on the magnitude of Q_{jet}. The probability that the tagged hemisphere contained the initial b quark is well approximated from the opposite hemisphere Q_{jet} using,

$$P_b^{Q_{jet}} = \frac{1}{1 + exp(\alpha Q_{jet})} \qquad (4.31)$$

where α is determined from the Monte Carlo to be -0.27. The average correct tag fraction from jet charge is 65%.
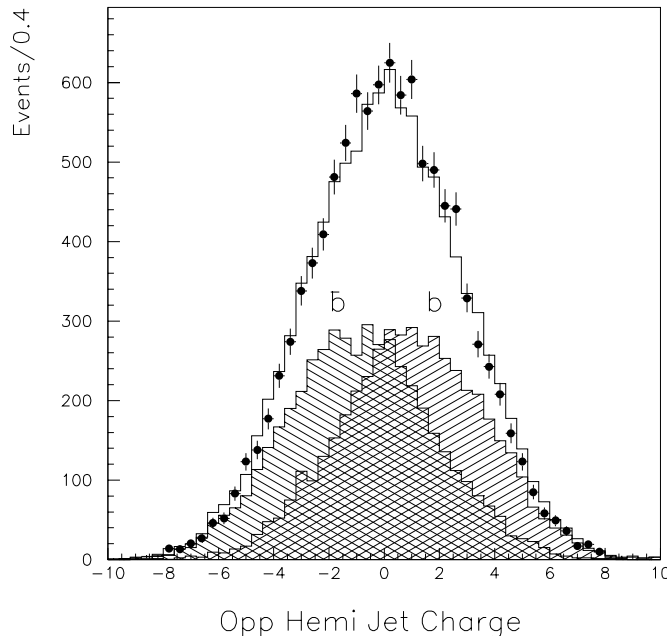
Figure 4.24: Comparison of the opposite hemisphere jet charge in the data (points) and MC (histograms). The MC histograms show the separation between b and $\bar{b}$ quarks. Note that the b and $\bar{b}$ labels refer to the tagged hemisphere where the jet charge was calculated in the opposite hemisphere. Therefore, the opposite jet charge tends to be positive for b quarks in the tagged hemisphere.

4.8.3 Topological Tags

Several other initial state tags are derived from the topological vertexing information described in section 4.7.3. The topological vertex information is not available for all selected events. Therefore, these tags were applied when available. The sensitive variables are:

- **reconstructed vertex charge**

  When a B_s^0 meson is produced in the tagged hemisphere, a b hadron is also produced in the opposite hemisphere. If the reconstructed vertex charge of the opposite b hadron is nonzero, it is likely to be a $B^{\pm}$. Therefore, the charge of the vertex tags the quark flavor, $Q_{vtx} > (<)0 \to \bar{b}(b)$. The purity of the

charge reconstruction depends on the p_T added mass so the b flavor probability is parametrized as a third order polynomial in terms of M_{p_T} for abs$(Q_{vtx}) = 1$ and abs$(Q_{vtx}) > 1$.

- **vertex charge dipole**

  The vertex charge dipole is a technique created at SLD that exploits the cascade $b \rightarrow c$ decay structure to tag the b quark flavor. In fact, one B_s^0 mixing analysis at SLD employs the charge dipole as the sole final state tag. Details of the charge dipole analysis can be found elsewhere [39]. The idea is to locate two well separated topological vertices, presumably the B and D. The probability of a single vertex fit to all secondary tracks is required to be less than 1%. The two vertex combination with the best χ^2 is then located and the charge dipole is calculated as,

  $$\delta q = L_{BD} \times \text{sign}(Q_D - Q_B) \qquad (4.32)$$

  where Q_B and Q_D are the B and D vertex charges and L_{BD} is the distance between the B and D vertices. The charge dipole tends to be > 0 if the decaying hadron contains a b and < 0 for a $\bar{b}$. The initial state flavor probability is parametrized as,

  $$P_{\delta q} = \frac{\alpha}{1 + \exp[\beta(\gamma - \delta q)]} \qquad (4.33)$$

  where α, β and γ are determined from Monte Carlo and depend on the decay length and Q_{vtx}.

- **high p_T leptons**

  Just as the charge of a high p_T lepton is used to tag the final state b quark flavor in the tagged hemisphere, leptons in the opposite hemisphere can be used to tag the initial state flavor. A positively charged high p_T lepton in the opposite hemisphere indicates a $\bar{b}$ was produced in that hemisphere and, thus, a b was produced in the tagged hemisphere. Note that the lepton charge actually indicates the final state b flavor so that this tag is *diluted* by mixing. However, mixing in the tagged and opposite hemispheres are uncorrelated and the majority of B hadrons do not mix or will decay before mixing.

Selected leptons are required to have $p_{tot} > 2$ GeV/c. If more than one lepton is identified, the one with the highest momentum transverse to the jet axis, p_T is selected. The purity of the lepton tag is a function of the lepton p_T. The larger the p_T, the more likely the lepton was produced in a B decay. Therefore, the lepton b flavor probability is parametrized as a fourth order polynomial in terms of the lepton p_T.

- **secondary kaons**

  The charges of secondary kaons also contain information on the initial state b flavor [24]. If the kaon was produced through the $b \rightarrow c \rightarrow s$ decay chain, the kaon charge should have the same charge sign as the b quark. Secondary kaons are located by considering the CRID information from those tracks attached to the topological B or D vertices. These tracks are required to have $p_{tot} > 0.8$ GeV/c and $|\cos\theta| < 0.68$ so that they are contained in the barrel CRID. In addition, the radius of the outer CDC hit is required to be at least 90 cm so that the track is well extrapolated into the CRID. For kaon selection we require $\log \mathcal{L}_K - \log \mathcal{L}_\pi > 5(3)$ for track momenta $< (>)$ 2.5 GeV/c to reject pions. In addition $\log \mathcal{L}_K - \log \mathcal{L}_p$ is required to be > -1 so that the track is K/p ambiguous or better. If more than one kaon is located, the sum of the kaon charges is calculated. The correct tag probability is determined from the MC to be 0.69 and 0.79 for kaon charge sums of 1 and 2 (absolute value) respectively.

All the various initial state tags are combined to produce P_b, the probability that the initial quark in the lepton hemisphere was a b rather than a $\bar{b}$. The distributions of P_b for the data and MC are plotted in figure 4.25. The MC histograms also indicate the separation in b and $\bar{b}$ quarks obtained. The average purity of the combined tag is about 75% given the electron beam polarization obtained in the data.

4.9 Mixing

It is now possible to tag individual events as mixed or unmixed based on the initial and final state tags. Recall that the final state b quark charge is tagged by the
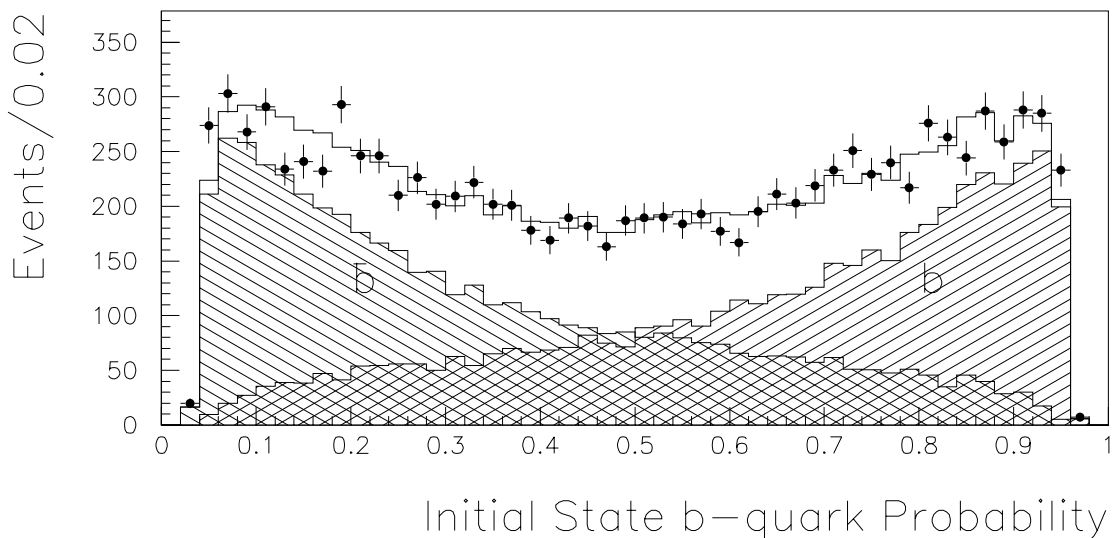
Figure 4.25: The combined initial state tag probability P_b in the data and MC. $P_b > 0.5$ suggests an initial state b quark.

high p_T lepton charge. A negative lepton indicates a b quark decay while a positive lepton indicates a $\bar{b}$. Similarly, P_b tells us the probability that the initial quark was a b as opposed to a $\bar{b}$. Therefore, we can tag those events with $P_b > (<)0.5$ and $Q_{lep} = +1(-1)$ as mixed while other combinations are considered unmixed. Note that this distinction is made only for the purpose of plots and consistency checks. The likelihood fit that produces our final results (see chapter 5) does not explicitly categorize a given event as mixed or unmixed.

Overall, 39% of the data events are tagged as mixed as compared to 38% in the fully reconstructed $q\bar{q}$ Monte Carlo. The mixed fraction as a function of reconstructed proper time is plotted in figure 4.26. The mixed fraction does appear to increase with proper time as expected from equation 1.73. However, the visible increase in mix fraction is due to B_d^0 mixing. The B_s^0 mixing occurs too quickly to be visible on a plot of this type.

A further test of our initial and final state tags is to plot the polarized forward-backward asymmetry. Figure 4.27 shows the thrust axis distribution signed by the lepton charge and beam polarization. For $P_e < 0$, b quarks tend to scatter in the
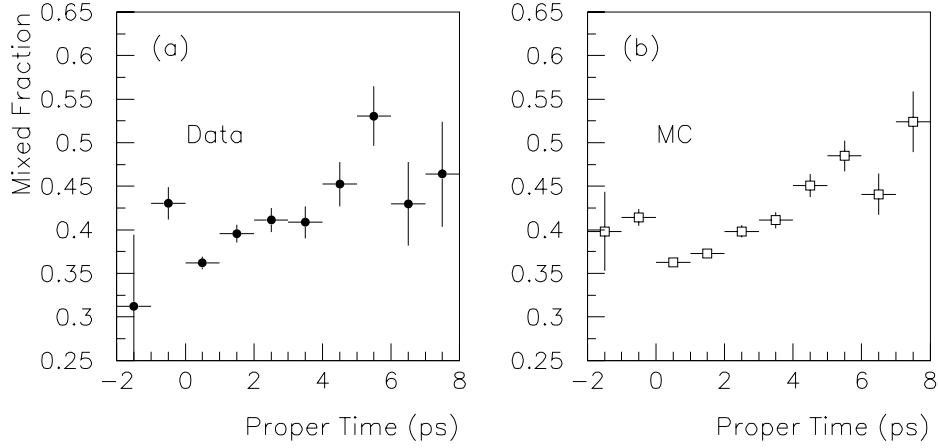
Figure 4.26: The mixed fraction versus reconstructed proper time in the data (a) and $q\bar{q}$ Monte Carlo (b).

forward (e^- beam) direction and to decay into negatively charged leptons. Therefore, $\text{sign}(P_e Q_{lep})\cos\theta_{thr}$ should be predominantly positive. The $\bar{b}$ quarks tend to scatter in the backward direction but the lepton charge is positive so $\text{sign}(P_e Q_{lep})\cos\theta_{thr}$ should again be predominantly positive. The same is true for $P_e > 0$. Figures 4.27(a) and (b) show the asymmetry for $Q_{vtx} \neq 0$ and $Q_{vtx} = 0$ respectively. The asymmetry is diluted in the neutral sample due to mixing of the neutral Bs which flips the sign of the lepton. The good agreement of these plots gives confidence that our tagging ability is well simulated by the MC and that we are sensitive to mixing.
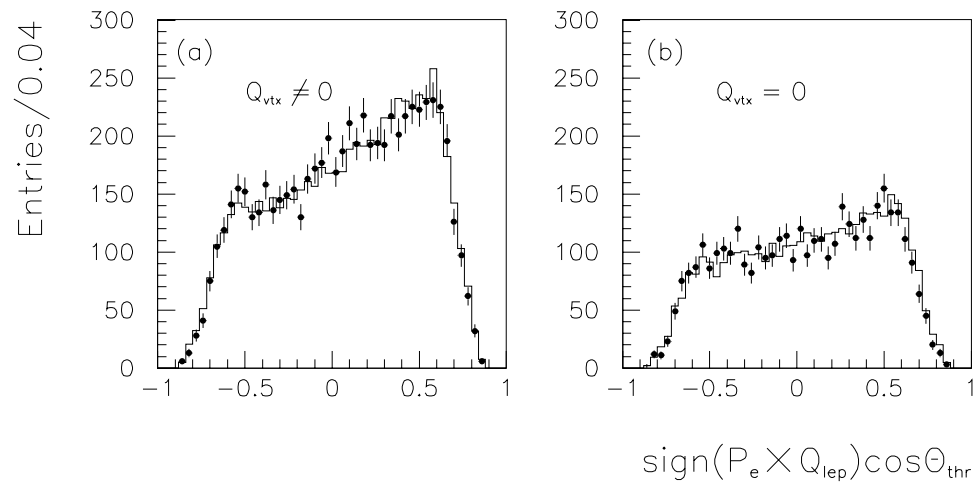
Figure 4.27: The thrust axis distribution signed by the polarization and lepton charge. Plots (a) and (b) show $Q_{vtx} \neq 0$ and $Q_{vtx} = 0$ respectively.

Chapter 5

Maximum Likelihood Analysis

In this chapter, the maximum likelihood analysis that was used to extract values of Δm_d and Δm_s from the reconstructed data will be discussed. In addition, an amplitude fit was performed for the B_s^0 mixing analysis which forms a frequency spectrum of the mixing signal. The amplitude fit results were used to set limits on Δm_s.

5.1 Likelihood Functions

5.1.1 Event Classification

For the maximum likelihood analysis, the data sample was divided into ten categories that are expected to demonstrate unique reconstructed proper time distributions. These categories are:

1. $l^{\pm}$ candidates originating in B_d^0 decays.

2. $l^{\pm}$ candidates originating in B_s^0 decays.

3. $l^{\pm}$ candidates originating in B^+ decays.

4. $l^{\pm}$ candidates originating in b-baryon decays.

5. $l^{\pm}$ candidates originating in cascade $B_d^0 \to c \to l^{\pm}$ decays, $B_d^0 \to \bar{c} \to l^{\pm}$ decays, and $B_d^0 \to \tau \to l^{\pm}$ decays.

6. $l^{\pm}$ candidates originating in cascade $B_s^0 \to c \to l^{\pm}$ decays, $B_s^0 \to \bar{c} \to l^{\pm}$ decays, and $B_s^0 \to \tau \to l^{\pm}$ decays.

7. $l^{\pm}$ candidates originating in cascade $B^+ \to c \to l^{\pm}$ decays, $B^+ \to \bar{c} \to l^{\pm}$ decays, and $B^+ \to \tau \to l^{\pm}$.

8. $l^{\pm}$ candidates originating in cascade $b - \text{baryon} \to c \to l^{\pm}$ decays, $b - \text{baryon} \to \bar{c} \to l^{\pm}$ decays, and $b - \text{baryon} \to \tau \to l^{\pm}$ decays.

9. $l^{\pm}$ candidates originating in $c\bar{c}$ events.

10. $l^{\pm}$ candidates originating in light quark decays or from fragmentation.

We assume that these categories describe all possible sources of lepton candidates. Note that the lepton candidate is not necessarily a true lepton. We will include contamination from lepton misidentification by introducing a mistag rate, η, for each category. Also, the small fraction of lepton candidates produced from the decays of long lived particles or detector interaction are included in the cascade charm categories. In the next several sections we will discuss the treatment of the $b\bar{b}$ categories (1-8). The non-$b\bar{b}$ backgrounds will be handled separately later.

5.1.2 $b\bar{b}$ Physics Functions

The likelihood functions for $b\bar{b}$ events are composed of terms describing the probability for observing a mixed or unmixed event from each of the above categories as a function of proper time. Recall that the probability for a $B_{d,s}^0 (\bar{B}_{d,s}^0)$ to decay as a $B_{d,s}^0 (\bar{B}_{d,s}^0)$ can be expressed as,

$$P_u(t) = \frac{e^{-t/\tau_{d,s}}}{2\tau_{d,s}}(1 + \cos \Delta m_{d,s} t) \tag{5.1}$$

where t is the true proper time of the $B_{d,s}^0$ decay, $\tau_{d,s}$ is the average $B_{d,s}^0$ lifetime and $\Delta m_{d,s}$ is the mass difference between the two mass eigenstates. CP violation effects are assumed to be small and have been neglected. The u subscript refers to unmixed.

Similarly, the probability that the $B_{d,s}^0$ will mix and decay as it's antiparticle is given by,

$$P_m(t) = \frac{e^{-t/\tau_{d,s}}}{2\tau_{d,s}}(1 - \cos \Delta m_{d,s} t). \qquad (5.2)$$

Using these basic expressions, we form two functions, $F_{unmix}(t)$ and $F_{mix}(t)$, that describe the time distributions of events where the lepton charge would agree or disagree, respectively, with the true initial quark flavor. Unfortunately, the charge of the lepton candidate does not always tag the final b quark flavor correctly. Therefore, each of the above categories is divided into a correctly tagged sample and an incorrectly tagged sample by introducing the mistag rate, η_k, where k refers to the lepton source. $F_{unmix}(t)$ can then be expressed as,

$$F_{unmix}(t) = \sum_k f_k \frac{e^{-t/\tau_k}}{2\tau_k}[(1 - \eta_k)(1 + \cos \Delta m_k t) + \eta_k(1 - \cos \Delta m_k t)] \qquad (5.3)$$

where f_k is the fraction of events from category k, and τ_k and Δm_k are the average lifetime and mass difference between the two mass eigenstates of the b hadron producing source k. The sum is over all lepton sources and Δm_k is assumed to be 0 for B^+ and Λ_b. Note that there is a contribution from those events that were actually unmixed and tagged correctly, plus a contribution from events that mixed but were tagged incorrectly. A similar expression is obtained for $F_{mix}(t)$ by interchanging η_k and $1 - \eta_k$. For completeness, the full expressions are included below.

$$
\begin{aligned}
F_{unmix}(t) \;=\; & f_{B_d^0}\frac{e^{-t/\tau_{B_d^0}}}{2\tau_{B_d^0}}[(1 - \eta_d)(1 + \cos \Delta m_d t) + \eta_d(1 - \cos \Delta m_d t)] \qquad (5.4)\\
& + f_{B_s^0}\frac{e^{-t/\tau_{B_s^0}}}{2\tau_{B_s^0}}[(1 - \eta_s)(1 + \cos \Delta m_s t) + \eta_s(1 - \cos \Delta m_s t)]\\
& + f_{B^+}(1 - \eta_+)\frac{e^{-t/\tau_{B^+}}}{2\tau_{B^+}}\\
& + f_{\Lambda_b}(1 - \eta_\Lambda)\frac{e^{-t/\tau_{\Lambda_b}}}{2\tau_{\Lambda_b}}\\
& + f'_{B_d^0}\frac{e^{-t/\tau_{B_d^0}}}{2\tau_{B_d^0}}[(1 - \eta'_d)(1 + \cos \Delta m_d t) + \eta'_d(1 - \cos \Delta m_d t)]\\
& + f'_{B_s^0}\frac{e^{-t/\tau_{B_s^0}}}{2\tau_{B_s^0}}[(1 - \eta'_s)(1 + \cos \Delta m_s t) + \eta'_s(1 - \cos \Delta m_s t)]
\end{aligned}
$$

$$+f'_{B+}(1-\eta'_+)\frac{e^{-t/\tau_{B+}}}{2\tau_{B+}}$$

$$+f'_{\Lambda_b}(1-\eta'_\Lambda)\frac{e^{-t/\tau_{\Lambda_b}}}{2\tau_{\Lambda_b}}$$

and

$$
\begin{aligned}
F_{mix}(t) \;=\; & f_{B_d^0}\frac{e^{-t/\tau_{B_d^0}}}{2\tau_{B_d^0}}[\eta_d(1+\cos\Delta m_d t)+(1-\eta_d)(1-\cos\Delta m_d t)] \qquad (5.5)\\[2mm]
& +f_{B_s^0}\frac{e^{-t/\tau_{B_s^0}}}{2\tau_{B_s^0}}[\eta_s(1+\cos\Delta m_s t)+(1-\eta_s)(1-\cos\Delta m_s t)]\\[2mm]
& +f_{B+}\eta_+\frac{e^{-t/\tau_{B+}}}{2\tau_{B+}}\\[2mm]
& +f_{\Lambda_b}\eta_\Lambda\frac{e^{-t/\tau_{\Lambda_b}}}{2\tau_{\Lambda_b}}\\[2mm]
& +f'_{B_d^0}\frac{e^{-t/\tau_{B_d^0}}}{2\tau_{B_d^0}}[\eta'_d(1+\cos\Delta m_d t)+(1-\eta'_d)(1-\cos\Delta m_d t)]\\[2mm]
& +f'_{B_s^0}\frac{e^{-t/\tau_{B_s^0}}}{2\tau_{B_s^0}}[\eta'_s(1+\cos\Delta m_s t)+(1-\eta'_s)(1-\cos\Delta m_s t)]\\[2mm]
& +f'_{B+}\eta'_+\frac{e^{-t/\tau_{B+}}}{2\tau_{B+}}\\[2mm]
& +f'_{\Lambda_b}\eta'_\Lambda\frac{e^{-t/\tau_{\Lambda_b}}}{2\tau_{\Lambda_b}}
\end{aligned}
$$

The primes on the fractions f, and mistags η distinguish the cascade charm categories from the direct B decays.

5.1.3 Efficiency and Resolution

The physics functions, $F_{unmix}(t)$ and $F_{mix}(t)$ above are functions of the true B decay proper time. The next step is to transform them into functions of the reconstructed proper time, t_{rec}, that we expect to observe in the data. This involves two effects. First, we must account for any proper time biases that may be introduced due to
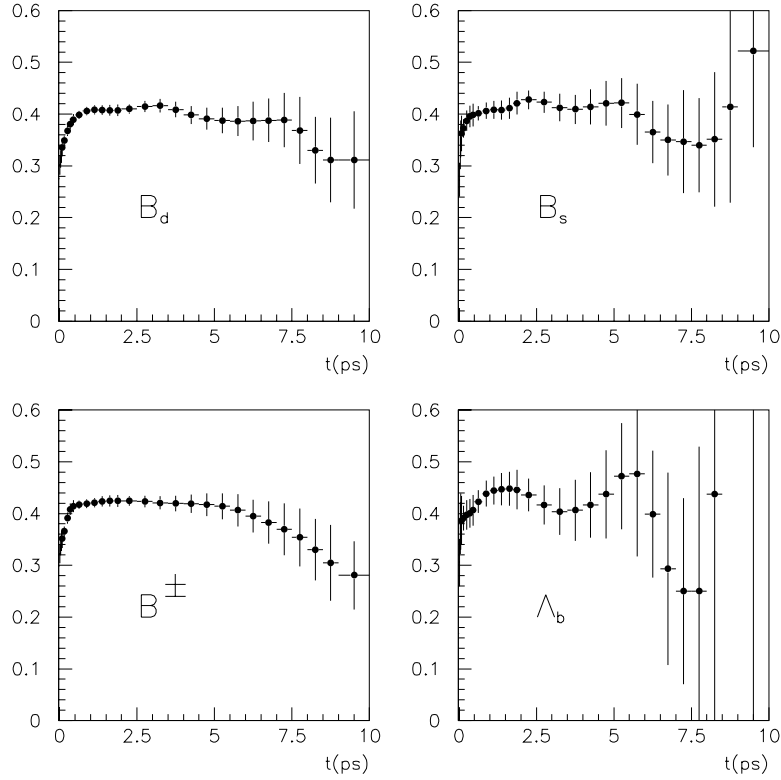
Figure 5.1: The vertex efficiency is defined to be the fraction of events that pass the analysis cuts versus true B decay proper time in the MC.

the event selection cuts. This effect was considered by introducing a vertex efficiency function, $\epsilon^k_{vtx}(t)$, for each lepton source k. The vertex efficiency is simply the fraction of events that pass the analysis cuts as a function of the true proper time of the B decay. This efficiency was measured separately in the Monte Carlo for B^0_d, B^0_s, B^+, and Λ_b decays and is shown in figure 5.1. Note that the vertex efficiency functions are fairly flat except at the small proper time region where they tend to fall off rapidly. This effect is due to the vertex mass cut that we impose to discriminate against $c\bar{c}$ and uds events. At small proper time it is more difficult to locate a secondary topological vertex that is distinct from the IP and the efficiency drops.

The second effect that must be considered is the proper time resolution. In this analysis, we measure the B decay length and boost independently and then combine

them to form the decay proper time,

$$t_{rec} = \frac{L}{\beta\gamma c}. \tag{5.6}$$

The average decay length and boost residuals were plotted in figures 4.9 and 4.17. Performing two gaussian fits to the distributions of $L - L_{true}$ and $(\beta\gamma - \beta\gamma_{true})/\beta\gamma_{true}$, we obtain the gaussian widths σ_L^α and σ_P^α. The α index refers to the core and tail of the distributions. For now we will assume that these measurements are uncorrelated so that the proper time resolution, σ_t, is given by,

$$\sigma_t^{\alpha\beta} = \sqrt{\left(\frac{\sigma_L^\alpha}{\beta\gamma c}\right)^2 + (\sigma_P^\beta t)^2}. \tag{5.7}$$

We see that σ_t is a function of t and that resolution degrades as a function time. There is a constant term determined by σ_L and an increasing term with slope given by σ_P.

Given these residuals we can form a gaussian resolution function relating the true and reconstructed proper times,

$$G(t, t_{rec}) = \sum_{\alpha=1}^{2} \sum_{\beta=1}^{2} f_L^\alpha f_P^\beta \frac{1}{\sqrt{2\pi}\sigma_t^{\alpha\beta}} e^{-\frac{1}{2}((t-t_{rec})/\sigma_t^{\alpha\beta})^2} \tag{5.8}$$

where f_L^α and f_P^β are the core and tail fractions of the decay length and boost residuals and $\sigma_t^{\alpha\beta}$ is given by equation 5.7.

In practice, we have more information than is contained in the average residuals. For both the decay length and boost reconstruction, methods have been developed that allow us to estimate their resolution on an event-by-event basis. An increase in sensitivity can be gained by estimating the proper time resolution for each event and using likelihood functions that have been appropriately smeared. This is due to the fact that the B_s^0 oscillation frequency is quite large and only those events with $\sigma_t \sim 1/2\Delta m_s$ are sensitive to it. Therefore, we can extend our sensitivity to larger values of Δm_s by recognizing those events with good resolution.

The decay length reconstruction was described in section 4.7.1. Basically, the B decay position is located by forming a weighted point of closest approach of all charged tracks along the selected lepton track. As we would expect, the decay length

resolution depends on the spread in the positions of the individual POCAs. The estimated decay length resolution, σ_{vtx}, was given by equation 4.14.

Fitting the decay length residuals in bins of $\log(\sigma_{vtx})$ we obtain the plots shown in figure 5.2. These fits show a strong correlation between the actual decay length resolution and σ_{vtx} for the $B \to l^{\pm}$ sample in the MC. The correlation in the $B \to c \to l^{\pm}$ sample was found to be rather weak and so the average residuals were used in this case. The fitted curves were used to estimate the decay length resolution of each event in the maximum likelihood analysis.
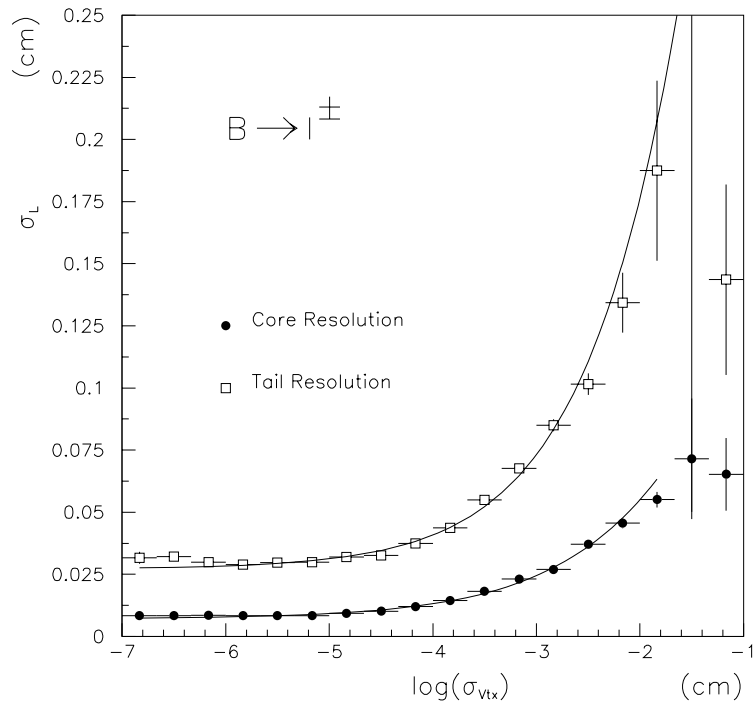
Figure 5.2: The core and tail widths of a two gaussian fit to the decay length residual in bins of σ_{vtx}. The core fraction is 60%

A similar procedure was applied to the boost. Recall that the boost reconstruction begins by locating the B decay position and then attaching charged tracks to the vertex. The sum of the attached track energies is denoted $E_B^{\pm}$. The boost is then

completed by adding some fraction of the LAC neutral cluster energy as discussed in section 4.7.2. At SLD, the vertex detector and CDC provide very precise tracking information that allows us to discriminate between primary and secondary tracks with high efficiency and purity. Thus, $E_B^{\pm}$ can be calculated very accurately. By comparison, the LAC information used to determine the neutral contribution to the boost is relatively imprecise due to problems with the track-cluster association, cluster overlap, and the LAC energy scale. Furthermore, it is very difficult to separate out clusters produced by B decay particles. Therefore, we have found that the boost resolution depends strongly on the amount of charged track energy associated with the decay vertex. Figure 5.3 shows the core (70%) and tail widths of the relative boost residual binned by $E_B^{\pm}$ for each B type. The fits to these curves are used to estimate the boost resolution for each event.

Once an estimate of the decay length and boost resolution is made per event, the resolution function can be derived as in equation 5.8. The functions relating σ_{vtx} and $E_B^{\pm}$ to σ_L and σ_P depend on the lepton source so that the resolution function is source dependent as well. Of course, this expression produces a gaussian function centered at $t = t_{rec}$ and, therefore, does not account for any systematic shifts in the reconstruction. For leptons produced directly in B decays, the effect of the proper time shift is minor. However, for leptons produced in cascade charm decays we tend to reconstruct the D decay vertex. Therefore, there is a significant shift in the reconstructed decay length due to the finite charm lifetime which translates into a positive shift in proper time. To account for this effect, an estimate of the proper time shift is calculated for each event,

$$\langle \Delta t \rangle_k^{\alpha\beta} = \frac{\langle \Delta L \rangle_k^{\alpha}}{\beta\gamma c} - \langle \Delta\beta\gamma/\beta\gamma_{true} \rangle_k^{\beta} t \qquad (5.9)$$

where $\langle \Delta L \rangle_k$ and $\langle \Delta\beta\gamma/\beta\gamma_{true} \rangle_k$ are the means of the gaussians used to fit the average decay length and boost residuals for lepton category k. The shift is then included in the resolution function by substituting

$$t_{rec} \to t_{rec} - \langle \Delta t \rangle_k^{\alpha\beta}. \qquad (5.10)$$

The results of the event-by-event resolution estimate were checked in the Monte Carlo. Figure 5.4 shows the actual proper time residuals, $t_{rec} - t$, as the data points and the
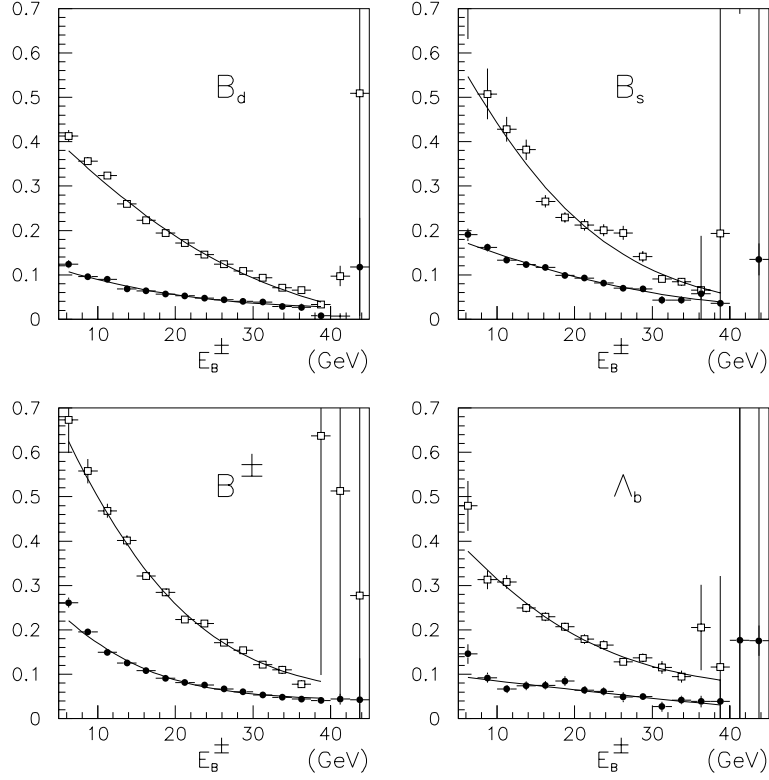
Figure 5.3: These plots show the width of the relative boost residual as a function of $E_B^\pm$ for each B type. The dark circles represent the 70% core while the open squares represent the tail.

calculation as the solid histogram for the $b\bar{b}$ MC. The good agreement suggests we were justified in neglecting correlations between the decay length and boost resolutions.

Given the vertex efficiency and resolution function, we may now transform $F_{unmix}(t)$ and $F_{mix}(t)$ into functions of t_{rec},

$$P_{mix}(t_{rec}) = \sum_k f_k \int_0^\infty F_{mix}^k(t)\epsilon_{vtx}^k(t)G^k(t, t_{rec}, \sigma_{vtx}, E_B^\pm)dt \qquad (5.11)$$

and

$$P_{unmix}(t_{rec}) = \sum_k f_k \int_0^\infty F_{unmix}^k(t)\epsilon_{vtx}^k(t)G^k(t, t_{rec}, \sigma_{vtx}, E_B^\pm)dt \qquad (5.12)$$

where the f_k are the fractions of each lepton source in the sample, F^k are the physics functions, ϵ_{vtx}^k are the vertex efficiency functions and G^k are the resolution functions.
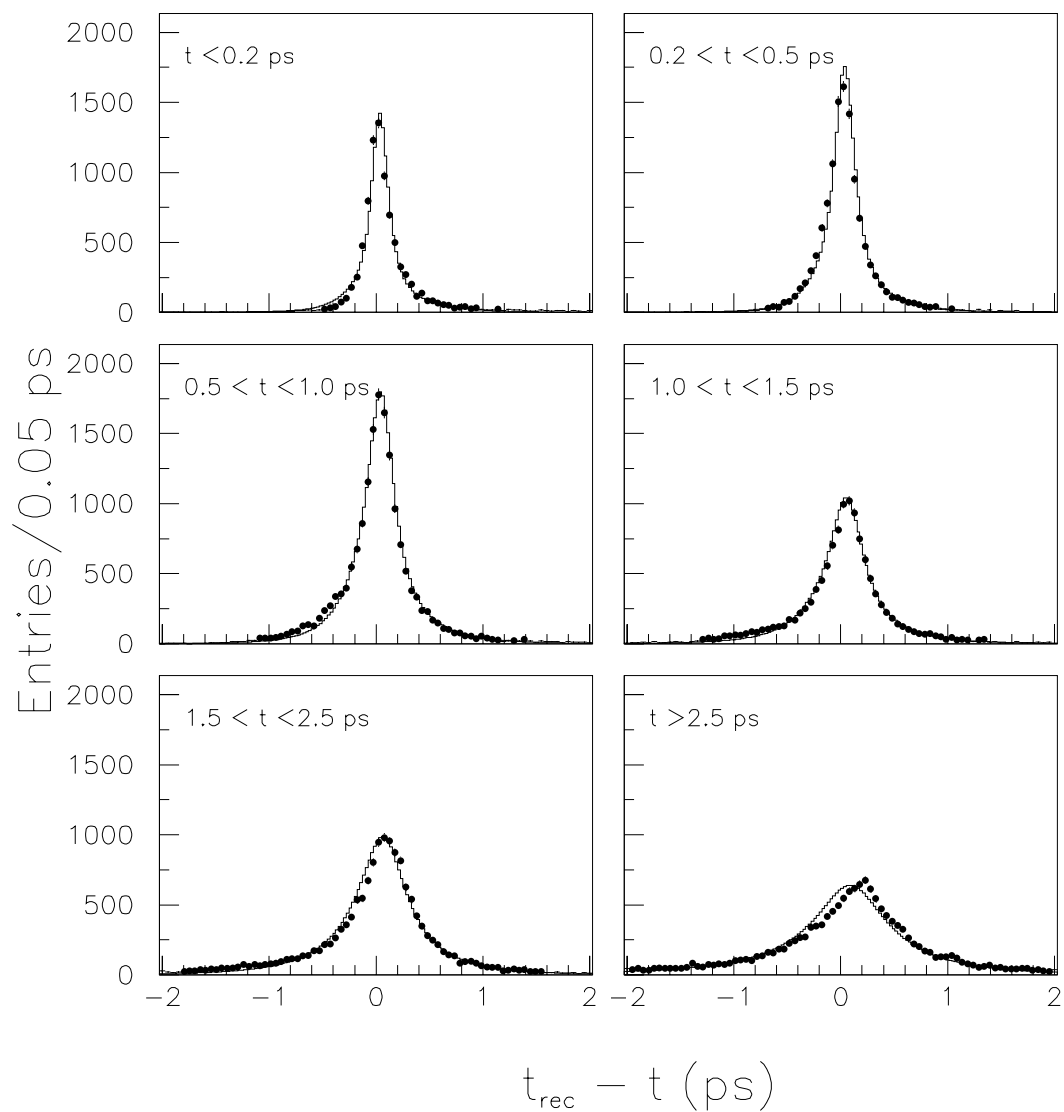
Figure 5.4: Comparison of the MC proper time residuals and the event-by-event estimation in bins of true proper time. The data points are the fully reconstructed MC residuals while the histograms are the analytical calculation.

One final detail needs to be addressed. During the integrations above we applied source dependent efficiencies and resolution functions. Due to differences in these functions, the resulting integrals may no longer be normalized with respect to each other. To account for this discrepancy, we calculate a normalization integral for each source k,

$$I_{Norm}^k = \sum_{events} \int_{-\infty}^{\infty} [P_{unmix}^k(t_{rec}) + P_{mix}^k(t_{rec})] dt_{rec}. \qquad (5.13)$$

The sum over data is necessary to include the proper distribution of $E_B^{\pm}$ and σ_{vtx} for the estimated resolutions. The fractions f_k in equation 5.12 above are actually the fraction of each lepton source determined from the MC divided by the normalization integral.

5.1.4 Non-$b\bar{b}$ Backgrounds

The non-$b\bar{b}$ backgrounds are divided into two categories, $c\bar{c}$ and uds. As described in section 5.1.1, the $c\bar{c}$ category includes those lepton candidates produced directly in the decays of charmed hadrons in $Z^0 \to c\bar{c}$ events. Similarly, the uds category includes leptons produced directly in uds events. In addition, this category also includes any lepton candidate produced from fragmentation, regardless of the quark flavor. The reason for this is that fragmentation leptons produce a reconstructed proper time distribution very similar to that of uds decays. Also, both uds and fragmentation leptons tend to be tagged as mixed or unmixed with nearly equal probability.

To include the non-$b\bar{b}$ backgrounds in the likelihood functions, the reconstructed proper time distributions in the MC were parametrized. For the uds component, the fitting function was the sum of three gaussians. To describe the $c\bar{c}$ component, we used a single gaussian for $t_{rec} < 0$ and two exponentials for $t_{rec} > 0$. These are merely the simplest functions that provided a good fit to the Monte Carlo distributions. The proper time distributions and their fits, P_{uds} and $P_{c\bar{c}}$, are plotted in figure 5.5. The fitting functions were normalized with respect to the $b\bar{b}$ components by integrating over t_{rec} as described above. Finally, the fraction of background events tagged as mixed was determined from the Monte Carlo. For the uds component, the fraction of events that are tagged as mixed, which we will denote as λ_{uds}, is 50%. For the
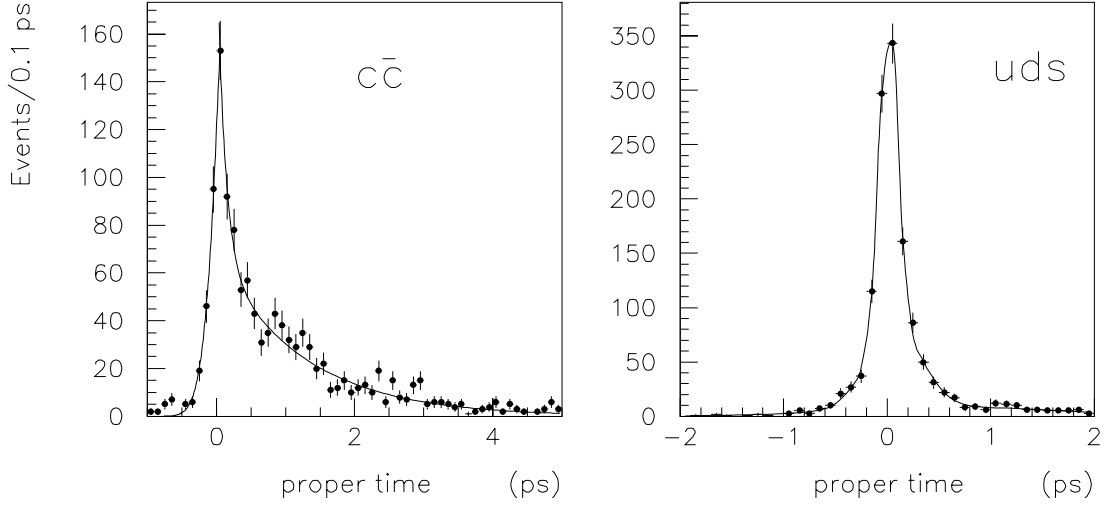
Figure 5.5: The non-$b\bar{b}$ background reconstructed proper time distributions and the likelihood fitting functions.

$c\bar{c}$ events, the fraction tagged as mixed depends on the initial state tag due to the forward-backward asymmetry, A_c. For the initial state tag described in section 4.8, $\lambda_{c\bar{c}} = 54\%$.

Due to the non-$b\bar{b}$ backgrounds, equations 5.11 and 5.12 above are modified as follows,

$$P_{mix}(t_{rec}) \rightarrow P_{mix}(t_{rec}) + f_{c\bar{c}}\lambda_{c\bar{c}}P_{c\bar{c}}(t_{rec}) + f_{uds}\lambda_{uds}P_{uds}(t_{rec}) \tag{5.14}$$

and

$$P_{unmix}(t_{rec}) \rightarrow P_{unmix}(t_{rec}) + f_{c\bar{c}}(1 - \lambda_{c\bar{c}})P_{c\bar{c}}(t_{rec}) + f_{uds}(1 - \lambda_{uds})P_{uds}(t_{rec}). \tag{5.15}$$

5.1.5 Initial State Tag

To summarize, $P_{unmix}(t_{rec})$ and $P_{mix}(t_{rec})$ describe the expected reconstructed proper time distributions of lepton charges that would agree or disagree respectively with a perfect initial state tag. Therefore, these functions describe the final state tagging of

P_b	Q_{lep}	W_{unmix}
> 0.5	-1	P_b
> 0.5	+1	$1 - P_b$
< 0.5	-1	P_b
< 0.5	+1	$1 - P_b$

Table 5.1: The determination of W_{unmix} from the initial and final state tags P_b and Q_{lep}.

the analysis. But to determine whether a given event is mixed or unmixed we must factor in the correlation with the initial state tag. Recall that the initial state b quark probability P_b is determined for each event primarily from the polarization and jet charge as described in section 4.8. P_b represents the probability that the initial quark flavor was b as opposed to $\bar{b}$. To determine an unmixed probability from the initial state tag alone, W_{unmix}, we consider the correlation between P_b and the lepton charge (recall that $b \rightarrow l^-$ and $\bar{b} \rightarrow l^+$ since $b \rightarrow cW^-$ with $W^- \rightarrow l^-\nu$). Table 5.1 shows the relation of W_{unmix} to the initial and final state tags P_b and Q_{lep}. Basically, if the initial and final state tags agree then the event was likely unmixed and W_{unmix} is the larger of P_b and $P_{\bar{b}} = 1 - P_b$.

So the W functions assume the final state tag (Q_{lep}) is correct and determine an unmixed probability solely from the initial state tag. Finally, the likelihood function is given by,

$$\mathcal{L} = \prod_{events} [W_{unmix} \cdot P_{unmix} + (1 - W_{unmix}) \cdot P_{mix}]. \qquad (5.16)$$

5.2 Amplitude Fit

A B_s^0 mixing analysis involves searching for time dependent oscillations in the fraction of mixed events. Therefore, we can use a fourier style analysis to attempt to identify the frequency components of the mixing signal. In the likelihood analysis, the frequency spectrum of the signal was examined by performing an *amplitude fit* [80]. The procedure is to modify the B_s^0 oscillatory terms in the likelihood functions

by introducing a new parameter, $\mathcal{A}$,

$$\frac{1}{2}(1 \pm \cos \Delta m_s t) \rightarrow \frac{1}{2}(1 \pm \mathcal{A} \cos \Delta m_s t). \tag{5.17}$$

For fixed values of Δm_s the $-\log \mathcal{L}$ is minimized with respect to the parameter $\mathcal{A}$. $\mathcal{A}$ is essentially the normalized fourier amplitude of the mixing signal for a given frequency Δm_s. We expect $\mathcal{A} \approx 1$ if oscillations exist at that frequency and $\mathcal{A} \approx 0$ at frequencies far from the true value of Δm_s. Therefore, instead of looking for a minimum in the $-\log(\mathcal{L})$ versus Δm_s we now look for peaks in the amplitude. Many of the general features of the amplitude fit can be understood through fourier analysis. Some of the main results will be described here. Reference [80] may be consulted for more detail.

Consider a simplified mixing analysis function given by,

$$P^{unlike}(t) - P^{like}(t) = [f_s(1 - 2\eta)\cos(\omega t) + (1 - f_s)(1 - 2\eta)]\Gamma \exp(-\Gamma t) \tag{5.18}$$

where f_s is the B_s^0 fraction and η is the combined initial and final state mistag rate. Γ is assumed to be $1/\tau_B \approx 0.65 \text{ ps}^{-1}$. The expected fourier transform (FT) of this signal in a data sample of n events is,

$$\begin{aligned} \text{FT}(\nu) \quad &\approx \frac{n f_s (1-2\eta)}{2} \left(\frac{\Gamma^2}{\Gamma^2 + (\nu-\omega)^2} + \frac{\Gamma^2}{\Gamma^2 + (\nu+\omega)^2} \right) \\ &+ n(1 - f_s)(1 - 2\eta) \frac{\Gamma^2}{\Gamma^2 + \nu^2}. \end{aligned} \tag{5.19}$$

Therefore, we expect a peak in the frequency spectrum at $\nu = \omega$ with a Breit-Wigner shape of width $\sim 2\Gamma$. The second term of the Breit-Wigner can be neglected for $\omega > \Gamma$ and it is assumed that the background term can be subtracted out.

Of course, there will be other effects due to proper time resolution, statistical noise and backgrounds. Recall from section 5.1.3, that the likelihood physics functions are smeared by convoluting with a gaussian resolution function to account for the proper time reconstruction. To simulate this effect in the FT analysis we can employ the convolution theorem which states that the FT of the convolution of two functions is proportional to the product of the individual FTs of those functions. That is,

$$FT[(P \otimes G)(t)](\nu) = \sqrt{2\pi} FT[P(t)](\nu) \times FT[G(t)](\nu) \tag{5.20}$$

where $P(t)$ represents our physics function and $G(t)$ is the resolution function. Therefore, the expected frequency distribution in equation 5.20 should be modified by a factor given by the FT of the resolution function. The FT of a gaussian is simply another gaussian but the calculation is complicated by the time dependence in the boost component of the resolution. The approximate result is,

$$FT[G(t)](\nu) \equiv D(\omega, \sigma_L, \sigma_p) = \exp\left(\frac{-\sigma_L^2 \omega^2}{2}\right) r(\omega, \sigma_p). \qquad (5.21)$$

The first term is a gaussian of width $1/\sigma_L$ and describes the damping of the FT peak due to the decay length resolution σ_L. We see that the expected peak amplitude decreases as the frequency ω increases. The second term accounts for the boost resolution and can be approximated by,

$$r(\omega, \sigma_p) \approx \sqrt{\pi} Y \exp(Y^2) \text{ERFC}(Y), \qquad (5.22)$$

with

$$Y = \frac{1}{\sqrt{2}} \frac{\Gamma}{\sigma_p \omega}, \qquad \text{ERFC}(x) = \frac{2}{\sqrt{\pi}} \int_x^\infty e^{-t^2} dt. \qquad (5.23)$$

This term also results in the reduction of the FT peak amplitude as ω is increased. We can conclude that the fourier amplitude becomes more difficult to measure as the frequency increases when there is uncertainty in the proper time reconstruction. So including proper time resolution, mistag and backgrounds, the expected size of the peak in the FT at $\nu = \omega$ is given by,

$$FT(\omega) \equiv a(\omega) = \frac{n f_s (1 - 2\eta)}{2} D(\omega, \sigma_L, \sigma_p). \qquad (5.24)$$

Figure 5.6 shows the expected FT frequency distribution for Δm_s values of 2.0, 5.0, 8.0, and 12.0 ps^{-1}. These curves were calculated with parameters chosen to simulate this analysis: $n \sim 10500$, $f_s = 12\%$, $\eta = 30\%$, $\sigma_L^{core} = 125\mu\text{m}(60\%)$, $\sigma_L^{tail} = 500\mu\text{m}$, $\sigma_p^{core} = 9\%(65\%)$, and $\sigma_p^{tail} = 30\%$. As expected the peak amplitude decreases as Δm_s increases. The solid curve is the expected peak height of equation 5.24.

We have seen that the damping function D decreases rapidly with ω. Therefore, the expected peak in the FT decreases in magnitude as the true mixing frequency increases. To make a successful measurement, the peak must be significantly larger
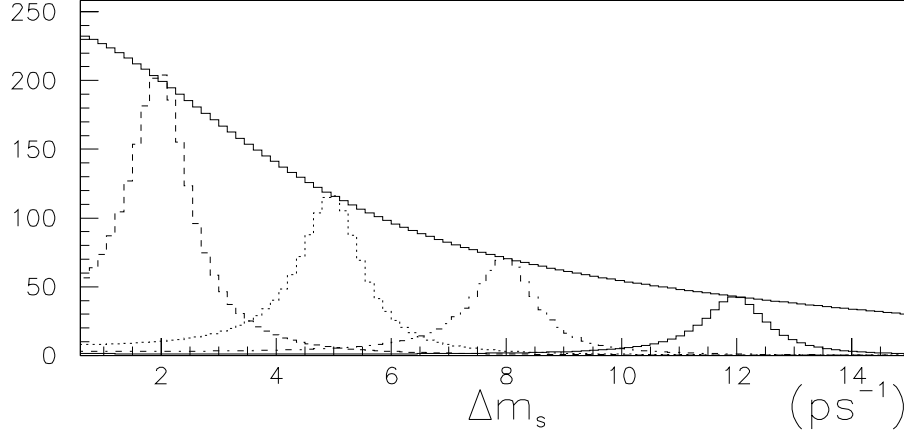
Figure 5.6: The expected FT of the data (equation 5.20) with Δm_s values of 2.0, 5.0, 8.0, and 12.0 ps^{-1} after background subtraction. The solid curve is the expected peak height from equation 5.24.

than the statistical noise which depends only on the total number of events in the data sample,

$$\sigma(FT) = \sqrt{\frac{n}{2}}. \tag{5.25}$$

These fluctuations are expected to be gaussian and independent of frequency. The signal-to-noise ratio is, therefore,

$$S/N = \sqrt{\frac{n}{2}} f_s (1 - 2\eta) \, D(\omega, \sigma_L, \sigma_p). \tag{5.26}$$

This equation can be used to estimate the *sensitivity* of a B_s^0 mixing analysis which is the limit that would be set in 50% of experiments. Since the statistical fluctuations are gaussian, the 95% confidence level sensitivity is given by the frequency where $S/N = 1.645$. The S/N ratio versus Δm_s is plotted in figure 5.7 for the same parameters listed above that simulate this analysis. The expected sensitivity for this analysis, considering statistical uncertainty only, is seen to be ~ 5.0 ps^{-1}.

Returning to the amplitude fit, it can be shown that the amplitude $\mathcal{A}$ is equivalent to a normalized fourier amplitude,

$$\mathcal{A}(\nu) = \frac{d(\nu)}{a(\nu)} = \frac{F(\omega)}{F(\nu)} \frac{\Gamma^2}{\Gamma^2 + (\nu - \omega)^2} \tag{5.27}$$
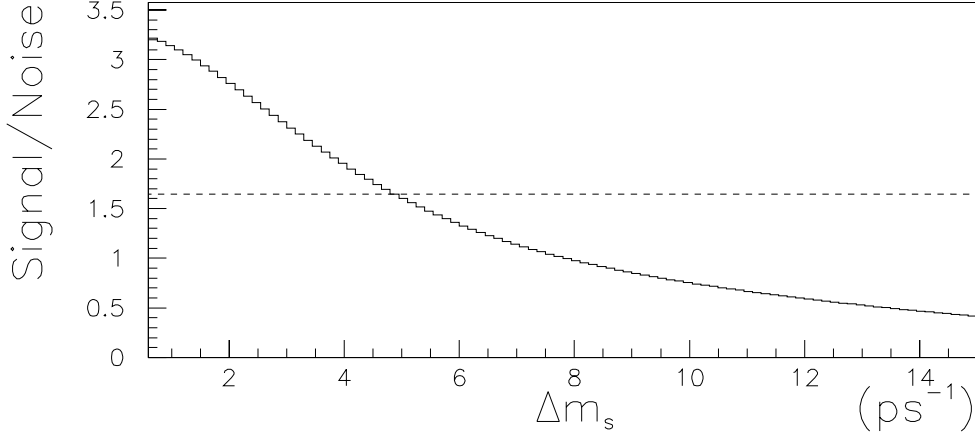
Figure 5.7: The expected signal-to-noise ratio vs Δm_s for an analysis similar to the one presented here.

where $d(\nu)$ represents a fourier transform of the data and $a(\nu)$ is the expected peak amplitude. $F(\nu)$ describes the B_s^0 fraction, mistag and proper time resolution,

$$F(\nu) = f_s(1 - 2\eta)D(\nu, \sigma_L, \sigma_p). \tag{5.28}$$

We see that the expected amplitude distribution retains the Breit-Wigner shape with $\mathcal{A} = 1$ at $\nu = \omega$ where ω is assumed to be the true mixing frequency. For $|\nu - \omega| > 2\Gamma$, $\mathcal{A}$ is expected to be ≈ 0. The statistical uncertainty in $\mathcal{A}$ is,

$$\sigma(\mathcal{A}) = \frac{\sigma_d}{a(\nu)} \tag{5.29}$$

where σ_d is the statistical noise in the FT of the data. Since $a(\nu)$ decreases with frequency due to proper time resolution, we expect the uncertainty in $\mathcal{A}$ to grow as a function of Δm_s.

The likelihood fits for $\mathcal{A}$ are generally well behaved and are nearly parabolic at the minima. The $\pm 1\sigma$ errors , $\sigma_{\mathcal{A}}$, are easily estimated by the $\pm 1/2$ unit of $\log \mathcal{L}$ range about the minimum. If no measurement of Δm_s can be made, a lower limit can be determined by the frequency at which $\mathcal{A} + 1.645\sigma_{\mathcal{A}}$ crosses the $\mathcal{A} = 1$ line. More precisely, we can exclude any value of Δm_s for which $\mathcal{A} + 1.645\sigma_{\mathcal{A}} < 1$. This frequently

involves the exclusion of certain regions in Δm_s due to statistical fluctuations in the measured $\mathcal{A}$. Of course, systematic errors must also be included in the determination of the limit. The intrinsic sensitivity of the experiment is determined by the frequency at which $1.645\sigma_{\mathcal{A}} = 1$.

The amplitude fit procedure has been tested in various ideal cases. Figure 5.8 shows the results of the likelihood and amplitude fits performed on a pure B_s^0 Monte Carlo sample. For this test, perfect proper time reconstruction was assumed as well as perfect initial and final state tagging. Both fits clearly indicate a signal at the MC input Δm_s of 10 ps^{-1}. The amplitude curve reaches a peak at $\mathcal{A} = 1$ while the likelihood shows the expected minimum at this value. The error bars on the amplitude measurements are due to the limited number of events in the fit (~ 5000) and are constant as a function of Δm_s.

It is also interesting to observe the evolution of the amplitude fit as we depart from the ideal case. Figure 5.9 shows the amplitude results for several situations. The fit in figure 5.9(a) was performed again on a pure B_s^0 sample with perfect proper time reconstruction but the initial and final state mistag has been included. The errors on the amplitude measurements are still constant but have increased in magnitude due to the mistag rate, η. Decreasing the B_s^0 fraction would produce a similar result. Note the approximately constant line at $\mathcal{A} \approx 0.1$. This curve is the $1.645\sigma_{\mathcal{A}}$ line which determines the sensitivity of the experiment. With perfect proper time reconstruction, we would obtain infinite sensitivity since our ability to measure $\mathcal{A}$ is independent of frequency. Fit (b) includes mistagging as well as the fully reconstructed proper time for the same set of B_s^0 events. Therefore, the likelihood functions have been smeared as described above and the uncertainty in the amplitude measurement grows as Δm_s increases. As the oscillation period becomes comparable to the proper time resolution, we lose sensitivity to the mixing. The sensitivity curve now increases with Δm_s.

Figure 5.10 shows the -log $\mathcal{L}$ versus amplitude fits for several values of Δm_s from amplitude fit (b) in figure 5.9. The minimum of the -log $\mathcal{L}$ curve is ~ 0 at small values of Δm_s, is consistent with 1 at the MC input value of 10 ps^{-1}, and returns to ~ 0 at larger Δm_s. The width of the minimum steadily increases. The $\pm 1\sigma$ uncertainty is determined by the $\mathcal{A}$ range over which the -log$(\mathcal{L})$ varies by half a unit as shown by
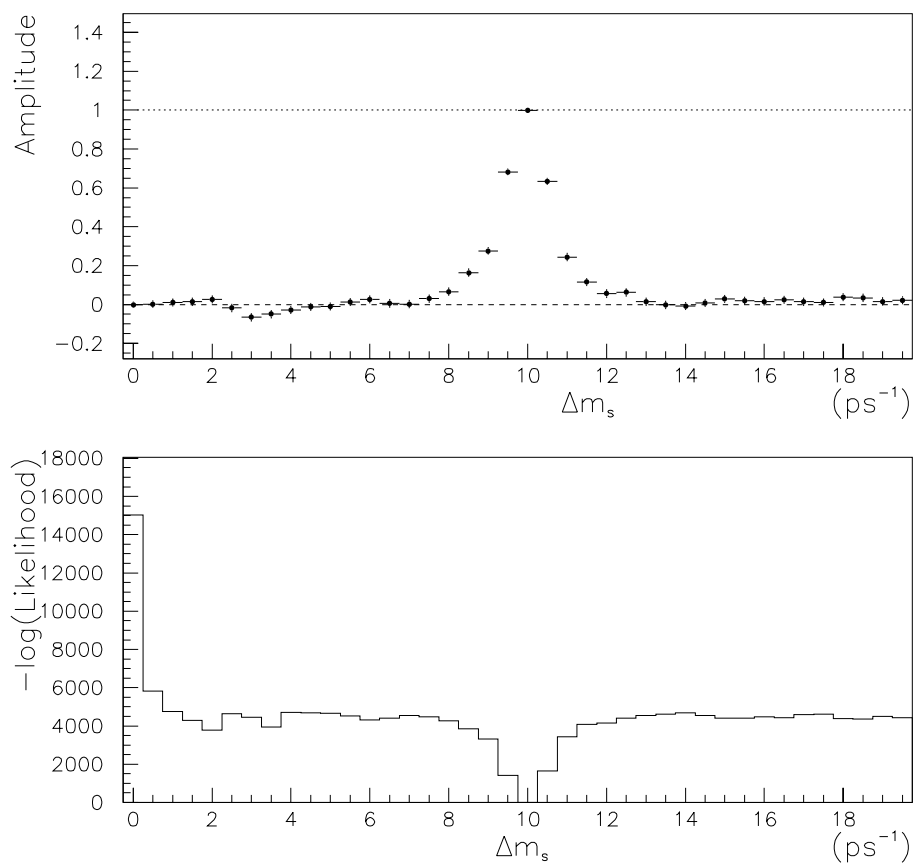
Figure 5.8: The amplitude and likelihood fit results performed on the MC for the ideal case of pure B_s^0 events with perfect proper time reconstruction and perfect intial and final state tags. The MC input Δm_s is 10 ps^{-1}.

the dashed horizontal lines.
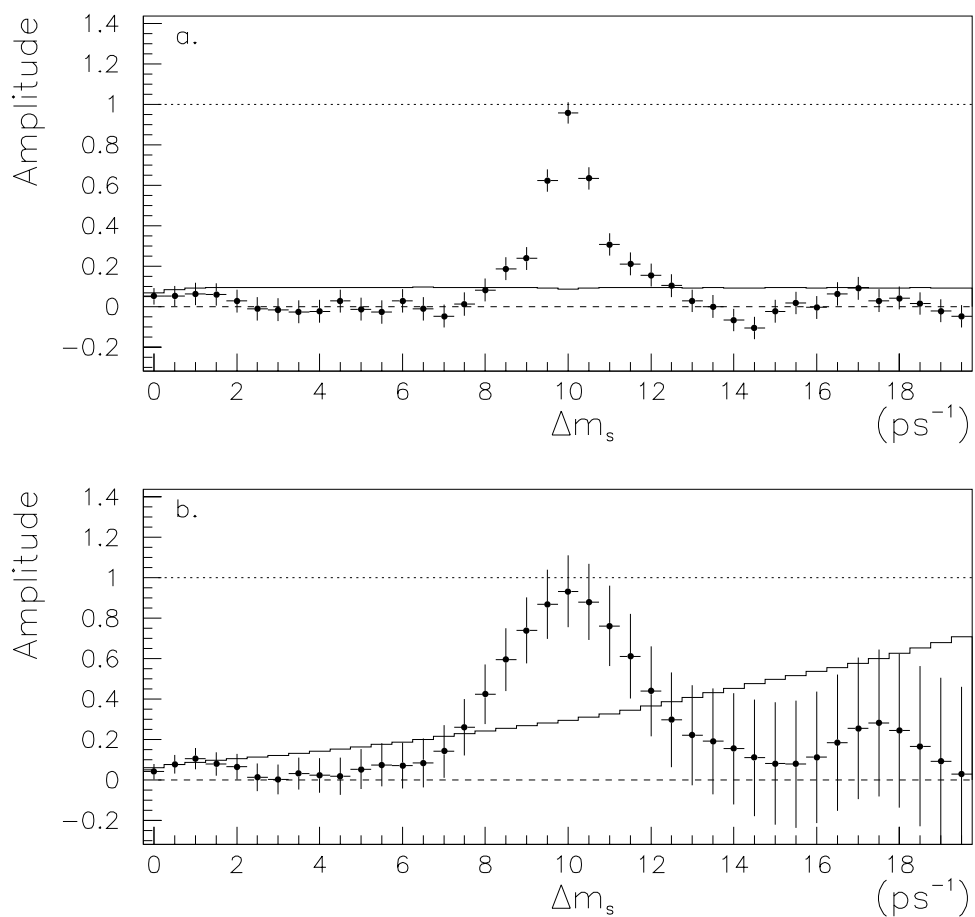
Figure 5.9: Plot (a) shows the amplitude fit performed on a sample of 5000 B_s^0 events with perfect proper time reconstruction but realistic tagging. Plot (b) is the same set of data where realistic proper time reconstruction has been included.
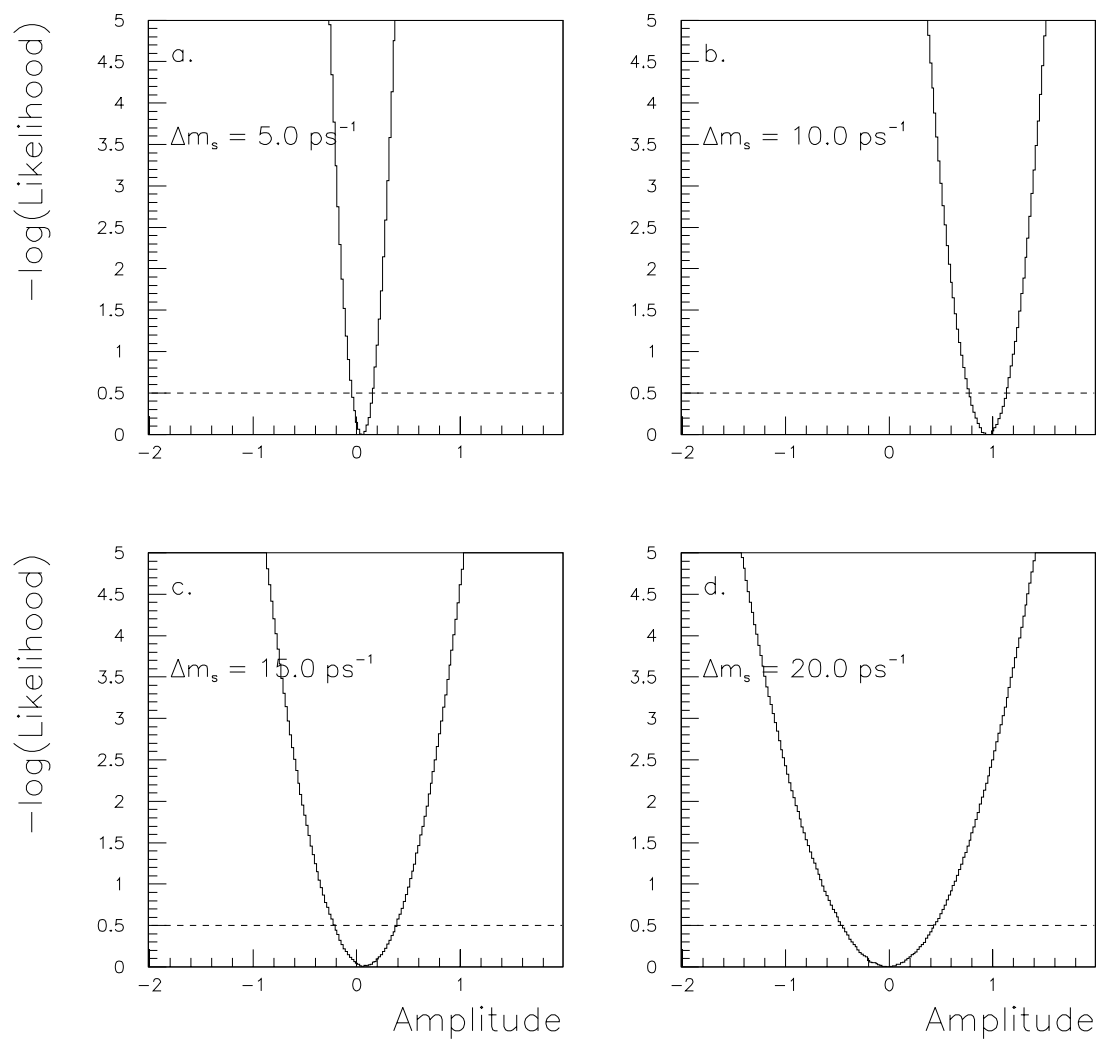
Figure 5.10: The -log $\mathcal{L}$ versus amplitude for $\Delta m_s = 5.0$ (a), 10.0 (b), 15.0 (c) and 20.0 (d) ps^{-1}. The MC input value is 10.0 ps^{-1}.

Chapter 6

Results and Conclusions

In this chapter, the results of the likelihood and amplitude fits will be presented for the $B_s^0 - \bar{B}_s^0$ mixing analysis. The systematic uncertainties that influence the measurement will also be examined. In addition, several consistency checks including a measurement of Δm_d will be presented. Finally, we will conclude by discussing the implications of this measurement on the determination of the CKM matrix.

6.1 $B_s^0 - \bar{B}_s^0$ Mixing Results

Figure 6.1 shows the amplitude versus Δm_s for the inclusive semileptonic analysis using the full 1996-1998 SLD data. From the approximately 400k hadronic events collected by SLD during this period, 9691 semileptonic events were selected. The amplitude errors are statistical only. The solid error curve represents $\mathcal{A} + 1.645\sigma_{\mathcal{A}}$ while the dotted curve represents the sensitivity, $1.645\sigma_{\mathcal{A}}$. A discussion of excluded regions of Δm_s will be postponed until systematic errors have been included. However, we see that the statistical uncertainty produces a sensitivity near 5 ps^{-1} as expected from the discussion in section 5.2. Table 6.1 lists the nominal values of the parameters assumed in the amplitude fit as defined in chapter 5. These input parameters have been adjusted to coincide with current measurements whenever possible. Monte Carlo fits assumed the Monte Carlo input values for the various parameters.

Several checks of the amplitude fit procedure have been performed. First, the

148
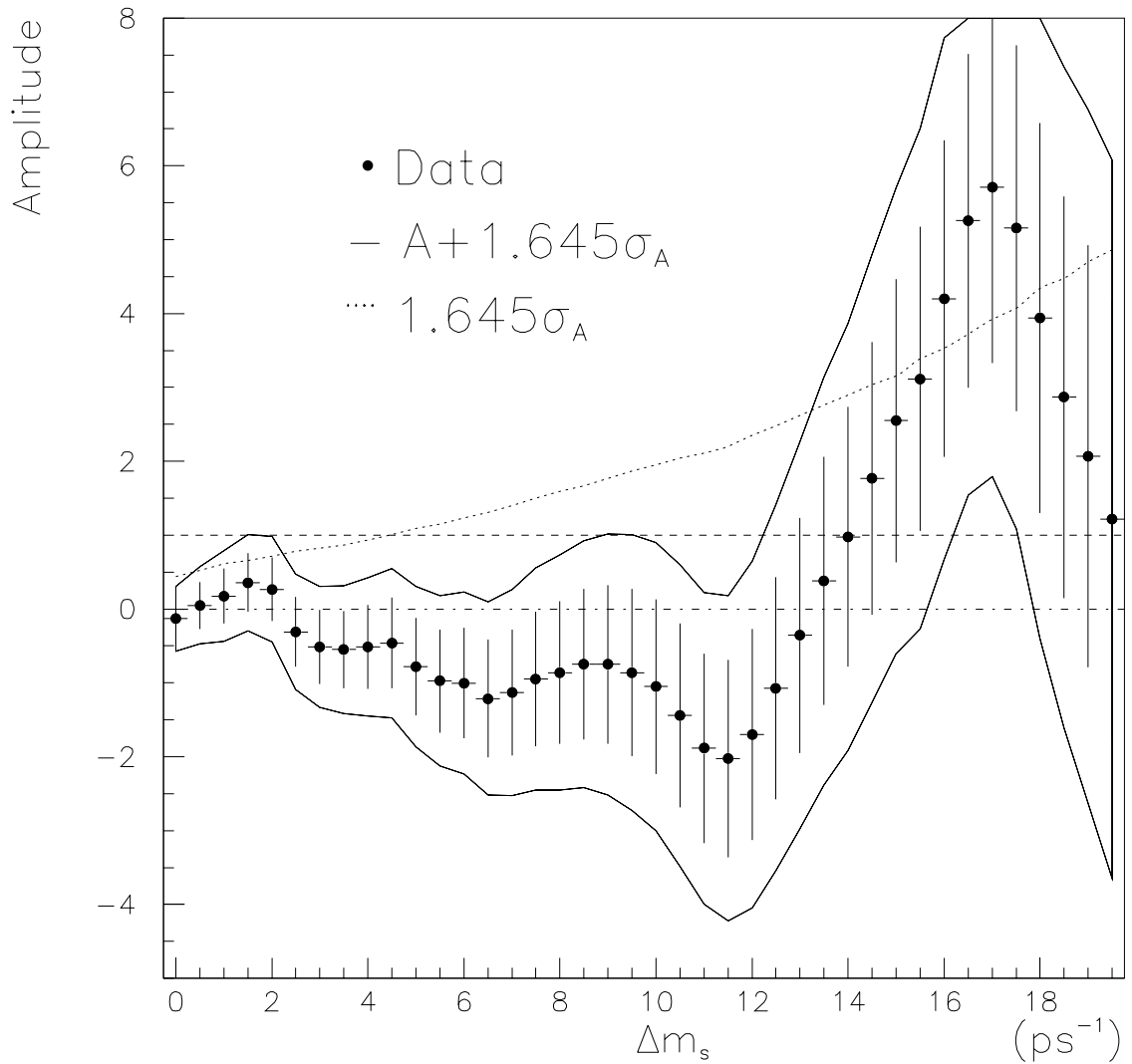
Figure 6.1: Amplitude fit for the full 96-98 SLD data set using the inclusive semileptonic analysis described in this thesis. The error bars are statistical only. The dotted curve is $1.645\sigma_{\mathcal{A}}$ and represents the intrinsic sensitivity of the experiment.

Signal Category	Fraction(%)	Final State Mistag(%)
$B_d^0 \to l^\pm$	31.9	2.1
$B_s^0 \to l^\pm$	8.5	2.2
$B^\pm \to l^\pm$	32.8	1.5
$\Lambda_b \to l^\pm$	7.4	1.8
$B_d^0 \to c \to l^\pm$	8.5	74.7
$B_s^0 \to c \to l^\pm$	2.2	73.9
$B^\pm \to c \to l^\pm$	7.4	67.1
$\Lambda_b \to c \to l^\pm$	1.2	55.5
$c\bar{c}$	4.9	NA
uds+fragmentation	5.8	NA
Parameter	Value	
$\tau(B_d^0)$	1.56 ps	
$\tau(B_s^0)$	1.54 ps	
$\tau(B^\pm)$	1.65 ps	
$\tau(\Lambda_b)$	1.22 ps	
A_b	0.935	
A_e	0.15	
α	0.27	
λ_{uds}	0.50	
λ_{cc}	0.54	
Δm_d	0.477 ps^{-1}	

Table 6.1: Nominal values of the constrained amplitude fit parameters.

amplitude fit was tested on many Monte Carlo samples of similar size as the data with an input $\Delta m_s = 10$ ps^{-1}. Figure 6.2 shows the amplitude plots for the nine $b\bar{b}$ Monte Carlo subsets. The fits demonstrate that for event samples of this size, there is considerable variation in the shape of the amplitude curve and rather large deviations from the physical range (0 to 1) are common. However, the sensitivity curves in the Monte Carlo plots are consistent and agree well with the data. Note that the sensitivity is slightly higher in these fits than in the data due to the lack of $c\bar{c}$ and uds contamination. Furthermore, when the nine fits are averaged we obtain the amplitude curve shown in figure 6.3 (a). The amplitude is consistent with 0 at small Δm_s and increases to 1 at $\Delta m_s = 10$ ps^{-1}, the Monte Carlo input value. So with larger samples, the statistical fluctuations average out as expected. Therefore,

the excursions out of the physical range in the data amplitude does not necessarily indicate a problem with the fit.

We may also check that the fluctuations in the measured amplitudes are consistent with their statistical uncertainty. This test was performed by making a histogram of the measured amplitude divided by the uncertainty, $\mathcal{A}/\sigma_\mathcal{A}$, for each amplitude measurement where we expect $\mathcal{A} \approx 0$ in the nine Monte Carlo fits. Therefore, amplitude measurements in the region $8.0 < \Delta m_s < 12.0$ were omitted. We expect this distribution to approach a unit gaussian centered at 0. Figure 6.3 (b) shows the result. A single gaussian fit yields an average of 0.064 ± 0.061 and width of 1.015 ± 0.051.

Chapter 5 included examples of the amplitude results for various ideal cases such as perfect tags and pure B_s^0 samples. In all cases the amplitude fit performed as expected and was able to identify mixing at the Monte Carlo input value. As we shall see shortly, the likelihood fit has also been applied to $B_d^0 - \bar{B}_d^0$ mixing where we obtain a value of Δm_d consistent with the world average and with the expected uncertainty. Therefore, it appears the statistical behavior of the amplitude fit is well understood.

6.2   Systematic Errors

In addition to the statistical uncertainty on the measured $\mathcal{A}$ values, we must also consider the systematic uncertainties due to physics modelling, detector resolution, and so forth. Most of these effects can be studied simply by varying the input parameters assumed in the amplitude fit within their expected uncertainty. The variation in the measured amplitude, $\mathcal{A}$ and $\sigma_\mathcal{A}$, then determine the systematic error. The systematic error is defined by [80],

$$\sigma_\mathcal{A}^{syst} = \mathcal{A}^{new} - \mathcal{A}^{nom} + (1 - \mathcal{A}^{nom})\frac{\sigma_\mathcal{A}^{new} - \sigma_\mathcal{A}^{nom}}{\sigma_\mathcal{A}^{nom}} \tag{6.1}$$

where $\mathcal{A}^{nom}$ is the measured amplitude using the nominal input parameters and $\mathcal{A}^{new}$ is the amplitude obtained after the variation of a given parameter. The statistical uncertainties, $\sigma_\mathcal{A}^{nom}$ and $\sigma_\mathcal{A}^{new}$, are similarly defined. Note that the systematic error is a function of Δm_s. That is, a systematic error must be calculated for each amplitude
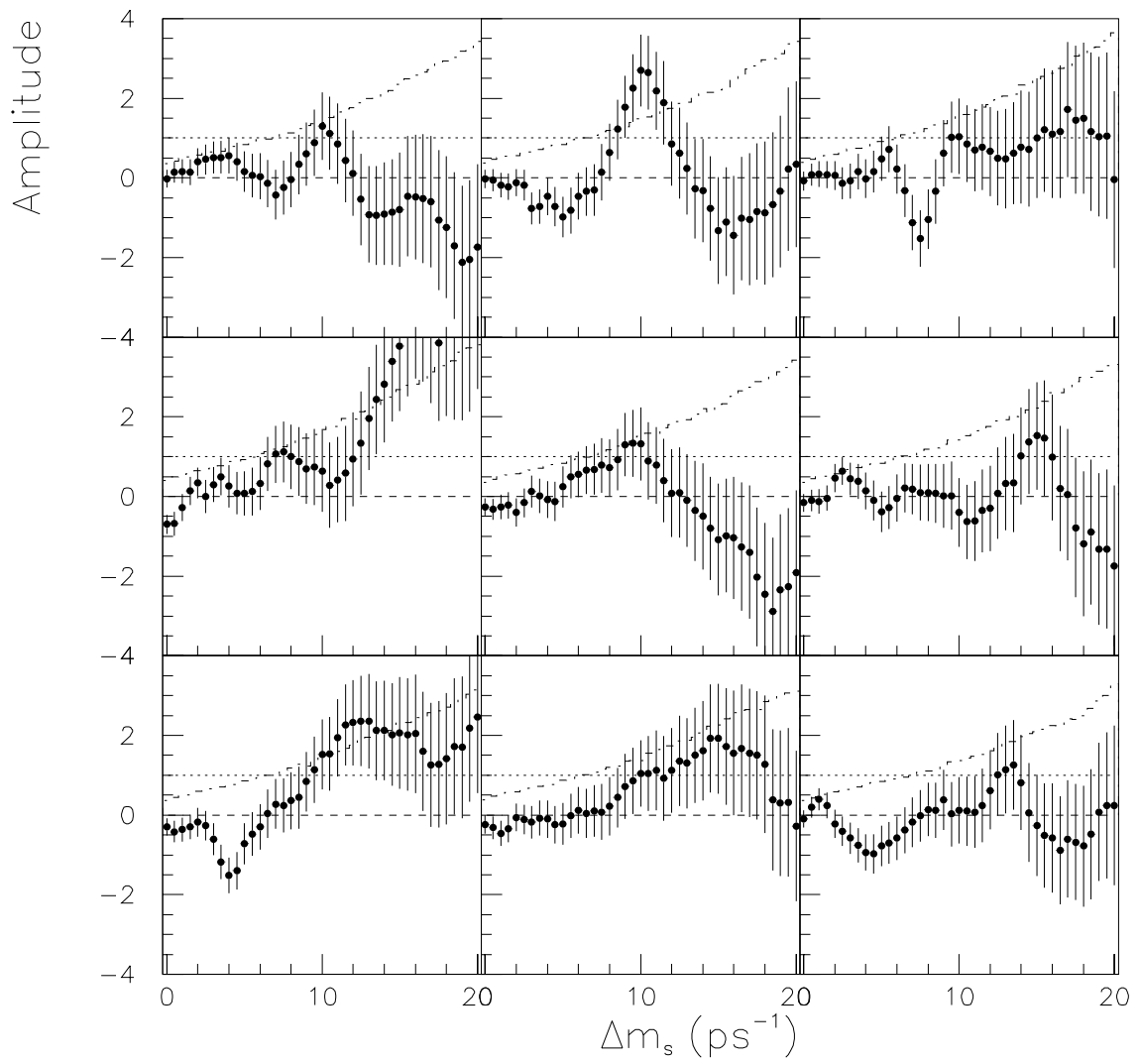
Figure 6.2: The amplitude fit results for nine data size subsamples of $b\bar{b}$ MC.
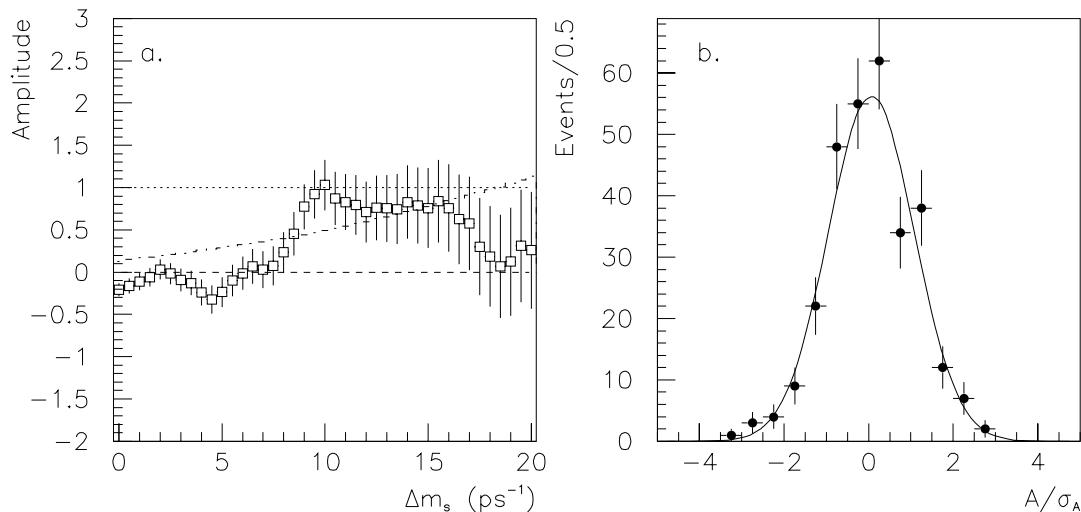
Figure 6.3: Plot (a) is the average of the nine $b\bar{b}$ amplitude fits in figure 6.2. Plot (b) is the $\mathcal{A}/\sigma_{\mathcal{A}}$ distribution of each amplitude measurement of the same nine fits. The region $8.0 < \Delta m_s < 12.0$ where we expect non-zero amplitudes in the MC has been excluded.

measurement. Since we are using the amplitude measurements to set limits, the systematic error depends on both the variation in the measured amplitude itself as well as the change in the statistical uncertainty in the amplitude. A brief explanation of each systematic error considered will be given below.

6.2.1 Sample Composition

The composition of the selected data events is estimated from the Monte Carlo. The resulting fractions, defined in section 5.1.1, are then scaled to match existing measurements before being entered into the amplitude fit. These measurements will be described shortly. The nominal sample fractions assumed by the fit are listed in table 6.1. Systematic errors in the sample composition may be introduced from various sources. First, we must consider the uncertainties in the physics models used to produce the Monte Carlo. The fraction of a given type of decay in the final sample depends on both the production rates of the various B hadrons as well as the B

decay model. Recall that the SLD Monte Carlo is based on the JETSET 7.4 event generator tuned by the CLEO B decay model. Finally, there are the detector issues such as selection bias and mistag rates. Each of these sources of systematic error will be considered independently.

First, we consider the production rates of B hadrons in $Z^0 \to b\bar{b}$ decays. The general procedure is to assume that $f_{B_d^0} + f_{B^+} + f_{B_s^0} + f_{\Lambda_b} = 1$ and that $f_{B_d^0} = f_{B^+}$. Λ_b is used here to represent all b baryons so the first assumption implies that we are neglecting B_c mesons. The second assumption is justified by CLEO measurements of the ratio of $B_d^0 \bar{B}_d^0$ to $B^+ B^-$ decays at the $\Upsilon(4S)$ as well as the near equality of B_d^0 and B^+ masses. Therefore, measurements of $f_{B_s^0} = \mathcal{B}(\bar{b} \to B_s^0)$ and $f_{\Lambda_b} = \mathcal{B}(\bar{b} \to \Lambda_b)$ allow us to solve for the two remaining fractions.

Direct branching ratio measurements have been employed to make estimates of both $f_{B_s^0}$ and f_{Λ_b}. The first consists of a measurement of the combined branching ratio, $\mathcal{B}(\bar{b} \to B_s^0) \cdot \mathcal{B}(B_s^0 \to D_s^- l^+ \nu X)$ [81]. Assuming $SU(3)$ symmetry, $\mathcal{B}(B_s^0 \to D_s^- l^+ \nu X)$ can be estimated from the $B_d^0/B^\pm$ semileptonic branching fractions, the total b semileptonic decay fraction, and b hadron lifetimes. Therefore, $\mathcal{B}(\bar{b} \to B_s^0)$ can be extracted from the combined branching ratio measurement. The result is $f_{B_s^0} = 11.6^{+3.4}_{-2.9}\%$ [32].

The b-baryon production rate has been similarly measured from the product branching ratios $\mathcal{B}(b \to \Lambda_b^0) \cdot \mathcal{B}(\Lambda_b^0 \to \Lambda_c^+ l^- \bar{\nu} X)$ [82] and $\mathcal{B}(b \to \Xi_b) \cdot \mathcal{B}(\Xi_b^- \to \Xi^- l^- \bar{\nu} X)$ [83, 84]. Combining these results with a direct measurement from the number of protons in b events [85] yields $f_{\Lambda_b} = 10.2^{+2.3}_{-2.1}\%$.

A second technique used to measure $f_{B_s^0}$ involves time integrated mixing measurements. The total time integrated fraction of B_d^0 or B_s^0 mesons that decay as mixed is,

$$\chi_{d,s} = \frac{1}{2} \frac{(\Delta m_{d,s} \tau_{B_{d,s}})^2}{(\Delta m_{d,s} \tau_{B_{d,s}})^2 + 1}. \tag{6.2}$$

Current lower limits on Δm_s allow us to set $\chi_s = 1/2$ to a very good approximation. Therefore, the time integrated mixed fraction of a combined b hadron sample is $\bar{\chi} = g_{B_s^0} \chi_s + g_{B_d^0} \chi_d$ where $g_{B_s^0}$ and $g_{B_d^0}$ are the product of the production fractions and semileptonic branching ratios [32]. As before, we assume $f_{B_d^0} = f_{B^\pm}$ and $f_{B_d^0} + f_{B^\pm} +$

b Hadron	Measured Fraction(%)	SLD MC(%)
B^+	$39.5^{+1.3}_{-1.4}$	40.6
B^0_d	$39.5^{+1.3}_{-1.4}$	40.6
B^0_s	10.8 ± 1.4	11.4
Λ_b	$10.2^{+2.3}_{-2.1}$	7.4

Table 6.2: Fractions of weakly decaying B hadron species in $Z^0 \to b\bar{b}$ decays.

$f_{B^0_s} + f_{\Lambda_b} = 1$. Therefore, measurements of $\bar{\chi}$, Δm_d and f_{Λ_b} allow an estimate of $f_{B^0_s}$. A combined LEP and SLD fit yields $\bar{\chi} = 12.14 \pm 0.43\%$ [86]. Assuming the value of $f_{\Lambda_b} = 10.2^{+0.023}_{-0.021}$ discussed above and the world average for Δm_d, the B^0_s fraction is estimated to be $f_{B^0_s} = 10.6 \pm 1.6\%$. The results from direct branching ratio measurements and mixing measurements can be combined to give $f_{B^0_s} = 10.8 \pm 1.4\%$. These results are summarized in table 6.2 along with the SLD Monte Carlo values.

Since we are selecting semileptonic events, it is also important to consider the b semileptonic decay model. The SLD Monte Carlo assumes semileptonic decay rates of 11.0% for B^0_d, B^0_s and B^+ and 10.5% for Λ_b which gives a weighted average of 10.96% for all b hadrons. The latest measurements suggest $\mathcal{B}(b \to l^- \bar{\nu} X) = 10.45 \pm 0.21\%$ [1] for an equal mixture of B^0_d and B^+ at the $\Upsilon(4S)$. For a mixture of b hadrons including B^0_s and Λ_b as well, the current world average is, $\mathcal{B}(b \to l^- \bar{\nu} X) = 10.99 \pm 0.23\%$ [1]. These measurements suggest similar semileptonic branching ratios for the different B species. Furthermore, the uncertainties are much smaller than those for the B production fractions. The relevant uncertainty for this analysis is the uncertainty on the product of the production fraction and the semileptonic decay rate for each B species relative to the others. This will determine the fraction of a given type of decay in our final sample. Therefore, as systematic errors we have varied $f_{B^0_s} = 10.8 \pm 1.5\%$ and $f_{\Lambda_b} = 10.2 \pm 2.5\%$. Variation of the B^0_d and $B^{\pm}$ branching ratios would have essentially the same effect as varying the B^0_s fraction due to the similar lifetimes and masses. Only the relative amount of B^0_s is important so the B^0_d and $B^{\pm}$ fractions were not varied independently.

Another important consideration is the number of lepton candidates produced directly in B decays versus those from cascade charm decays. The cascade charm decays exhibit a different reconstructed proper time distribution and mistag rate. Two

sources of cascade charm have been considered. The first, $b \to c \to l^+$ refers to leptons produced in the decay of the charm quark which remains after the b quark emits a W^-. This lepton carries the wrong tagging information. However, the W^- emitted by the b quark may form a charmed hadron containing a $\bar{c}$ quark. A semileptonic decay of this charmed hadron produces a l^- which carries the correct tagging information. This process is referred to as $b \to \bar{c} \to l^-$. Uncertainty in the relative amounts of leptons produced from these three sources can introduce systematic errors. The Monte Carlo branching ratios are in good agreement with current measurements. Therefore, the fractions obtained from the Monte Carlo were varied in accordance with $\mathcal{B}(b \to l) = 0.1112 \pm 0.0025$, $\mathcal{B}(b \to c \to l) = 0.080 \pm 0.004$, and $\mathcal{B}(b \to \bar{c} \to l) = 0.016 \pm 0.004$ [86].

Finally, we must consider the background contamination from $c\bar{c}$ and uds events. Section 4.7.4 described how the majority of this background is removed by placing cuts on the topological vertex mass and the number of significant tracks. The remaining background fractions are determined from the Monte Carlo to be $f_{c\bar{c}} = 5.7\%$ and $f_{uds} = 1.8\%$. To estimate the uncertainty in these fractions, histograms of the reconstructed proper time in the Monte Carlo and data were compared. The $c\bar{c}$ and uds events are concentrated at small proper times so that these histograms are sensitive to the background fractions. A χ^2 fit was performed comparing the shapes of these histograms as the normalization of the $c\bar{c}$ and uds components was varied in the Monte Carlo. We found that a 1 σ variation was obtained when the background fractions were varied by $\pm 20\%$.

6.2.2 b Hadron Lifetimes

In the section above, we discussed the composition of the data sample. The fractions that were considered refer to the total time integrated fractions of a given decay mode in our sample. Since we are performing a time dependent analyses, however, we must also consider the b hadron lifetimes. The time integrated fractions combined with the lifetimes determine the relative fraction of a given decay mode that we expect to observe as a function of proper time. In other words, the lifetimes determine the time

Parameter	Nominal $\pm$ range
B_d^0 lifetime	1.56 ± 0.04 ps
$B^{\pm}$ lifetime	1.65 ± 0.04 ps
B_s^0 lifetime	1.54 ± 0.07 ps
b baryon lifetime	1.22 ± 0.05 ps

Table 6.3: B hadron lifetimes.

evolution of the sample.

The naive spectator model predicts that b quarks decay independently of the other quarks in the B hadron and thus predicts $\tau(B^+) = \tau(B_d^0) = \tau(B_s^0) = \tau(\Lambda_b)$. However, we know that strong interactions within the hadron can play an important role. In the D meson system, for example, we observe lifetime differences that follow the pattern $\tau(D^+) \sim 2.3\tau(D_s) \sim 2.5\tau(D^0) \sim 5\tau(\Lambda_c^+)$. We expect these lifetime differences to scale with the mass of the heavy quark as $(1/m_q)^2$ so that lifetime differences on the order of 10-20% are expected among the B hadrons [13, 87].

Recent measurements suggest somewhat larger lifetime differences than expected. The current world averages are $\tau(B_d) = 1.56 \pm 0.04$ ps, $\tau(B_s) = 1.54 \pm 0.07$ ps, $\tau(B^{\pm}) = 1.65 \pm 0.04$ ps, and $\tau(\Lambda_b) = 1.22 \pm 0.05$ ps [32]. Table 6.3 lists the nominal B hadron lifetimes assumed in the amplitude fit and the uncertainty used to determine the systematic error.

6.2.3 $B_d^0 - \bar{B}_d^0$ Mixing

$B_d^0 - \bar{B}_d^0$ mixing can affect the amplitude fit if it is not well simulated by the likelihood functions. Recall that the amplitude fit minimizes the $-\log \mathcal{L}$ versus $\mathcal{A}$ for various values of Δm_s to form a frequency spectrum of the data. While scanning Δm_s near Δm_d it is possible to see some interference. We expect mixing in this region and the effect has, hopefully, been accounted for in the B_d^0 terms of the likelihood functions. If B_d^0 mixing is not well simulated, however, the amplitude will take on nonzero values in an attempt to correct the discrepancy. Fortunately, this effect should only be significant near Δm_d and, therefore, should not effect our ability to place a limit on Δm_s. The likelihood fits assume the current world average of $\Delta m_d = 0.477 \pm 0.02$ ps^{-1}

[32].

6.2.4   Proper Time Resolution

The proper time resolution determines the rate at which the uncertainty on the individual amplitude measurements grow as a function of Δm_s. Therefore, resolution is one of the major factors that determines the sensitivity of the experiment. In this analysis, the proper time resolution is estimated on an event-by-event basis. As described in chapter 5, separate estimates of the decay length and boost resolutions are combined into an estimate of the proper time resolution. This procedure was checked in the Monte Carlo where we found that the calculated resolution function describes the Monte Carlo very well. Figure 5.4 shows the excellent agreement between the resolution function and the proper time residuals in bins of true proper time. Therefore, we must determine the magnitude of any possible discrepancies between data and Monte Carlo detector resolution. Recall from chapter 3 that after standard SLD Monte Carlo production several corrections to the charged particle tracking were necessary to make the MC match the data. We apply additional impact parameter smearing as well as a tracking efficiency correction where a small percentage of MC tracks are tossed out. Both of these corrections suggest that the detector resolution in the data is slightly degraded with respect to the MC. Furthermore, these corrections express the extent to which we do not understand the tracking system.

To determine the decay length resolution uncertainty, the analysis was run on the MC without the above corrections. As expected, the decay length resolution improves. Based on double gaussian fits to the decay length residuals, the core width decreases by $\sim 6\%$ while the tail width decreases by $\sim 2\%$. To be conservative, the decay length resolution was varied by $\pm 7.5\%$ in the amplitude fit as a systematic error.

Applying the same procedure as described above, the boost resolution was found to improve by $\sim 3\%$ in both the core and tail width when tracking corrections are turned off. Therefore, the boost resolution is less sensitive than the decay length to the tracking corrections. This is expected since the boost calculation also involves

calorimetry. Recall from section 4.7.2 that the calorimetry component of the boost reconstruction involves measuring the amount of unassociated cluster energy in the EM calorimeter. Comparing the data with the $q\bar{q}$ MC we find that the average neutral EM energy reconstructed in the data is about 7.6 GeV as compared to 8.6 GeV in the MC. This represents a $\approx 15\%$ discrepancy. However, the average reconstructed B energy is about 31 GeV so the calorimetry component is responsible for about 20%. Therefore, we take the systematic uncertainty in the average B energy due to calorimetry to be 3%. Combining this in quadrature with the 3% uncertainty due to tracking we obtain a total uncertainty of 4%. The assumed boost resolution in the likelihood fit was thus varied by 5% as a systematic error.

6.2.5   Initial State Tag Purity

The total initial state tag incorporates three main components: the polarization tag, opposite hemisphere jet charge, and opposite hemisphere topological tags. These components are combined to form the initial state b quark probability, P_b. Systematic errors may be introduced by an inaccurate assessment of the correct tag probability.

Recall that the b quark probability from polarization is calculated as,

$$P_b^{\mathrm{pol}} = \frac{1}{2}(1 + \tilde{A}_{FB}^b) \tag{6.3}$$

where

$$\tilde{A}_{FB}^b = 2A_b \left(\frac{A_e - P_e}{1 - A_e P_e} \right) \left(\frac{\cos\theta}{1 + \cos^2\theta} \right). \tag{6.4}$$

The calculation of P_b^{pol} thus depends on A_b, A_e, P_e and $\cos\theta$. The parameter A_e has been accurately measured but there is considerably more uncertainty in A_b. Furthermore, $\tilde{A}_{FB}^b$ does not depend strongly on A_e. Therefore, we use $A_e = 0.150$ and the uncertainty is neglected. The thrust axis is used to estimate $\cos\theta$, the initial directions of the $b\bar{b}$ quark pair. Monte Carlo estimates indicate a resolution of about 35 mrad on the angle θ. Technically, the equation for $\tilde{A}_{FB}^b$ should be smeared by this amount. This effect was found to be negligible. Therefore, the main sources of systematic uncertainty in the polarization tag is the measured polarization and A_b.

The luminosity weighted polarization results were listed in table 2.1. The uncertainties are 0.5% for 1996 and 0.8% for 1997-98 and are purely systematic [46]. In the mixing analysis, we use the polarization measurement on an event-by-event basis. A single polarization measurement takes about 3 minutes and corresponds to about 3000 Compton interactions resulting in a statistical error of about 2%. However, the polarization measurement is uncorrelated with the rest of the analysis such as proper time reconstruction and final state tagging. Therefore, the critical parameter is luminosity weighted polarization. To be conservative, the magnitude of the polarization is varied by $\pm 1\%$ to evaluate the systematic uncertainty. This variation induces a change of 0.75% in the average correct tag probability from polarization alone and 0.26% for the combined initial state tag.

The SM value of A_b is derived from the expression $A_b = 2a_b v_b/(a_b^2 + v_b^2)$ where a_b and v_b are defined in table 1.3 in terms of $\sin^2 \theta_w$. The current measured value of $\sin^2 \theta_w$ yields $A_b = 0.9347 \pm 0.0001(-0.0002)$ [1]. A_b has also been directly measured at LEP and SLD [88]. The four LEP experiments measure the forward-backward asymmetry of the b quark which is proportional to $A_e A_b$. A_b is then extracted by assuming the LEP average $A_e = 0.1469 \pm 0.0027$. The result is $A_b = 0.899 \pm 0.025$. At SLD, the polarized electron beam allows us to measure the polarized forward-backward asymmetry of the b quark which removes the dependence on A_e. Therefore, A_b can be measured directly. The SLD average is $A_b = 0.867 \pm 0.035$ which gives a combined LEP/SLD average of $A_b = 0.881 \pm 0.018$. These results include measurements up to ICHEP 1998. The LEP and SLD averages are in very good agreement but their combination differs from the SM value by 3σ. If the SM value is correct, this discrepancy is either a statistical fluctuation or a systematic error in the direct measurements. Alternatively, the discrepancy is an indication of new physics and $A_b \sim 0.88$. In either case, we can be confident A_b is not significantly above the SM value. In this analysis, we assume the SM value for A_b and allow a negative variation of 0.04 as a systematic error. Note that decreasing A_b dilutes the initial state tag. Therefore, the negative variation will increase the uncertainty on our amplitude measurements which is the relevant variation for setting a limit on Δm_s. The decrease in A_b represents a 2.14% decrease in the average correct tag probability calculated from polarization alone. For

the combined initial state tag, the correct tag probability drops by 0.76%.

The purity of the jet charge tag is indicated by the parameter α in equation 4.31. In this analysis we have used $\alpha = 0.27$ which was deduced from the Monte Carlo. The jet charge technique has also been used at SLD to measure A_b. This analysis utilizes a self-calibration technique that is able to extract α from the data [89]. The resulting uncertainty on α is due to the data statistics. The result for the 1997-98 data was $\alpha = 0.2879 \pm 0.0081$ [90] which is a relative uncertainty of 2.8%. The parameter α was varied by 3% to evaluate our systematic error. This variation represents an uncertainty in the correct tag probability of about 1.1% for jet charge alone and 0.39% for the combined initial state tag.

Combining the above effects in quadrature, we obtain an uncertainty of about 0.9% on the combined correct tag probability due to uncertainties in the polarization and jet charge components. The uncertainty due to the inclusion of the topological tags has not been evaluated. However, these tags form a small contribution to the total combined tag and we have conservatively allowed a 2% variation on the correct tag probability.

6.2.6   Lepton Misidentification

After event selection, the Monte Carlo suggests that the fraction of lepton candidates that have been misidentified is about 5.5% as shown in table 4.2. The misidentified leptons are mostly $\pi^{\pm}$ and $K^{\pm}$. They are produced in roughly equal amounts from B decays, cascade charm decays and fragmentation. When these tracks are produced in B decays, the statistical method used here to determine the B decay length should still provide reasonable results. The main effect of the misid is on the final state mistag rate. But assuming the misidentified leptons are randomly charged, the final state tag should still be about 50% correct. Given the small fraction of misidentified leptons, even large uncertainties in the misid rate will produce fairly minor changes in the final state mistag rate. Therefore, we expect lepton misid systematics to be small.

Both the muon and electron misidentification levels have been checked with $\pi^{\pm}$s

produced in K_s^0 decays in the data. There is good agreement between data and Monte Carlo. The uncertainty level is estimated from data statistics to be $\sim$ 10-15% for the 1996-98 data. Therefore, the misid rate was varied by $\pm 15\%$ as a systematic error.

The systematic errors are listed in table 6.4 at Δm_s = 2.0, 5.0, and 10.0 ps^{-1}. The total statistical and systematic errors are listed as well as the individual systematic sources. Figures 6.4 and 6.5 show the individual systematic uncertainties versus Δm_s. The solid curves correspond to the positive variation of the parameter while the dotted curves correspond to the negative variation. The largest systematic uncertainty is due to the B_s^0 production fraction. The uds and $c\bar{c}$ fractions also make a considerable contribution. These backgrounds are concentrated at small proper times where we are most sensitive to mixing. The decay length and boost resolution systematics become important at large values of Δm_s as expected.

Figure 6.6 shows the amplitude versus Δm_s for the full 1996-98 data including systematic errors. The vertical error bars are statistical only. The two solid error curves represent $\mathcal{A} + 1.645\sigma_\mathcal{A}$ with and without the systematic errors. The dotted curve is $1.645\sigma_\mathcal{A}$ and represents the expected sensitivity. The sensitivity, including systematic uncertainty, is found to be 3.8 ps^{-1}. The increase in the total systematic error at small Δm_s is the result of interference with $B_d^0 - \bar{B}_d^0$ mixing.

6.3   Setting a Limit on Δm_s

The amplitude fit consists of measured values of the amplitude and its uncertainty $(\mathcal{A}_m, \sigma_{\mathcal{A}_m})$ as a function of frequency. The probability density of the amplitude at a given Δm_s is represented by $G(\mathcal{A}, \mathcal{A}_m, \sigma_{\mathcal{A}_m})$, a single gaussian centered at $\mathcal{A}_m$ with width $\sigma_{\mathcal{A}_m}$. As described in chapter 5, we expect the amplitude to be consistent with 1 at the true value of Δm_s and 0 far from the true value . Therefore, a given value of Δm_s can be excluded at 95% CL if [36],

$$\int_1^\infty G(\mathcal{A}, \mathcal{A}_m, \sigma_{\mathcal{A}_m}) d\mathcal{A} < 5\%. \tag{6.5}$$

Equivalently, Δm_s is excluded at 95% CL if

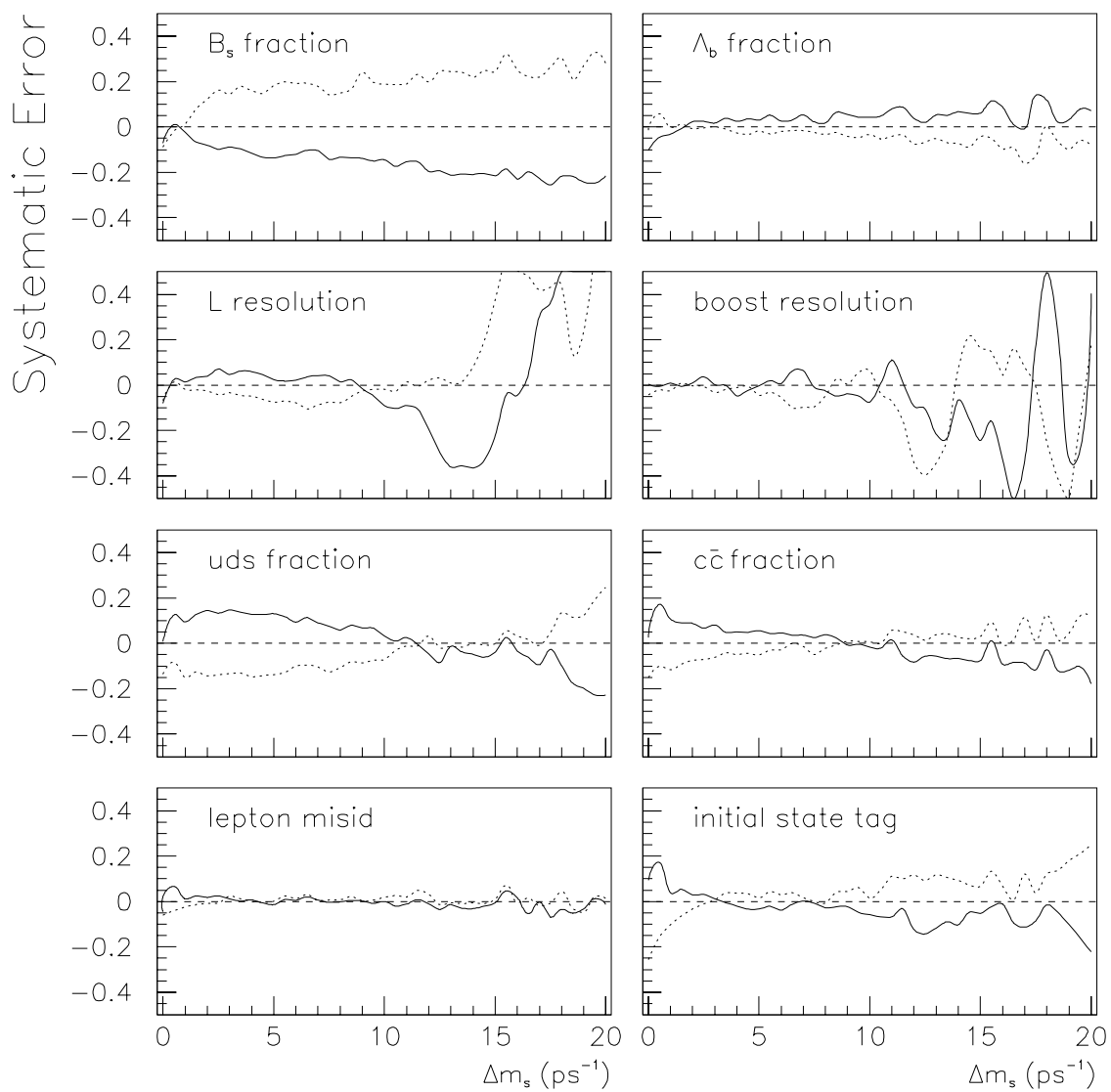$$\mathcal{A}_m + 1.645\sigma_{\mathcal{A}_m} < 1. \tag{6.6}$$

Figure 6.4: Systematic errors due to B production fractions, proper time resolution, background fractions and mistag.
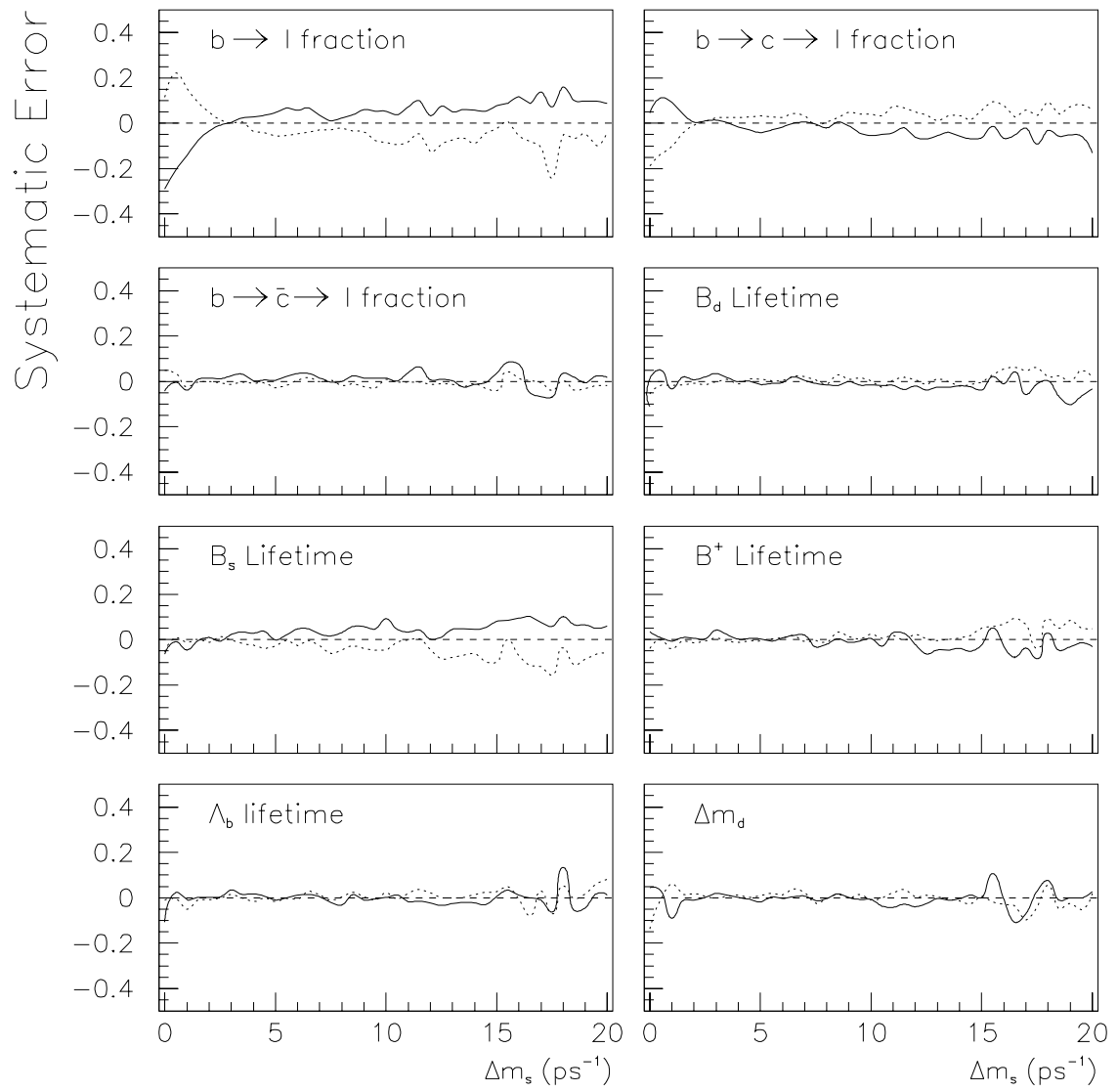
Figure 6.5: Systematic errors due to B decay branching ratios, lifetimes, and Δm_d.

Δm_s	2 ps^{-1}	5 ps^{-1}	10 ps^{-1}
Measured Amplitude $\mathcal{A}$	0.267	-0.780	-1.052
$\sigma_{\mathcal{A}}^{stat}$	0.433	0.660	1.185
$\sigma_{\mathcal{A}}^{syst}$	+0.224	+0.243	+0.240
	−0.190	−0.239	−0.239
$f_s = \mathcal{B}(b \to B_s^0)$	−0.081	−0.137	−0.145
	0.122	0.182	0.189
$f_\Lambda = \mathcal{B}(b \to b - baryon)$	0.023	0.030	0.043
	−0.008	−0.017	−0.033
uds fraction	0.145	0.131	0.032
	−0.142	−0.138	−0.071
$c\bar{c}$ fraction	0.088	0.056	−0.017
	−0.075	−0.051	0.008
decay length resolution	0.038	0.024	−0.090
	−0.025	−0.075	−0.018
boost resolution	0.009	−0.003	−0.074
	−0.002	−0.045	0.064
τ_{B_d}	0.007	−0.014	−0.015
	−0.008	0.009	0.003
τ_{B_s}	0.010	−0.001	0.092
	−0.012	−0.028	−0.044
$\tau_{B^\pm}$	0.006	0.004	0.005
	−0.014	−0.005	0.023
τ_Λ	0.003	−0.010	0.001
	−0.009	−0.016	0.022
Δm_d	−0.011	−0.019	−0.008
	0.019	0.009	−0.009
$\mathcal{B}(b \to l)$	−0.034	0.047	0.053
	0.048	−0.057	−0.084
$\mathcal{B}(b \to c \to l)$	0.005	−0.041	−0.054
	−0.009	0.032	0.041
$\mathcal{B}(b \to \bar{c} \to l)$	0.015	0.006	0.014
	−0.001	−0.027	0.008
lepton misidentification	0.018	−0.014	0.000
	−0.007	0.001	0.019

Table 6.4: Measured values of the amplitude $\mathcal{A}$ and it's statistical and systematic uncertainties at three values of Δm_s.
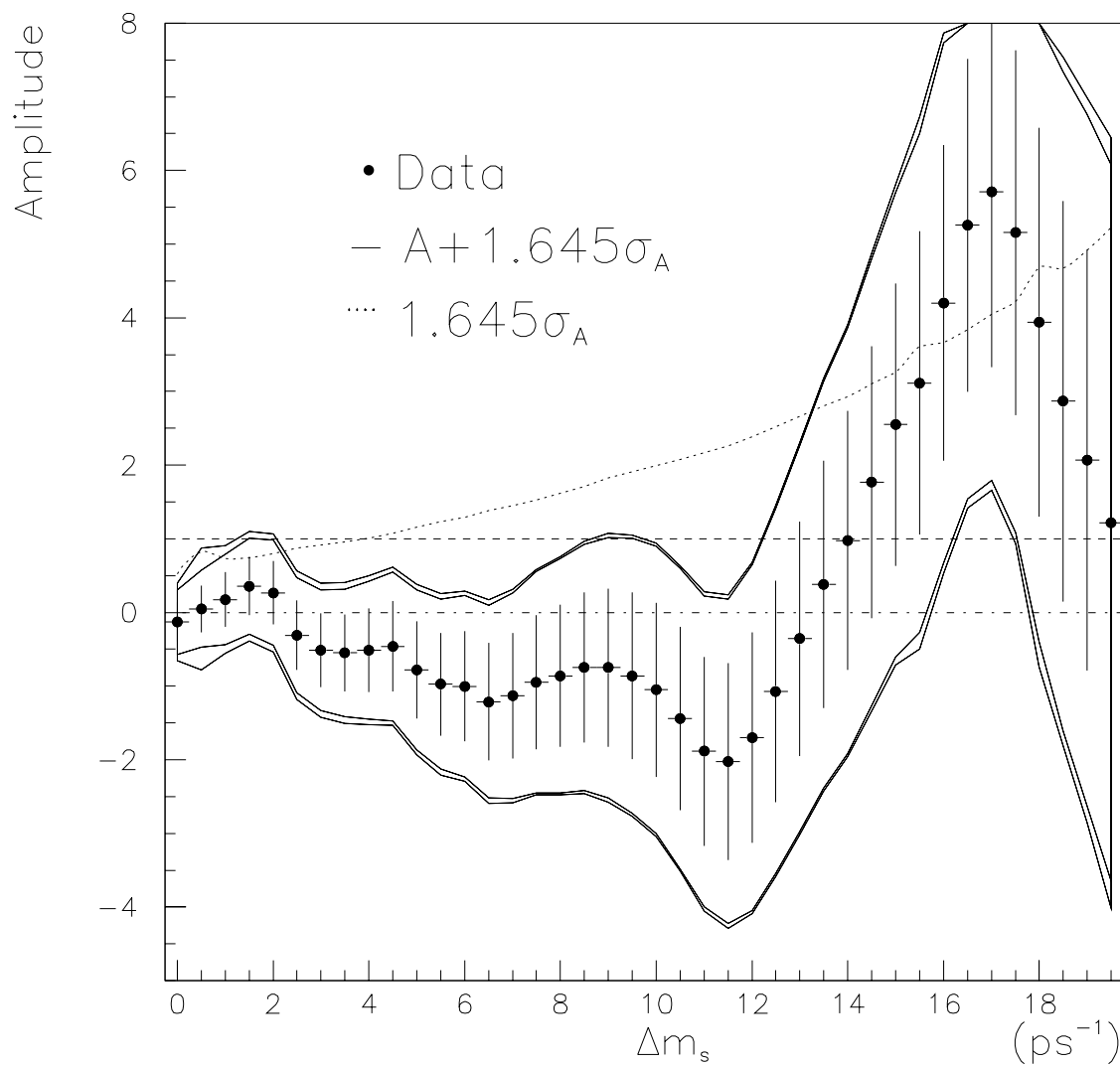
Figure 6.6: Amplitude fit for the full 96-98 SLD data set from the inclusive semileptonic analysis including systematic errors. The solid curves are $\mathcal{A} + 1.645\sigma_{\mathcal{A}}$ (stat) and $\mathcal{A} + 1.645\sigma_{\mathcal{A}}$ (stat+sys). The dotted curve is $1.645\sigma_{\mathcal{A}}$ (stat+sys) which represents the intrinsic sensitivity of the experiment.

This is the standard method for determining the excluded region of Δm_s. It is the true single-sided 95% CL in which we expect the true value of Δm_s to be excluded in 5% of equivalent experiments. Applying this technique to the results in figure 6.6, we conclude that three regions may be excluded at 95% CL:

$$\Delta m_s \quad < 1.3 \text{ ps}^{-1},$$
$$2.0 < \quad \Delta m_s \quad < 8.6 \text{ ps}^{-1}, \text{ and}$$
$$9.8 < \quad \Delta m_s \quad < 12.2 \text{ ps}^{-1}.$$

The technique described above often allows the exclusion of relatively large values of Δm_s due to 'lucky' negative fluctuations in the measured amplitude. This is certainly true for our data. For this reason, amplitude fit results are sometimes presented using a more conservative technique where the effects of negative fluctuations are removed by renormalizing the probability distributions. The motivation is that negative amplitudes are 'unphysical' and may produce artificially high limits. Therefore, it is instructive to consider the origin of negative amplitudes. In a standard Fourier analysis there are no negative Fourier amplitudes. This is because the Fourier transform allows an additional phase degree of freedom that accounts for the relative phases of the signal frequency components. In the amplitude fit, however, the phase is fixed. The likelihood equations assume that the mixed fraction will vary as $1/2(1 - \cos \Delta mt)$. At $t = 0$, the mixed fraction is required to be 0 and increasing. If statistical fluctuations or biases in the proper time reconstruction result in an apparent oscillation out of phase with what is expected, the amplitude can become negative. Therefore, we conclude that negative amplitudes are acceptable and physically significant when reasonably consistent with statistical fluctuations.

The probability of excluding a given value of Δm_s at 95% CL based on the measured sensitivity (and assuming the expected value of $\mathcal{A}$ is 0 at that frequency) is given by the *exclusion probability*. It is defined as,

$$\mathcal{P}_{\text{limit}} = 1 - \int_{1-1.645\sigma_\mathcal{A}}^{\infty} G(\mathcal{A}, 0, \sigma_\mathcal{A}) d\mathcal{A} \tag{6.7}$$

The exclusion probability for our data is plotted in figure 6.7. We see that the probability for an experiment with our sensitivity to exclude Δm_s of 12.0 ps^{-1} is
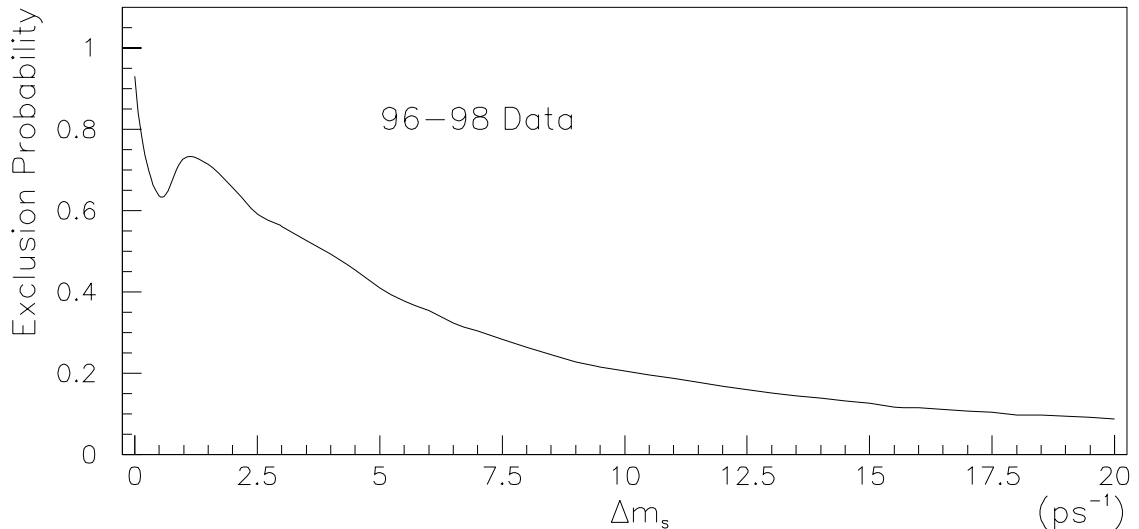
Figure 6.7: The probability to exclude a given value of Δm_s at 95% CL due to statistical fluctuations in the data assuming mixing does not occur at that frequency.

about 15%. Therefore, the excluded regions in the data are reasonably likely assuming gaussian fluctuations of the measured amplitudes.

6.4 $B_d^0 - \bar{B}_d^0$ Mixing

B_d^0 mixing provides an ideal check of the B_s^0 mixing results. First, the data analysis is essentially identical. The only difference comes in the likelihood fit where we have fixed Δm_s and minimized the $-\log(\mathcal{L})$ with respect to Δm_d. We have set Δm_s at 15 ps^{-1}, above the currently excluded region. Furthermore, the B_d^0 branching ratio is much larger than B_s^0 and the oscillation frequency is slower so that Δm_d has now been measured to within $\sim 4\%$. Therefore, we have a well measured calibration point which is within our sensitivity.

The likelihood fit results are shown in figure 6.8. Figure 6.8(a) shows the mixed fraction versus reconstructed proper time. The points are the full 1996-98 data set. An event is tagged as mixed if the initial and final state tags disagree. That is, $P_b > (<) 0.5$ and $Q_{lep} = +1(-1)$ indicates a mixed event. The solid curve is the
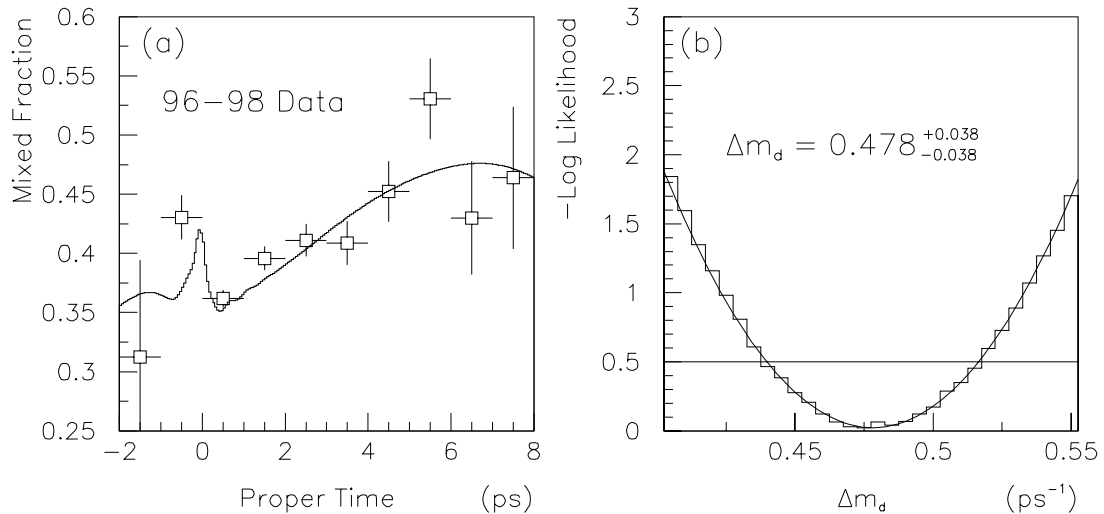
Figure 6.8: Plot (a) shows the mixed fraction versus proper time for the full 1996-98 data set. The solid curve is the expected mixed fraction from the likelihood equations assuming the best fit value for Δm_d and $\Delta m_s = 15$ ps^{-1}. Plot (b) shows the $-\log \mathcal{L}$ versus Δm_d.

calculated mixed fraction versus proper time from the likelihood equations with the best fit value of Δm_d and $\Delta m_s = 15$ ps^{-1}. The negative proper time is the result of negative decay lengths where the B vertex was reconstructed behind the IP with respect to the vertex momentum. The peak at $t \approx 0$ ps is due to the contamination of $c\bar{c}$ and uds backgrounds in this region. These backgrounds tend to be tagged equally mixed or unmixed. Figure 6.8(b) shows the $-\log \mathcal{L}$ versus Δm_d. The minimum was fit to a second order polynomial to determine the central value and uncertainty. The 1 σ statistical uncertainty is given by the Δm_d range over which the $-\log(\mathcal{L})$ varies by 1/2 a unit relative to the minimum. The result is,

$$\Delta m_d = 0.478 \pm 0.038 \text{ ps}^{-1} \text{ (stat)}. \qquad (6.8)$$

This result is in very good agreement with the current world average [32], $\Delta m_d = 0.477 \pm 0.018$ ps^{-1}. It also agrees with the previous B_d^0 result produced with a similar analysis on the 1993-95 SLD data [75], $\Delta m_d = 0.486 \pm 0.065$ (stat) ± 0.035 (syst) ps^{-1}. In addition, the statistical uncertainty is consistent with what we expect from the previous 1993-95 measurement by simply scaling for the increase in data. This provides

further confirmation that the statistical uncertainty is reasonable.

6.5   Combination with other analyses

The inclusive semileptonic analysis is only one of several analyses performed at SLD. All analyses at SLD use the same initial state tagging technique. The final state flavor determination and proper time reconstruction, however, depend on the specific analysis. Currently, two other techniques are added to the inclusive lepton technique presented here to obtain the SLD combined result. The Lepton+D analysis also uses the charges of leptons produced in semileptonic B decays to tag the final state b flavor. In this case, however, topological vertexing is also used to partially reconstruct a D vertex downstream from the selected lepton. This vertex is required to have a reconstructed mass < 1.95 GeV. The lepton p_T with respect to the D vertex line of flight is required to be greater than 0.9 GeV/c which decreases backgrounds from $b \to c \to l$. The B decay position is located by intersecting the D vertex momentum with the lepton. A double gaussian fit to the decay length residual yields a core width of 90 μm and tail width of 283 μm with a 60% core fraction. Finally, the B vertex charge is required to be 0 to enhance the B_s^0 fraction. The average final state correct tag probability is about 91%. The Lepton+D analysis also uses the boost algorithm described in section 4.7.2. The efficiency of the Lepton+D analysis is lower than that of the analysis described here but the decay length, proper time and final state tag are all improved.

The third technique is called the Charge Dipole and is unique to SLD. This analysis attempts to exploit the charge structure of the dominant $b \to c$ decay sequence by reconstructing two, well separated topological vertices (in addition to the e^+e^- interaction vertex) corresponding to the B and D decay vertices in the $B \to D + X$ decay chain. We require the probability of a single vertex fit to all charged tracks to be less than 1%. The charged tracks are then arranged in all two vertex combinations and the one with the lowest χ^2 is selected. The total vertex mass is required to be greater than 2 GeV and the sum of the charges of all tracks associated with the B decay is required to be 0 to enhance the B_s^0 fraction. The downstream vertex is

assumed to be the D while the upstream vertex is the B. The charge dipole is then calculated as,

$$\delta q = L_{BD} \times \text{sign}(Q_D - Q_B) \tag{6.9}$$

where Q_B and Q_D are the charges of the B and D vertices and L_{BD} is the distance between them. Positive values of δq indicate a final state b quark. The purity of the tag depends on the magnitude of the charge dipole and reaches a maximum of about 80%.

To obtain a final limit on B_s^0 mixing the various analyses must be combined. The combination of independent amplitude fits is fairly simple. However, all of the SLD analyses were performed on the same data so we must be careful in accounting for the overlap. The method adopted here was to rank the analyses in order of sensitivity per event. Each analysis was then required to remove those events already selected by a more sensitive analysis. The results, in order of decreasing sensitivity, were: Lepton+D, Lepton+Tracks, Charge Dipole. Therefore, this analysis was required to remove events already selected by the Lepton+D.

The statistical overlap with the Lepton+D events was determined to be 11% in 1996, and 16% in both 1997 and 1998. Therefore, there was a total loss in statistics of about 15%. The most significant effect, however, is the loss of B_s^0 events since the Lepton+D technique requires the vertex charge to be 0 in order to increase the B_s^0 fraction. The resulting Monte Carlo sample has a $B_s^0 \to l^\pm$ fraction of $\sim 7.7\%$ as compared to $\sim 8.8\%$ in the full sample or a 12.5% relative change. Technically, all of the Monte Carlo parametrizations that go into the likelihood fits should be reevaluated after the removal of the Lepton+D events. This was checked and no significant change could be found in resolution or vertex efficiency shapes. Therefore, only the assumed sample composition was changed after removing these events.

A comparison of the SLD mixing analyses is presented in table 6.5. The combined SLD amplitude fit is shown in figure 6.9. We are able to exclude at 95% CL: $\Delta m_s < 5.3\text{ps}^{-1}$ and $6.0\text{ps}^{-1} < \Delta m_s < 11.5\text{ps}^{-1}$. The sensitivity of the experiment is 6.6 ps^{-1}. Therefore, a portion of the excluded range is due to a negative fluctuation in the measured amplitude. Note also that the LEP experiments have already excluded the small range between 5.3 and 6.0 ps^{-1} that is missed by SLD.
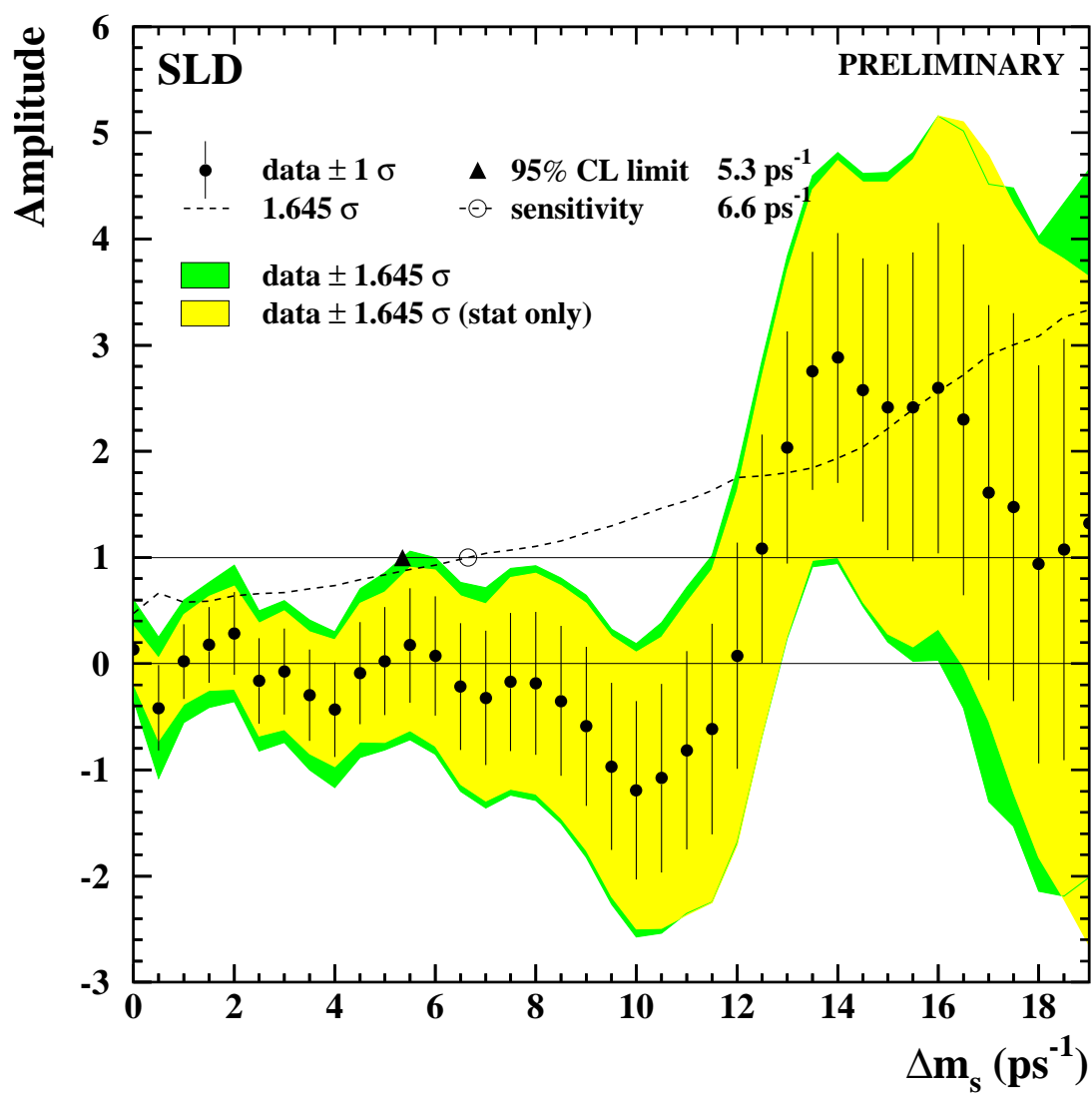
Figure 6.9: SLD combined amplitude fit for the full 96-98 data set.

Table 6.5: Summary and comparison of the SLD mixing analyses

	Lepton+D	Lepton+Tracks	Charge Dipole
B_s^0 Fraction	0.15	0.10	0.15
$udsc$ fraction	0.02	0.075	0.025
mistag rate	0.21	0.31	0.38
σ_L^{core} (μm)	90	125	141
σ_L^{tail} (μm)	283	520	479
L core fraction	0.60	0.62	0.60
σ_p^{core} (%)	0.07	0.09	0.08
σ_p^{tail} (%)	0.22	0.30	0.26
Boost core fraction	0.60	0.66	0.60
Sample size	2352	8864	8211

6.6   Conclusions

A combined world average has been compiled by the B Oscillations Working Group from the latest LEP, CDF and SLD results which includes the work presented in this thesis [32]. The averaging procedure takes into account common systematic uncertainties as well as differing parameter values assumed by the various analyses. The combined amplitude plot is shown in figure 6.10. The 95% confidence level allowed region is now:

$$\Delta m_s > 12.3 \text{ ps}^{-1}. \tag{6.10}$$

The structure of the amplitude in the region around 15 ps^{-1} is greater than 1.645 standard deviations from 0 and is becoming suggestive of a B_s^0 mixing signal. The greatest deviation from 0 is at 14.75 ps^{-1} with a significance of 2.6 standard deviations. This is consistent with 0 at a single sided confidence level of 0.4%. However, the measured amplitudes values are well above 1 and, therefore, out of the physical region. To be conservative, the non-physical region can be excluded from the confidence level calculation. In that case, the amplitude is consistent with 0 at 3.1%.

The current measurements of Δm_d and limits on Δm_s have been utilized to constrain the ρ and η parameters of the CKM matrix in the Wolfenstein parametrization
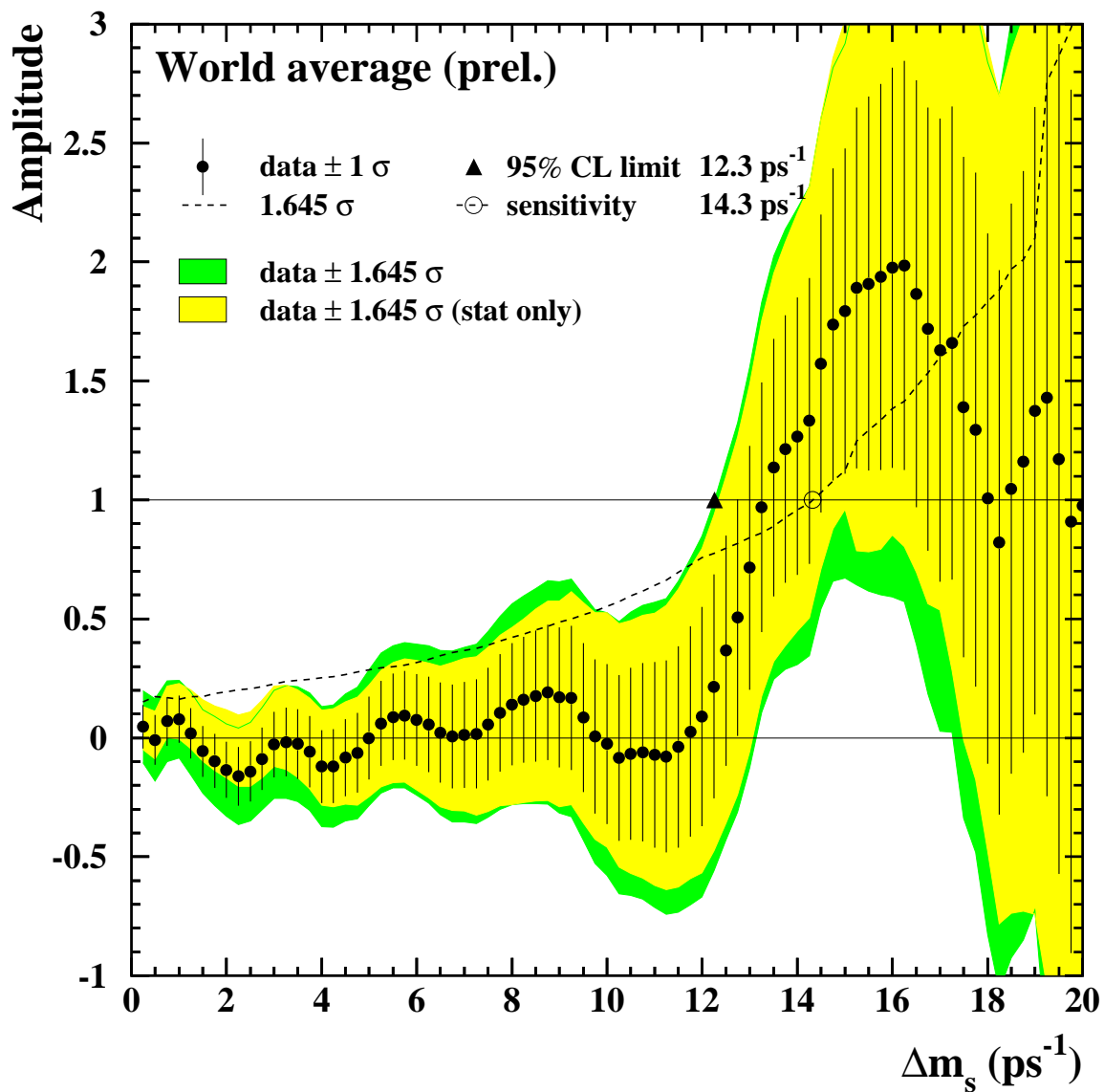
Figure 6.10: World Average amplitude vs Δm_s as of May 99 including results from LEP, CDF, and SLD. A 95% confidence level lower limit on Δm_s is set at 12.3 ps^{-1}.
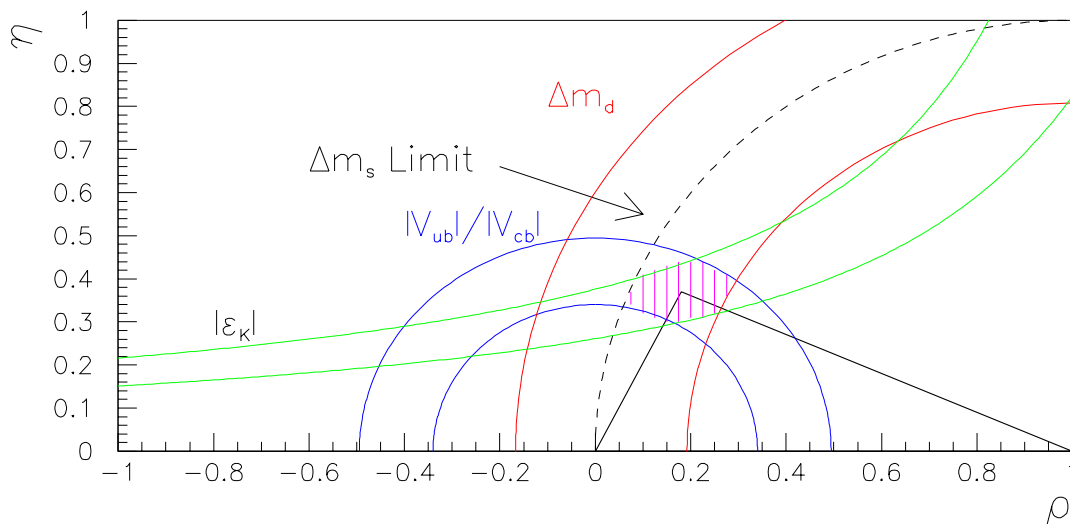
Figure 6.11: Current constraints on ρ and η.

as discussed in section 1.4.1 [18]. The results are shown in figure 6.11. The bands are the $\pm 1\sigma$ allowed regions of the determined by the measurements of Δm_d, ϵ_K, and $|V_{ub}/V_{cb}|$. The dashed curve represents the current lower limit on Δm_s at 12.3 ps^{-1}. The region to the left of this curve is excluded at 95% confidence level. Note that the limit on Δm_s already excludes a significant portion of the remaining allowed region from the Δm_d, ϵ_K, and $|V_{ub}/V_{cb}|$ measurements. As limits on Δm_s increase, this curve will move to the right until a measurement is made.

In conclusion, SLD has made significant progress towards a measurement of B_s^0 mixing. Despite a factor of ~ 25 deficit in statistics as compared to the LEP experiments, SLD is now producing competitive results. This is made possible by three main features of the SLC/SLD:

- The highly polarized electron beam which provides a pure and highly efficient initial state tag.

- The small, stable beam spot of the SLC.

- The precise pixel vertex detector VXD3 which allows excellent decay length reconstruction. Due to SLD's precise vertexing we obtain very good proper

time resolution. Therefore, the SLD results have made a particularly strong impact on the world averages at large Δm_s.

SLD is currently updating the results shown here due to a recent upgrade in the charged tracking reconstruction. Significant improvements in the decay length resolution (20-30%) are expected for all analyses. In addition, two new analyses are currently in development and should be included in the SLD average in the near future. The first attempts to explicitly reconstruct a D_s^+ in the $\phi\pi^+$ and $K^{*0}K^+$ decay modes. CRID information may be used to identify the charged kaons. Reconstructing the D_s^+ decay exclusively produces a large B_s^0 fraction of $\sim 33\%$. In addition, excellent decay length resolution is obtained. Initial results indicate a core decay length residual of about 50 μm with 160 μm tails.

The second analysis in development is called the lepton-kaon analysis. It is sensitive to the decays,

$$
\begin{aligned}
B_s^0 &\to D_s^{**-} \ l^+\nu \\
D_s^{**-} &\to K^- D^{*0}
\end{aligned}
\tag{6.11}
$$

which produce opposite sign lepton-kaon pairs. B^+ and B_d^0 decays produce predominately same sign lepton-kaon pairs and are thus suppressed. This analysis also results in a large B_s^0 fraction of $\sim 26\%$. The decay length resolution is expected to be 70 μm in the core and 330 μm in the tails. Although the data sample is expected to be small for these analyses, the gain in B_s^0 fraction means they should make a significant contribution to the SLD average.

In the coming years the world sensitivity to Δm_s should increase dramatically. Figure 6.12 shows B_s^0 mixing sensitivities of various experiments now and in the near future. Note that the SLD entry includes the tracking upgrades and additional analyses mentioned above. Therefore, the expected SLD sensitivity for 1999 is larger than presented in this thesis. Beyond 2000, several experiments at the Tevatron and LHC expect to reach sensitivities that are likely to produce B_s^0 mixing discoveries. Combined with upcoming results from the B factories, the future of b physics promises to be very interesting.
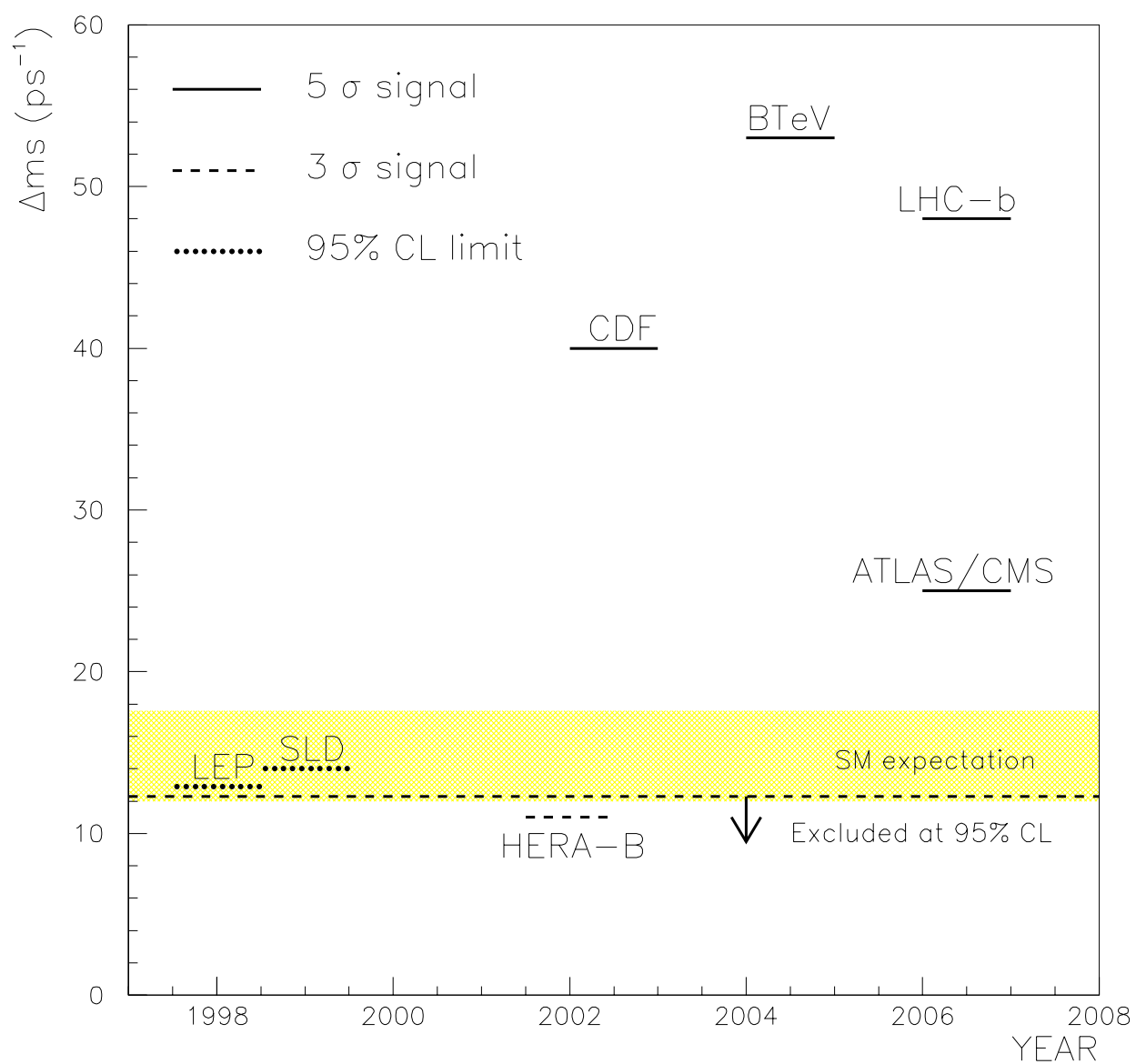
Figure 6.12: Expected sensitivity to B_s^0 mixing from various collaborations in the coming years.

Bibliography

[1] Particle Data Group. Review of Particle Physics. *Eur. Phys. J. C*, 3(1-4), 1998.

[2] Super-Kamiokande Collaboration. Evidence for Oscillation of Atmospheric Neutrinos. *Phys. Rev. Lett.*, 81:1562, 1998.

[3] D. Bailin and A. Love. *Introduction to Gauge Field Theory*. IOP Publishing Ltd, 1993.

[4] Vernon D. Barger and Roger J.N. Phillips. *Collider Physics*. Addison-Wesley Publishing Company, Inc., 1997.

[5] L. Wolfenstein. Parametrization of the Kobayashi-Maskawa Matrix. *Phys. Rev. Lett.*, 51:1945, 1983.

[6] Gordon Kane. *Modern Elementary Particle Physics: The Fundamental Particles and Forces?* Perseus Books Publishing, L.L.C., 1993.

[7] CDF Collaboration. A Measurement of $\sin 2\beta$ from $B \to J/\psi K_s^0$ with the CDF Detector, 5 February 1999. CDF/PUB/BOTTOM/CDF/4855.

[8] David Griffiths. *Introduction to Elementary Particles*. John Wiley and Sons, Inc., 1987.

[9] Halzen and Martin. *Quarks and Leptons: an Introductory Course in Modern Particle Physics*. John Wiley and Sons, Inc., 1984.

[10] Jorge P. Fernandez. Measurements of A_{lr}, A_{lepton}, and A_b from SLD , 5-9 Jan 1999. SLAC-PUB-8081.

[11] M. Gell-Mann and A. Pais. Behavior of Neutral Particles Under Charge Conjugation. *Phys. Rev.*, 97(3):1387–1389, 1955.

[12] K. Lande *et al.* Observation of Long-Lived Neutral *V* Particles. *Phys. Rev.*, 103:1901–1903, 1956.

[13] Sheldon Stone, editor. *B Decays*. World Scientific Publishing Co., 1992.

[14] C. Jarlskog, editor. *CP Violation*. World Scientific Publishing Co., 1989.

[15] M. Beneke, G. Buchala and I. Dunietz. Mixing Induced CP Asymmetries in Inclusive *B* Decays, September 1996. SLAC-PUB-7275.

[16] M. Beneke and G. Buchalla and I. Dunietz. The Width difference in the $B_s - \bar{B}_s$ system. *Phys. Rev.*, D54:4419–4431, 1996.

[17] M. Beneke, G. Buchalla, C. Greub, A. Lenz, and U. Nierste. Next-to-leading order QCD corrections to the lifetime difference of B(s) mesons. *Phys. Lett.*, B459:631, 1999.

[18] F. Parodi, P. Roudeau, and A. Stocchi. Constraints on the parameters of the CKM matrix by end 1998, 1999.

[19] A. Ali and D. London. CP violation and flavor mixing in the standard model: 1996 update. *Nucl. Phys. Proc. Suppl.*, 54A:297–308, 1997.

[20] ARGUS Collaboration. Observation of $B^0 - \bar{B}^0$ Mixing. *Phys. Lett. B*, 192(1,2):245, 1987.

[21] CLEO Collaboration. $B^0 \bar{B}^0$ Mixing at the $\Upsilon(4S)$. *Phys. Rev. Lett.*, 62(19):2233, 1989.

[22] The SLD Collaboration. Measurement of time dependent $B_d^0 - \bar{B}_d^0$ mixing using inclusive semileptonic decays, July 25-31 1996. SLAC-PUB-7228.

[23] The SLD Collaboration. Preliminary Measurements of Time Dependent $B_d^0 - \bar{B}_d^0$ Mixing Using Topology and Charge Selected Semi-Leptonic *B* Decays, July 25-31 1996. SLAC-PUB-7229.

[24] The SLD Collaboration. Preliminary Measurements of the Time Dependence of $B_d^0 - \bar{B}_d^0$ Mixing with Kaon and Charge Dipole Tags, July 25-31 1996. SLAC-PUB-7230.

[25] ALEPH Collaboration. Improved Measurement of the $B_d^0 - \bar{B}_d^0$ Oscillation Frequency. *Z Phys. C*, 75:397, 1997.

[26] DELPHI Collaboration. Measurement of $B_d^0 - \bar{B}_d^0$ Oscillations. *Z Phys. C*, 76:579, 1997.

[27] L3 Collaboration. Measurement of the $B_d^0 - \bar{B}_d^0$ Oscillation Frequency. *Eur. Phys. J. C*, 5:195, 1998.

[28] The OPAL Collaboration. An Updated Study of B Meson Oscillations using Dilepton Events. *Z Phys. C*, 76:417, 1997.

[29] The OPAL Collaboration. A Study of B Meson Oscillations Using Hadronic Z^0 Decays Containing Leptons. *Z Phys. C*, 76:401, 1997.

[30] The OPAL Collaboration. A Measurement of the B_d^0 Oscillation Frequency Using Leptons and $D^{*\pm}$ Mesons. *Z Phys. C*, 72:377, 1996.

[31] CDF Collaboration. Measurement of $B^0 - \bar{B}^0$ Oscillation Frequency Using $\pi - B$ Meson Charge-Flavor Correlations in $p\bar{p}$ Collisions at $\sqrt{s} = 1.8$ TeV. *Phys. Rev. Lett.*, 80:2057, 1998.

[32] The LEP B Oscillations Working Group. Combined Results on B^0 Oscillations from Winter 1999 Conferences, May 21 1999.

[33] The ALEPH Collaboration. Study of the $B_s^0 \bar{B}_s^0$ oscillation frequency using $D_s^- l^+$ combinations in Z decays. *Phys. Lett. B*, 377:205, 1996.

[34] The ALEPH Collaboration. Study of the B_s^0 oscillations and lifetime using fully reconstructed D_s^- decays. *Eur. Phys. J C*, 4:367, 1998.

[35] The ALEPH Collaboration. Search for B_s^0 oscillations using inclusive lepton events. *Eur. Phys. J C*, 7:553, 1999.

[36] DELPHI Collaboration. Search for $B_s^0 - \bar{B}_s^0$ oscillations. *Phys. Lett. B*, 414:382, 1997.

[37] OPAL Collaboration. A Study of B_s^0 Meson Oscillation Using Hadronic Z^0 Decays Containing Leptons, 22 June 1999. CERN-EP/99-085 Submitted to Eur. Phys. J C.

[38] CDF Collaboration. A Search for $B_s^0 - \bar{B}_s^0$ Oscillations Using the Semileptonic Decay $B_s^0 \rightarrow \phi l^+ X \nu$. *Phys. Rev. Lett.*, 82:3576, 1999.

[39] The SLD Collaboration. Time Dependent $B_s^0 - \bar{B}_s^0$ Mixing Using Inclusive and SemiLeptonic B Decays at SLD, July 23-29 1998. SLAC-PUB-7885.

[40] M.Woods. The polarized electron beam for the SLAC Linear Collider, September 10-14 1996. SLAC-PUB-7320.

[41] Paul Emma. The Stanford Linear Collider, May 1-5 1995. SLAC-PUB-95-6866.

[42] Martin Breidenbach. SLC and SLD-Experimental Experience with a Linear Collider, April 26-30 1993. SLAC-PUB-6313.

[43] John T. Seeman. Status of the Stanford Linear Collider, July 25 - August 2 1992. SLAC-PUB-6127.

[44] P.Raimondi et al. Recent Luminosity Improvements at the SLC, 1998.

[45] M.Woods. The scanning Compton polarimeter for the SLD experiment, September 9 1996. SLAC-PUB-7319.

[46] P.L. Reinertsen. Precise Measurement of the Weak Mixing Angle from Leptonic Polarization Asymmetries at the SLD Experiment, September 14-17 1998. SLAC-PUB-8029.

[47] K.Abe et al. Design and performance of the SLD vertex detector: a 307 Mpixel tracking system. *Nucl. Instr. and Meth. in Phys. Res.*, A(400):287–343, 1997.

[48] SLD. *SLD Design Report*, May 1984.

[49] M.D. Hildreth et al. Performance of the SLD Central Drift Chamber. In *IEEE Transactions of Nuclear Science, Proceedings of the IEEE Nuclear Science Symposium*, October 30 - November 5 1994.

[50] David W.G.S. Leith. Status of Cherenkov Ring Imaging Systems. *Nucl. Instr. and Meth. in Phys. Res.*, A(265):120–136, 1988.

[51] M. Cavalli-Sforza et al. Construction and testing of the SLD Cerenkov Ring Imaging Detector, January 15-19 1990. SLAC-PUB-5123.

[52] SLD Collaboration. Request for SLD Run Extension. Technical report, Stanford Linear Accelerator Center, August 1998.

[53] K.Abe et al. Obtaining physics results from the SLD CRID. *Nucl. Instr. and Meth. in Phys. Res.*, A(371):195–199, 1996.

[54] D. Axen et al. The lead-liquid argon sampling calorimeter of the SLD detector. *Nucl. Instr. and Meth. in Phys. Res.*, A(328):472–494, 1993.

[55] Eric Vella. SLD Liquid Argon Calorimeter, September 29-October 2 1992. SLAC-PUB-5953.

[56] David C. Williams. *The Left-Right Forward-Backward Asymmetry for b quarks at the SLD*. PhD thesis, Massachussetts Institute of Technology, 1994.

[57] S.C. Berridge et al. First Results from the SLD Silicon Calorimeters. *IEEE Trans.Nucl.Sci.*, 39:1242–1248, 1992.

[58] Torbjorn Sjostrand. High-Energy-Physics Event Generation with PYTHIA 5.7 and JETSET 7.4. *Comput. Phys. Commun.*, 82:74, 1994.

[59] B. Andersson, G. Gustafson, G. Ingelman, and T. Sjostrand. Parton fragmentation and string dynamics. *Phys. Rept.*, 97:31, 1983.

[60] C. Peterson *et al.* . *Phys. Rev. D*, 27:105, 1983.

[61] CLEO *B* decay model provided by P. Kim and the CLEO Collaboration.

[62] Nathan Isgur, Daryl Scora, Benjamin Grinstein, and Mark B. Wise. Semileptonic B and D Decays in the Quark Model. *Phys. Rev.*, D39:799, 1989.

[63] R. Brun, R. Hagelberg, M. Hansroul, and J. C. Lassalle. Geant: Simulation program for particle physics experiments. user guide and reference manual. CERN-DD-78-2-REV.

[64] M. J. Corden, C. H. Georgiopoulos, R. Brun, F. Bruyant, and J. L. Dekeyser. Progress towards a vectorized version of the geant monte carlo program. *Comput. Phys. Commun.*, 57:268, 1989.

[65] John Coller. private communication.

[66] J.D. Fox. Electronic Technology and the SLD Detector. *Nuclear Physics B(Proc. Supp.)*, 23A:227–238, 1991.

[67] John M. Yamartino. Hadronic Event Selection Using the LAC, November 4 1992. SLD Physics Note 14.

[68] P.N. Burrows et al. Estimate of Combined Triggering and Selection Efficiency for Hadronic Events. Technical report, SLD, 1993. SLD Note 229.

[69] K. Abe et al. Measurements of R_b with impact parameters and displaced vertices. *Phys. Rev. D*, 53(3):1023–1038, 1996.

[70] JADE Collaboration. Experimental Investigation of the Energy Dependence of the Strong Coupling Strength. *Phys. Lett. B*, 213(2):235–241, 1988.

[71] Donatella Falciai. Electron Identification in SLD with a Neural Network. Technical report, University of Perugia, December 1995. SLD Physics Note 44.

[72] Leif Lonnblad Carsten Peterson, Thorsteinn Rognvaldsson. JETNET 3.0: A Versatile Artificial Neural Network Package. *Comput. Phys. Commun.*, 81:185–220, 1994.

[73] Giampiero Mancinelli. Improved Muon Identification at SLD. Technical report, Rutgers University, February 1998. SLD Physics Note 65.

[74] C.Baltay M.Liu, S.Manly. Statistical and Topological Approach to B Vertex Reconstruction. Technical report, Yale University, 1996. SLD Physics Note 49.

[75] Ming Xiong Liu. *Measurement of Time Dependent B_d^0 Mixing at SLD*. PhD thesis, Yale University, 1997.

[76] Eric Church. *A measurement of the b quark fragmentation function at $\sqrt{Q^2} = 45.6$ GeV*. PhD thesis, University of Washington, 1996.

[77] Saul Gonzales. First-Pass Determination of the Energy Scale in the SLD. Technical report, SLD, October 1993. SLD Physics Note 24.

[78] David J. Jackson. A topological vertex reconstruction algorithm for hadronic jets. *Nucl. Instr. and Meth. in Phys. Res.*, A(388):247–253, 1997.

[79] David Jackson. ZVTOP - A Topological Vertex Finding Algorithm for Hadronic Jets. Technical report, Rutherford Appleton Laboratory, 1995. SLD Physics Note 37.

[80] H.G. Moser and A. Roussarie. Mathematical methods for $B^0\bar{B}^0$ oscillation analyses. *Nucl. Instr. and Meth. in Phys. Res.*, A(384):491–505, 1997.

[81] The ALEPH Collaboration. A Measurement of $|V_{cb}|$ from $\bar{B}^0 \to D^{*+}l^-\bar{\nu}_l$. *Phys. Lett. B*, 359:236, 1995.

[82] The ALEPH Collaboration. Measurement of the b baryon lifetime and branching fractions in Z decays. *Eur. Phys. J. C*, 2:197, 1998.

[83] The ALEPH Collaboration. Strange b baryon production and lifetime in Z decays. *Phys. Lett. B*, 384:449, 1996.

[84] The DELPHI Collaboration. Production of Strange B-baryons decaying into $\Xi^\pm - l^\mp$ pairs at LEP. *Z. Phys. C*, 68:541, 1995.

[85] The ALEPH Collaboration. A measurement of the semileptonic branching ratio $BR(b - baryon \to pl\bar{\nu}X)$ and a study of inclusive $\pi^\pm$, $K^\pm$, $(p,\bar{p})$ production in Z decays, December 1998. CERN-PPE/97-153.

[86] The LEP Collaborations: ALEPH, DELPHI, L3 and OPAL, the LEP Electroweak Working Group and the SLD Heavy Flavor Group. A Combination of Preliminary Electroweak Measurements and Constraints on The Standard Model, 2 December 1997. CERN-PPE/97-154.

[87] M. Neubert and C.T. Sachrajda. Spectator Effects in Inclusive Decays of Beauty Hadrons. *Nucl. Phys. B*, 483:339, 1997.

[88] The LEP Collaborations: ALEPH, DELPHI, L3 and OPAL, the LEP Electroweak Working Group and the SLD Heavy Flavor and Electroweak Groups. A Combination of Preliminary Electroweak Measurements and Constraints on The Standard Model, 8 February 1999. CERN-EP/99-15.

[89] Victor Serbo. *Measurement of the Polarized Forward-Backward Asymmetry of b quarks at SLD*. PhD thesis, University of Wisconsin, 1997.

[90] Victor Serbo. private communication.